Thèse n° 7389

Invariant solutions underlying small- and large-scale structures in turbulent boundary layers

Présentée le 30 octobre 2020

à la Faculté des sciences et techniques de l'ingénieur
Complexité émergente dans les systèmes physiques
Programme doctoral en mécanique

pour l'obtention du grade de Docteur ès Sciences

par

Sajjad AZIMI

Acceptée sur proposition du jury

Prof. C. Ancey, président du jury
Prof. T. Schneider, directeur de thèse
Prof. L. S. Tuckerman, rapporteuse
Prof. C.-C. P. Caulfield, rapporteur
Prof. F. Gallaire, rapporteur

École
polytechnique
fédérale
de Lausanne

2020

To my family and Firoozeh for their constant support and love

Acknowledgements

I would like to acknowledge several great individuals without whom this thesis would have not been possible. First and foremost, I wish to express my gratitude to my supervisor, prof. Tobias M. Schneider. Thank you Tobias for providing this opportunity for me to join your team. You convincingly encouraged me to start this journey and never give up. Without your persistent support and guidance, I would have not been able to complete this thesis. I really appreciate your enthusiasm for solving scientific problems and your principle as a scientist to deliver accurate and high-quality results. Thanks for helping me with scientific writing and preparing this thesis.

I would like to pay my special regards to prof. Colm P. Caufield, prof. Françoise Gallaire, and prof. Laurette Tuckermann for reviewing this thesis and for their valuable comments on the manuscript. I also appreciate prof. Christophe Ancey for accepting to preside over the jury.

The work presented in this thesis is completed in the collaboration with a number of great researchers. I'm thankful to prof. John Gibson and Massimiliano Culpo for the collaboration on the progress of the code *channelflow 2.0*. I was lucky to collaborate also with prof. Carlo Cossu during my PhD. Thank you Carlo for all the scientific discussions that we had. I'm glad that I could benefit from your knowledge.

I'm indebted to my friends in ECPS who made the lab an ideal place for work. Thanks to all ECPS members, past and present, for making my PhD a wonderful journey. Thank you Petra for your assistance during this journey. Thank you Tobias Kreilos for the theoretical supports in the beginning of my PhD which made the initial phase of the PhD so much easier for me. Thank you Simon for your technical and theoretical guidance. I learnt a lot from you. Thank you Florian for sharing offices with me and for all the useful discussions about life and work. I really enjoyed working with you and I never forget all the memories in our older, old and new offices in EPFL. I'm sorry that I would insist to keep the window blinds half-open. Also, I really appreciate the time that you took to translate my abstract to German. Thank you Emilio for creating such incredible moments in ECPS. I will always remember your interesting politically-correct comments. Thank you Alessia for organising those wonderful group activities including the amazing barbecues and parties. Thank you Omid for helping me in the last year of my PhD, and for sharing the office space with me; I will never forget our talks and our Pasur breaks. Thanks to our postdocs, Mirko and Ayse, for your precious scientific and non-scientific tips and for being such good friends. I wish you all the best in your new careers. Thank you Geoffroy for helping me with my French language, especially for translating my abstract to French. Your time with us in Lausanne was short, but very instructive. I'm also

grateful to prof. John Kolinski and his group, EMSI, especially Ramin and Lebo. Thanks to LFMI members especially Gioelle, Isha, Eunok, and Shahab. Thank you for the shared group activities; we had so much fun together.
I wish to show my deepest gratitude to all my friends in Switzerland. A special thanks to Majid who was my flatmate in the first year of my PhD and gave me a lot of useful tips about living in Switzerland. I wish you a happy life with your lovely family. I'm thankful to all my friends; in particular, Abolfazl and Mohaddeseh, Naser and Lida, Hosein, and Saleh. Thank you for all the happy moments and all the unforgettable memories we shared.
Last but not least, I would like to thank my wife, Firoozeh, for her patience and understanding. Thank you for standing by me through the hard times. Thank you for your unconditional love and your countless sacrifices. I would not be able to finish this thesis without your support. I would also like to express my sincere gratitude to the rest of my family who believed in me and selflessly helped me become who I am now. I'm extremely grateful for your endless love and continual encouragement before and especially during my graduate studies.

Lausanne, 20 August 2020 Sajjad Azimi

Abstract

Flows of gases and liquids interacting with solid objects are often turbulent within a thin boundary layer. As energy dissipation and momentum transfer are dominated by the boundary layer dynamics, many engineering applications can benefit from an improved understanding of physical mechanisms underlying wall-bounded turbulence. Turbulence is often treated as a random stochastic process. The existence of recognisable flow structures with spatial and temporal coherence emerging within turbulent fluctuations however suggests a deterministic description in terms of interacting coherent flow structures. In transitional flows, coherent structures have been related to non-chaotic steady and time-periodic invariant solutions of the Navier-Stokes equations suggesting a description of turbulence as a chaotic walk through a forest of invariant solutions in the system's state space.

The aim of this thesis is to transfer this dynamical systems picture from transitional flows to turbulent boundary layers and to make progress towards describing fully developed wall-bounded turbulence in terms of invariant solutions of the flow equations. We construct invariant solutions underlying two types of important coherent structures in a parallel boundary layer. First, we identify travelling wave solutions of the fully nonlinear Navier-Stokes equations that capture universal small-scale coherent structures in the near-wall region. The travelling waves are asymptotically self-similar and scale in inner units when the Reynolds number approaches infinity. Together with theoretical arguments, the existence of the self-similar solutions suggests all state-space structures supporting turbulence may become self-similar and a dynamical systems description of near-wall turbulence at infinite Reynolds numbers may be possible.

Second, we describe coherent structures spanning the entire turbulent boundary layer. These so-called large-scale motions carry most of the turbulent kinetic energy and physically emerge within a background of small-scale fluctuations. Using spatial filtering approaches, we show that large-scale motions can be isolated from small-scale fluctuations. This allows us to associate large-scale coherent structures with exact solutions of filtered Navier-Stokes equations. We specifically construct several travelling waves and periodic orbits capturing self-sustained large-scale motions at friction Reynolds numbers beyond 1000. We thereby report the first invariant solutions capturing large-scale coherent structures in a boundary layer flow.

While individual invariant solutions successfully capture specific features of turbulence, large sets of invariant solutions and especially of periodic orbits are believed to provide the foundation for a quantitative and predictive description of turbulent flows in terms of invariant solutions. To allow for the construction of sufficiently complete libraries, we propose a novel

adjoint-based variational method for finding periodic orbits of spatio-temporally chaotic systems.
Most numerical results were obtained using *channelflow 2.0* (channelflow.ch). This open-source software was developed and published by a research team that includes the author of this thesis.

Keywords: turbulent boundary layers, invariant solutions, dynamical systems method, coherent structures, small-scale streaks, large-scale motions, direct numerical simulations, large-eddy simulations, variational methods

Résumé

Les écoulements de gaz ou liquides autour d'objets solides sont souvent turbulents à l'intérieur d'une fine couche limite. Comme la dissipation énergétique et le transfert de moment sont dominés par la dynamique de cette couche limite, une meilleure compréhension des mécanismes physiques mis en jeu dans la turbulence de parois bénéficierait à de nombreux problèmes en ingénierie. La turbulence est souvent traitée comme un processus stochastique aléatoire. Cependant, l'existence dans l'écoulement de structures distinctives, avec une cohérence au sein des fluctuations turbulentes à la fois spatiale et temporelle, suggère au contraire une dissipation déterministe en termes de structures cohérentes de l'écoulement et de leurs interactions. Dans les écoulements de transition, ces structures cohérentes ont été associées à des solutions des équations de Navier-Stockes non-chaotiques, permanentes, temporellement périodiques et invariantes. Ainsi, la turbulence se laisse interpréter dans l'espace d'états de la théorie des systèmes dynamiques comme une progression chaotique au travers d'une multitude de solutions invariantes.

L'objectif de cette thèse est de mobiliser cette représentation dynamique des écoulements de transition pour l'appliquer à la turbulence de couche limite, et d'améliorer la description de la turbulence pleinement développée en termes de solutions invariantes des équations de l'écoulement. Nous construisons ici dans une couche limite parallèle des solutions invariantes à la base de deux types de structures cohérentes importantes.Type equation here.

Premièrement, nous identifions les solutions en onde progressive des équations de Navier-Stokes, ici totalement non-linéaires, qui capturent les structures cohérentes universelles de petites échelles dans la région proche-paroi. Les ondes progressives sont asymptotiquement auto-similaires et s'alignent en unités internes quand le nombre de Reynolds tend vers l'infini. L'existence de ces solutions auto-similaires ainsi que des arguments théoriques indiquent que toute structure de l'espace d'états supportant la turbulence pourrait devenir auto-similaire et qu'une description de la turbulence proche-paroi au travers de la théorie des systèmes dynamiques serait possible.

Deuxièmement, nous décrivons les structures cohérentes qui traversent la couche limite turbulente dans sa totalité. Ces déplacements dits de grande échelle transportent la majorité de l'énergie cinétique turbulente et s'extraient physiquement des fluctuations de petite échelle. A l'aide d'approches de filtrage spatial, nous montrons que ces déplacements de grande échelle peuvent être isolés des autres fluctuations de petites échelles. Ceci nous permet d'associer ces structures cohérentes de grande échelle avec des solutions exactes des équations de Navier-Stokes filtrées. Nous construisons spécifiquement plusieurs ondes progressives et orbites

périodiques qui capturent les déplacements autonomes de grande échelle à des nombres de Reynolds de friction supérieurs à 1000. Nous reportons ainsi les premières solutions invariantes capturant les structures cohérentes de grande échelle dans un écoulement de couche limite.
Alors que des solutions invariantes seules réussissent à capturer une caractéristique spécifique de la turbulence, de grands ensembles de solutions invariantes, et particulièrement d'orbites périodiques, sont censés assurer la base d'une description quantitative et prédictive des écoulements turbulents en termes de solutions invariantes. Pour permettre la construction d'une bibliothèque suffisamment complète, nous proposons une nouvelle méthode variationnelle basée sur les adjoints afin de déterminer les orbites périodiques de systèmes chaotiques spatio-temporels.
La plupart des résultats numériques ont été obtenus en utilisant *channelflow 2.0* (channelflow.ch). Ce logiciel open-source a été développé et publié par un groupe de recherche dont fait partie l'auteur de cette thèse.

Mots clefs : couche limite turbulente, trainée-strie de petite échelle, déplacement a grande échelle, théorie des systèmes dynamiques, simulations numériques directes (DNS), simulations de grands tourbillons, méthodes variationnelles

Zusammenfassung

Strömen Gase oder Flüssigkeiten entlang fester Oberflächen, sind sie oft innerhalb einer dünnen Grenzschicht turbulent. Da Energiedissipation und Impulstransport sich hauptsächlich aus der Grenzschichtdynamik ergeben, können viele technische Anwendungen von einem verbesserten Verständnis der Grenzschichtturbulenz und ihrer zugrundeliegenden physikalischen Mechanismen profitieren. Turbulenz wird oft als zufälliger, stochastischer Prozess beschrieben. Die Existenz von beobachtbaren Strömungsstrukturen mit räumlicher und zeitlicher Kohärenz, welche in Gegenwart turbulenter Fluktuationen entstehen, legt wiederum eine deterministische Beschreibung anhand wechselwirkender kohärenter Strömungsstrukturen nahe. Im Zusammenhang von Turbulenzübergängen wurden kohärente Strukturen mit nicht-chaotischen, sprich stationären und zeitlich periodischen, invarianten Lösungen der Navier-Stokes-Gleichungen verknüpft. Dieser Zusammenhang suggeriert eine 'Dynamische Systeme Darstellung' von Turbulenz im Zustandsraum des Systems, in welcher Turbulenz anhand chaotischer Zustandsraumtrajektorien durch einen Wald von invarianten Lösungen beschrieben werden kann.

Das Ziel dieser Dissertation ist es, die 'Dynamische Systeme Darstellung', bekannt durch Anwendungen auf Turbulenzübergänge, zu Anwendungen auf turbulente Grenzschichten zu transferieren. Dieser Transferschritt leistet einen Beitrag zu einer Beschreibung von vollentwickelter Turbulenz durch invariante Lösungen der Strömungsgleichungen. Es werden hier invariante Lösungen konstruiert, welche zwei Typen von relevanten kohärenten Strukturen in einer parallelen Grenzschicht zugrunde liegen. Zum einen werden laufende Wellenlösungen der voll-nichtlinearen Navier-Stokes-Gleichungen konstruiert, welche universelle kleinskalig-kohärente Strukturen in der wandnahen Region erfassen. Die laufenden Wellen sind asymptotisch selbst-ähnlich und skalieren in inneren Einheiten, wenn die Reynoldszahl gegen Unendlich strebt. Es wird theoretisch argumentiert, dass die Existenz von selbstähnlichen Lösungen darauf hindeutet, dass alle Strukturen im Zustandsraum, welche turbulente Dynamik unterstützen, möglicherweise selbstähnlich werden. Somit wäre eine 'Dynamische Systeme Darstellung' von wandnaher Turbulenz bei unendlich großer Reynoldszahl möglich.

Zum anderen werden kohärente Strukturen beschrieben, welche über die gesamte turbulente Grenzschicht ausgedehnt sind. Diese großskaligen Bewegungen tragen die meiste kinetische Energie der Turbulenz und entstehen physikalisch aus einem Hintergrund von kleinskaligen Fluktuationen. Durch räumliches Filtern wird gezeigt, dass großskalige Bewegungen von kleinskaligen Fluktuationen isoliert werden können. Dieser Ansatz ermöglicht es, den großskalig-kohärenten Strukturen exakte Lösungen der gefilterten Navier-Stokes-Gleichungen

zuzuordnen. Insbesondere werden etliche laufende Wellenlösungen und periodische Orbits konstruiert, welche großskalige Bewegungen erfassen, die sich jenseits einer auf Wandschubspannungsgeschwindigkeit basierenden Reynoldszahl von 1000 selbst aufrechterhalten. In der Konsequenz beschreibt diese Arbeit erstmals invariante Lösungen, welche die großskalig-kohärenten Strukturen in einer turbulenten Grenzschichtströmung erfassen.
Während einzelne invariante Lösungen spezifische Turbulenzeigenschaften korrekt erfassen können, wird allgemein vermutet, dass nur eine große Menge von invarianten Lösungen – insbesondere von periodischen Orbits – die Grundlage für eine quantitative und vorhersagende 'Dynamische Systeme Darstellung' von turbulenten Strömungen sein kann. Um die Konstruktion ausreichend großer Sammlungen von Lösungen zu ermöglichen, schlägt diese Arbeit eine neue Variationsmethode basierend auf adjungierten Operatoren vor, mittels derer sich periodische Orbits eines raum-zeitlich chaotischen Systems finden lassen.
Die meisten numerischen Ergebnisse wurden mit Hilfe von *channelflow 2.0* (channelflow.ch) gewonnen. Diese Open-Source-Software wurde durch Beiträge des Autoren dieser Dissertation innerhalb einer Gruppe von Wissenschaftlern entwickelt und veröffentlicht.

Stichwörter: Turbulente Grenzschicht, Kleinskalige Streaks, Großskalige Bewegungen, Dynamische Systeme Theorie, Direkte Numerische Simulationen, Grobstruktursimulationen, Variationsmethode

Contents

1 Introduction

Contents

When the flow of liquids or gases reaches sufficiently high velocities, the flow becomes turbulent and is characterised by chaotically varying swirling motions varying in space and time. Since most practically relevant flows ranging from air flow in the trachea to atmospheric flows are turbulent, understanding physical processes driving the turbulent dynamics is key for many applications in engineering and beyond. A very common flow situation arises when a moving fluid interacts with a solid object. This includes the flow of air around cars and aircraft but also atmospheric flows interacting with the earth's surface and flows in turbines, where the working fluid interacts with the walls of the device. The presence of a solid wall, on which the flow has to satisfy no-slip boundary conditions, only influences the flow in a thin layer above the wall, which gives rise to the concept of a boundary layer. At sufficiently high flow speeds, the boundary layer is turbulent. In such a turbulent boundary layer flow, the flow is turbulent within the a thin layer close to the wall while far from the wall and outside the boundary layer, the flow may remain smooth and laminar. The intensity of turbulence is characterised by the dimensionless *Reynolds number Re* that measures the ratio of the flow inertia to the fluid viscosity. The higher the Reynolds number is, the larger is the range of length scales of energetic turbulent fluctuations within the turbulent flow. Most practically relevant turbulent boundary layer flows occur at very high Reynolds numbers so that the scale separation – the ratio between the largest and the smallest energetic swirling motions contributing to turbulent fluctuations – is large. Understanding the physical processes within turbulent boundary layer flow at high Reynolds numbers and the interaction of structures at different scales is of great importance for modelling and controlling turbulent flows. Increased understanding of boundary layer turbulence may obviously impact important technological

applications such as the design of next-generation wind farms and lower-drag aerial and marine vehicles.

1.1 Coherent structures in turbulent boundary layers

High-Reynolds-number turbulent boundary layers, schematically shown in figure 1.1(*a*), contain recognisable coherent structures that evolve in time and interact with other structures in the flow (Jiménez, 2018). These coherent structures exist at different length scales, forming a hierarchy. The distribution of coherent structures in a turbulent flow depends on their distance from the wall as postulated by Townsend's attached eddy hypothesis (Townsend, 1976; Marusic & Monty, 2019). Structures of a specific scale can be found at all heights, provided that their size is not larger than their distance from the wall. This idea is schematically shown in figure 1.1(*b*). Close to the wall, in the near-wall region, only small scale structures can be found while larger scales develop further away from the wall. The largest coherent structures of the turbulent flow span the entire turbulent domain and thus scale with the thickness of the turbulent boundary layer. The attached eddy hypothesis is supported by flow statistics such as power spectra. In the near wall-region, the power spectra peaks for small-scale structures while at larger distance from the wall, the energy peak shifts towards larger scales, as shown in figure 1.1(*c*).

The two distinct peaks in power spectra highlight the importance of two types of energetic structures at two scales: The small scale structures in the near-wall region as well as the largest structures with the size of the boundary layer thickness. Visualisations of turbulent flows show that these structures physically correspond to streamwise-elongated streaks, with spanwise modulations of the streamwise velocity. The streaky coherent structures in the near-wall region are visualised in figure 1.1(*d*). The large-scale streaky coherent structures with the size of the boundary layer thickness, known as large-scale motions, are shown in figure 1.1(*e*).

Universal near-wall dynamics: At sufficiently high Reynolds numbers, the small-scale coherent structures in the near-wall region show a universal spacing of $\lambda_z^+ \sim 100$, where length is measured in wall units (Kline *et al.*, 1967). Inner or wall units are based on the wall-shear τ_w and yield the characteristic scales of turbulent flows in the near-wall region, namely the friction velocity $u_\tau = \sqrt{\tau_w/\rho}$ and the viscous length unit $\delta_\tau = \nu/u_\tau$. Here ρ is the density and ν the kinematic viscosity of the fluid. At sufficiently high Reynolds numbers, the turbulent flow in the near-wall region is observed to be universal and independent of the flow parameters when lengths and velocities are rescaled by these characteristic scales of turbulence (Kim, Moin & Moser, 1987; Pope, 2000; Marusic, Mathis & Hutchins, 2010). Further away from the wall in the outer region, flow is not universal and depends on the specific parameters of the flow. The friction Reynolds number $Re_\tau = \delta_{99}/\delta_\tau$ measures the scale separation between the flow in the outer region and the small-scale structures in the near-wall region; Re_τ thereby characterises fully developed turbulence along a wall and indicates the strength of turbulence.

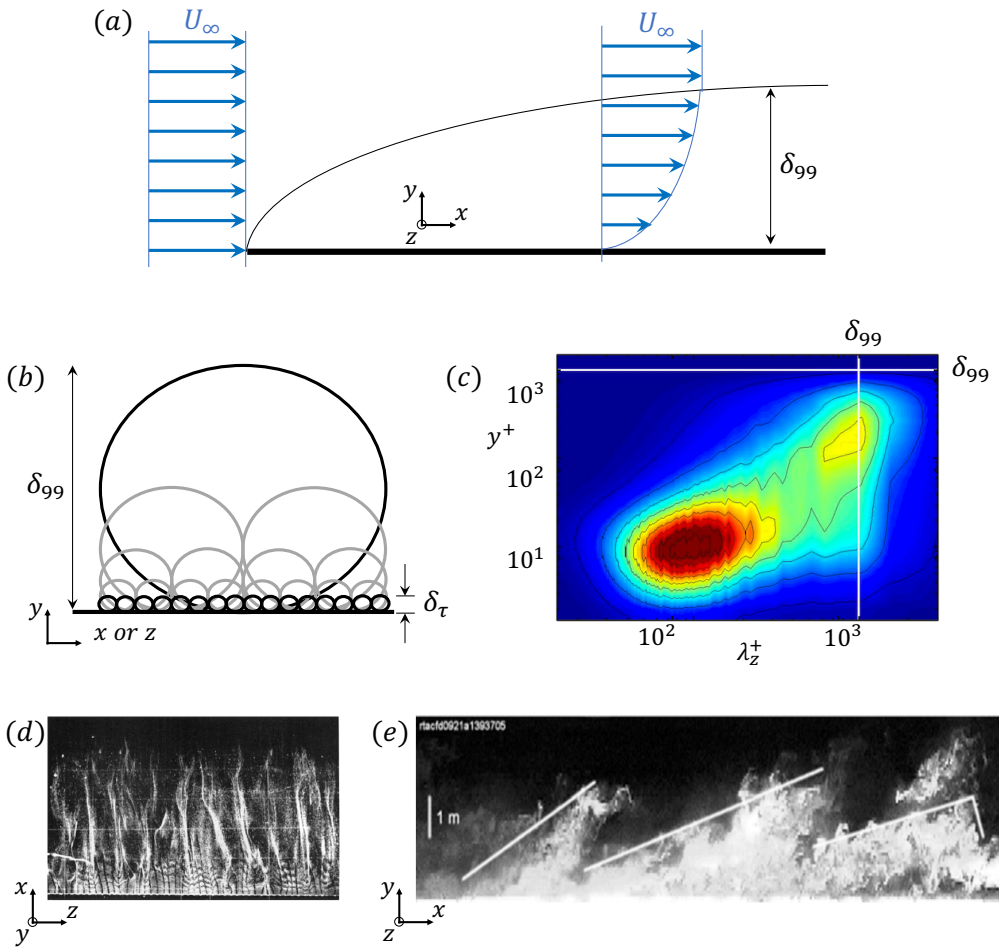

Figure 1.1 – (*a*) Schematic of the boundary layer flow. A free stream with velocity U_∞ interacts with a flat plate. The boundary layer thickness δ_{99} is defined as the distance from the wall where the mean velocity reaches 99% of the free stream velocity. (*b*) Schematic of Townsend's attached eddy hypothesis (adapted from Hwang (2015)). The length scale of all structures is proportional to their distance from the wall. The small-scale structures in the near-wall region (small thick black circles) scale with the characteristic length scale of turbulence in the near-wall region, the inner length scale δ_τ, while Large-scale motions, LSMs, (large thick black circle) scale with the thickness of the boundary layer δ_{99}. (*c*) Power spectra of a boundary layer flow at $Re_\tau = 1300$ in terms of the spanwise wave length λ_z^+ and the distance from the wall y^+ where the plus sign indicates that the variables are rescaled by δ_τ (from Schlatter *et al.* (2010)). For y^+ in the near wall region a peak associated with near-wall small-scale structures is observed, and further away from the wall a peak characterising LSMs emerges. (*d*) Small-scale streaky structures in the near-wall region, visualised by releasing H_2 gas bubbles in the flow (from Kline *et al.* (1967)). The flow is in the upward direction x. The flow in the near-wall region is dominated by elongated streaks oriented in downstream direction. (*e*) Large-scale motions, LSMs, visualised by releasing smoke in the turbulent boundary layer flow (from Hommema & Adrian (2003)). The flow is from left to right. These large-scale structures carry most of the turbulent kinetic energy.

Large-scale motions in the outer region: Further away from the wall in the *outer region*, large-scale streaky motions with the size of the boundary layer thickness δ_{99} develop. Large-scale motions carry a significant fraction of the turbulent kinetic energy and contribute significantly to the Reynolds shear stress (Guala, Hommema & Adrian, 2006). Despite their importance for global momentum transport, there is no general agreement on how the large-scale motions are generated and sustained in a turbulent flow. One hypothesis relates the formation of the large-scale motions to the collective effect of hairpin vortices which themselves are actively fed by the small-scale structures in the near-wall region (Adrian, 2007). Based on this idea, the generation of the large-scale motions is suggested to be a consequence of the dynamics of the active small-scale structures in the near-wall region. However, a growing number of numerical and experimental studies suggest that large-scale motions are not necessarily fed by the small-scale structures. Flores & Jiménez (2006) and Flores, Jiménez & Del Álamo (2007) show that the dynamics of large-scale motions is not affected by changing the wall roughness that destructs the near-wall small-scale dynamics. This observation implies that the generation of large-scale motions does not necessarily depend on the dynamics of small-scale structures in the near-wall region. Hwang & Cossu (2010*c*) and Rawat, Cossu, Hwang & Rincon (2015) damp the small-scale structures in confined turbulent flows by increasing the strength of the filtering in the large-eddy simulation paradigm. They show that large-scale motions can be isolated from the dynamics of the near-wall small-scale structures, and are thus self-sustained. Experimental results of (Kevin, Monty & Hutchins, 2019*b*) in a turbulent boundary layer flow suggest that the characteristics of large-scale motions are consistent with those of a coherent self-sustained process in the near-wall region Hamilton, Kim & Waleffe (1995); Waleffe (1995). This observation suggests that the large-scale motions can be self-sustained in the same way that the near-wall small-scale structures are self-sustained.

Dynamical system approach to turbulence: Turbulence is often described as a random stochastic process (Frisch, 1995). However, turbulence is governed by the deterministic Navier-Stokes equations and, as described above, turbulent wall-bounded flows contain recognisable structures that evolve and interact in the flow (Jiménez, 2018). This suggests an understanding of the turbulent dynamics in terms of interacting coherent structures as the building elements of the flow and leads to a deterministic treatment of turbulence as a chaotic dynamical system satisfying the flow equations. Within this dynamical systems picture, coherent structures are related to low-dimensional invariant sets in the state space of the flow equations. Turbulent trajectories approach these invariant sets and reside in their neighbourhoods for significant time. When a turbulent trajectory approaches such invariant sets, coherent structures emerge in the flow. The low-dimensional invariant sets supporting turbulence include steady and time-periodic solutions, known as invariant solutions, and their dynamical connections (Cvitanović, Artuso, Mainieri, Tanner & Vattay, 2016). Due to the remarkable similarity between invariant solutions and transiently observed coherent structures, the invariant solutions are often termed 'exact coherent structures'. Many invariant solutions of the three-dimensional Navier-Stokes equations have successfully been computed

for confined flows and at low Reynolds-number transitional regime. They are shown to be transiently visited by the dynamics (Gibson, Halcrow & Cvitanović, 2008; Kawahara, Uhlmann & van Veen, 2012; Suri, Tithof, Grigoriev & Schatz, 2017; Reetz & Schneider, 2020*a*) and capture many characteristic features of transitional flows (Avila, Mellibovsky, Roland & Hof, 2013; Reetz, Kreilos & Schneider, 2019). Individual invariant solutions are shown to be able to capture statistics of turbulent flows (Kawahara & Kida, 2001).

In this thesis, we aim for transferring the dynamical system concepts that have proven useful for describing turbulence at the transitional regime, to fully turbulent boundary layers. First we study the universal dynamics of turbulent flows in the near-wall region at high Reynolds numbers by identifying invariant solutions that capture the self-similarity of small-scale coherent structures. Second, we study the dynamics of large-scale motions in boundary layer flows. Whether the large-scale motions in turbulent boundary layer flows are energetically driven by small-scale structures or if they can be self-sustained is not known. We follow the approach of Hwang and Cossu (Hwang & Cossu, 2010*c*), and filter out small-scale structures to isolate the dynamics of large-scale motions. We thereby show that large-scale motions are self-sustained and directly extract energy from the mean shear. We further study invariant solutions of the filtered equations that represent the dynamics of large-scale motions and thereby apply the dynamical systems approach not to the standard Navier-Stokes equations but the filtered evolution equations that underlie the Large-Eddy-Simulation paradigm. The results of this thesis are a step towards a full deterministic description of wall-bounded turbulence at high Reynolds numbers. While individual invariant solutions can capture specific properties of the turbulent flow, a full deterministic description that quantitatively predicts statistical properties would require a large number of invariant solutions and specifically a large number of periodic orbits. To pave the way for computing large sets of periodic orbits, we develop a robust adjoint-based variational method, that is matrix-free and globally convergent.

The system – a parallel boundary layer: Instead of considering a developing boundary layer, we choose to study the asymptotic suction boundary layer flow, ASBL, (Schlichting, 2004). In the ASBL homogeneous suction through a porous wall arrests the growth of the boundary layer thickness creating a parallel boundary layer with continuous translational symmetry in the streamwise direction. The translational symmetry simplifies the numerical simulations and allows for travelling wave solutions to exists. Compared to other parallel flows such as channel flow, in ASBL the kinetic energy peak associated with large-scale motions is relatively weak when compared to the near-wall energy peak (Schlatter & Örlü, 2011; Bobke, Örlü & Schlatter, 2016). Consequently, ASBL is dominated by the strong near-wall small-scale structures. The advantage of this property for our study is twofold; First, since the large-scale motions are weak compared to the energetically strong small scale structures in the near-wall region, finding a branch of exact invariant solutions that underlies the universal dynamics in the near-wall region might be easier. Even at finite Reynolds numbers, the influence of non-universal large-scale motions on the universal small-scale motions is reduced compared to other flows. Second, this property of the ASBL may suggest that the weak large-scale motions are driven by

the strong small-scale structures in the near-wall region. Showing that the weak large-scale motions of the ASBL are self-sustained even in the presence of strong near-wall small-scale structures strongly suggest that the large-scale motions are self-sustained in all boundary layer flows. Moreover, global conservation laws in the ASBL allow to analytically express inner scales in terms of the outer scales and the Reynolds number. One can consequently study the near-wall turbulent dynamics in a domain with prescribed size measured in inner units and thereby identify invariant solutions capturing the universal self-similar scaling of near-wall turbulence.

1.2 Numerical dynamical systems analysis

Within the dynamical system perspective of turbulence, the turbulent flow corresponds to a chaotic walk between dynamically connected unstable invariant solutions that, together with their interconnected stable and unstable manifolds, form the backbone of a chaotic set supporting the turbulent dynamics. Invariant solutions including equilibria, travelling waves, periodic orbits and relative periodic orbits satisfy the equation

$$\sigma f(\mathbf{u}, T) - \mathbf{u} = 0,$$

where σ is a symmetry operator and $f(\mathbf{u}, T)$ is the evolution of the velocity field $\mathbf{u}$ under the governing equations of motion over the time interval T. A description of the turbulent flow based on invariant solutions requires identifying invariant solutions by numerically solving this equation.

At finite Reynolds number Re, motions smaller than the Kolmogorov scale are damped by viscosity. Consequently a turbulent flow satisfying the Navier-Stokes equations for finite Re can be described by a finite number of degrees of freedom and the dynamics is governed by a finite dimensional dynamical system (Kawahara *et al.*, 2012). The number of degrees of freedom for the dynamical system grows with $Re^{9/4}$ (Landau & Lifschitz, 1959). Consequently, even at the transitional regime with $Re \sim 100$, the number of degrees of freedom is in the order of $10^5 \sim 10^6$. Thus, analysing the dynamical system of turbulence especially at high Reynolds numbers requires fast and efficient numerical tools. To handle the high-dimensional dynamical systems, a team of developers including the author of this thesis have developed and implemented the required numerical tools in the open-source software *channelflow 2.0*. The software solves the Navier-Stokes equations and provides state-of-the-art numerical tools for dynamical system analysis including tools to identify invariant solutions, continuation tools for constructing bifurcation diagrams, and stability analysis tools. The structure of the code allows for straightforward extensions of the code. Thereby not only the standard Navier-Stokes equations but also modified equations can be treated. We extended the code to perform large-eddy simulations required for filtering large-scale motions. The code structure of *channelflow 2.0* and details of the LES extension are discussed in chapter 2.

1.3 Structure of the thesis

Following this introduction, the flow system as well as the numerical tools are introduced. The structure of the developed software and selected numerical methods that have been implemented to improve the performance of the code are explained. In the final section of chapter 2, the extension of the software for performing large-eddy simulations is discussed. The results of the research are then given in the next five chapters:

In Chapter 3, the universal dynamics of turbulence in the near-wall region is studied. We show that the universal dynamics can be captured by exact invariant solutions. These invariant solutions can be continued to high Reynolds number where they become asymptotically self-similar.

In chapter 4, we isolate the dynamics of large-scale motions from small-scale structures by filtering the equations of motion. We thereby demonstrate that large-scale motions in turbulent boundary layer flows are self-sustained. The temporal dynamics of large-scale motions is studied and shown to differ from the dynamics of LSMs in confined flows.

The dynamical system of the filtered equations describe the dynamics of the large-scale motions deterministically. Invariant solutions of the filtered equations and their dynamical connections can thus support the dynamics of LSMs. Chapter 5 presents a number of exact invariant solutions of the filtered equations. These invariant solutions capture several self-sustained processes of large-scale motions.

In chapter 6 we study the symmetries of the ASBL. Specifically, we show that the symmetries of the ASBL cannot support the mechanism of homoclinic snaking in shear flows (Schneider, Gibson & Burke, 2010*a*). Homoclinic snaking is a mechanism by which a localised solution grows additional structures at its fronts while undergoing a sequence of saddle-node bifurcations (e.g. Knobloch, 2015). The importance of homoclinic snaking in shear flows is that it resembles the homoclinic snaking process in the simple one-dimensional Swift-Hohenberg equation remarkably well, suggesting a connection between shear flows and the model equation.

All the invariant solutions of the flow equations are computed by the common shooting method. For future research, we suggest an alternative method for finding periodic orbits; The adjoint-based variational method for finding periodic orbits of a general dynamical system is detailed in chapter 7. This method is matrix-free and globally convergent. Using the variational method, large sets of invariant solutions can be computed.

The thesis closes with a summary of the results as well as some suggestions for future research directions in chapter 8.

2 System and methods

Contents

In this thesis, we study small- and large-scale coherent structures in the asymptotic suction boundary layer flow by numerical simulations. The simulations are carried out by using the open source software *channelflow 2.0* (www.channelflow.ch, Gibson, Reetz, Azimi, Ferraro, Kreilos, Schrobsdorff, Farano, Yesil, Schütz, Culpo & Schneider (2019)). *channelflow 2.0* is developed by a team of developers including the author of this thesis. In this chapter, we explain the considered system, and the developed numerical tools. The structure of the chapter is as follows. In section 2.1, we introduce the asymptotic suction boundary layer as the considered flow system. In section 2.2, first we summarise the main features of the software *channelflow 2.0*. This section is then followed by describing selected methods that are developed and implemented to improve the linear algebra tools of the software. These methods include a multishooting method to facilitate computations of long periodic orbits,

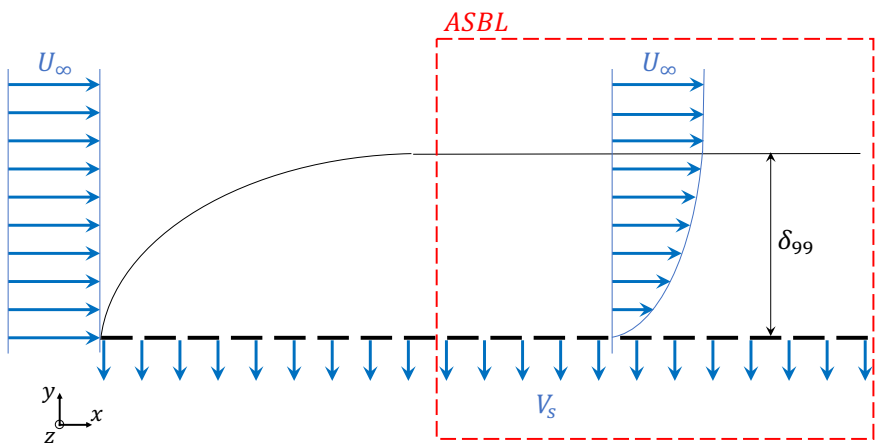

Figure 2.1 – Schematic of asymptotic suction boundary layer flow. The turbulent boundary layer thickness δ_{99} is the height where the mean streamwise velocity reaches 99% of the free stream velocity U_∞. The boundary layer thickness δ_{99} grows with the downstream distance from the leading edge of the plate. Asymptotic suction boundary layer flow (ASBL) is reached where the growth of the boundary layer thickness δ_{99} is arrested by the suction into the wall.

the accumulative Krylov subspace method that significantly improves the convergence rate of Newton's method, and a modified arclength continuation method to improve continuations of invariant solutions. Finally in section 2.3, the extension of *channelflow 2.0* for performing large-eddy simulations (LES) is detailed.

2.1 Asymptotic suction boundary layer flow

A boundary layer flow is the flow of a viscous fluid over a wall that is immersed in a free stream. The flow satisfies no-slip condition at the wall and approaches the free stream velocity far from the wall. Within the boundary layer, the velocity varies from zero to free stream velocity. The boundary layer thickness δ_{99} is defined by the distance from the wall to the height where the mean streamwise velocity equals 99% of the free stream velocity. We consider the flow of a uniform velocity U_∞ over a flat plate with constant and uniform wall-normal suction V_s. From the leading edge of the plate, The boundary layer thickness δ_{99} grows with the downstream distance from the leading edge. The growth of the boundary layer thickness is compensated by the wall-normal suction. After a transient growth, δ_{99} asymptotically reaches a constant value and the flow becomes parallel to the plate, as schematically shown in figure 2.1. This parallel boundary layer flow is called the asymptotic suction boundary layer (ASBL). In the ASBL, the downstream momentum that enters the boundary layer from the free stream is in a balance with the wall-shear. This balance of momentum keeps the boundary layer flow parallel.

2.1.1 Governing equations

We assume that the flow is incompressible and the fluid is Newtonian. The streamwise, wall-normal and spanwise directions are denoted by $\check{x}$, $\check{y}$ and $\check{z}$, respectively. The governing equations for the (dimensional) velocity $\check{\mathbf{u}} = (\check{u}, \check{v}, \check{w})$ and pressure $\check{p}$ are the Navier-Stokes equations,

$$\frac{\partial \check{\mathbf{u}}}{\partial \check{t}} + \check{\mathbf{u}} \cdot \nabla \check{\mathbf{u}} = -\frac{1}{\rho} \nabla \check{p} + \nu \nabla^2 \check{\mathbf{u}}, \tag{2.1}$$

complemented by the continuity equation,

$$\nabla \cdot \check{\mathbf{u}} = 0. \tag{2.2}$$

Here, ρ is the density and ν the kinematic viscosity of the fluid. The boundary conditions at the wall are the no-slip condition for the streamwise and spanwise velocity components and the constant and uniform suction for the wall-normal velocity component:

$$\check{\mathbf{u}}(\check{y} = 0) = (0, -V_s, 0). \tag{2.3}$$

Far above the wall ($y \to \infty$), the velocity approaches to the free stream velocity

$$\check{u}(\check{y} \to \infty) = (U_\infty, -V_s, 0), \tag{2.4}$$

where the condition for the wall-normal velocity component follows from the continuity equation. In the free stream the pressure is constant.

2.1.2 Laminar solution

In the laminar regime, the flow is stationary and homogeneous in the streamwise and spanwise directions. With this symmetry assumptions, the Navier-Stokes equations are simplified to

$$\begin{aligned}
\check{v}\frac{\partial \check{u}}{\partial \check{y}} &= -\frac{1}{\rho}\frac{\partial \check{p}}{\partial \check{x}} + \nu \frac{\partial^2 \check{u}}{\partial \check{y}^2}, \\
\check{v}\frac{\partial \check{v}}{\partial \check{y}} &= -\frac{1}{\rho}\frac{\partial \check{p}}{\partial \check{y}} + \nu \frac{\partial^2 \check{v}}{\partial \check{y}^2}, \\
\check{v}\frac{\partial \check{w}}{\partial \check{y}} &= -\frac{1}{\rho}\frac{\partial \check{p}}{\partial \check{z}} + \nu \frac{\partial^2 \check{w}}{\partial \check{y}^2},
\end{aligned}$$

and the continuity equation becomes

$$\frac{\partial \check{v}}{\partial \check{y}} = 0.$$

From the continuity equation and the boundary condition of the wall-normal velocity at the wall (2.3), we infer $\check{v} = -V_s$. The $\check{y}$-momentum equation and the boundary condition

for pressure shows that for the laminar solution pressure in the boundary layer is equal to the constant pressure of the free stream. Integrating the Navier-Stokes equations with the boundary conditions (2.3) and (2.4) yields the analytical laminar solution of ASBL $\check{\mathbf{U}}_l = \left(\check{U}_l, \check{V}_l, \check{W}_l\right)$:

$$\begin{aligned} \check{U}_l &= U_\infty \left(1 - \exp(-\check{y} V_s/\nu)\right), \\ \check{V}_l &= -V_s, \\ \check{W}_l &= 0. \end{aligned} \tag{2.5}$$

The displacement thickness of the boundary layer δ^* based on the laminar solution is

$$\delta^* = \frac{1}{U_\infty} \int_0^\infty \left(U_\infty - \check{U}_l\right) d\check{y} = \frac{\nu}{V_s}. \tag{2.6}$$

2.1.3 Non-dimensionalisation and control parameters

We choose to nondimensionalise the system by using the free stream velocity U_∞ as a velocity scale and the laminar displacement thickness $\delta^* = \nu/V_s$ as a length scale. The nondimensional system of coordinates are denoted by $(x = \check{x}/\delta^*, y = \check{y}/\delta^*, z = \check{z}/\delta^*)$. The nondimensional velocity components are denoted by $\mathbf{u} = (u, v, w) = 1/U_\infty(\check{u}, \check{v}, \check{w})$. $t = \check{t}/\left(\frac{\nu}{V_s U_\infty}\right)$ is the nondimensional time, and $p = \check{p}/(\rho U_\infty^2)$ is the nondimensional pressure. Inserting the nondimensional variables in the governing equations of the system yields the nondimensionalised Navier-Stokes equations

$$\frac{\partial \mathbf{u}}{\partial t} + \mathbf{u} \cdot \nabla \mathbf{u} = -\nabla p + \frac{1}{Re} \nabla^2 \mathbf{u}, \tag{2.7}$$

and the nondimensionalised continuity equation

$$\nabla \cdot \mathbf{u} = 0. \tag{2.8}$$

Here, the Reynolds number

$$Re = \frac{U_\infty \nu / V_s}{\nu} = \frac{U_\infty}{V_s} \tag{2.9}$$

is the only control parameter of the system. The nondimensional laminar solution of the ASBL takes the form $\mathbf{U}_l = \left(1 - \exp(-y), -1/Re, 0\right)$.

In both the laminar and turbulent ASBL, the wall shear is in balance with the downstream momentum that enters the boundary layer from the free stream:

$$\tau_w = \rho U_\infty V_s, \tag{2.10}$$

where τ_w is the averaged wall shear. This analytical expression for the wall shear of the flow allows us to analytically express the inner velocity scale $u_\tau = \sqrt{\tau_w/\rho}$ and the inner length

scale $\delta_\tau = \nu / u_\tau$, that are the scales of the flow in the inner region (Pope, 2000), as functions of known parameters of the flow:

$$\begin{aligned} u_\tau &= \sqrt{U_\infty V_s} = \frac{U_\infty}{\sqrt{Re}}, \\ \delta_\tau &= \frac{\nu}{\sqrt{U_\infty V_s}} = \frac{\delta^*}{\sqrt{Re}}. \end{aligned} \tag{2.11}$$

The variables that are rescaled by these inner scales are denoted by a superscript plus sign. The friction Reynolds number $Re_\tau = \delta_{99}/\delta_\tau$ measures the scale separation between the length scale of the flow in the outer region δ_{99} and the length scale of the flow in the inner region δ_τ. In the ASBL, the friction Reynolds number can be expressed in terms of the control parameter as

$$Re_\tau = \left(\delta_{99}/\delta^*\right)\sqrt{Re}. \tag{2.12}$$

2.1.4 Properties of the turbulent ASBL

While the laminar solution of ASBL is linearly stable up to $Re = 54370$ (Hocking, 1975), in practice transition to turbulence is observed for $Re > 270$ (Khapko, Schlatter, Duguet & Henningson, 2016). The turbulent ASBL is characterised by high scale separations. Even at the smallest Reynolds number where turbulent ASBL is sustained, $Re = 270$, the friction Reynolds number measuring the scale separation is relatively large $Re_\tau \approx 500$ (Khapko *et al.*, 2016) when compared to other shear flows such as plane Couette flow where close to the onset of turbulence $Re_\tau = 30-50$ (Brethouwer, Duguet & Schlatter, 2012). According to equation (2.12), the friction Reynolds number Re_τ scales with δ_{99} and $\sqrt{Re}$. In contrast to δ_τ, the turbulent boundary layer thickness δ_{99} is not given in terms of the control parameter Re, and thus needs to be determined a posteriori by simulations of the flow. The simulations of Schlatter & Örlü (2011), Bobke *et al.* (2016) and Khapko *et al.* (2016) show that both the boundary layer thickness δ_{99} and the friction Reynolds number Re_τ grow significantly with Re for values between $Re = 270$ and $Re = 400$. The friction Reynolds number of turbulent ASBL at $Re = 333$ is $Re_\tau \approx 2000$, and at $Re = 400$ is $Re_\tau \approx 5800$. The turbulent ASBL is thus characterised by high scale separations.

The high scale separations associated with the turbulent ASBL implies that even in the lowest Reynolds number where the turbulent flow is observed $Re = 270$ the large-scale motions are well-developed (Khapko *et al.*, 2016). The kinetic energy of the large-scale motions in the turbulent ASBL is, however, relatively weak compared to the kinetic energy of the near-wall small-scale structures (Schlatter & Örlü, 2011; Bobke *et al.*, 2016).

2.1.5 Numerical domain

The asymptotic suction boundary layer flow occupies the semi-infinite space reaching from the wall to infinity. To carry out numerical simulations of the ASBL, we consider a finite flow domain up to a certain height $y = H$. The height $y = H$ is well above the boundary layer thickness so that the flow velocity at $y = H$ can be approximated by the free stream velocity. We therefore replace the boundary condition of the ASBL at infinity by Dirichlet boundary conditions at $y = H$. The boundary conditions of the numerical domain in the wall-normal direction are

$$\begin{aligned} \mathbf{u}(y=0) &= (0, -1/Re, 0)\,, \\ \mathbf{u}(y=H) &= (1, -1/Re, 0)\,. \end{aligned} \tag{2.13}$$

Replacing the boundary conditions of the ASBL at $y = \infty$ by the boundary conditions at $y = H$ modifies the streamwise component of the laminar solution of the ASBL, U_l:

$$U_l = \frac{1}{1-\exp(-H)}(1-\exp(-y)). \tag{2.14}$$

For $H \to \infty$ the prefactor becomes one and the profile becomes equal to the laminar solution of the ASBL in the semi-infinite domain.

In the simulation of turbulent ASBL, the height of the numerical domain H needs to be large enough so that turbulent flow structures that are formed in the boundary layer next to the wall are not affected by the presence of the numerical upper boundary at $y = H$. For all of our simulations we check the independence of the results from the height of the numerical domain H.

In the streamwise and spanwise directions, the numerical domain has a finite length L_x and a finite width L_z. Periodic boundary conditions are imposed in these lateral directions:

$$\begin{aligned} \mathbf{u}(-L_x/2, y, z) &= \mathbf{u}(L_x/2, y, z), \\ \mathbf{u}(x, y, -L_z/2) &= \mathbf{u}(x, y, L_z/2). \end{aligned} \tag{2.15}$$

The periodic boundary conditions in the lateral directions are compatible with the translational symmetry of the ASBL $\mathbf{u}(x+\sigma_x, y, z+\sigma_z) = \mathbf{u}(x, y, z)$ where σ_x and σ_z are arbitrary shifts in the streamwise and spanwise directions. Consequently, all velocity fields with the periodic boundary conditions (2.15) form a symmetry subspace for the dynamics of the unbounded ASBL. This implies that any solution in the numerical box with the periodic boundary conditions is also a solution of the flow in the unbounded domain. Dynamically, imposing periodic boundary conditions allows us to remove the scales of the flow that are larger than the size of the numerical box. Removing scales larger than the size of the numerical box helps us to isolate coherent structures at specific length scales and study them as individual structures Jiménez (2018).

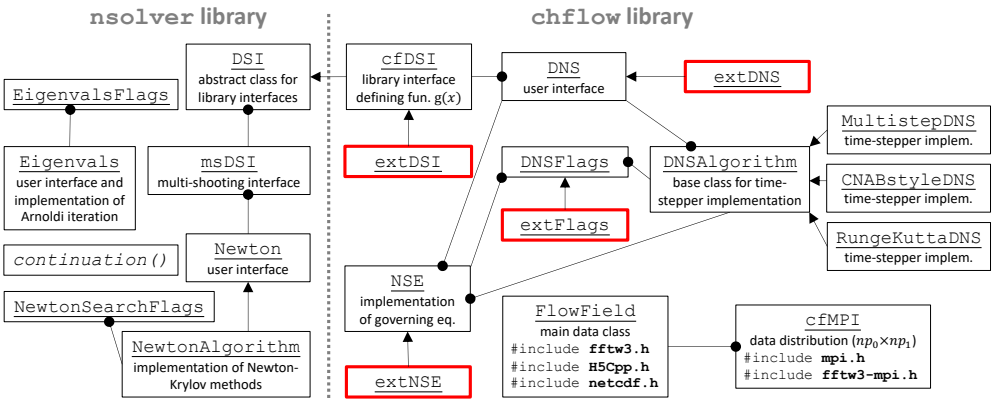

Figure 2.2 – Class diagram of *channelflow 2.0* (reprinted from Reetz (2019) with permission). Relations between classes are indicated by arrows and oval arrows. An inheritance is indicated by an arrow from the derived class to the base class. An oval arrow indicates dependence: an arrow pointing from class A towards class B means that a member of type B is used in A. For extending *channelflow 2.0* to solve Navier-Stokes equations with additional forcing terms, the red-framed classes should be implemented.

2.2 Numerical simulations: *channelflow 2.0*

To solve the Navier-Stokes equations (2.7) subject to the Dirichlet boundary conditions in the wall-normal direction (2.13) and periodic boundary conditions in the streamwise and the spanwise directions (2.15), we use the open source software *channelflow 2.0* (www.channelflow.ch, Gibson *et al.* (2019)). *channelflow 2.0* is developed and published as the result of the collaboration between the members of *Emergent Complexity in Physical Systems* (ECPS) including the author of this thesis, *Scientific IT and Application Support* (SCITAS) in EPFL and John F. Gibson (University of New Hampshire). The software is based on a serial code developed by John F. Gibson (Gibson, 2011, 2012). The detailed features of the numerical tools provided by the software are given in (Gibson *et al.*, 2019), and the code structure and numerical schemes are explained in Reetz (2019). Here, we first summarise the main features of the code. Then, we explain selected numerical methods that are developed and implemented in the software to improve the performance of its linear algebra tools.

2.2.1 Review of the code

channelflow 2.0 is a pseudo-spectral code to perform direct numerical simulations for flows between two parallel walls in numerical boxes with no-slip boundary conditions at the walls (2.13) and periodic boundary conditions in wall-parallel directions (2.15). The software uses a Fourier-Chebychev-Fourier discretization in the streamwise, wall-normal and spanwise directions, respectively. *channelflow 2.0* also provides numerical tools for dynamical systems analysis. The class diagram of the code is shown in figure 2.2. The code is composed of two separate libraries: `chflow` that contains classes to perform direct numerical simulations, and

`nsolver` containing numerical methods for dynamical systems analysis. These two libraries interact via an interface class, namely the dynamical system interface `DSI`, that relates state space vectors $\vec{\xi}$ to velocity fields $\mathbf{u}$ for the computation of their temporal evolutions.

Within the `chflow` library, the numerical schemes for time-stepping the equations are implemented separately from the classes representing the Navier-Stokes equations. `DNSAlgorithm` is an interface for time-stepping schemes. The classes deriving from `DNSAlgorithm` implement different numerical schemes to solve

$$\frac{\partial \mathbf{u}}{\partial t} = L(\mathbf{u}) - N(\mathbf{u}), \tag{2.16}$$

where we split the right-hand side of the equation into the linear operator L and the nonlinear operator N. For the Navier-Stokes equations (2.7) these operators are given by

$$\begin{aligned} L(\mathbf{u}) &= -\nabla p + \frac{1}{Re}\nabla^2 \mathbf{u}, \\ N(\mathbf{u}) &= \mathbf{u} \cdot \nabla \mathbf{u}. \end{aligned} \tag{2.17}$$

The time-stepping classes deriving from `DNSAlgorithm` request for the computation of the linear and nonlinear terms of the equations from the class of the Navier-Stokes equations, `NSE`. The time-stepping schemes provided by *channelflow* treat the linear term implicitly and the nonlinear term explicitly (see Gibson (2012) for details).

channelflow 2.0 can be extended to solve Navier-Stokes equations with additional forcing terms involving additional models such as convection (Reetz & Schneider, 2020*a*; Reetz, Subramanian & Schneider, 2020). As a result of the abstraction of `DNSAlgorithm`, extending *channelflow 2.0* only requires the implementation of classes that represent new governing equations. In figure 2.2, these required classes are indicated by red frames:

- `extDNS` is an interface for time-stepping the governing equations. It employs the numerical time-stepping schemes provided by the sub-classes of `DNSAlgorithm`.
- `extNSE` is the class representing the governing equations. It implements the linear and nonlinear terms.
- `extFlags` contains the numerical and physical parameters required by the governing equations.
- `extDSI` is the interface of the extended code with the `nsolver` library.

In section 2.3, the extension of the code for performing large-eddy simulations is explained.

2.2.2 Numerical methods in `nsolver`

The library `nsolver`, contained in the software *channelflow 2.0*, provides numerical tools for dynamical system analysis including Newton-solver methods for computing invariant solutions. Invariant solutions, including equilibria, travelling waves, periodic orbits and relative periodic orbits, satisfy the equation

$$\vec{g}(\vec{\xi}, \vec{a}) = \sigma \vec{f}(\vec{\xi}, T) - \vec{\xi} = \vec{0}. \tag{2.18}$$

In this equation, σ is a symmetry operator and $\vec{f}(\vec{\xi}, T)$ is the evolution of the state-space vector $\vec{\xi}$ under the governing equations over the time interval T. The additional unknown variables including the streamwise phase speed, c_x, the spanwise phase speed, c_z, and the time period T are combined in $\vec{a} = (c_x, c_z, T)$. To simplify the notation, we omit the vector signs in the remainder of this section. Assuming that ξ is m-dimensional and a is d-dimensional, equation (2.18) is underdetermined with m constraints for $m + d$ unknowns. To form a system with equal number of constraints and unknowns, d additional constraints on the solution ξ are defined: $c(\xi) = 0$, where c is a d-dimensional vector function. Specifically in *channelflow*, these constraints are chosen to be geometric orthogonality conditions that enforce specified spatial and temporal phases.

Newton-solver methods search for roots of the equations $g(\xi, a) = 0$ and $c(\xi) = 0$ by Newton's method. A guess $(\tilde{\xi}, \tilde{a})$ is iteratively updated based on the linear approximation of the equations around the guess:

$$\frac{\partial g_i}{\partial \xi_j}(\tilde{\xi}, \tilde{a}) d\xi_j + \frac{\partial g_i}{\partial a_k}(\tilde{\xi}, \tilde{a}) da_k \approx -g_i(\tilde{\xi}, \tilde{a}),$$
$$\frac{\partial c_k}{\partial \xi_j}(\tilde{\xi}) d\xi_j \approx 0.$$

where $d\xi$ and da are the desired updates of $\tilde{\xi}$ and $\tilde{a}$, respectively. In every Newton step, this system of linear equations is solved for $(d\xi, da)$ by matrix-free Krylov subspace methods (Edwards, Tuckerman, Friesner & Sorensen, 1994). Newton's method converge to the solution of equation (2.18) if the initial condition is chosen sufficiently close to the solution. The radius of convergence can be improved by employing the Hookstep trust-region optimization method (Viswanath, 2007).

In the framework of the research leading to this thesis, the following methods are implemented in the `nsolver` library:

- A multishooting method (Sánchez & Net, 2010) to facilitate the computation of long periodic orbits.
- An improved Newton-solver method based on Flexible GMRES (flexible generalised minimal residual method, Saad (2003)).

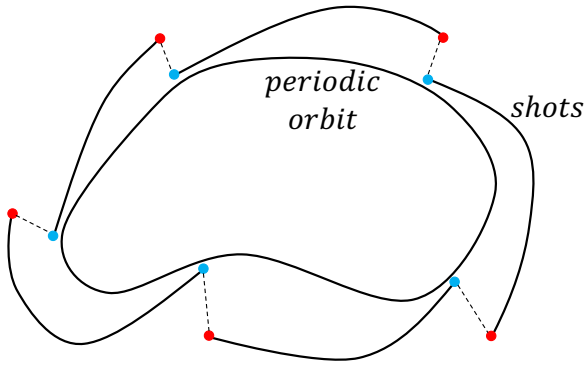

Figure 2.3 – Schematic of the multishooting method. The closed curve shows a periodic orbit. The blue circles indicate initial guesses for the shots. The solid line segments show the shots, the evolution of the initial guesses under the governing equations, and the red circles indicate the final point of every shot. When final point of all the shots match with the initial points of the subsequent shots, the multishooting method is converged to a periodic orbit.

- A modified arclength continuation method for following invariant solutions along their solution branches.

These methods are published as a part of the open-source software *channelflow 2.0*.

Multishooting method

Finding periodic orbits by solving for roots of equation (2.18) is based on a shooting method. The shooting method considers an initial value problem yielding trajectories satisfying the evolution equations and varies the initial condition until the solution closes on itself and becomes periodic. In chaotic systems such as turbulence, trajectories separate exponentially in time. Small changes in the initial conditions are thus exponentially amplified by time-advancing. As a result, finding unstable periodic orbits by shooting method is an ill-conditioned problem. Owing to the finite numerical precision of computations and the exponential amplification of errors, long and unstable periodic orbits are entirely impossible to converge. An example of a solution that appears to be periodic but cannot be converged by the shooting method is the edge state of ASBL (Kreilos, Veble, Schneider & Eckhardt, 2013). To deal with the exponential growth of errors along a periodic orbit, the multishooting method can be employed.

The multishooting method splits a periodic orbit into a number of segments that are connected at their initial and final points. All segments, hereafter called *shots*, satisfy the evolution equations over an equal time interval $T_s = T/n_s$, where T is the period of the periodic orbit and n_s denotes the number of shots. Consequently, the time during which errors grow exponentially is divided by n_s. Thereby the error amplification decreases enormously and long periodic orbits become computationally accessible. The multishooting method is schematically visualised in figure 2.3, where a periodic orbit and shots from guessed initial points are

shown. The guessed initial points are not located on the periodic orbit, and the shots are not connected to each other. When the method converges, the shots become connected pieces of the periodic orbit. In this case, the final points of all the shots match with the initial points of the subsequent shots.

The multishooting method searches for the initial points of all the shots ξ^l (where superscript l denotes the shot number), and the vector of additional unknown variables $\tilde{a}$, that includes the time period T. ξ^l and $\tilde{a}$ satisfy the following equations

$$\begin{aligned} &g^l(\xi^l, \xi^{l+1}, a) = f(\xi^l, T_s) - \xi^{l+1} = 0 \quad \text{for} \quad 0 \le l < n_s - 1, \\ &g^{n_s-1}(\xi^{n_s-1}, \xi^0, a) = \sigma f(\xi^{n_s-1}, T_s) - \xi_0 = 0. \end{aligned} \tag{2.19}$$

Assuming that the state space is m-dimensional, the system of equations (2.19) contains $n_s \cdot m$ constraints for $n_s \cdot m + d$ unknowns. To form a fully determined system, equations (2.19) are thus complemented by d additional geometric constraints

$$c(\xi^0) = 0. \tag{2.20}$$

These constraints enforce specified spatial and temporal phases for the initial point of the first shot ξ^0. The system of equations (2.19) and (2.20) is solved by Newton's method. In Newton's method, a linear approximation of the equations is considered for iteratively updating a guess $(\tilde{\xi}^l, \tilde{a})$:

$$\begin{aligned} &\frac{\partial g_i^l}{\partial \xi_j^l}(\tilde{\xi}^l, \tilde{\xi}^{l+1}, \tilde{a})\, d\xi_j^l - I_m\, d\xi_i^{l+1} + \frac{\partial g_i^l}{\partial a_k}(\tilde{\xi}^l, \tilde{\xi}^{l+1}, \tilde{a})\, da_k \approx -g_i^l(\tilde{\xi}^l, \tilde{\xi}^{l+1}, \tilde{a}) \quad \text{for} \quad 0 \le l < n_s - 1, \\ &\frac{\partial g_i^{n_s-1}}{\partial \xi_j^{n_s-1}}(\tilde{\xi}^{n_s-1}, \tilde{\xi}^0, \tilde{a})\, d\xi_j^{n_s-1} - I_m\, d\xi_i^0 + \frac{\partial g_i^{n_s-1}}{\partial a_k}(\tilde{\xi}^{n_s-1}, \tilde{\xi}^0, \tilde{a})\, da_k \approx -g_i^{n_s-1}(\tilde{\xi}^{n_s-1}, \tilde{\xi}^0, \tilde{a}), \\ &\frac{\partial c_k}{\partial \xi_j^0}(\tilde{\xi}^0) d\xi_j^0 \approx 0, \end{aligned}$$

where I_m is the identity matrix of size m, and $(d\xi^l, da)$ is the update of the guess. In every Newton step, the system of linear equations is solved for $(d\xi^l, da)$ by the matrix-free Krylov-subspace methods, provided by the library `nsolver`.

The multishooting method can be used to compute long periodic orbits that cannot be converged by the standard shooting method. This is exemplified in figure 2.4, where the convergence of the multishooting method to the edge state solution of ASBL (Kreilos *et al.*, 2013) for increasing number of shots is shown. The multishooting method with one shot $n_s = 1$ is the standard shooting method for finding periodic orbits. Unlike the standard shooting method with $n_s = 1$, the multishooting method with $n_s = 3$ and $n_s = 7$ converges to the periodic orbit. The method with $n_s = 7$ converges at a faster rate than the method with $n_s = 3$. Higher number of shots improves the convergence rate of Newton's method at the cost of increasing the size of the system of linear equations that needs to be solved in every Newton step.

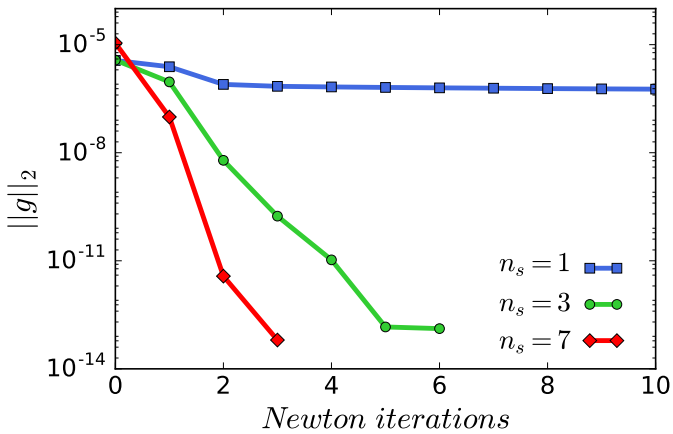

Figure 2.4 – Convergence of the long periodic orbit edge state of the ASBL (Kreilos *et al.*, 2013) at $Re = 400$ by using the multishooting method. The residual of equation (2.18) as a function of the number of Newton steps is plotted. The convergence is plotted for one shot (blue line), three shots (green line), and seven shots (red line). Newton's method with one shot (not using multishooting) does not converge. The periodic orbit is converged by using at least three shots. The convergence rate for seven shots (red line) is higher than the rate for three shots.

Multishooting makes it possible to compute long periodic orbits, but it has a small radius of convergence. An alternative approach for finding periodic orbits is discussed in chapter 7 where successful convergence to periodic orbits is independent of the time period of the respective orbit.

An improved Newton-solver method: accumulating Krylov subspace by flexible GMRES

In every Newton step, a system of linear equations of the form $Ax = b$ is solved, where A is an m-by-m matrix. *channelflow* provides matrix-free Krylov-subspace methods for solving the system of linear equations. In these methods, direct access to the matrix A is not required. Instead only the action of the matrix on a test vector q, Aq is required. As A is the Jacobian, Aq represents a directional derivative that can be approximated using finite differences. An approximation of the solution of the system of linear equations is found in the Krylov subspace:

$$K_n = span\left\{b, Ab, A^2b, A^3b, ..., A^{n-1}b\right\}, \tag{2.21}$$

where n is the dimension of the Krylov subspace that is much smaller than the dimension of the unknown vector, m. Here, we first explain the GMRES method for constructing the approximate solution in the Krylov subspace. Then flexible GMRES as a variant of the GMRES method is discussed. Then we describe the idea of accumulating the Krylov subspace in Newton steps using the flexible GMRES method.

GMRES: The GMRES method yields an approximation of the solution x_n in the Krylov subspace of dimension n, that minimises the Euclidean norm $r_n = ||Ax_n - b||$ (Saad & Schultz, 1986). The Krylov subspace is iteratively expanded by Arnoldi iterations (Arnoldi, 1951; Antoulas, 2005) until r_n is sufficiently small. In Arnoldi iterations, the orthonormalised basis vectors of the Krylov subspace, $\{q_1, q_2, q_3, ..., q_n\}$, are saved in a matrix Q_n, where $q_1 = b/||b||$. The solution in the Krylov subspace can thus be expressed as a linear combination of the basis vectors: $x_n = Q_n y_n$, where y_n is an n-dimensional vector containing the coefficients of the basis vectors. The Krylov subspace is expanded by evaluating the product Aq_n and orthonormalising the result with respect to the basis vectors in Q_n. The projections of the product Aq_n on the basis vectors are saved in an upper Hessenberg matrix $\tilde{H}_n$ of size $n+1$-by-n. Using the key relation,

$$AQ_n = Q_{n+1}\tilde{H}_n,$$

and the orthonormality of Q_n, r_n can be expressed in terms of the coefficients y_n:

$$r_n = ||Ax_n - b|| = ||AQ_n y_n - b|| = ||Q_{n+1}\tilde{H}_n y_n - b|| = ||\tilde{H}_n y_n - Q_{n+1}^T b|| = ||\tilde{H}_n y_n - \beta e_1||$$

where $\beta = ||b||$ and $e_1 = (1, 0, 0, ..., 0)^T$. Minimising r_n is thus carried out by finding the coefficient vector y_n. If the minimised r_n is sufficiently small, the approximated solution of the linear equations in the Krylov subspace $x_n = Q_n y_n$ is returned, otherwise the process is repeated by adding an extra dimension to the Krylov subspace.

Flexible GMRES: Flexible GMRES is a variant of GMRES for solving a system of linear equations of the form $Ax = b$ (Saad, 2003). Similar to GMRES, flexible GMRES method constructs an approximate solution x_n that minimises the norm $r_n = ||Ax_n - b||$ in a subspace of the full space of the solution. The subspace is however not necessarily the Krylov subspace, but instead, is spanned by any arbitrary set of vectors $V_n = \{v_1, v_2, ..., v_n\}$. The approximated solution can be expressed as a linear combination $x_n = V_n y_n$, where y_n is the vector of coefficients. The vector b with the products of the matrix A and the vectors $v \in V_n$ span a second subspace Q_{n+1} containing orthonormalised basis vectors $\{q_1 = b/||b||, q_2, ..., q_n, q_{n+1}\}$. The projections of the products p on the basis vectors in Q_n are saved in the upper Hessenberg matrix $\tilde{H}_n$ of size $n+1$-by-n. The defined matrices are related by

$$AV_n = Q_{n+1}\tilde{H}_n.$$

Using this equation and the orthonormality of Q, the residual $r_n = ||Ax_n - b||$ can be expressed as

$$r_n = ||Ax_n - b|| = ||AV_n y_n - b|| = ||Q_{n+1}\tilde{H}_n y_n - b|| = ||\tilde{H}_n y_n - Q_{n+1}^T b|| = ||\tilde{H}_n y_n - \beta e_1||.$$

where $\beta = ||b||$ and $e_1 = (1, 0, 0, ..., 0)^T$. The coefficient vector y_n that minimises r_n yields the approximate solution $x_n = V_n y_n$. Similar to GMRES, this process is repeated until the residual

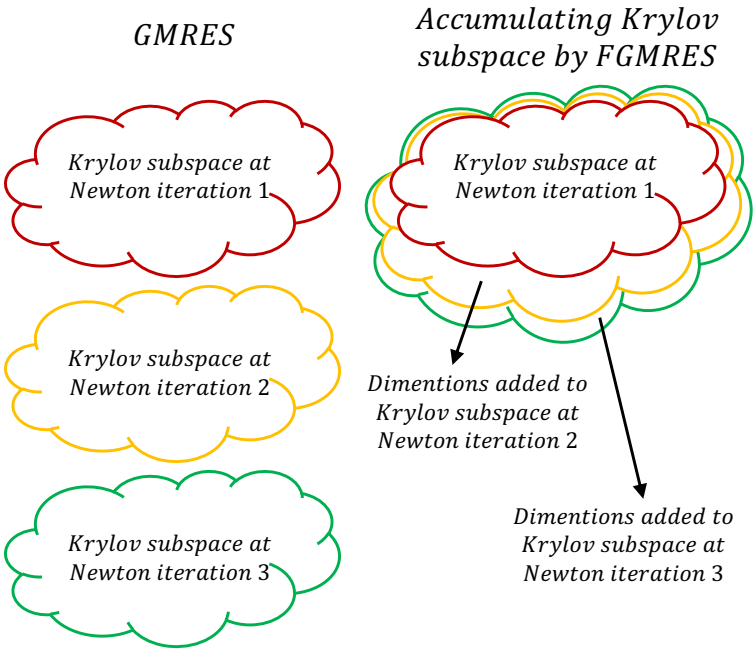

Figure 2.5 – Schematic of Krylov subspaces used for solving the system of linear equations associated with Newton's steps. The standard GMRES method is compared with the method of accumulative Krylov subspace by using the flexible GMRES. Unlike the GMRES method, the accumulative Krylov subspace method does not create a new Krylov subspace in every Newton step, but it expands the subspace of the previous Newton steps.

r_n is sufficiently small.

Accumulating the Krylov subspace by flexible GMRES: The difference between the flexible GMRES and the GMRES method is the subspace in which the approximate solution is constructed. In the flexible GMRES the subspace can be spanned by any arbitrary set of vectors. This method allows us to construct a modified subspace with fewer $A \cdot q$ evaluations compared to the Krylov subspace for the GMRES method. We develop the method of accumulating the Krylov subspace by flexible GMRES based on the idea that the computations of the previous Newton steps can be used to enrich the Krylov subspace of the current step. In every Newton step, instead of creating a new Krylov subspace, the subspace of the previous Newton steps is used as an initial subspace for the current step. This initial subspace is then expanded by Arnoldi iterations. This is schematically visualised in figure 2.5, where Krylov subspaces are compared for the GMRES method and the method of accumulating Krylov subspace by flexible GMRES.

For every Newton step, the vectors q and the computed matrix-vector products Aq, spanning the Krylov subspace, are saved. The vectors q, that are saved in previous Newton steps, span an initial subspace, and the already-computed products Aq and the vector b are orthonormalised

Algorithm 2.1 Accumulating Krylov subspace by flexible GMRES method.

```
solve the equations of the first Newton step by GMRES
set n equal to the dimension of the created Krylov subspace
for i = 1,2,...,n−1 do
    save all the basis vectors v_i ← q_i
    save all the computed products p_i ← A q_i
end for
while ||g||_2 > ε_Newton do                                   ▷ Newton steps
    compute b
    for i = 1,2,...,n−1 do        ▷ orthonormalising the Krylov subspace with respect to b
        iterate (v_i, p_i)                  ▷ flexible GMRES iteration by v_i, and p_i = A v_i
    end for
    i ← n
    while r_n > ε_GMRES do        ▷ expanding the Krylov subspace by Arnoldi iterations
        if i = n then
            v_i ← b/||b||
        else if i > n then
            v_i ← q_i             ▷ the last computed basis vector of the Krylov subspace
        end if
        compute A v_i                          ▷ the most time-consuming operation
        iterate (v_i, A v_i)                   ▷ flexible GMRES iteration by q_i and A q_i
        save v_i
        save p_i ← A v_i
        i ← i + 1
    end while
    n ← i                                  ▷ dimension of the accumulated Krylov subspace
end while
```

starting from the current vector b to construct the matrices Q_{n+1} and $\tilde{H}_n$ of the flexible GMRES method. The initial subspace is then expanded by Arnoldi iterations starting from the current vector b until the residual $r_n = ||Ax_n - b||$ becomes sufficiently small. The method is detailed in algorithm 2.1.

Newton's method updates the vector of unknowns (ξ, a) by solving the system of linear equations $Ax = b$ for $x = (d\xi, da)$. The matrix A is a function of the vector of unknowns (ξ, a). Consequently, A changes in every Newton step. Using the matrix-vector products from previous Newton steps $A_{previous} \cdot q$ is thus an approximation of the products in the current Newton step $A_{\text{current}} \cdot q$. The error of the approximating products is first order in the update of the vector of unknowns, $A_{\text{previous}} \cdot q = A_{\text{current}} \cdot q + \mathcal{O}(d\xi, da)$. As a result of this approximation, Newton iteration based on the accumulating Krylov subspace method converge more slowly than Newton iteration based on the standard GMRES method. However, solving the system of linear equations in every Newton step requires much fewer Arnoldi iterations. Consequently, accumulating the Krylov subspace significantly decreases the overall number of required matrix-vector product evaluations. In our calculations of invariant solutions, accumulating

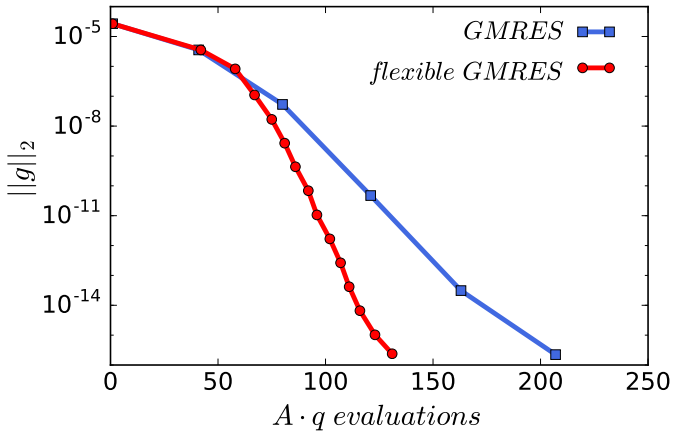

Figure 2.6 – Convergence of two different solvers to the snaking equilibrium solution of the plane Couette flow (Schneider *et al.*, 2010*a*) at $Re = 200$. The residual of equation (2.18), $||g||_2$, as a function of the number of matrix-vector product evaluations is plotted. The blue line shows the convergence of the standard GMRES method. The red line indicates the convergence of the method of accumulative Krylov subspace by flexible GMRES. The blue squares and red circles on the lines separate Newton steps. The convergence is greatly improved by using the accumulative Krylov subspace method.

the Krylov subspace with the flexible GMRES reduces the cost of computations by about 40%. This is evidenced in figure 2.6 where the convergence of the GMRES method and the method of accumulating Krylov subspace by flexible GMRES are compared for the snaking equilibrium solution in the plane Couette flow (Schneider *et al.*, 2010*a*). Although the total number of Newton steps for the method of accumulating Krylov subspace is higher, the total number of matrix-vector evaluations is reduced by almost 40%.

The significant reduction of computational costs is observed despite the fact that, at each Newton step, a system of linear equations of the form $Ax = b$ with massively varying residual vector b is solved for the update $x = (d\xi, da)$. Close to the final solution, Newton updates only slightly modify the matrix A, containing the Jacobian augmented by appropriate constraints, but the vector b, representing residuals, will change significantly in each Newton step and Krylov subspaces are constructed starting from this changing vector b. This raises the question why the Krylov subspaces of the previous Newton steps provide a suitable augmentation of the subspace for the current step. In the Newton-GMRES method, at every Newton step, the Krylov subspace is spanned by power iterations of the matrix A starting from the initial vector b, $\{A^j b | j \in [0, 1, 2, ..., n-1]\}$. For increasing order j, power iterations for any b tend to the eigenvector of A corresponding to the leading eigenvalue (von Mises & Pollaczek-Geiringer, 1929). If the leading eigenvalue is complex, power iterations yield a vector rotating in the plane spanned by the pair of leading eigenvectors. This convergence of the power iterations towards the pair of leading eigenvectors of matrix A is confirmed in figure 2.7, where the orientations of the two-dimensional planes spanned by the last two power iterations, $A^{j-1}b$ and $A^j b$, are compared at subsequent Newton steps. Technically, we compute the angle between the planes

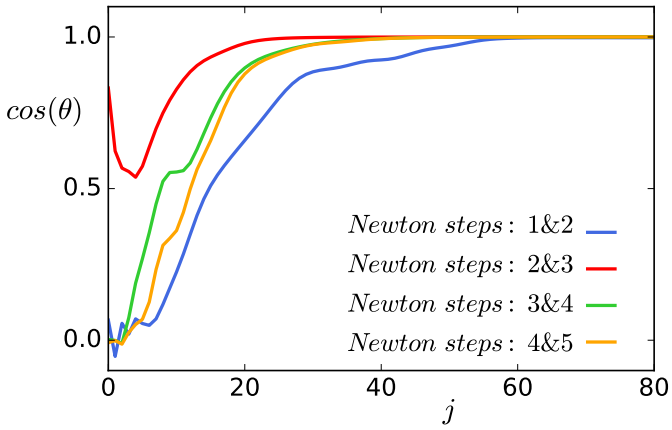

Figure 2.7 – Accelerating convergence by approximating Krylov subspaces using information of previous Newton steps. Orientations of the two-dimensional planes spanned by the last two power iterations, $v_1 = A^{j-1}b$ and $v_2 = A^j b$, are compared at the Newton steps of the standard Newton-GMRES method given in figure 2.6 (blue line with squares). Cosine of the angle θ between the planes at the first and the second Newton steps (blue), the second and the third (red), the third and the fourth (green), and the fourth and the last Newton steps (yellow) are plotted as functions of the iteration order j. The At low order j the orientations of the two-dimensional planes depend on the vector b and thus vary between the two Newton steps. Consequently, planes are misaligned. However, at high order j the angle between the planes tends to zero, indicating convergence to the leading eigenvectors of A. High order power iterations $A^j b$ with large j are thus independent of the vector b and reflect properties of the asymptotically constant matrix A.

at two subsequent Newton steps. The angle between planes spanned by z_1/z_2 and z_3/z_4, respectively, is given by

$$\cos(\theta) = \frac{\langle z_1 \wedge z_2, z_3 \wedge z_4 \rangle}{(\langle z_1 \wedge z_2, z_1 \wedge z_2 \rangle \langle z_3 \wedge z_4, z_3 \wedge z_4 \rangle)^{0.5}},$$

where $z_1 \wedge z_2$ is the blade between z_1 and z_2, and $\langle z_1 \wedge z_2, z_3 \wedge z_4 \rangle$ is a norm given by $\langle z_1, z_3 \rangle \langle z_2, z_4 \rangle - \langle z_1, z_4 \rangle \langle z_2, z_3 \rangle$ with $\langle \cdot, \cdot \rangle$ representing the inner product.

At low order j the two-dimensional planes depend on the initial b and vary between Newton steps, but at high order j the angle between the planes for all of the Newton steps tends to zero, indicating convergence to the b-independent leading eigenvectors of A. Since the matrix A only slightly changes between Newton steps, using the Krylov subspaces of the previous Newton steps to initialise the subspace of the current step reduces the number of required matrix-vector products by involving the power iterations for high order j that are approximately aligned for all Newton steps. The subspace is then expanded by power iterations starting from the vector b of the current Newton step to include the contribution of the respective lower order iterations. Thus in the method of accumulating the Krylov subspace by flexible GMRES, the constructed subspace at every Newton step is spanned by low order iterations starting from the current vector b and Krylov subspaces of the previous steps that

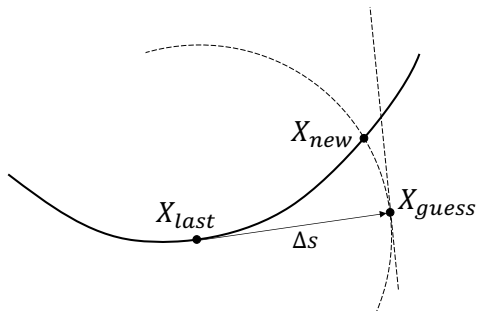

Figure 2.8 – Schematic of numerical arclength continuation along the solution branch (thick solid line). X_{last} is the last converged solution, X_{guess} an initial guess for the new solution along the branch, and X_{new} is the desired new solution, in the space of solutions $X = (\xi, a, \mu)$. The method searches for X_{new} by predicting an initial guess X_{guess} and correcting the guess by Newton's method. Unlike the pseudo-arclength continuation where the new solution is found in the plane tangent to the sphere with the radius Δs around X_{last}, in our modified arclength continuation both X_{guess} and X_{new} have a fixed distance Δs from X_{last}.

include the b-independent high order iterations characteristic of the asymptotically constant matrix A.

Modified arclength continuation method

Numerical continuation methods follow an invariant solution as an independent parameter μ is varied. The methods thereby construct bifurcation diagrams. The original numerical continuation method in *channelflow* is the parametric continuation method. The parametric continuation is a predictor-corrector method that generates a guess at a fixed value of μ by an extrapolation of the already-computed invariant solutions. Newton's method are then used to converge this guess to the solution at the fixed value of μ. In the parametric continuation of a solution close to a turning point in the parameter μ, the guess for the next numerical continuation steps can be generated in the range of μ where there is no solution. Consequently, close to the turning points, many attempts of Newton's method fail. To improve the numerical continuation of invariant solutions we developed and implemented a modified arclength continuation in *channelflow 2.0*.

The arclength method treats the independent parameter μ as an extra unknown in the continuation. In every numerical continuation step, the solution (ξ, a) and the independent parameter μ should be determined. We denote the vector of unknowns by $X = (\xi, a, \mu)$. The solution branch is parameterised by the arclength s in the space of solutions X. To form a fully determined system of equations for finding solutions, an extra constraint is needed. In the common pseudo-arclength continuation method (e.g. Dijkstra, Wubs, Cliffe, Doedel, Hazel, Lucarini, Salinger, Phipps, Sanchez-Umbria, Schuttelaars, Tuckerman & Thiele, 2014), the search for a new solution is constrained to a plane that is orthogonal to the direction of the solution branch dX/ds, with a prescribed distance Δs from the last computed solution X_{last}.

The arclength continuation method implemented in *channelflow 2.0* uses another constraint. Instead of a plane in the space of solutions $X = (\xi, a; \mu)$, the search for a new solution is constrained to a sphere with radius Δs around the last converged solution X_{last}. The new solution X_{new} should thus have a prescribed arclength distance Δs from the last converged solution X_{last}, as shown in figure 2.8.

Complementing the equations for invariant solutions by the defined nonlinear arclength constraint, the system of equations for finding a new solution along the solution branch is

$$\begin{aligned}
&g(\xi, a; \mu) = 0,\\
&c(\xi) = 0,\\
&(\xi - \xi_{last})^2 + (a - a_{last})^2 + \left(\mu - \mu_{last}\right)^2 = \Delta s^2
\end{aligned}$$

The solution of this system of equations can be constructed by Newton's method. An initial guess $\tilde{X} = (\tilde{\xi}, \tilde{a}, \tilde{\mu})$ that satisfies the arclength constraint is considered. $\tilde{X}$ is updated by the solution of the linearized equations:

$$\begin{aligned}
&\frac{\partial g_i}{\partial \xi_j}(\tilde{\xi}, \tilde{a}) d\xi_j + \frac{\partial g_i}{\partial a_k}(\tilde{\xi}, \tilde{a}) da_k \approx -g_i(\tilde{\xi}, \tilde{a}),\\
&\frac{\partial c_k}{\partial \xi_j}(\tilde{\xi}) d\xi_j \approx 0,\\
&\left(\tilde{\xi} - \xi_{last}\right)_j d\xi_j + (\tilde{a} - a_{last})_k da_k + \left(\tilde{\mu} - \mu_{last}\right)_j d\mu \approx 0.
\end{aligned} \tag{2.22}$$

As a result of the linearization, after every Newton step the updated $\tilde{X}$ is found in the plane tangent to the sphere of radius Δs around X_{last}. To ensure that $\tilde{X}$ satisfies the arclength constraint, after every Newton step the vector $\tilde{X}$ is projected onto the sphere:

$$\left(\tilde{\xi}, \tilde{a}, \tilde{\mu}\right)_{modified} = (1 - \alpha)\left(\xi, a, \mu\right)_{last} + \alpha\left(\tilde{\xi}, \tilde{a}, \tilde{\mu}\right), \tag{2.23}$$

where the coefficient α is given by

$$\alpha = \frac{\Delta s}{\left(\left(\tilde{\xi} - \xi_{last}\right)^2 + (\tilde{a} - a_{last})^2 + \left(\tilde{\mu} - \mu_{last}\right)^2\right)^{0.5}} = \frac{\Delta s}{\left(\Delta s^2 + d\xi^2 + da^2 + d\mu^2\right)^{0.5}}.$$

We denote the update of $\tilde{X}$ in every Newton step by $x = (d\xi, da, d\mu)$. After every Newton step, the error of $\tilde{X}$ from the solution X_{new} is second order in x. Since $\alpha = 1 + \mathcal{O}(x^2)$, modifying $\tilde{X}$ by equation (2.23) does not change the order of the error. The error of $\tilde{X}_{modified}$ from the solution X_{new} thus remains second order in x. The modified arclength method is detailed in algorithm 2.2.

Using the modified arclength continuation method allows us to continue invariant solutions past saddle-node bifurcations easily. This is evidenced in figure 2.9, where continuation of the 'wall-mode' solution of Kreilos *et al.* (2016) in the ASBL by the modified arclength continuation method is compared with the continuation of the solution by the parametric

Algorithm 2.2 Modified arclength continuation.

```
Find enough number of initial solutions                                  ▷ for extrapolation
set X_last                          ▷ the last converged solution in direction of continuation
set Δs
set the maximum number of Newton steps N_n
while μ ≠ μ_target do                                                    ▷ continuation loop
    make a guess X_guess by extrapolation to the distance Δs from X_last
    X̃ ← X_guess
    for i ← 1 to N_n do                                                  ▷ Newton steps
        update X̃ by solving equations (2.22)                             ▷ one Newton step
        modify X̃ by relation (2.23)                  ▷ project X̃ onto the sphere with radius Δs
    end for
    if X̃ converged then
        X_last ← X̃
        adapt Δs                                  ▷ depending on the convergence history
    else
        reduce Δs
    end if
end while
```

continuation method. The parametric continuation method cannot continue the solution past the saddle-node bifurcation at $Re = 348$, while the modified arclength continuation computes the solution well beyond the saddle-node bifurcation, to lower Reynolds numbers and to the upper branch (higher e_{cf} at $Re = 400$).

2.3 Large-eddy simulations

Large-eddy simulations (LES) introduced by Smagorinsky (1963) is the concept of simulating the turbulent scales that are larger than a prescribed filter width. In LES, turbulent structures at small scales are filtered out by a low-pass filter. Filtering out small scales allows for reducing the numerical resolution. LES is thus commonly used for the simulation of turbulent flows at high Reynolds numbers where large scale separations render direct numerical simulations of the flow numerically inaccessible. In this research however, the reason of using LES is not to reduce the computational cost of the simulations. Following Hwang & Cossu (2010*c*), we use LES to isolate large-scale motions by filtering out smaller-scale structures of the turbulent ASBL while the smaller-scale structures are well-resolved.

Denoting the coordinate system by $x_i = (x, y, z)$, the governing equations of motion for the filtered velocity $\overline{\mathbf{u}} = \overline{u}_i = (\overline{u}, \overline{v}, \overline{w})$ are the filtered Navier-Stokes equations (Pope, 2000)

$$\frac{\partial \overline{u}_i}{\partial t} + \overline{u}_j \frac{\partial \overline{u}_i}{\partial x_j} = -\frac{\partial \overline{q}}{\partial x_i} + \nu \frac{\partial^2 \overline{u}_i}{\partial x_j^2} - \frac{\partial \overline{\tau}^r_{ij}}{\partial x_j}, \tag{2.24}$$

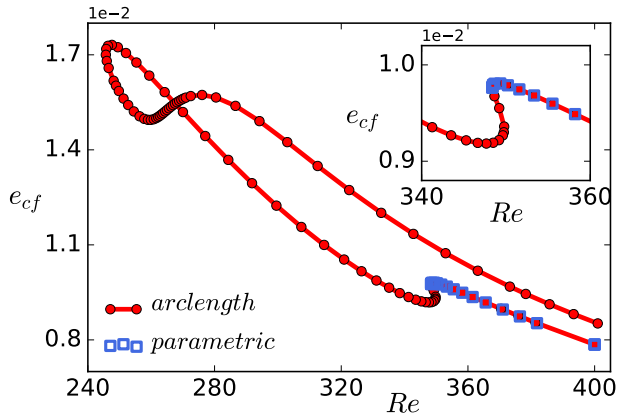

Figure 2.9 – Continuation of the wall-mode solution of Kreilos *et al.* (2016) in the Reynolds number. Cross-flow kinetic energy per length of the wall $e_{cf} = 1/L_x \int_0^{L_x} \left(v^2 + w^2\right) dxdydz$ as a function of Re is shown. Two numerical continuation methods provided in the `nsolver` library are used to perform the numerical continuation from the solution at $Re = 400$ on the lower branch (lower e_{cf}) to lower Re. The empty blue squares show the solution branch obtained by the parametric continuation method. The solution branch obtained by the arclength continuation method is indicated by red full circles. The arclength continuation method successfully continues the solution from the lower branch (lower e_{cf}) through saddle-node bifurcations to the upper branch while the parametric continuation method fails to follow the solution beyond the first saddle-node bifurcation (magnified in the inset).

with the continuity equation

$$\frac{\partial \overline{u}_i}{\partial x_i} = 0. \tag{2.25}$$

The filtering action is denoted by an overbar. $\overline{q} = \overline{p} + tr(\overline{\tau}^R)/3$ is a modified pressure with $\overline{\tau}^R = \overline{u_i u_j} - \overline{u_i}\,\overline{u_j}$. The residual stress tensor $\overline{\tau}^r = \overline{\tau}^R - tr(\overline{\tau}^R)\mathbf{I}/3$ captures the contribution of the scales smaller than the filter width in the dynamics of the filtered velocity. The residual stress tensor is a function of the total velocity field $\mathbf{u}$ that is not available in the simulations of the filtered velocity $\overline{\mathbf{u}}$. A model to express $\overline{\tau}$ in terms of the filtered velocity field is thus needed to close the equations. Among many models that are developed for this purpose, we employ the famous and widely used static Smagorinsky model (Smagorinsky, 1963).

2.3.1 Static Smagorinsky model

The static Smagorinsky model (Smagorinsky, 1963) expresses the residual stress tensor τ^r by

$$\overline{\tau}^r_{ij} = -2\nu_t \overline{S}_{ij} \tag{2.26}$$

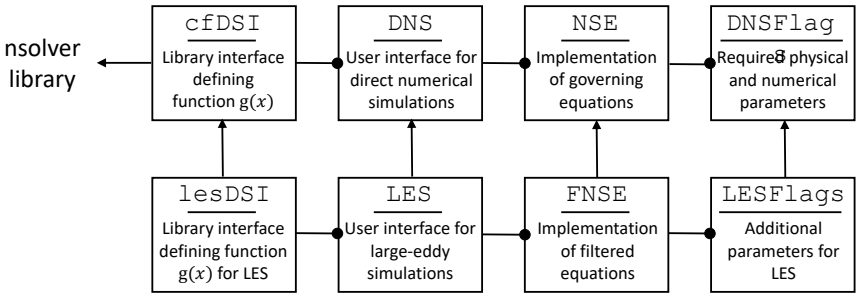

Figure 2.10 – The derived classes to extend *channelflow 2.0* for large-eddy simulations. Similar to figure 2.2, the arrows and oval arrows indicate inheritance and dependence, respectively. These classes link to the provided time-stepping classes in the `chflow` library to advance the filtered Navier-Stokes equations in time.

where $\overline{S}_{ij}$ is the rate of the strain tensor of the filtered velocity field and ν_t is the eddy viscosity. The eddy viscosity ν_t is given by

$$\nu_t = D(C_s\overline{\Delta})^2\overline{S}, \tag{2.27}$$

where $\overline{S} = \sqrt{2\overline{S}_{ij}\overline{S}_{ij}}$ is a measure of the local shear and $\overline{\Delta} = \sqrt[3]{\overline{\Delta}_x\overline{\Delta}_y\overline{\Delta}_z}$ is the geometric average of the grid spacing in all three directions. The wall damping function $D = 1 - \exp\left(-\left(y^+/A^+\right)^3\right)$ with $A^+ = 25$ enforces a zero stress residual at the wall (Kim & Menon, 1999). C_s is the static Smagorinsky constant, a parameter that can be set externally to tune the results of LES with respect to the DNS results. The static Smagorinsky constant C_s controls the filter width. Increasing C_s filters out an increasing range of scales (Mason & Callen, 1986).

2.3.2 Implementation

We extended the software *channelflow 2.0* to perform large-eddy simulations by solving the filtered Navier-Stokes equations (2.24) with the static Smagorinsky model (2.26). Compared to the unfiltered Navier-Stokes equations (2.7), the filtered equations (2.24) contain an additional nonlinear forcing term in terms of the residual stress tensor τ^r. As a result of the separation of the dynamical system analysis tools and the time-stepping algorithms from the governing equations in *channelflow 2.0*, extending the software to solve Navier-Stokes equations with additional forcing terms only requires the implementation of classes that represent the governing equations of the new system. We implement the required classes for the filtered Navier-Stokes equations with the static Smagorinsky model:

- `LES` is the user interface that handles time-advancing the filtered equations. This interface links the filtered equations with the time-stepping schemes provided in the `chflow` library.
- `FNSE` represents the filtered Navier-Stokes equations. This class computes the lin-

ear and nonlinear terms of the evolution equation separately and provide them to the time-stepping algorithms. The additional forcing term of the filtered equations $\partial(-2\nu_t \overline{S}_{ij})/\partial x_j$ is calculated and returned within the nonlinear term.

- `LESFlags` contains the parameters required by the static Smagorinsky model including the Smagorinsky constant C_s.
- `lesDSI` is the interface with the `nsolver` library.

The relations of the implemented classes for extending *channelflow 2.0* with the other classes of the software are shown in figure 2.10.

2.3.3 Validation

We validate the implemented LES code against semi-analytical solutions of the filtered equations and results of direct numerical simulations. First, we show that the stable laminar solution converged by the three-dimensional LES agrees with the semi-analytical laminar solution of the filtered equations. Then, we compare turbulent simulations by the implemented LES code to the results of the DNS.

'Laminar' solution of the filtered equations with static Smagorinsky model

Depending on the Reynolds number and symmetry constraints, large-eddy simulations can converge to a stationary laminar solution. Due to the extra forcing term in the LES model the profile of this solution differs from the laminar solution of the Navier-Stokes equations ((2.7)). The laminar solution of the filtered equations with the static Smagorinsky model is physically not relevant, since LES is a model for turbulence and the forcing term embedded in the LES equations accounts for the effect of velocity fluctuations of small scales. Here, however, we use the laminar solution of the filtered equations in order to validate that the forcing term in the LES model is correctly calculated in our code.

Assuming that the spanwise component of the laminar solution is zero and the streamwise component is only a function y, the continuity equation (2.25) and the boundary conditions at the walls (2.13) yield the wall-normal component of the laminar solution $\overline{v} = -1/Re$. The streamwise component of the laminar solution can be obtained by solving the streamwise component of the filtered Navier-Stokes equations (2.24). This equation can be simplified to

$$-\frac{1}{Re}\frac{d\overline{u}}{dy} = \frac{1}{Re}\frac{d^2\overline{u}}{dy^2} - \frac{d\overline{\tau}^r_{12}}{dy}.$$

The simplified required residual stress tensor component $\overline{\tau}^r_{12}$ is

$$\tau^r_{12} = -2\nu_t S_{12} = -C_s^2 h(y)\left(\frac{d\overline{u}}{dy}\right)^2,$$

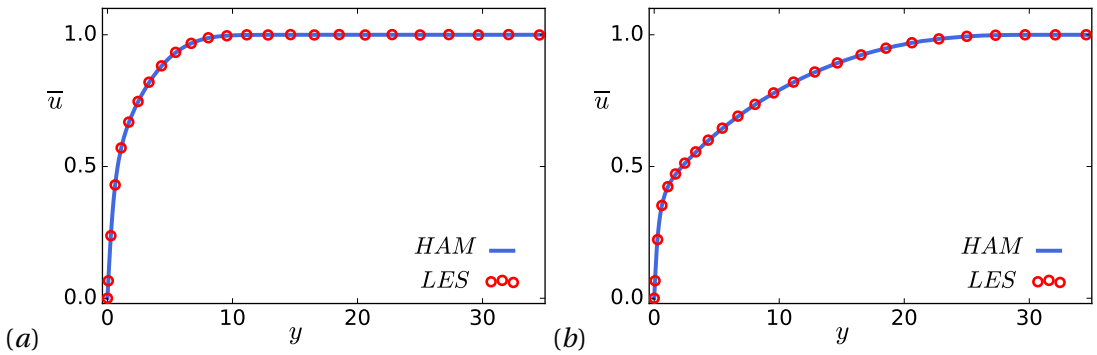

Figure 2.11 – Validation of the implemented LES extension of *channelflow 2.0* against the laminar solution of the filtered Navier-Stokes equations with static Smagorinsky model for (*a*) $C_s = 0.1$, and (*b*) $C_s = 0.3$. The blue line shows the solution profile of the ODE (2.28) obtained by the semi-analytical homotopy analysis method (HAM). The red circles show the stable laminar solution of the LES. The profiles are in excellent agreement, justifying the calculations of the LES forcing term.

where

$$h(y) = -\left(1 - \exp\left(-y\sqrt{Re}/A^+\right)^3\right)\overline{\Delta}^2(y),$$

is a function of the wall-normal coordinate y collecting the wall-damping function and the geometric average of the grid spacing. Both are known functions of y. Inserting $\overline{\tau}^r_{12}$ in the simplified filtered Navier-Stokes equation yields

$$\frac{d^2\overline{u}}{dy^2} + \frac{d\overline{u}}{dy} + C_s^2 Re \frac{d}{dy}\left(h(y)\left(\frac{d\overline{u}}{dy}\right)^2\right) = 0. \tag{2.28}$$

The boundary conditions of this equation are the no-slip conditions:

$$\overline{u}(y=0) = 0,$$
$$\overline{u}(y=H) = 0.$$

For $C_s = 0$, the additional forcing term vanishes, and the equation can be solved analytically. The solution of the equation for $C_s = 0$ becomes the laminar solution of the ASBL (2.14). For $C_s > 0$, the equation is nonlinear and has no known analytical solution, but can easily be solved numerically. We compare this 'laminar' solution to results of full three-dimensional LES.

At $Re = 300$, large-eddy simulations of the flow in a numerical box of extension $[L_x = 192, H = 100, Lz = 84]$ converge to the stable laminar solution of the filtered equations. The box is discretized by $[N_x = 48, N_y = 61, N_z = 42]$ collocation points in the streamwise, wall-normal and spanwise directions, respectively. The simulations are performed at two different values of the static Smagorinsky constant, $C_s = 0.1$ and $C_s = 0.3$. At both values of C_s, the simulations

converge to the corresponding stable laminar solutions. The computation of the forcing term in the implemented LES code is then validated by comparing the converged stable laminar solution to the solution of the ordinary differential equation (2.28). This ordinary differential equation (ODE) is solved by the semi-analytical homotopy analysis method (HAM) (Liao, 1999). The solution profiles obtained by the LES are in excellent agreement with the solutions of the ODE for both values $C_s = 0.1$ and $C_s = 0.3$, as shown in figure 2.11. These results validate the implementation of the forcing term in the filtered Navier-Stokes equations by the LES code.

Turbulent ASBL simulations

In the static Smagorinsky model, the constant C_s controls the magnitude of the additional forcing term of the LES model. The constant C_s thereby controls the filter strength. It is thus possible to adjust C_s externally such that LES reproduces statistical properties of DNS well. We call the Smagorinsky constant that reproduces the statistics of DNS the reference C_s. Depending on the flow system, the value of the reference C_s varies between $C_s \sim 0.04$ (Härtel & Kleiser, 1998) and $C_s \sim 0.17$ (Lilly, 1966). Here, we find the reference value of C_s in the ASBL at $Re = 300$ corresponding to the friction Reynolds number $Re_\tau = 1168$. We demonstrate that the statistics of the flow that are obtained by the implemented LES model at the reference value of C_s agree well with the statistics of the DNS.

The statistics of several large-eddy simulations with different values of C_s are compared with the statistics of a direct numerical simulation. For the DNS all relevant scales of the turbulent flow are resolved while for the LES the numerical grid is coarser and the scales smaller than the filter width are modelled. The DNS is carried out in a numerical box of extension ($L_x = 256,\ H = 150,\ L_z = 128$) which is discretized by ($N_x = 256,\ N_y = 241,\ N_z = 256$) collocation points in the streamwise, wall-normal and spanwise directions, respectively. The numerical box for the LES has a size of ($L_x = 256,\ H = 100,\ L_z = 128$), and is resolved with ($N_x = 64,\ N_y = 61,\ N_z = 64$) collocation points. For time-stepping the equations, a third order accurate semi-implicit backward differentiation method is employed. The 2/3 dealiasing rule is applied in the streamwise and the spanwise directions.

Figure 2.12 shows the boundary layer thickness δ_{99}, the friction Reynolds number Re_τ, the turbulent displacement thickness δ^* and the turbulent momentum thickness θ as a function of C_s. According to this figure, at $C_s = 0.045$ all of these boundary layer properties are equal to the values obtained from the DNS simulation. This observation suggests that $C_s = 0.045$ is the reference Smagorinsky constant for the considered flow. This is further studied in figures 2.13 and 2.14 where the statistics of the LES with $C_s = 0.045$ are compared with the DNS statistics. In figure 2.13, the mean and the root mean squared (r.m.s.) profiles for the DNS and the LES with $C_s = 0.045$ are shown. Figure 2.14 visualises contours of premultiplied power spectra for both the DNS and the LES with $C_s = 0.045$. The profiles and the contours of the LES with $C_s = 0.045$ agree well with those of the DNS. $C_s = 0.045$ is thus the reference Smagorinsky constant, and the LES with $C_s = 0.045$ can reproduce the DNS results.

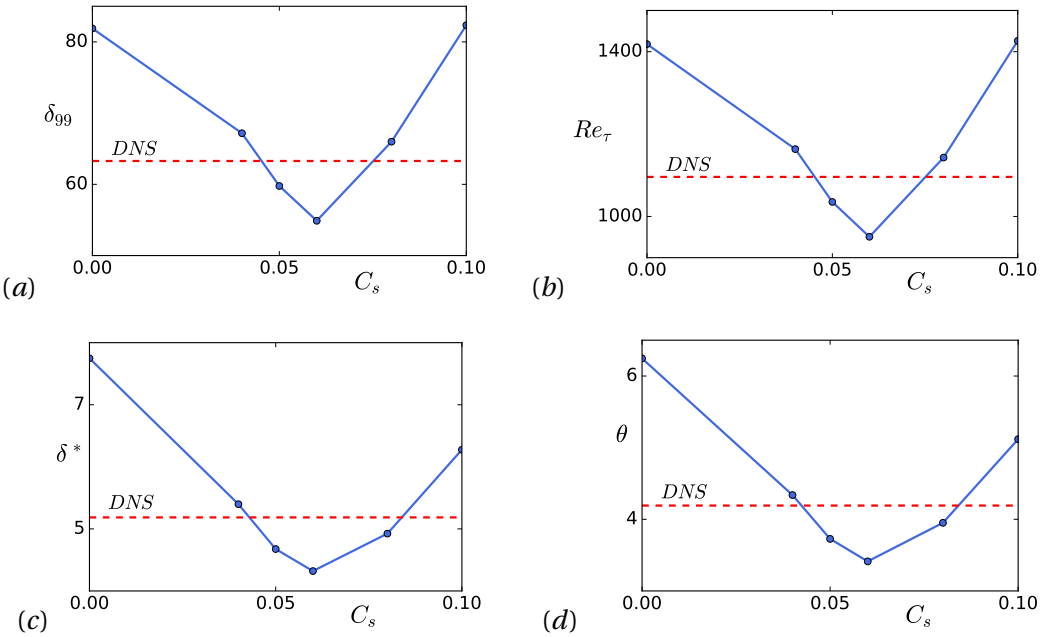

Figure 2.12 – Boundary layer properties as functions of the static Smagorinsky constant C_s: (a) turbulent boundary layer thickness δ_{99}, (b) the friction Reynolds number Re_τ, (c) turbulent displacement thickness $\delta^* = \int_0^H (1-u)\,dy$, and (d) turbulent momentum thickness $\theta = \int_0^H u(1-u)\,dy$. For $C_s = 0.045$ the boundary layer properties are close to the values given by the DNS. We choose the reference value $C_s = 0.045$ for large-eddy simulations to reproduce the results of DNS. Note that at the higher value of the Smagorinsky constant, $C_s = 0.08$, the boundary layer properties are close to the DNS values, but higher-order statistics (not shown) are not satisfactory.

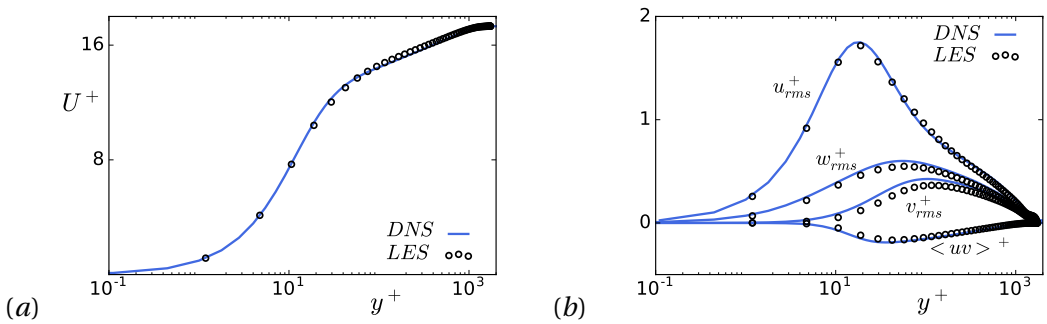

Figure 2.13 – (a) Mean streamwise velocity, and (b) root mean squared (r.m.s.) velocity components expressed in inner units as functions of the wall-normal coordinate y^+, for the DNS (blue line) and the LES with the value of $C_s = 0.045$ (empty circles). All profiles obtained by the LES are in excellent agreement with the results of the DNS.

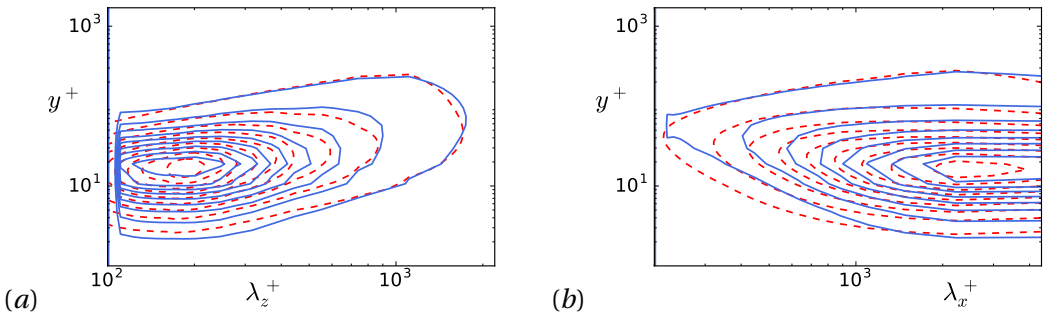

Figure 2.14 – Contours of spanwise premultiplied power spectra (panel *a*) and streamwise premultiplied power spectra (panel *b*) of the streamwise velocity for direct numerical simulations (red dashed lines) and large-eddy simulations with the value $C_s = 0.045$ (blue sold lines). The contour levels for the DNS and the LES are the same. The location and the sharpness of the energy peak for the LES are in good agreement with those for the DNS. This observation indicates that the LES can reproduce the dynamics of the resolved scales.

3 Self-similar invariant solution in the near-wall region

Remark: This chapter is largely inspired by a publication titled "Self-similar invariant solution in the near-wall region of a turbulent boundary layer at asymptotically high Reynolds numbers"

Sajjad Azimi[1] and Tobias M. Schneider[1]

[1]Emergent Complexity in Physical Systems Laboratory (ECPS),
École Polytechnique Fédérale de Lausanne, CH-1015 Lausanne, Switzerland

Journal of Fluid Mechanics **888**, A15 (2020)

Contents

Chapter summary

At sufficiently high Reynolds numbers, shear-flow turbulence close to a wall acquires universal properties. When length and velocity are rescaled by appropriate characteristic scales of the turbulent flow and thereby measured in *inner units*, the statistical properties of the flow

become independent of the Reynolds number. We demonstrate the existence of a wall-attached non-chaotic exact invariant solution of the fully nonlinear three-dimensional Navier-Stokes equations for a parallel boundary layer that captures the characteristic self-similar scaling of near-wall turbulent structures. The branch of travelling wave solutions can be followed up to $Re = 1\,000\,000$. Combined theoretical and numerical evidence suggests that the solution is asymptotically self-similar and exactly scales in inner units for Reynolds numbers tending to infinity. Demonstrating the existence of invariant solutions that capture the self-similar scaling properties of turbulence in the near-wall region is a step towards extending the dynamical systems approach to turbulence from the transitional regime to fully developed boundary layers.

3.1 Introduction

Invariant solutions of the fully nonlinear three-dimensional Navier-Stokes equations are known to play an important role in the dynamics of turbulence at low Reynolds numbers. For virtually all canonical shear flows, invariant solutions in the form of equilibria, travelling waves and periodic orbits, have been computed. The solutions act as transiently visited building blocks for the dynamics (Gibson *et al.*, 2008; Kawahara *et al.*, 2012; Suri *et al.*, 2017) and capture many characteristic features of transitional flows including self-organised turbulent–laminar patterns such as puffs in pipe flow and laminar–turbulent stripes in Couette flow (Avila *et al.*, 2013; Reetz *et al.*, 2019).

To extend the approach to describe turbulence in terms of invariant solutions from the transitional regime to developed turbulent wall-bounded flows at high Reynolds numbers relevant for many engineering applications, invariant solutions capturing the characteristics of those fully turbulent boundary layer flows are required. At sufficiently high flow speeds, turbulent fluctuations in a layer close to the wall show a typical spacing of streaky motions that is universal and independent of the specific flow parameters, when distances are measured in inner or wall units (Kline *et al.*, 1967; Kim *et al.*, 1987). The wall-shear stress τ_w controls the characteristic scales of turbulence, namely the friction velocity $u_\tau = \sqrt{\tau_w/\rho}$ and the viscous length unit $\delta_\tau = \nu/u_\tau$. ρ is the density and ν the kinematic viscosity of the fluid. After rescaling velocities and distances with these characteristic scales, the turbulent flow in the *inner region* close to the wall becomes independent of the Reynolds number (Jiménez, 2018).

The self-similar inner region interacts with the *outer region* further away from the wall. Here, turbulent fluctuations do not scale in inner units but change with Reynolds number. The characteristic length scale of the outer region l_{out} depends on the specific flow system. For a semi-infinite open flow domain the outer scale is given by the boundary layer thickness of the turbulent flow. In confined flows, such as channel flow, the turbulent boundary layer cannot freely expand so that confinement effects limit the outer scale to the distance between the walls. The higher the flow speed and thus wall shear, the thinner is the inner region. The friction Reynolds number $Re_\tau = u_\tau l_{out}/\nu = l_{out}/\delta_\tau$ measures the scale separation between

the self-similar near-wall inner scale and the characteristic outer scale of the turbulent flow; Re_τ thereby characterises fully developed turbulence along a wall and indicates the strength of turbulence.

To capture the universal small-scale motions of turbulence in the inner region close to the wall, invariant solutions are required that are localised at the wall, exist at very high Reynolds numbers and scale in inner units defined by the mean wall-shear stress of turbulence. However, to date, attempts to find invariant solutions of the Navier-Stokes equations capturing the universal features of the small-scale motions in the near-wall region have mostly failed. Rawat *et al.* (2015) were unable to find a near-wall solution connected to the Nagata equilibrium (Nagata, 1990), the solution of Jiménez & Simens (2001) requires non-physical artificial damping and the wall-attached solution of Neelavara, Duguet & Lusseyran (2017) fails to scale in inner units. Deguchi (2015) identifies a solution which scales in inner units at high Reynolds numbers but is not localised at the wall. More recently Eckhardt & Zammert (2018) present two solutions in plane Couette flow, one localised in the centre of the channel and one attached to the wall. The solutions are followed up to a Couette Reynolds number of $Re = 100\,000$, and become approximately Reynolds number independent when rescaled by the inner length scale. Likewise Yang, Willis & Hwang (2019) follow a wall-attached solution in fixed-flux channel flow up to $Re_\tau = 268$ and show that the solution approximately scales in inner units. Both Eckhardt & Zammert (2018) and Yang *et al.* (2019) use inner units corresponding to the wall drag of the solution itself, which differs from the mean wall drag of turbulence at the same controlled relative plate velocity in Couette or controlled flux in channel flow.

Here we present a wall-attached solution of a parallel boundary layer at Reynolds numbers up to 1 000 000. For large Reynolds numbers, the solution scales in inner units based on the mean turbulent wall drag. Combined numerical and theoretical evidence suggest an exactly self-similar solution, that is asymptotically independent of Reynolds number when rescaled in terms of inner units. The wall-attached solution thus captures the characteristic scaling behaviour of the near-wall turbulence universally observed in wall-bounded flows at high flow speeds.

3.2 The asymptotic suction boundary layer

Previous attempts to identify high-Reynolds-number invariant solutions in the near-wall region have considered confined shear flows such as channel flow. Owing to the universal nature of near-wall turbulence at sufficiently high Reynolds number we instead consider a boundary layer in a semi-infinite domain. To avoid the complications associated with non-parallelism of the flow, we study the fully turbulent asymptotic suction boundary layer (ASBL), where moderate suction at the wall keeps the base flow parallel in the downstream asymptotic regime (Schlichting, 2004).

We consider the flow developing over a flat plate immersed in a uniform stream of velocity U_∞ with constant and uniform suction V_s into the plate (figure 3.1). Sufficiently far downstream,

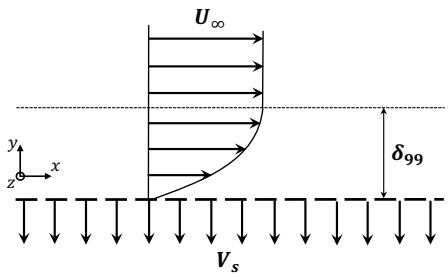

Figure 3.1 – Schematic of the asymptotic suction boundary layer flow. The streamwise, wall-normal and spanwise directions are denoted by x, y, and z, the corresponding velocities are denoted by u, v and w, respectively. The height where the mean streamwise velocity is 99% of the free-stream velocity is called the boundary layer thickness and denoted by δ_{99}.

where wall friction balances streamwise momentum loss due to the suction, the boundary layer thickness reaches a constant value and 'asymptotic suction boundary layer' flow is reached. The laminar exact solution of the Navier-Stokes equations is $\check{U}/U_\infty = 1 - \exp(-\check{y}V_s/\nu)$, where $\check{U}$ is the (dimensional) streamwise velocity, $\check{y}$ the (dimensional) wall-normal coordinate and ν is the kinematic viscosity of the fluid. This laminar solution is characterised by a constant displacement thickness $\delta^* = \nu/V_s$ and can be recast in dimensionless form $U = 1 - e^{-y}$ by using δ^* as reference length and U_∞ as reference velocity. We prescribe the Reynolds number based on the laminar boundary layer displacement thickness $Re = U_\infty\delta^*/\nu = U_\infty/V_s$. This Reynolds number, referred to as 'the Reynolds number' is commonly used as control parameter for ASBL and needs to be distinguished from the friction Reynolds number Re_τ. Despite its linear stability up to $Re = 54370$ (Hocking, 1975), the laminar ASBL solution is in practice only observed for $Re \lesssim 270$ (Khapko *et al.*, 2016); above this value the flow is turbulent.

There is numerous experimental, numerical and theoretical support for the fact that, close to a wall, high-Reynolds-number turbulence is universal and independent of the specific system in which it is observed (Pope, 2000; Jiménez, 2018). At high Re the universal near-wall turbulent dynamics in the small inner region decouples from large-scale flow in the outer region. Since the universal features of near-wall turbulence can be studied in any wall-bounded shear flow, one may choose to consider a specific flow based on convenient properties of the non-universal outer scale dynamics.

ASBL flow has two key properties that are advantageous for studying near-wall turbulence when compared to other commonly studied canonical flows such as the fixed-flux channel flow considered by Yang *et al.* (2019):

1. Inner length and velocity scales capture properties of the turbulent state and are thus in general not known *a priori*. In ASBL, however, momentum conservation allows us to directly control the wall drag so that the characteristic scale of near-wall turbulence can be expressed directly in terms of the control parameters of the flow. Consequently, one can carry out numerical studies in a domain whose size is fixed in inner units of the

turbulent state. For some other canonical flows, this is not possible: for channel flow with constant flux, as studied by Yang *et al.* (2019), the imposed control parameter is the Reynolds number based on the mean flow rate. A turbulent simulation or experiment is required to determine the wall shear of the turbulence τ_w and quantities can be rescaled with the inner velocity scale $u_\tau = \sqrt{\tau_w/\rho}$ and the inner length scale $\delta_\tau = \nu/u_\tau$ only *a posteriori*. If not the flux but the applied pressure gradient were fixed, also in channel flow, inner length and velocity scales could be determined *a priori*.

2. For a confined shear flow such as channel flow where the outer scale is given by the separation of two bounding walls, numerically resolving a near-wall solution at high Re_τ in general implies numerically resolving the entire flow domain including both walls with sufficient resolution to handle the large separation between outer and inner scales. For ASBL, localisation of the flow at a single wall allows us to not fully resolve outer scales, but focus on the near-wall region.

3.3 Determining the minimal flow unit in inner units

We consider a numerical domain of length L_x, width L_z and height H, where periodic boundary conditions are applied in the x and z directions. On the upper and lower boundaries, we impose Dirichlet conditions $\mathbf{u}(x,0,z) = \mathbf{u}(x,H,z) = \mathbf{0}$, with $\mathbf{u}$ the deviation from the laminar solution. ASBL has continuous translational symmetries in x and z so that the periodic boundary conditions are compatible with the equivariance group of the flow problem. Consequently, any solution found in the periodic domain also exists in the infinitely extended system. Based on turbulent simulations, we choose L_x and L_z such that small-scale near-wall motions are faithfully captured. This defines the minimal flow unit (MFU). The height H is chosen to be large enough so that the flow detaches from the top boundary and becomes independent of the domain height.

To determine the MFU in ASBL, we extract the most energetic length scales of the near-wall region from energy spectra. A turbulent ASBL at $Re = 333$ is simulated in a large domain of size $L_x = 243, H = 225, L_z = 121.5$ (similar to simulations of Schlatter & Örlü (2011) and Bobke *et al.* (2016); more details about the simulation are provided in appendix 3.6). The premultiplied streamwise energy spectrum peaks at $y^+ = 17$, where the plus superscript indicates quantities measured in terms of inner units. At this wall-normal location, the peaks in the streamwise and spanwise premultiplied energy spectra are located at $\lambda_x^+ = 633$ and $\lambda_z^+ = 170$, respectively. We consequently choose the length and the width of the MFU as $L_x^+ = 633$ and $L_z^+ = 170$ in inner units. This ensures that the most energetic modes of the near-wall region are captured. A height of $H^+ = 632$ is sufficient to guarantee the complete detachment of all flow structures from the upper wall, as shown in appendix 3.6. Note that the required height of the flow domain remains considerably smaller than the turbulent boundary layer thickness δ_{99} defining the outer scale. As discussed in Bobke *et al.* (2016), this is related to the limited width of the MFU, disallowing the formation of the large-scale structures that

extend far into the outer region of the turbulent boundary layer. The MFU capturing small-scale near-wall motions thus has a size of $L_x^+ = 633, H^+ = 632, L_z^+ = 170$ in inner units. Since the inner-unit location of the near-wall energy peak is independent of the Reynolds number, reflecting the inner-unit scaling of turbulence, the inner-unit box size determined here for $Re = 333$ remains unchanged for higher Reynolds numbers.

Momentum conservation in the ASBL requires that the ratio of the friction velocity to the free-stream velocity is $u_\tau / U_\infty = 1/\sqrt{Re}$, where $u_\tau = \sqrt{\tau_w/\rho}$, with τ_w the mean wall friction. The viscous unit is $\delta_\tau = \delta^* / \sqrt{Re}$ where $\delta_\tau = \nu / u_\tau$ and δ^* is the displacement thickness of the laminar flow. Consequently, in ASBL both the inner velocity scale u_τ and the inner length scale δ_τ are directly given in terms of the externally controlled Reynolds number and do not need to be computed from turbulent statistics. Thus we can exactly prescribe the size of a computational box in inner units, and continue invariant solutions towards high Reynolds numbers. As we increase Re, we change the size of the minimal flow unit in outer units in such a way that the size remains exactly constant in inner units.

3.4 Invariant solutions in the minimal flow unit

We aim at finding a wall-attached invariant solution that can be followed to very high Re. Instead of computing a 'starting' solution at low Reynolds numbers close to the transition, where interaction with large-scale features of the flow, and in particular interaction between the two walls in Couette and Poiseuille flows, might have prevented the finding of a genuine 'one-wall' solution in the near-wall inner region to start the continuation from, we immediately consider a value of $Re = 1000$, well above transition to avoid any potential low Reynolds number effect in the selection of the solution branch. Moreover, in ASBL the kinetic energy associated with the non-universal and system-dependent large-scale features of the flow is relatively weak when compared to other flows (Schlatter & Örlü, 2011; Bobke *et al.*, 2016). Consequently, even at moderate Re, the flow dynamics is dominated by the near-wall dynamics, which may aid in identifying a solution branch representing a universal wall-attached high Re solution. At $Re = 1000$, edge tracking (Skufca, Yorke & Eckhardt, 2006; Schneider, Eckhardt & Yorke, 2007) within the mirror symmetry subspace $[u, v, w](x, y, -z) = [u, v, -w](x, y, z)$ yields a travelling wave solution in the MFU determined above.

The invariant solution computed at $Re = 1000$ is used as starting point for a continuation in Reynolds number where the size of the domain is kept constant in inner units, and therefore shrinks in outer units, when Re is increased. As shown in figure 3.2, we can continue the solution up to $Re = 1\,000\,000$ with both size of the box and magnitude of the solution decreasing in outer units. Figure 3.3 shows contours of the streamwise-averaged wall-normal velocity of the invariant solution in inner units at different Reynolds numbers. The solution structures remain almost unchanged over a wide range of Reynolds number when expressed in inner units.

To provide context for the achieved value of Re, we characterise the scale separation of fully

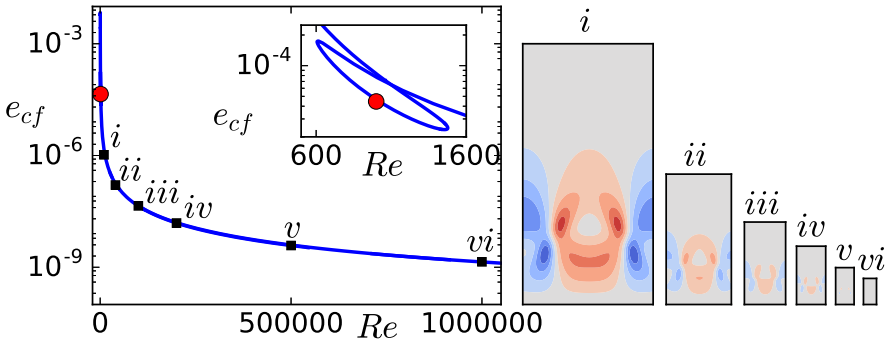

Figure 3.2 – Continuation of the invariant solution to high Reynolds numbers in outer units. Cross-flow kinetic energy per area of the wall $e_{cf} = 1/(L_x L_z) \int_{MFU} \left(v^2 + w^2\right) dxdydz$ in the MFU as a function of Re. Note that in outer units velocities are non-dimensionalised by U_∞ and lengths by ν/V_s, so e_{cf} is in units of $U_\infty^2 \nu/V_s$. The red dot indicates where the solution has been identified by edge tracking (see also inset for a magnification of the relevant parameter range). Visualisations of the invariant solution show contours of the streamwise-averaged wall-normal velocity at $Re = 10\,000$, $40\,000$, $100\,000$, $200\,000$, $500\,000$, and $1\,000\,000$.

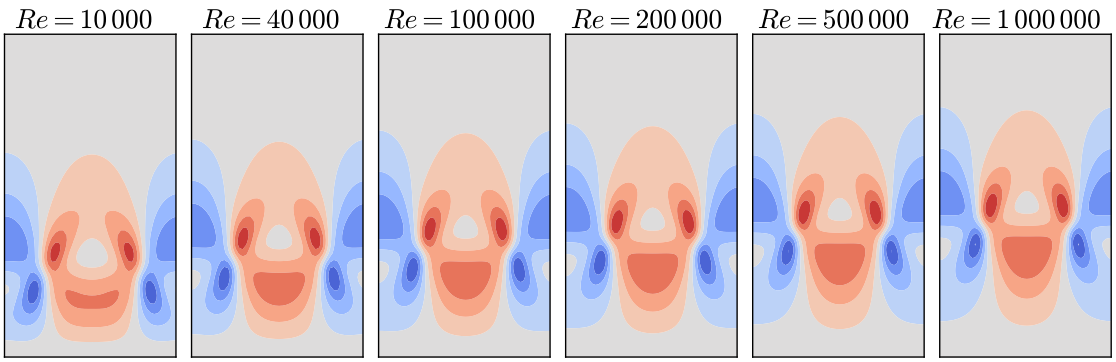

Figure 3.3 – Invariant solution visualised in inner units. Contours of streamwise-averaged wall-normal velocity, normalised by friction velocity u_τ at the same values of Re as in figure 3.2. The contour levels are $v^+ = v/u_\tau = \{\pm 0.015, \pm 0.045, \pm 0.075, \pm 0.105, \pm 0.135\}$. The solution is localised at the wall so that only the lower half of the numerical domain is shown.

developed turbulent flow at the same imposed value of Re and in a large domain. While ASBL has the advantage that the self-similar near-wall inner scale δ_τ is directly controlled by Re, determining the outer scale, commonly associated with the turbulent boundary layer thickness δ_{99}, requires extensive turbulent simulations. To be domain independent, these simulations need to be carried out in domains considerably larger than the MFU to allow for structures in the outer region, including those large compared to the wavelength imposed by the periodic MFU box, to develop. Those simulations can only be carried out for moderate Re. Using large eddy simulations, Schlatter & Örlü (2011); Bobke *et al.* (2016) determined the turbulent boundary layer thickness of ASBL as $\delta_{99} = 101$ for $Re = 333$ and $\delta_{99} = 290$ for $Re = 400$. Khapko *et al.* (2016) observed δ_{99} to grow linearly in Re for values between 260 and 333. For higher Re, the evolution of the turbulent boundary layer thickness is unknown. Since

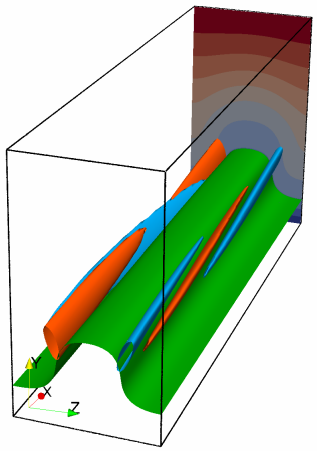

Figure 3.4 – Three-dimensional structure of the invariant near-wall solution at $Re = 40\,000$. The travelling wave is dominated by a strong low-speed streak (situated in the centre of the figure) sandwiched between weaker high-speed streaks located closer to the wall and flanked by alternating mirror-symmetric pairs of counter-rotating vortices. The low-speed streak is visualised by the green streamwise velocity isosurface ($u = 0.2\,U_\infty$). Vortices are indicated by streamwise vorticity isosurfaces of ω_x at half of the maximum value with red/blue for positive/negative values. Due to the localisation of the structures near the wall, only the lower half of the computational domain is shown.

$\delta_\tau = 0.001$ at the highest achieved Reynolds number, the fully developed turbulent flow at $Re = 10^6$ has a scale separation of at least 290 000, even if the growth of the turbulent boundary layer thickness does not extend much beyond $Re \sim 400$.

At high Re the converged invariant solution remains localised near the wall. The structure of the travelling wave solution is dominated by spanwise-periodic alternating low- and high-speed streaks flanked by counter-rotating vortical structures, as shown in figure 3.4 where we present the solution at $Re = 40,000$. The solution is dominated by streamwise oriented streaks. In figure 3.5 we quantify the streamwise variation of the flow field by the amplitudes of the first three streamwise Fourier modes ($||\mathbf{u}_0^+(y,z)||_2$, $||\mathbf{u}_1^+(y,z)||_2$, and $||\mathbf{u}_2^+(y,z)||_2$). For increasing Re the inner-unit amplitudes approach constant values indicating a solution scaling in inner units. Moreover, the amplitude of the downstream independent zero mode is more than two orders of magnitude larger than the amplitude of the first mode and three orders of magnitude larger than the amplitude of the second mode. This confirms that the invariant solution is dominated by streamwise invariant structures.

The relatively small bending of the low-speed streak (see figures 3.4 and 3.5) of the identified near-wall invariant solutions is consistent with features of lower-branch solutions found at large scales in large domains with size typical of transitional (e.g. Wang, Gibson & Waleffe, 2007) and turbulent large-scale motions (e.g. Rawat, Cossu & Rincon, 2016). In boxes remaining constant in outer units, this type of Navier-Stokes solution assumes a critical-layer structure for high Reynolds numbers (Wang *et al.*, 2007; Deguchi & Hall, 2014*a*,*b*; Park & Graham, 2015)

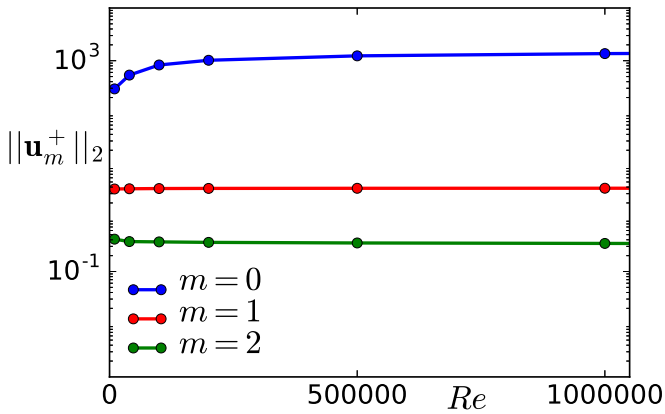

Figure 3.5 – Amplitude of the first three streamwise Fourier modes of the invariant solution expressed in inner units ($||\mathbf{u}_0^+(y,z)||_2$, $||\mathbf{u}_1^+(y,z)||_2$, and $||\mathbf{u}_2^+(y,z)||_2$) as a function of Re. The amplitudes approach constant values indicating a solution that scales in inner units. The zero Fourier mode ($m = 0$) dominates indicating a predominantly downstream invariant solution.

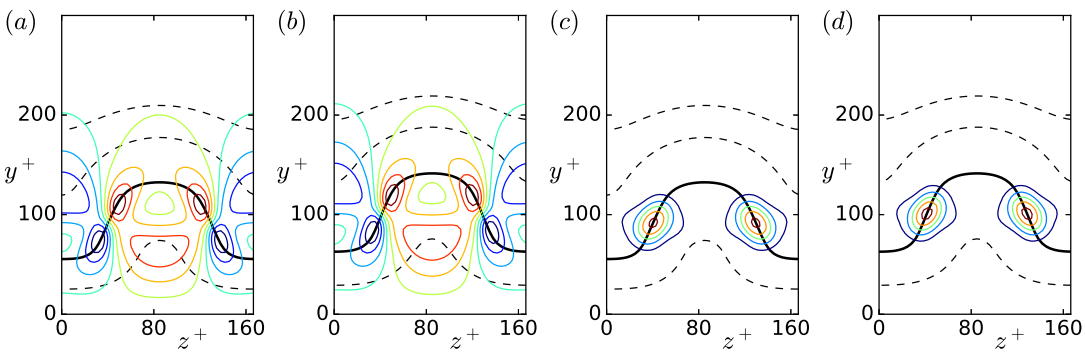

Figure 3.6 – Contours of the streamwise Fourier modes of the invariant solutions' wall-normal velocity (coloured contour lines). The zeroth mode $v_0^+(y^+,z^+)$ (panels a and b) and the first mode $v_1^+(y^+,z^+)$ (panels c and d) shown in inner units at $Re = 40\,000$ (panels a and c) and $Re = 100\,000$ (panels b and d). The critical layer where the zeroth streamwise mode of the streamwise velocity equals the travelling wave's phase speed ($u_0(y,z) = c$) is also shown (bold solid black line) as well as the levels $u_0(y,z)/c = 0.6, 1.4, 1.8$ (dashed black lines). Only the lower half of the numerical box is shown.

where the streaks' unstable mode concentrates near the critical layer. In the present case, however, the entire solution is downscaled in height, lateral wavelength and global amplitude when the Reynolds number increases (figure 3.2). There is no modification of the internal structure or a concentration near the critical layer. The zeroth streamwise Fourier mode of the wall-normal velocity $v_0^+(y,z)$ (associated with the streamwise vortices inducing the streaks), as well as the first streamwise Fourier mode $v_1^+(y,z)$ (associated with the streaks' instability mode) are asymptotically constant when expressed in inner units as Re increases, as shown in figure 3.6.

The root mean squared (r.m.s.) velocity profiles of the travelling wave solution expressed in

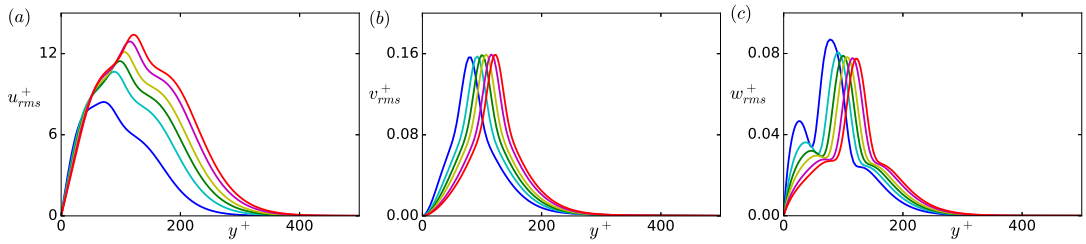

Figure 3.7 – Root mean squared (r.m.s.) profiles of the travelling wave solutions expressed in inner units $u^+_{i,rms}(y^+) = \left[1/(L^+_x L^+_z)\int_0^{L^+_x}\int_0^{L^+_z}\left(u^+_i(x^+,y^+,z^+) - u^+_{i,mean}(y^+)\right)^2 dx^+ dz^+\right]^{1/2}$ at Reynolds numbers equal to 10000 (blue), 40000 (cyan), 100000 (green), 200000 (yellow), 500000 (magenta), and 1000000 (red). (*a*) r.m.s. profiles of the streamwise velocity u^+_{rms}, (*b*) r.m.s. profiles of the wall-normal velocity v^+_{rms}, (*c*) r.m.s. profiles of the spanwise velocity w^+_{rms}. For increasing Re, the r.m.s. profiles asymptotically collapse, indicating scaling in inner units. Note that the variation of Re over two orders of magnitude corresponds to a full order of magnitude change in the height and lateral wavelengths of the solution in outer units (cf. figure 3.2).

inner units asymptotically collapse onto a single curve when Re is increased (figure 3.7). This provides further confirmation that the travelling wave solution scales in inner units.

The small change of the solution with Re (figures 3.3 and 3.6), the asymptotically constant values of inner-unit amplitudes (figure 3.5), and the asymptotically converging rms profiles (3.7) provide strong evidence that the fully resolved travelling wave solution asymptotes towards a self-similar solution at high Re. To investigate if the solution indeed becomes independent of Reynolds number for $Re \to \infty$ when expressed in similarity variables defined by rescaled length and velocity scales, we use the friction velocity, $u_\tau = U_\infty/\sqrt{Re}$, and the viscous unit, $\delta_\tau = \delta^*/\sqrt{Re}$, to non-dimensionalise the evolution equations. The Navier-Stokes equation for the inner-unit velocity deviation from the laminar solution reads

$$\frac{\partial \mathbf{u}^+}{\partial t^+} + \mathbf{U}^+\cdot\nabla\mathbf{u}^+ + \mathbf{u}^+\cdot\nabla\mathbf{U}^+ + \mathbf{u}^+\cdot\nabla\mathbf{u}^+ = -\nabla p^+ + \nabla^2\mathbf{u}^+ \tag{3.1}$$

where $\mathbf{u}^+$ is the non-dimensionalised velocity deviation vector, and $\mathbf{U}^+$ is the non-dimensionalised laminar solution. The non-dimensionalised laminar solution in ASBL

$$\mathbf{U}^+ = Re^{1/2}\left(1-\exp\left(-y^+ Re^{-1/2}\right)\right)\hat{\mathbf{e}}_\mathbf{x} - Re^{-1/2}\hat{\mathbf{e}}_\mathbf{y} \tag{3.2}$$

is a function of the Reynolds number, $Re = \frac{U_\infty}{V_s}$, and the wall-normal coordinate, y^+. The boundary conditions for the velocity deviation from the laminar base flow are periodic in the streamwise and in the spanwise directions and zero-velocity at both the lower and upper walls. In the rescaled system with the given governing equation and the boundary conditions expressed in inner units, only the laminar base flow depends on Re. For Re tending to infinity, the laminar base flow within the numerical box asymptotes to $\mathbf{U}^+ = y^+\hat{\mathbf{e}}_\mathbf{x}$ and thus no longer depends on the Reynolds number. Therefore, when Re is large, the rescaled system in

inner units loses any dependence on the Reynolds number, and any solution of the system approaches a self-similar solution. Thus, any invariant solution that can be continued to asymptotically high Reynolds numbers in a box which has a fixed size in inner units becomes asymptotically self-similar. This suggests that the invariant solution that we present in this chapter represents a self-similar solution of the Navier-Stokes equations in the near-wall inner region of the asymptotic suction boundary layer flow at high Reynolds numbers.

The analysis shows that as Re tends to infinity, the equations for ASBL solutions expressed in inner units lose the dependence on Reynolds number so that any solution of those equations is self-similar and scales in inner units. Remarkably, we also observe that the partial differential equations including boundary conditions that any wall-attached solution of ASBL satisfies at asymptotically high Re, are identical to those describing plane Couette flow (PCF) at a value of the typically used Couette Reynolds number $Re_{PCF} = {H^+}^2/4$, based on half the gap height and half the velocity difference. Boundary conditions of ASBL enforce zero wall-parallel velocity and a non-zero wall-normal suction. Expressed in inner units the suction velocity is $V_s^+ = 1/\sqrt{Re}$. For large Re, suction effects thus vanish and, asymptotically, the standard no-slip boundary conditions of PCF are reached. Consequently, at asymptotically high Re, any wall-attached solution of ASBL corresponds to a wall-attached solution of PCF. The value of the Couette control parameter Re_{PCF} formally depends on the arbitrarily chosen H^+ reflecting the fact that a solution localised at the wall, only depends on the shear rate at the wall while the distance of the second upper wall and thereby the value of Re_{PCF} is irrelevant. Thus, at asymptotically high Re, all state-space structures representing wall-attached flow fields in the MFU of ASBL have counterparts in high-Reynolds-number PCF, such as those identified by Eckhardt & Zammert (2018). This suggests that the relevant state-space structures for near-wall turbulence that we identified in ASBL are universal in that they are not only independent of Re when expressed in inner units but also do not depend on the specific shear-flow system considered. In fact, at sufficiently high Re, close to the wall, any wall-bounded shear flow is characterised by a universal shear profile, indistinguishable from PCF or ASBL and thus supports the same wall-attached solutions. This suggests that the entire state space of the near-wall region including the invariant solutions and their dynamical connections become independent of Re and independent of the flow system. If invariant solutions, their heteroclinic connections and the entire state-space structures are universal, the deterministic dynamics supported by those structures is also universal. This provides an explanation of the well-known fact that at sufficiently high flow speeds the statistics of near-wall turbulence becomes independent of the flow system.

3.5 Conclusion and discussion

The aim of this work is to demonstrate the existence of an exact invariant solutions of the Navier-Stokes equations that capture spatial scales typical of turbulent motions in the near-wall region of a boundary layer at high Reynolds numbers. In a minimal flow unit of ASBL, chosen to capture the energetic scales of near-wall turbulent motions, a wall-attached travel-

ling wave solution has been computed by edge tracking at $Re = 1000$. We exploit the fact that ASBL allows us to express the viscous length scale δ_τ of the developed turbulent state in terms of the Reynolds number. We thus continued the solution to high Re in the minimal flow unit, whose size remains constant in inner units but shrinks in outer units for increasing Re. The fully resolved solution can be followed up to $Re = 1\,000\,000$. We provide numerical and theoretical evidence that the invariant solutions become exactly self-similar as Re tends to infinity. Remarkably, the solution scales in inner units so that the individual fully resolved invariant solution of the Navier-Stokes equations captures the self-similar behaviour characteristic of near-wall-turbulent statistics. Moreover, in the high-Re asymptotic limit, solutions of ASBL simultaneously constitute solutions of plane Couette flow thus reflecting the universality of near-wall turbulence.

Assuming that all relevant invariant solutions capturing near-wall motions can be continued to asymptotically high Re, our analysis suggests that entire state-space structures, including invariant solutions and their dynamical connections, become independent of Reynolds number when expressed in inner units. To provide further support for this picture, future research should aim at computing increasingly more complex state-space structures underlying near-wall turbulence in the high-Re limit captured by the evolution equations expressed in inner units. This includes periodic orbits as well as orbits connecting invariant solutions.

Since the governing equations rescaled in inner units become asymptotically independent of Reynolds number, the complexity of the state space of near-wall turbulence and the number of relevant invariant solutions may not increase with Re but remain constant, leading to a saturation of complexity in the near-wall region of turbulent flows. Such a saturation of complexity cannot be expected in the outer region of turbulent flows. It may thus be possible to eventually provide a predictive and quantitative description of turbulence in terms of a manageable number of invariant solutions (Chandler & Kerswell, 2013; Cvitanović *et al.*, 2016) not only for transitional flows but also for the universal near-wall region of wall-bounded turbulence at very high Reynolds numbers. The self-similar exact invariant solution in the near-wall region of a boundary layer reported here is a significant step towards extending the invariant solution approach to turbulence from transitional flows to near-wall region of fully developed boundary layers.

3.6 Appendix: Methods

We use the `ChannelFlow 2.0` code (Gibson *et al.*, 2019) to solve the nonlinear Navier-Stokes equations expressed in perturbation form

$$\frac{\partial \mathbf{u}}{\partial t} + \mathbf{U}\cdot\nabla\mathbf{u} + \mathbf{u}\cdot\nabla\mathbf{U} + \mathbf{u}\cdot\nabla\mathbf{u} = -\nabla p + \frac{1}{Re}\nabla^2\mathbf{u}, \tag{3.3}$$

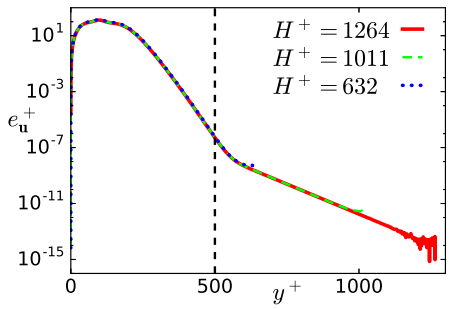

Figure 3.8 – Fluctuation energy profile of the solution expressed in inner units $e_{\mathbf{u}}^+ = u_{rms}^{+2} + v_{rms}^{+2} + w_{rms}^{+2}$ at $Re = 100\,000$ as a function of y^+ for three different box heights. The vertical dashed line shows the height up to which r.m.s. plots are shown in figure 3.7. At $y^+ = 500$, $e_{\mathbf{u}}^+$ has dropped by nine orders of magnitude relative to its maximum.

where $\mathbf{u}$ is the perturbation relative to the laminar base flow $\mathbf{U}$ given by $\mathbf{U} = [U = 1 - e^{-y}, V = -1/Re, W = 0]$. These momentum equations are complemented by the continuity equation $\nabla \cdot \mathbf{u} = 0$, periodic boundary conditions in the streamwise and in the spanwise directions and the no-slip boundary conditions $\mathbf{u} = \mathbf{0}$ at $y = 0$ and $y = H$. To close the system, a zero average pressure gradient in both the streamwise and spanwise directions is imposed. The system of equations is discretised using a spectral collocation method based on Fourier–Chebychev–Fourier expansions in the streamwise, wall-normal and spanwise directions, respectively. The third-order accurate semi-implicit backward differentiation method is used for time marching. Time steps are chosen such that the Courant-Friedrichs-Lewy (CFL) number remains in the range of 0.4–0.6.

For the large direct numerical simulations at $Re = 333$, the large domain of size $L_x = 243$, $H = 225$, $L_z = 121.5$ has been discretised with $N_x = 256$, $N_y = 301$, $N_z = 256$ collocation nodes in the streamwise, wall-normal and spanwise directions, respectively. The simulation is initialised with a random field and after statistical steady state has been reached, the statistics are calculated from a time series of 300 000 advective time units.

The exact invariant travelling wave solutions have been computed using the Newton-Krylov-Hookstep method. We use a numerical resolution of $N_x = 48$, $N_y = 181$, and $N_z = 48$ collocation points for the MFU with $L_x^+ = 633$, $L_z^+ = 170$, and $H^+ = 632$. Convergence is obtained when $||\left(\mathbf{u}_{x-cT,y,z}|_{t=T} - \mathbf{u}_{x,y,z}\right)||_2/T$ is less than 10^{-13}, where $T = 20$ and $||.||_2$ is not the energy norm of the velocity field but the L2-norm of the vector of independent Fourier–Chebychev coefficients of the operand. For $Re > 100,000$ we carry out computations for the system expressed in inner units (equation 3.1). The solution vector itself has a typical magnitude $||\mathbf{u}_{x,y,z}||_2$ of the order of 10 so that the residual is approximately 14 orders of magnitude smaller.

The height of the MFU is chosen such that the solution is independent of H^+. This is confirmed in figure 3.8 where fluctuation energy profiles for three different box heights are depicted. As shown, increasing the box height from $H^+ = 632$ by 60% and 100% does not change the solution near the wall. As shown in figure 3.7, the solution is well localised below $y^+ = 500$,

the range over which rms profiles are plotted. At $y^+ = 500$, the energy has already dropped by nine orders of magnitude below its maximum. This confirms that our choice of $H^+ = 632$ is sufficiently large to ensure the solution is independent of H^+.

4 Self-sustained large-scale motions in the turbulent ASBL

Remark: This chapter is largely inspired by a pre-print titled "Self-sustained large-scale motions in the asymptotic suction boundary layer"

Sajjad Azimi[1], Carlo Cossu[2] and Tobias M. Schneider[1]

[1]Emergent Complexity in Physical Systems Laboratory (ECPS),
École Polytechnique Fédérale de Lausanne, CH-1015 Lausanne, Switzerland

[2]LHEEA, UMR 6598 CNRS Centrale Nantes, F-44300 Nantes, France

Submitted to *Journal of Fluid Mechanics*

Contents

Chapter summary

Large-scale motions, also known as superstructures, are dynamically relevant coherent structures in a wall-bounded turbulent flow, that span the entire domain in wall-normal direction and significantly contribute to the global energy and momentum transport. Recent investigations in channel and Couette flow, suggest that these large-scale motions are self-sustained, implying they are not driven by small-scale motions at the wall. Whether large-scale motions are self-sustained has however not yet been answered for open boundary layers, which are relevant for many applications. Here, using the asymptotic suction boundary layer flow at the friction Reynolds number $Re_\tau = 1\,168$ as a testbed, we show that large-scale motions are self-sustained also in boundary layers. Together with the previous investigations in confined flows, this observation provides strong evidence of the robust and general nature of coherent self-sustained processes in turbulent wall-bounded flows. The dynamics of the large-scale self-sustained process involving the growth, breakdown and regeneration of quasi-streamwise coherent streaks and vortices within the boundary layer shows temporal phase relations reminiscent of bursting as observed in buffer layer structures. The dynamics however differs from the quasi-periodic large-scale streak-vortex regeneration cycle observed in confined flows. Based on the similarity of the dynamics of large-scale motions in boundary layers and of small-scale buffer layer structures, we conjecture that the bursting behaviour is associated with the dynamical relevance of only one wall, while two confining walls lead to the quasi-periodic cycle.

4.1 Introduction

Wall bounded turbulence is characterised by coherent structures in a wide range of scales (Townsend, 1956). These structures range from small-scale streaky motions in the near-wall region (Kline *et al.*, 1967) to large-scale motions with the size of the geometrical constraint of the turbulent flow (Kovasznay, Kibens & Blackwelder, 1970; Komminaho, Lundbladh & Johansson, 1996; Kim & Adrian, 1999; Hutchins & Marusic, 2007). Large-scale and very-large scale motions, also known as superstructures, carry a significant fraction of the turbulent kinetic energy and contribute significantly to the Reynolds shear stress (Guala *et al.*, 2006).

Despite their importance for global momentum transport, there is no general consensus on the mechanism underlying the generation and the sustaining of large-scale motions in wall-bounded turbulent flows. A widespread interpretation relates the formation of the large-scale motions to scale-growths mechanisms of hairpin vortices which are themselves fed by the active buffer layer streaky structures (Kim & Adrian, 1999; Tomkins & Adrian, 2003). Based on these ideas, large-scale motions could not exist independently of the near-wall active small-scale streaky structures. However, an increasing number of numerical and experimental studies suggest that large-scale motions might be generated and sustained independently of driving due to the near-wall active small-scale motions: Flores & Jiménez (2006) and Flores *et al.* (2007) show that the dynamics of large-scale motions is not significantly affected when

the buffer-layer structures are destructed by means of wall roughness. This observation implies that buffer-layer active structures are not necessarily the only structures feeding large-scale motions. Pujals, García-Villalba, Cossu & Depardon (2009); Hwang & Cossu (2010*a*,*b*) and Willis, Hwang & Cossu (2010) show that large-scale motions efficiently extract energy directly from the turbulent mean flow via non-modal energy amplification mechanisms. Large-scale motions could therefore be self-sustained without feeding by smaller-scale hairpin structures. Hwang & Cossu (2010*c*, 2011) and Rawat *et al.* (2015) demonstrate that indeed, both large-scale and log-layer coherent motions can be self-sustained. They show that these motions survive in both channel and Couette flow, when smaller-scale active motions are artificially quenched and replaced by purely dissipative structures by means of overfiltered large-eddy simulations (LES). Using the same overfiltered LES approach Rawat *et al.* (2015) and Hwang, Willis & Cossu (2016) have been able to compute invariant coherent large-scale solutions of the (LES) filtered Navier-Stokes equations. Building on these results, Cossu & Hwang (2017) suggest that Townsend's attached eddies (Townsend, 1976), believed to be the skeleton of wall-bounded turbulence (Marusic & Monty, 2019), consist of quasi-streamwise *coherent* streaks and vortices which are self-sustained by a mechanism similar to the one sustaining transitional (Boberg & Brosa, 1988; Waleffe, 1995) and buffer-layer coherent structures (Jiménez & Moin, 1991; Hamilton *et al.*, 1995).

To date, evidence of the self-sustained nature of coherent large-scale motions has been provided only for the (internal) parallel pressure driven channel (Hwang & Cossu, 2010*c*, 2011) and Couette (Rawat *et al.*, 2015) flows at relatively low Reynolds numbers ($Re_\tau \simeq 550$ and $Re_\tau \simeq 128$ respectively). Related attempts in Hagen-Poiseuille flow have been inconclusive (Feldmann & Avila, 2018). Further evidence that large-scale motions are generically self-sustained is therefore needed, especially for high Reynolds number boundary layer flows such as those relevant for atmospheric dynamics or wind engineering and vehicle external aerodynamics, where large-scale motions greatly affect performance. Recent results of Kevin, Monty & Hutchins (2019*a*); Kevin *et al.* (2019*b*) indicate that the features of large-scale motions in experimentally studied turbulent boundary layers are consistent with those of a coherent self-sustained process. There is however no direct evidence that large-scale motions are self-sustained also in boundary layers.

In this study we investigate if large-scale motions are self-sustained in boundary layers at high Reynolds numbers. We follow the overfiltered large-eddy simulation (LES) approach (Hwang & Cossu, 2010*c*, 2011; Rawat *et al.*, 2015; Hwang *et al.*, 2016) where active small-scale structures are removed from the flow by increasing the width of the spatial filter in an LES while keeping the numerical grid constant. To avoid the difficulties related to both the non-parallel nature of growing turbulent boundary layers and to their strong local sensitivity to the upstream flow, we consider the asymptotic suction boundary layer (ASBL) flow (Schlichting, 2004). In ASBL, constant suction through the wall arrests the growth of the boundary layer thickness yielding parallel flow conditions. The kinetic energy associated with large-scale motions of turbulent flow in ASBL is relatively weak when compared to other flow systems (Schlatter & Örlü, 2011; Bobke *et al.*, 2016). This is evidenced by the ratio of the large-scale to the small-scale peaks

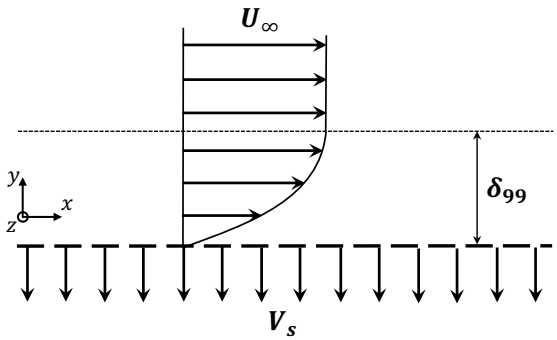

Figure 4.1 – Schematic of asymptotic suction boundary layer flow. The turbulent boundary layer thickness is δ_{99}, the height where the mean streamwise velocity reaches 99% of the free stream velocity U_∞. The value of the Reynolds number $Re = U_\infty / V_s$, given by the ratio of the free steam velocity and the uniform suction velocity V_s, is fixed to $Re = 300$.

in the energy spectrum being small compared to channel or Couette flow, where stronger large-scale motions are observed. Due to the relative strength of the small-scale structures, ASBL is a particularly appropriate flow to examine the self-sustained nature of large-scale motions. If the large-scale motions are found to be self-sustained even in the presence of the especially energetic near-wall small-scale structures of ASBL, such a finding would point towards a robust and generic self-sustaining mechanism of large-scale coherent motions in boundary layers.

The structure of the chapter is as follows. In section 4.2, we introduce the flow system, discuss the governing equations and specify numerical methods for solving those equations. In section 4.3 we first introduce a modified overfiltering approach that allows to successfully isolate large-scale motions from the dynamics of the damped near-wall small-scale structures. We thereby show that that large-scale motions in ASBL are self-sustained. Based on an analysis of one isolated large-scale motion, we describe the self-sustained mechanism and discuss its properties in comparison to similar processes reported in other flow systems. The results are discussed in the concluding section 4.4.

4.2 Methodology

4.2.1 Asymptotic suction boundary layer flow (ASBL)

We consider the flow of a uniform free stream of velocity U_∞ over a flat plate with uniform and constant wall-normal suction V_s. Far from the plate's leading edge, the growth of the boundary layer thickness is compensated by the wall suction and asymptotic suction boundary layer flow (ASBL) is reached (see figure 4.1). Here the downstream momentum that enters the boundary layer from the free stream exactly balances wall friction so that the boundary layer remains parallel. ASBL allows for a laminar solution of the form $\check{U}_l = U_\infty \left(1 - \exp\left(-\check{y}/\delta\right)\right)$, where $\check{U}_l$ is the (dimensional) streamwise velocity, $\check{y}$ the (dimensional) wall-normal coordinate and ν is

the kinematic viscosity of the fluid. We choose to non-dimensionalise the problem with the displacement thickness of the laminar solution $\delta^* = \nu / V_s$ as a length scale and the free-stream velocity U_∞ as velocity scale. Time is measured in units of δ^* / U_∞. The flow has a single control parameter, namely the Reynolds number $Re = U_\infty(\nu / V_s)/\nu = U_\infty / V_s$ based on the free-stream velocity and the laminar displacement thickness.

Properties of wall-bounded turbulence in the near-wall region are universal when measured in inner units of the flow. Momentum balance in ASBL allows us to express the inner velocity scale u_τ, and the inner length scale δ_τ relative to the outer units used for non-dimensionalisation in terms of the externally controlled Reynolds number, $u_\tau = U_\infty / \sqrt{Re}$ and $\delta_\tau = \delta^* / \sqrt{Re}$, respectively. The friction Reynolds number Re_τ, that measures the scale separation between the characteristic length scale of the large-scale motions δ_{99} and the characteristic length scale of the near-wall small-scale structures δ_τ, is equal to $Re_\tau = \delta_{99}\sqrt{Re}/\delta^*$. Throughout this chapter, all variables in inner units are denoted by a superscript plus sign.

ASBL is linearly stable up to $Re \approx 54370$ (Hocking, 1975). In practice, for $Re > 270$ the flow is turbulent (Khapko *et al.*, 2016). ASBL is characterised by high scale separations even at the smallest Reynolds numbers where turbulence is sustained (Khapko *et al.*, 2016). The kinetic energy associated with the large-scale motions is relatively weak compared to the energy of the small-scale streaky structures in the near-wall region (Schlatter & Örlü, 2011; Bobke *et al.*, 2016).

4.2.2 Governing equations

We consider the flow evolution under the filtered Navier-Stokes equations (Pope, 2000, see e.g.). These equations underlying LES describe the evolution of the filtered velocity, namely, the velocity contributions of spatial scales larger than a chosen filter width. With the streamwise, wall-normal and spanwise coordinates denoted by $\mathbf{x} = [x, y, z]$, respectively and the corresponding non-dimensional total velocity components indicated by $\mathbf{u} = [u, v, w]$, the governing equations for the filtered velocity are

$$\begin{aligned} &\frac{\partial \overline{u}_i}{\partial t} + \overline{u}_j \frac{\partial \overline{u}_i}{\partial x_j} = -\frac{\partial \overline{q}}{\partial x_i} + \nu \frac{\partial^2 \overline{u}_i}{\partial x_j^2} - \frac{\partial \overline{\tau}^r_{ij}}{\partial x_j} \\ &\frac{\partial \overline{u}_i}{\partial x_i} = 0. \end{aligned} \tag{4.1}$$

The action of the filter is denoted by an overbar. The influence of the scales smaller than the filter width on the filtered velocity is captured by the residual stress tensor $\overline{\tau}^r = \overline{\tau}^R - tr(\overline{\tau}^R)\mathbf{I}/3$, with $\overline{\tau}^R = \overline{u_i u_j} - \overline{u_i}\,\overline{u_j}$ and $\overline{q} = \overline{p} + tr(\overline{\tau}^R)/3$. The residual stress depends on the total unfiltered velocity field. To close the equations, the residual stress tensor $\overline{\tau}^r$ thus needs to be modelled and expressed in terms of the filtered velocity. We choose the static Smagorinsky (1963) model where the residual stress tensor is given by $\overline{\tau}^r_{ij} = -2\nu_t S_{ij}$ where S_{ij} is the rate of the strain

tensor of the filtered velocity field and ν_t is the eddy viscosity. ν_t is given by

$$\nu_t = D(C_s\overline{\Delta})^2\overline{S},$$

with $\overline{S} = \sqrt{2\overline{S}_{ij}\overline{S}_{ij}}$ and $\overline{\Delta} = \sqrt[3]{\Delta x \Delta y \Delta z}$ given in terms of the grid spacing in all three directions. The wall damping function $D = 1 - \exp\left(-\left(y^+/A^+\right)^3\right)$ ensures the residual stress to be zero at the wall. Following Kim & Menon (1999) we choose $A^+ = 25$. The only parameter varied, is the Smagorinsky constant C_s which controls the filter width (Mason & Callen, 1986) and thereby the strength of the filtering. We often consider values of C_s larger than reference values typically used in an LES that attempts to reproduce DNS results. In a standard LES, the filter width is adapted to the resolution of the numerical grid. Here, we instead follow the overfiltering approach of Hwang & Cossu (2010*c*), where the numerical grid resolution is chosen fine enough to resolve buffer-layer structures. Increasing C_s beyond its reference value allows us to explicitly filter out an increasingly large range of scales that could be resolved using the numerical grid.

In contrast to other more elaborate subgrid models used in LES simulations, the *static* Smagorinsky (1963) model prevents backscatter of energy from small-scale structures to large-scale motions but captures dissipation at small scales. This is key to investigate the self-sustained nature of large-scale motions by isolating them. If large-scale motions are sustained while small-scale active structures are quenched by the overfiltering, and there is no energy flux from the quenched scale to larger scales, the large-scale motions are self-sustained.

Energy is injected into the boundary layer at the constant rate of $I = V_s U_\infty^2/2$ per area of the plate. For statistically stationary turbulence, the time-averaged energy dissipation D equals the energy input. Consequently, the rate at which energy is dissipated in ASBL depends only on the free stream and suction velocity but is independent of C_s. Therefore, large-scale motions isolated by overfiltered simulations represent the physically correct energy input and dissipation rate at any given Reynolds number.

4.2.3 Numerical setup

To study the self-sustained nature of large-scale motions in ASBL we apply the overfiltering approach at $Re = 300$ corresponding to a friction Reynolds number $Re_\tau = 1168$. For our simulations, we consider a numerical domain of length L_x, width L_z and height H, where periodic boundary conditions are applied in the streamwise x and the spanwise z directions. Dirichlet boundary conditions are enforced on the wall $y = 0$ as well as on a top plane at $y = H$ parallel to and sufficiently far from the wall to approximate the semi-infinite space, $\overline{\mathbf{u}}(x, 0, z) = [0, -1/Re, 0]$; $\overline{\mathbf{u}}(x, H, z) = [1, -1/Re, 0]$. The box height H must be chosen sufficiently large so that flow structures completely detach from the top plane and results become independent of H. To close the problem, we impose zero mean pressure gradient in the streamwise and the spanwise directions.

Name	L_x	H	L_z	N_x	N_y	N_z	*Section*
RefDNS	256	150	128	256	241	256	4.3.1
RefLES	256	100	128	64	61	64	4.3.1
LESbox	512	100	256	128	61	128	4.3.2 – 4.3.4
LSMbox	192	100	84	48	61	42	4.3.5 & appendix 4.5

Table 4.1 – Parameters of the numerical domains used in this study. Given is the size of the domain $[L_x, H, Lz]$ and the number of grid points before dealiasing $[N_x, N_y, N_z]$. RefDNS and RefLES are used to determine a reference value of C_s for which the LES reproduces DNS results. Overfiltered simulations are carried out in the LESbox, while the detailed dynamics of a single isolated large-scale motion is studied in the LSMbox.

Grid	Δx	Δy_{min}	Δy_{max}	Δz	Δx^+	Δy^+_{min}	Δy^+_{max}	Δz^+
DNS-grid	1.5	0.04	0.98	0.5	26	0.67	21.2	13
LES-grid	6.0	0.13	2.62	3.0	104	2.2	45.3	52

Table 4.2 – Numerical grid resolutions used in this study. Δx and Δz indicate the spacing of the uniform grid in x and z direction. In wall-normal y direction, a non-uniform grid with spacing between Δy_{min} and Δy_{max} is used. All spacings are provided in outer units and in inner plus units, i.e. in units of δ_τ. The DNS-grid is used for direct numerical simulations, while LES simulations are carried out with the LES-grid.

The governing equations (4.1) are integrated in time using an extension of the code Channelflow 2.0 (Gibson *et al.*, 2019). Channelflow implements a pseudo-spectral method using a spectral Fourier-Chebychev-Fourier discretisation in the streamwise, the wall-normal and the spanwise directions, respectively. A third order accurate semi-implicit backward differentiation method is employed to advance the equations in time. The 2/3 dealiasing rule is applied in the streamwise and the spanwise directions.

The domain is discretised with $[N_x, N_y, N_z]$ collocation points in the streamwise, the wall-normal and the spanwise directions, respectively. Specific resolutions of the different domains used are provided in table 4.1. The chosen discretisations correspond to two different resolutions of the numerical grid: A fine resolution is used to accurately resolve all the scales of the flow in a direct numerical simulation, DNS. For large-eddy simulations, LES, we consider a second coarser resolution to reduce the computational cost of the simulations. Parameters of the chosen grid resolutions are summarised in table 4.2.

4.3 Results and discussion

In this section, we demonstrate that large-scale motions, LSMs, can be isolated from near-wall small-scale structures. First, we determine a reference value of the Smagorinsky constant C_s so that the LES reproduces statistical properties of a resolved DNS. The original overfiltering technique by Hwang & Cossu (2010*c*) is shown to not be able to filter out all small-scale structures

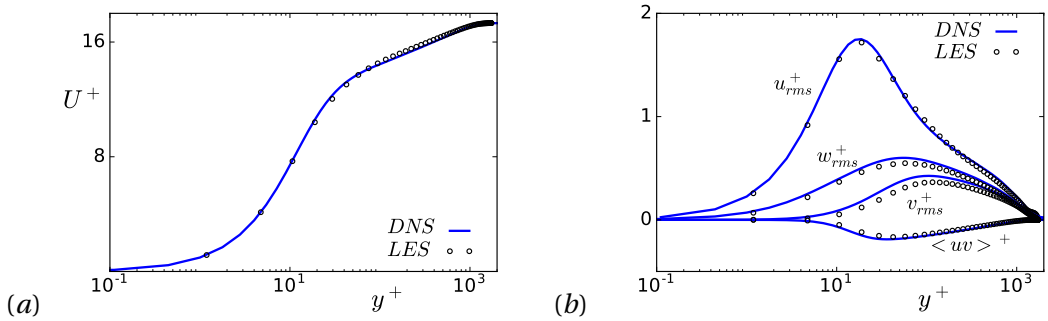

Figure 4.2 – (*a*) Mean streamwise velocity, and (*b*) root mean squared (r.m.s.) velocity components as functions of the wall-normal coordinate y, for both the DNS (blue solid line) and the LES with the optimal value of $C_s = 0.045$ (hollow circles). The mean and r.m.s. profiles from LES are in excellent agreement with the DNS. We thus choose $C_s = 0.045$ as reference value for LES reproducing DNS results.

without modifying properties of large scales. We however propose a modified overfiltering approach that ensures a physically correct mean profile and allows us to fully isolate LSMs from small-scale structures without modifying their properties. This demonstrates that LSMs are self-sustained in the ASBL. Finally, we describe details of the self-sustained process based on the dynamics of a single LSM periodically replicated in the horizontal plane.

4.3.1 Reference case - LES reproducing DNS statistics

We consider the flow at the Reynolds number $Re = 300$ to obtain the reference value of the Smagorinsky constant C_s at which the statistics of the LES best matches DNS results. A DNS is performed in a domain of extension $L_x = 256,\ H = 150,\ L_z = 128$ discretised with $N_x = 256,\ N_y = 241,\ N_z = 256$ points (the RefDNS domain from table 4.1). We carry out several LES in a domain of extension $L_x = 256,\ H = 100,\ L_z = 128$ resolved with $N_x = 64,\ N_y = 61,\ N_z = 64$ points (the RefLES domain from table 4.1) and vary the value of the Smagorinsky constant C_s until statistical properties of the LES solution match those of the DNS. For $C_s = 0.045$ the first- and second-order statistics of the LES very well match DNS results, as shown in figure 4.2. In the rest of this chapter, $C_s = 0.045$ is used as the reference value of Smagorinsky constant for LES simulations, performed in domains resolved with the LES-grid resolution from table 4.2.

4.3.2 Overfiltered LES using the original approach of Hwang and Cossu

Following the original overfiltering approach of Hwang & Cossu (2010*c*), we perform various LES for increasing values of the Smagorinsky constant C_s. The aim is to quench active small- and intermediate-scale structures by increasing C_s beyond the reference value at which the LES reproduces DNS results. The simulations are carried out in a domain with $L_x = 512,\ H = 100,\ L_z = 256$ discretised with $N_x = 128,\ N_y = 61,\ N_z = 128$ collocation points (LESbox from

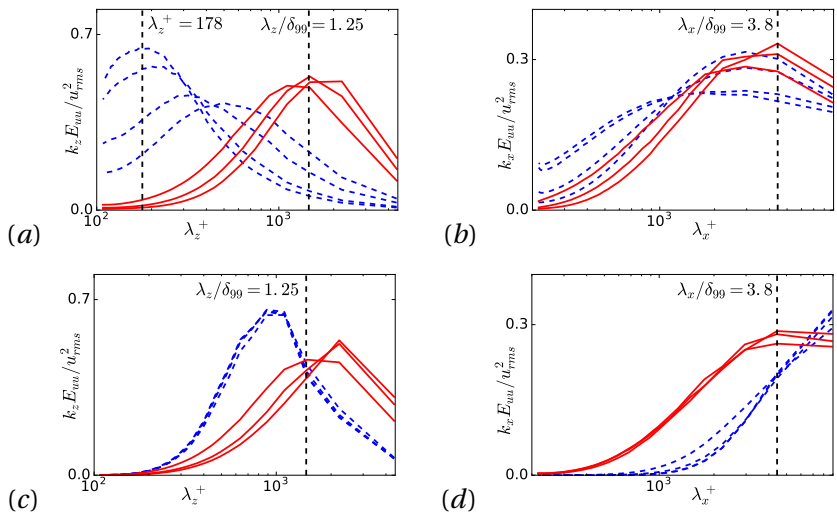

Figure 4.3 – Spanwise premultiplied power spectra of the streamwise velocity (panels *a* and *c*), and streamwise premultiplied power spectra of the streamwise velocity (panels *b* and *d*) obtained by the static Smagorinsky model with two different values of C_s: the reference value $C_s = 0.045$ (panels *a* and *b*); and a moderately increased value $C_s = 0.2$ (panels *c* and *d*). The data are extracted in the inner region at $y^+ = [19, 30, 58, 94]$ (blue dashed lines) and in the outer region at $y/\delta_{99} = [0.3, 0.51, 0.74]$ (red solid lines). Relative to the reference case, at elevated C_s, the energy peak corresponding to the large-scale motions (represented by red solid lines) moves towards larger scales. The inner peak capturing small-scale near-wall structures (represented by blue dashed lines) is damped but intermediate-scale structures (peak at $y^+ \approx 1000$ in the near-wall region) remain active. Consequently, there is no strength of overfiltering, for which all small- and intermediate-scale structures are quenched without deteriorating the LSMs.

table 4.1). We integrate the governing equations in time until statistical steady state is reached. For the reference $C_s = 0.045$ the boundary layer thickness in steady state reaches $\delta_{99} = 67.45$, which corresponds to a friction Reynolds number of $Re_\tau = 1\,168$. In outer scale units, i.e. in units of δ_{99}, the LESbox has a size of $(L_x \approx 8\delta_{99}, H \approx 1.5\delta_{99}, L_z \approx 4\delta_{99})$. The computational domain consequently accommodates several LSMs coexisting in the spanwise and in the streamwise directions.

We identify characteristic turbulent structures by computing both streamwise and spanwise premultiplied streamwise velocity power spectra for wall-parallel planes at multiple distances from the wall, as shown in figure 4.3. For distances in the near wall region ($y^+ < 100$) a peak associated with near-wall small-scale structures is observed, while further from the wall ($y \geq 0.3\delta_{99}$) a peak characterising LSMs emerges. We analyse the effect of increased C_s on the turbulent structures by observing modifications and shifts of the energy peaks characterising small-scale structures near the wall and LSMs, respectively. For the reference $C_s = 0.045$, the spanwise premultiplied spectra (panel *a*) show the near-wall peak at $\lambda_z^+ \approx 178$, while the peak characterising LSMs in the outer region is located at $\lambda_z = 1.25\,\delta_{99}$. In the streamwise direction

(panel *b*), the near-wall peak is located at $\lambda_x^+ \approx 1750$, and the outer peak at $\lambda_x \approx 3.8\delta_{99}$.

The aim of the overfiltering approach proposed by Hwang & Cossu (2010*c*) is to completely quench spectral peaks associated with small- and intermediate-scale active motions for values of C_s that do not deteriorate the large-scale features of the flow. However, while the approach was successful in confined flows, in the boundary layer considered here, the quantitative statistical properties of the large-scale motions are significantly affected by the filtering for values of C_s below the value required to completely quench small-scale structures. This is demonstrated in figure 4.3(*c* and *d*) where the energy spectra corresponding to the Smagorinsky constant $C_s = 0.2$ are reported. At this moderate $C_s = 0.2$, the near-wall peak at spanwise wavelength $\lambda_z^+ \approx 178$ has been successfully damped but intermediate-scale structures remain active, as evidenced by a clear peak at $y^+ \approx 1000$. While the moderate value of C_s is apparently not sufficient to quench all small-scale structures, the filtering already significantly distorts large-scale motions as evidenced by the spanwise outer peak shifting by approximately 50% relative to the reference case, to $\lambda_z \approx 1.9\delta_{99}$. Further evidence that already at $C_s = 0.2$ LSMs are significantly distorted by the overfiltering is given by the fact that the boundary layer thickness δ_{99} significantly grows and fails to saturate before interacting with the non-physical upper wall of the computational domain. In ASBL there is therefore no value of C_s at which small-scale structures are quenched without significantly deteriorating the LSMs. Consequently, isolating LSMs and investigating if LSMs are self-sustained requires a modified overfiltering approach.

4.3.3 Modification of the original overfiltering approach

As discussed in the previous section, the established overfiltering approach fails to isolate large-scale motions from smaller-scale structures in the ASBL. The large-scale motions are strongly affected by the filtering at the value of C_s that is required to damp the strong small-scale structures in the near-wall region. This problem might stem from the fact that compared to near-wall structures large-scale motions in the ASBL are weaker than in turbulent channels and Couette flow, where the established overfiltering approach was successful. Possibly due to the difference in relative strength, smaller-scale motions are alive at the values of C_s that significantly affect the LSMs. If C_s is sufficiently increased to quench all smaller-scale motions, the flow is thus left with significantly deteriorated LSMs having spatial scales which are significantly larger than those observed in the reference case representing a real physical flow.

The deterioration of LSMs is associated with the non-physical growth of the boundary layer thickness representing an incorrect mean velocity profile. These non-physical modifications of large-scale mean flow properties reflect the errors introduced by overfiltering with a subgrid model that can only capture some of the physics of turbulence at scale smaller than the filter width. Since we have information on the physically correct mean profile based on DNS and the reference LES, the key idea is to use this additional information to correct for the errors introduced by the subgrid model in overfiltered simulations. We thus propose a modified

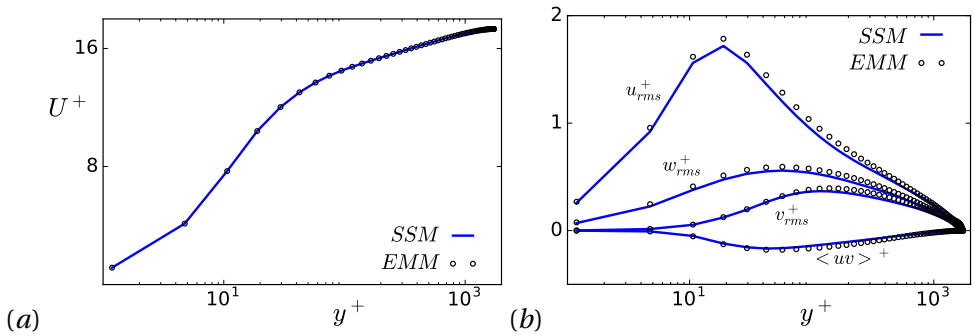

Figure 4.4 – (*a*) Mean velocity profile, and (*b*) root mean squared (r.m.s.) velocity fluctuations as functions of the wall-normal coordinate y, at the reference value of $Cs = 0.045$ for the static Smagorinsky model (SSM) and the enforced mean velocity model (EMM). Results from the EMM (hollow circles) match those of the SSM (blue solid lines). Consequently, the EMM faithfully reproduces correct velocity fluctuations.

overfiltering procedure where the known and physically correct mean profile is imposed.

The mean profile is given by the $(0,0)$ Fourier harmonic of the streamwise velocity. The mode is given by $\tilde{u}_{0,0}(y,t) = \langle \overline{u}(x,y,z,t) \rangle_{x,z}$, where the angle brackets indicate the spatial average in stream- and spanwise direction. Technically, we enforce the correct $(0,0)$ mode in each time step of the LES, $\tilde{u}_{0,0}(y,t) \equiv U(y)$, where $U(y)$ is the known mean profile. All other harmonics are computed as usual. The modified modelling approach, using the static Smagorinsky model *with* enforced mean velocity (from here on termed EMM), reproduces turbulent fluctuations computed from the established pure static Smagorinsky model without enforced mean (from here on termed SSM), when the reference Smagorinsky constant $C_s = 0.045$ is used. This is confirmed by matching r.m.s. profiles shown in figure 4.4.

4.3.4 Overfiltered LES with enforced mean velocity profile

Overfiltered large-eddy simulations are repeated using the modified approach preserving the turbulent mean flow to determine if it is possible to isolate LSMs from the dynamics of the near-wall small-scale structures. The simulations are carried out in the same numerical domain ($L_x = 512,\ H = 100,\ L_z = 256$) with the same grid resolution (see table 4.2) and the same Reynolds number ($Re = 300$) as in section 4.3.2. It is found that, as before, the reference value of Smagorinsky constant $C_s = 0.045$ is the one that best reproduces the results of the DNS.

As previously, premultiplied power spectra in both the near-wall and the outer region are used to quantify the effect of the filtering on small-scale structures near the wall and LSMs. As shown in figure 4.5, for the reference $C_s = 0.045$ (panels *a* and *b*) the peaks in the premultiplied spectra remain at their usual locations corresponding to the small-scale structures in the buffer layer ($\lambda_z^+ = 178$, $\lambda_z^+ = 1750$) and to the LSMs ($\lambda_z = 1.25\delta_{99}$, $\lambda_z = 3.8\delta_{99}$). When increasing C_s, the LSM peaks in the premultiplied spectra remain essentially unchanged while all peaks

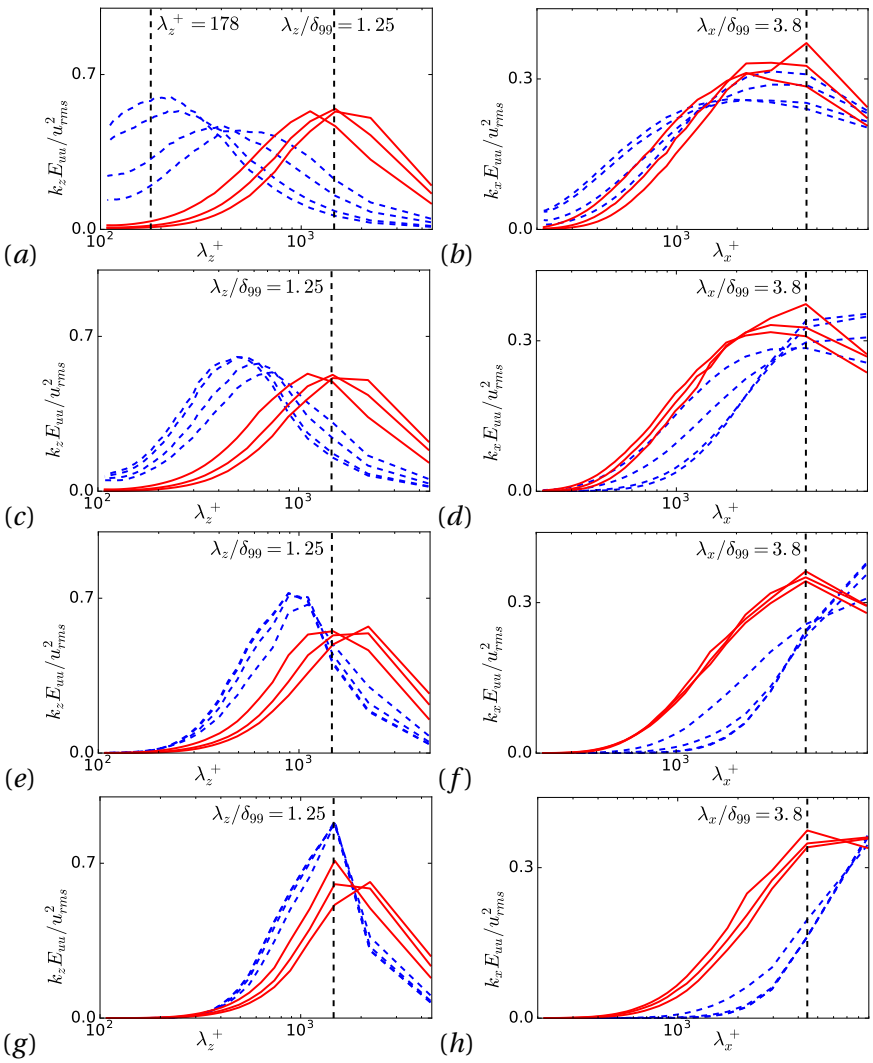

Figure 4.5 – Spanwise premultiplied power spectra of the streamwise velocity (panels *a*, *c*, *e* and *g*), and streamwise premultiplied power spectra of the streamwise velocity (panels *b*, *d*, *f* and *h*) obtained by the static Smagorinsky model with enforced mean velocity profile, EMM. The value of C_s is increased from top to bottom: the reference value $C_s = 0.045$ (panels *a* and *b*); $C_s = 0.1$ (panels *c* and *d*); $C_s = 0.2$ (panels *e* and *f*); and $C_s = 0.3$ (panels *g* and *h*). As in figure 4.3 the data is shown for the inner near-wall region at $y^+ = [19, 30, 58, 94]$ (blue dashed lines) and for the outer region at $y/\delta_{99} = [0.3, 0.51, 0.74]$ (red solid lines). When C_s is increased from the reference value, the energy peaks corresponding to the small-scale structures in the near-wall region (represented by blue dashed lines) shift towards larger scales while the energy peaks related to LSMs (represented by red solid lines) remain at their location. At $C_s = 0.3$ (panels *g* and *h*), all small and intermediate scales are damped while LSMs survive unchanged. Thus, the modified filtering approach successfully isolates LSMs from smaller-scale structures suggesting LSMs are self-sustained.

corresponding to smaller-scale structures are progressively quenched while shifting towards larger scales. At $C_s = 0.3$ (panels *g* and *h*), the near-wall peak at a spanwise wavelength

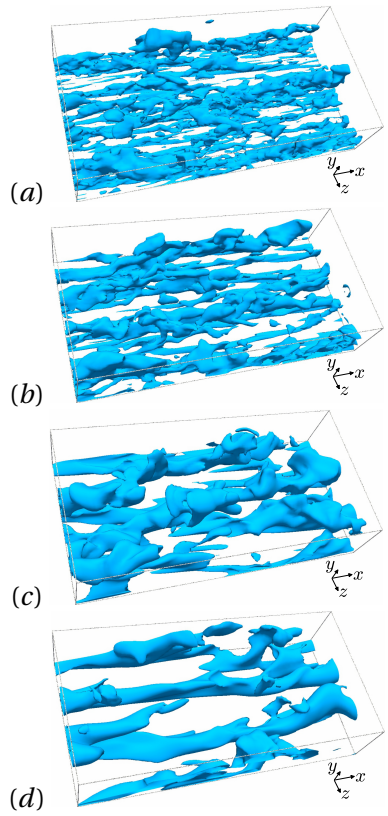

Figure 4.6 – Instantaneous flow fields for increasing C_s: (*a*) $C_s = 0.045$ (the reference case), (*b*) $C_s = 0.1$, (*c*) $C_s = 0.2$, and (*d*) $C_s = 0.3$. Isosurfaces ($u^+ = -0.52$) of the streamwise velocity deviation from the mean flow, i.e. low-speed streaks, are visualised. By increasing C_s, the velocity field of the LSMs become smooth, indicating that small-scale structures are damped out.

of $\lambda_z \approx 178$ has been successfully damped and there is also no peak at intermediate scales indicating that at $C_s = 0.3$ structures with spatial scales characteristic of buffer-layer and log-layer structures have been completely quenched. The outer peak (red lines), on the contrary, remains essentially unchanged both in the spanwise and the streamwise direction. We thus identified a value of the Smagorinsky constant at which all smaller-scale structures are successfully filtered out without distorting the LSMs. Consequently, the LSMs are successfully isolated from smaller-scale structures and appear to be self-sustained.

The effect of the overfiltering on the spatial characteristics of the flow structures is demonstrated in figure 4.6, where flow snapshots for increasing values of C_s are visualised. As expected based on the power spectra, increasing C_s removes the small-scale motions from the filtered flow while the characteristics of LSMs is preserved. For $C_s = 0.3$, the streaks of LSMs have become smooth, indicating that they are isolated from any smaller-scale velocity fluctuations.

Further evidence that the filtered LSMs are not distorted but resemble the spatial structure

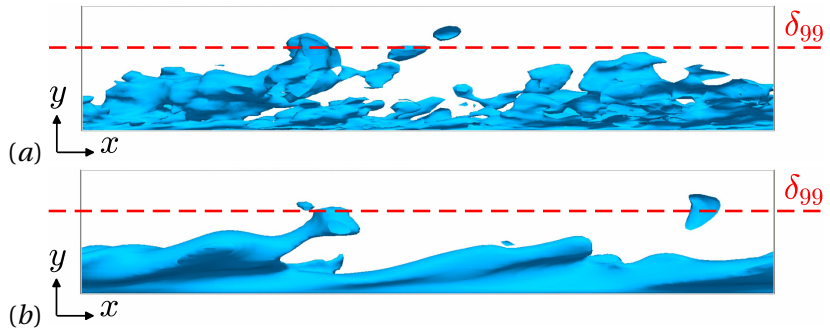

Figure 4.7 – Lateral view of the instantaneous flow fields at (a) $C_s = 0.045$ (the reference case) and (b) $C_s = 0.3$. Isosurfaces ($u^+ = -0.52$) of the streamwise velocity deviation from the mean flow are visualised, as in figure 4.6. The location of the turbulent boundary layer thickness δ_{99} is indicated by the dashed red line. The spatial structure of the isolated LSMs (panel b) resembles the spatial structure of the LSMs in the reference LES (panel a).

of the LSMs in the reference simulation is given in figure 4.7. Visualisations of low-speed streaks are compared between snapshots from the overfiltered simulation at $C_s = 0.3$ and the reference case with $C_s = 0.045$. The lateral view reveals that, indeed, the overfiltering does not change the scales of the LSMs. Specifically, the wall-normal scale on the order of the boundary layer thickness is preserved. Likewise, the ramp structure of LSMs, that is a characteristic of large-scale motions (Hommema & Adrian, 2003; Dennis & Nickels, 2011; Rawat *et al.*, 2015), is observed both in the reference simulation (panel a) and the overfiltered simulation (panel b). The unchanged scales and preserved ramp structure further confirms that the overfiltered velocity field indeed represents genuine, undistorted and thus physically correct LSMs.

Overall, the presented results confirm that large-scale motions are self-sustained in the asymptotic suction boundary layer flow. LSMs in the boundary layer are not fed by smaller-scale active coherent structures near the wall. As all smaller scales are quenched, the energetic driving of LSMs only involves large scales on the order of the boundary layer thickness. The large-scale driving involves interactions with the mean velocity profile, indicating the importance of a correct mean profile for isolating LSMs without deteriorating them.

4.3.5 Dynamics of LSM in the large-scale minimal flow unit

To investigate the dynamics of single, periodically replicated, LSMs and to study their self-sustained mechanism, we consider a computational domain that can accommodate a single LSM only, with the usual periodic boundary conditions in the horizontal plane. The overfiltered LES is thus carried out in the appropriate minimal flow unit for large-scale motions (Hwang & Cossu, 2010*c*; Rawat *et al.*, 2015). This horizontally-periodic domain, here referred to as the *LSMbox*, is the large-scale equivalent of the minimal flow unit for near-wall turbulence (Jiménez & Moin, 1991). In ASBL at $Re = 300$, the size of the LSMbox is ($L_x = 2.85\,\delta_{99} = 192, L_z = 1.25\,\delta_{99} = 84$). At the spatial resolution identical to previous overfil-

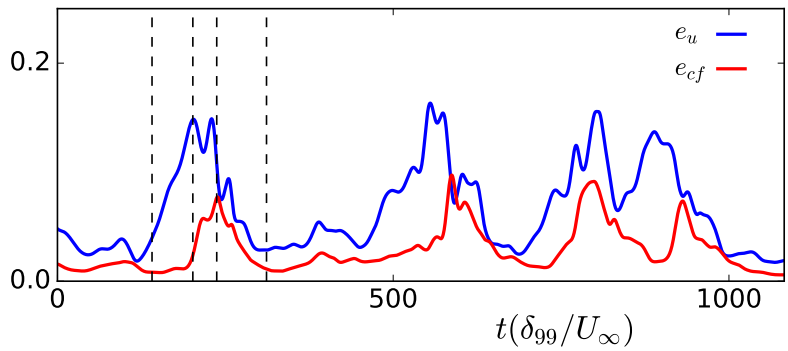

Figure 4.8 – Temporal evolution of the streamwise kinetic energy per area of the wall $e_u = 1/(L_x L_z)\int_{LSMbox} u^2 dxdydz$ and the cross-flow kinetic energy per area of the wall $e_{cf} = 1/(L_x L_z)\int_{LSMbox}\left(v^2+w^2\right)dxdydz$ for the overfiltered simulation with $C_s = 0.3$ in the LSMbox. The vertical dashed lines indicate the times at which the snapshots of the flow are visualised in figure 4.9.

tered LES, $N_x = 48$, $N_y = 61$, $N_z = 42$ collocation points are required for discretisation (see LSMbox in table 4.1).

Overfiltered LES in the minimal LSMbox for $C_s = 0.3$ confirm that the single isolated LSM remains self-sustained also in the large-scale minimal flow unit (details are discussed in appendix 4.5). This observation implies that the self-sustaining mechanism of LSMs is independent of even larger structures, that could in principle have been present in the larger LESbox studied above. Consequently, observations in ASBL agree with analogous observation in confined flows showing that LSMs are sustained independent of the dynamics of the small-scale structures in the near-wall region and independent of the presence of very-large-scale motions (VLSMs) (Rawat *et al.*, 2015).

In order to capture the dynamics of the self-sustained process we compute time series of the streamwise kinetic energy

$$e_u = 1/(L_x L_z)\int_{LSMbox} u^2 dxdydz,$$

which serves as a proxy for the intensity of streaks, and of the cross-flow kinetic energy

$$e_{cf} = 1/(L_x L_z)\int_{LSMbox}\left(v^2+w^2\right)dxdydz,$$

measuring the strengths of vortices. Both the streamwise kinetic and the cross-flow kinetic energy exhibit an aperiodic bursting behaviour, as shown in figure 4.8. While both components of energy evolve almost in phase, there is a small temporal phase-shift so that bursts of the streamwise kinetic energy e_u slightly precede bursts of the cross-flow energy e_{cf}. The evolution of quasi-streamwise streaks and vortices during one bursting cycle is visualised in figure 4.9 where snapshots of the flow are shown. The visualisations of the flow fields demonstrate that the self-sustained process of LSMs involves the interaction of streaks and vortical structures.

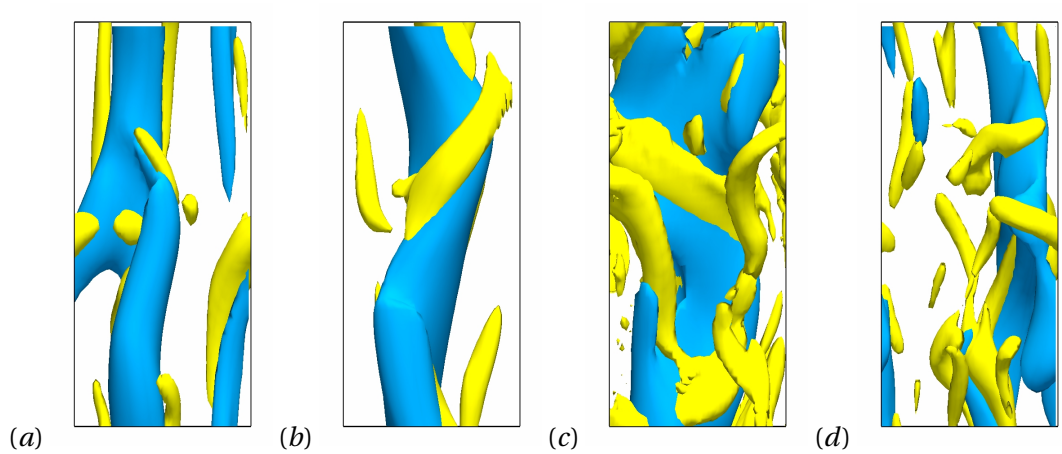

Figure 4.9 – Snapshots of the overfiltered velocity field at times indicated in figure 4.8. The streak is visualised by the isosurface of the streamwise velocity $u^+ = -0.52$ (blue), and vortices are visualised by the isosurface of the Q-criterion (Jeong & Hussain, 1995) with the iso-value of 3% of the maximum (yellow). The flow direction is upward and the view is oriented towards the wall. A large-scale motion is self-sustained by following the streak-vortices regeneration cycle: First, the downstream modulated streak, flanked by quasi-streamwise counter-rotating vortices, grows in amplitude (panels *a*, *b* and *c*). The streak then becomes unstable and breaks down (panels *c* and *d*). The resulting flow disorganises, vortices reorganise and the process repeats.

During a burst, sinuously bent streaks, that are flanked by quasi-streamwise counter-rotating vortices, grow in amplitude (panels *a*, *b* and *c*), until they undergo breakdown (panels *c* and *d*). Following breakdown the streaks and vortices are disorganised but they reorganise and the bursting process can start again. The large-scale self-sustained bursting process thus strongly resembles processes observed in buffer-layer minimal flow units (Jiménez & Moin, 1991).

4.4 Summary and conclusion

The goal of this study has been to investigate if coherent large-scale motions (LSM) are self-sustained in boundary layers. Together with previous investigations of confined channel and Couette flows, the study of an open boundary layer aims at clarifying whether the LSM coherent self-sustained process is universally active in high-Reynolds-number turbulent wall-bounded flows. To this end, the asymptotic suction boundary layer (ASBL) is chosen as testbed. The parallel nature of ASBL allows us to perform numerical simulations in a periodically continued domain and employ a filtering approach with properties that do not vary in stream- and spanwise direction. Since turbulent ASBL is dominated by the near-wall small-scale structures while large-scale motions are weaker than in other flow systems, ASBL is a particularly suitable system to study the self-sustained nature of large-scale motions. Isolation of the weak large-scale motions in ASBL is a strong evidence that the self-sustained nature of LSMs is a universal property of turbulent wall-bounded flows.

To determine whether LSMs are self-sustained or are driven by active motions at smaller scales we have built on the overfiltered large-eddy simulation (LES) approach where active small-scale structures are removed from the flow by increasing the LES spatial filter width while keeping a constant grid. This is realised by using the static Smagorinsky (1963) model in 'overfiltered' LES where the Smagorinsky constant C_s is increased above its reference value best reproducing DNS statistics.

Overfiltering attempts based on the original approach used in channel and Couette flows (Hwang & Cossu, 2010*c*, 2011; Rawat *et al.*, 2015; Hwang *et al.*, 2016) in ASBL are inconclusive because the quantitative statistical properties of the isolated LSMs are affected at the large values of C_s required to completely quench smaller-scale motions. To isolate LSMs we thus propose a modified overfiltering approach that preserves the original turbulent mean flow of the reference case. By using the modified method, the *enforced mean model* EMM, we isolate the LSMs in ASBL. Thereby for the first time in an open boundary layer flow, we show that large-scale motions are indeed self-sustained even in the presence of active smaller-scale structures in the near-wall region.

Additional simulations in the large-scale minimal flow unit, containing a single LSM periodically replicated in the horizontal directions, show that the LSM self-sustaining mechanism does also not depend on the dynamics of larger scales. The self-sustaining process of LSMs involves the aperiodic growth, breakdown and regeneration of sinuous streaks flanked by quasi-streamwise counter-rotating vortices. This provides further evidence to the claim that wall-bounded turbulence can be associated with a continuum of self-sustained processes involving the mutual forcing and regeneration of coherent quasi-streamwise vortices and streaks with spatial scales ranging from those of buffer-layer structures to those of large-scale motions (Hwang & Cossu, 2011; Cossu & Hwang, 2017).

While a self-sustained process is generically observed in wall-bounded flows, its dynamical details appear to be non-universal at large scale. In the ASBL, the observed large-scale process, that is associated with bursts in energy, is very similar to the one observed in buffer-layer minimal flow units (Jiménez & Moin, 1991) but differs from the one observed for LSMs in channel and Couette flow (Hwang & Cossu, 2010*c*; Rawat *et al.*, 2015). In channel and Couette flows the energies of large-scale streaks and quasi-streamwise vortices vary, most of the time, in phase opposition as in lower Reynolds number cases (Hamilton *et al.*, 1995; Waleffe, 1995). In ASBL and the buffer-layer minimal flow unit, the energy of streaks and vortices however varies approximately in phase during aperiodic bursting events. This observation suggest that these two dynamically different behaviours are associated with situations where a single wall is dynamically relevant (boundary layers, buffer layers) versus those where two walls are relevant to the process (such as the plane channel or Couette flow). Current investigations are under way to compute invariant solutions and determine the structure of the phase space of coherent large-scale motions in the asymptotic suction boundary layer in order to elucidate the nature of the observed aperiodic bursting motions.

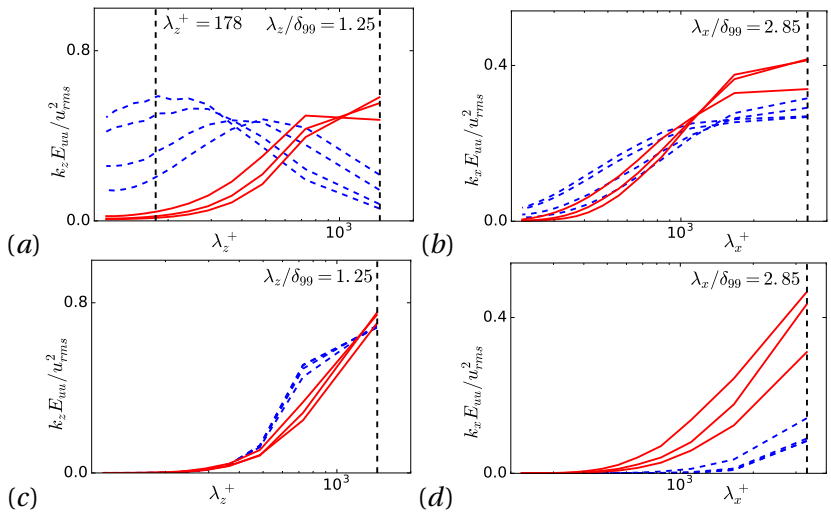

Figure 4.10 – Spanwise premultiplied power spectra of the streamwise velocity (panels *a* and *c*), and streamwise premultiplied power spectra of the streamwise velocity (panels *b* and *d*) for simulations with the enforced mean model, EMM, in the LSMbox, at different values of C_s: $C_s = 0.045$ (panels *a* and *b*); and $C_s = 0.3$ (panels *c* and *d*). The data is shown for the inner region at $y^+ = [19, 30, 58, 94]$ (blue dashed lines) and for the outer region at $y/\delta_{99} = [0.3, 0.51, 0.74]$ (red solid lines). In the absence of very-large-scale motions, a single LSM survive when the smaller-scale structures are damped.

4.5 Appendix: Self-sustained LSMs in the absence of very-large-scale motions

Overfiltered simulations with enforced mean velocity profile are carried out in the LSMbox to determine if it is possible to isolate a single LSM from the dynamics of the small-scale structures in the absence of motions at scales larger than LSMs, such as the very-large-scale motions. Premultiplied power spectra at wall-normal sections in the near-wall region and in the outer region for simulations with the reference value $C_s = 0.045$ and $C_s = 0.3$ are shown in figure 4.10. At the reference value of Smagorinsky constant $C_s = 0.045$, the spanwise and streamwise energy peaks corresponding to the near-wall small-scale structures (the peaks of the dashed blue lines) are present. The energy peaks due to the single LSM are located at $\lambda_z = L_z$ and $\lambda_x = L_x$. At $C_s = 0.3$ (bottom panels), the near-wall energy peaks are damped while the LSM survives. Consequently, LSMs appear to be self-sustained when the small-scale structures are quenched by the filtering action and very-large-scale motions are eliminated by the periodic boundary conditions of the LSMbox.

5 Invariant solutions representing large-scale motions of the turbulent ASBL

Remark: This chapter is largely inspired by a pre-print titled "Invariant solutions representing large-scale motions of the turbulent asymptotic suction boundary layer"

Sajjad Azimi[1], Carlo Cossu[2] and Tobias M. Schneider[1]

[1]Emergent Complexity in Physical Systems Laboratory (ECPS),
École Polytechnique Fédérale de Lausanne, CH-1015 Lausanne, Switzerland

[2]LHEEA, UMR 6598 CNRS Centrale Nantes, F-44300 Nantes, France

To be submitted to *Journal of Fluid Mechanics*

Contents

Chapter summary

Wall-bounded turbulent flows contain energetic coherent structures that span the entire turbulent domain in the wall-normal direction and contribute significantly to global energy and momentum transport. Both in confined flows and in boundary layers, these large-scale motions, also known as superstructures, can be isolated from small-scale near-wall structures and are self-sustained. Large-scale motions in all studied flows are sustained by the interaction of streaks and vortices but temporal correlations suggest that the specific self-sustaining mechanisms active in boundary layers differ from those sustaining large-scale motions in confined flows. To capture the self-sustaining mechanisms in a parallel boundary layer, we compute steady and time-periodic invariant self-sustained solutions of the filtered Navier-Stokes equations governing the dynamics of isolated large-scale motions of the asymptotic suction boundary layer at the friction Reynolds number $Re_\tau = 1\,168$. We identify seven travelling waves and two relative periodic orbits. Interactions of the large-scale streaks and vortices within these solutions are reminiscent of multiple known processes including the streak-vortex quasi-periodic regeneration cycle, a large-scale hairpin-based mechanism, and Waleffe's self-sustaining process (F. Waleffe 1997, PoF, vol. 9, 883-900). While all these processes are dynamically possible, only travelling waves underlying Waleffe's self-sustaining process are visited by the dynamics. The periodic orbits representing a regeneration cycle reminiscent of the dominant processes sustaining large-scale motions in confined flows, are not active.

Note: in the previous chapter 4, the value of the Smagorinsky constant C_s that can reproduce the statistical properties of DNS is called the 'reference value', but here we use the term 'reference value' for the vale of C_s that isolates large-scale motions from small-scale structures, namely $C_s = 0.3$.

5.1 Introduction

When an incoming flow of sufficiently high velocity interacts with a solid surface, a turbulent boundary layer develops. Such a high-Reynolds-number wall-bounded flow exhibits velocity fluctuations in a wide range of length- and time-scales (Townsend, 1956). Despite its stochastic nature, the turbulent flow contains recognisable coherent structures that are often dominated by downstream-oriented streaks (Jiménez, 2018). Coherent structures vastly vary in size, ranging from small-scale streaky structures in the near-wall buffer layer (Kline *et al.*, 1967) to large-scale motions that span the entire wall-normal extent of the flow (Kovasznay *et al.*, 1970; Komminaho *et al.*, 1996; Kim & Adrian, 1999; Hutchins & Marusic, 2007). For turbulence modelling and control, an accurate description of large-scale motions and their dynamics is particularly important. Large-scale motions, often also referred to as superstructures, represent a significant fraction of the total turbulent kinetic energy and they significantly contribute to the production of turbulent shear stresses (Guala *et al.*, 2006).

In wall-bounded turbulent flows, large-scale motions (LSMs) coexist with smaller-scale structures. It has been suggested that large-scale motions are energetically driven by coexisting smaller-scale structures (Wark, Naguib & Nagib, 1989; Tomkins & Adrian, 2003, see e.g.). However, Hwang & Cossu (2010*c*) and Rawat *et al.* (2015) managed to isolate large-scale motions in confined shear flows by means of overfiltered large-eddy simulations. They thereby demonstrated that large-scale motions are not energetically driven by smaller scale structures, and large-scale motions are thus self-sustained. Azimi, Cossu & Schneider (2020) extend these results to turbulent boundary layer flows. They isolate large-scale motions in asymptotic suction boundary layer flow (ASBL) and thereby show that LSMs are self-sustained also in open, unconfined boundary layer flows. The observations of Pujals *et al.* (2009); Hwang & Cossu (2010*a*,*b*); Willis *et al.* (2010) and Hwang & Cossu (2011) suggest that at all relevant scales of turbulent flows, coherent streaky structures are self-sustained. Coherent structures extract turbulent kinetic energy directly from the turbulent mean flow by means of a coherent lift-up effect. Coherent streamwise vortices amplify coherent streamwise streaks within a shear by displacing near-wall low-speed fluid towards the bulk and high-speed fluid in the bulk towards the wall.

The self-sustained process of large-scale motions involves the amplification of large-scale coherent streaks via the lift-up of streaks due to large-scale coherent quasi-streamwise vortices, the breakdown of streaks and the regeneration of vortices which reignite the process (Hwang & Cossu, 2010*c*; Rawat *et al.*, 2015; Azimi *et al.*, 2020). While these general components of the self-sustained process are robust and present in all wall-bounded flows studied so far, details of the streak-vortex interaction including the temporal evolution of large-scale streaks and vortices are flow-dependant. In plane channel and Couette flows, the energies contained in large-scale streaks and in quasi-streamwise vortices mostly vary in phase opposition (Hwang & Cossu, 2010*c*; Rawat *et al.*, 2015; Cossu & Hwang, 2017). This opposing phase in the temporal evolution of the kinetic energies of streaks and of vortices is characteristic of the specific self-sustained streak-vortex regeneration cycle proposed by Hamilton *et al.* (1995) and Waleffe (1995), hereafter called the HKW cycle. In the HKW cycle, the streaks are amplified by decaying vortices. When streaks reach a sufficiently large amplitude they become unstable (see Park, Hwang & Cossu, 2011; Alizard, 2015) and break down. This regenerates the vortices and leads to periodic dynamics with the amplitude of vortices and streaks varying out-of-phase. In parallel boundary layers, however, a different temporal evolution of large-scale streaks and quasi-streamwise vortices is observed. During aperiodic bursting events, the energies of streaks and vortices vary almost in phase (Azimi *et al.*, 2020). This is also observed for the autonomous buffer-layer self-sustained process (Jiménez & Moin, 1991).

The differing temporal phase relations of streak and vortex amplitudes in the self-sustained processes observed in confined flows and in parallel boundary layers, suggests that different physical amplification mechanisms may be present in open and in confined flows. To investigate those mechanisms underlying the self-sustained processes of large-scale motions in parallel boundary layers, we adopt a deterministic approach and attempt to identify exact invariant solutions capturing the processes. This dynamical systems approach has been

successful in rationalising properties of transitional flows. For confined flows at low Reynolds numbers, the physical mechanism underlying the HKW cycle has been captured by exact travelling wave solutions to the Navier-Stokes equations (Waleffe, 1998, 2001, 2003), where vortex lift-up and streak instability are in exact balance giving rise to a steady flow (Waleffe, 1997). Such unstable invariant solutions are transiently visited by the turbulent dynamics so that turbulence at moderate Reynolds numbers can be understood as a chaotic walk between invariant solutions that, together with their entangled stable and unstable manifolds, support the dynamics (Kerswell, 2005; Eckhardt, Schneider, Hof & Westerweel, 2007; Kawahara *et al.*, 2012). Invariant solutions act as building blocks for the dynamics (Gibson *et al.*, 2008; Suri *et al.*, 2017; Reetz & Schneider, 2020*a*). They capture characteristic features of transitional flow (Avila *et al.*, 2013; Reetz *et al.*, 2019) and are a means to isolate physical processes active in turbulence. At high Reynolds numbers, invariant solutions of the full Navier-Stokes equations have been computed in the near-wall region and shown to capture the universality of the dynamics in the buffer-layer (Yang *et al.*, 2019; Azimi & Schneider, 2020).

To transfer the dynamical systems approach from transitional flows to the dynamics of LSMs in high-Reynolds-number boundary layers we need to compute invariant solutions capturing the self-sustained processes of LSMs. Instead of invariant solutions of the standard Navier-Stokes equations, we consider solutions of equations appropriately describing the dynamics of LSMs when decoupled from small-scale fluctuations. As shown by Azimi *et al.* (2020), the dynamics of LSMs in the ASBL is faithfully captured by filtered Navier-Stokes equations with imposed mean flow. This approach filters smaller-scale structures out and isolates LSMs following the overfiltered large-eddy simulation (OLES) paradigm of Hwang & Cossu (2010*c*). Like the original Navier-Stokes equations, the filtered evolution equations describing the dynamics of LSMs constitute a system of nonlinear partial differential equations. Their dynamics can be studied using the same dynamical systems approach that has been successful in deterministically describing transitional wall-bounded turbulence at small Reynolds numbers. Following Rawat *et al.* (2015) and Hwang *et al.* (2016) we specifically compute exact invariant solutions of the filtered Navier-Stokes equations and identify both travelling waves and periodic orbits that capture characteristics of the LSM dynamics.

The first attempts to compute invariant solutions of the *filtered* Navier-Stokes equations as representative of large-scale motions have been carried out in confined flows. Rawat *et al.* (2015) compute an equilibrium solution in plane Couette flow at the relatively low friction Reynolds number of $Re_\tau = 128$. Their large-scale solutions are connected to the well-studied Nagata equilibrium solution (Nagata, 1990; Clever & Busse, 1992; Waleffe, 2003). Hwang *et al.* (2016) compute a set of invariant solutions of the filtered equations in plane channel flow at the higher friction Reynolds number $Re_\tau \approx 1000$ where large-scale motions are spatially separated from near-wall structures. They demonstrate that their upper branch solution is a reasonable proxy for the structure and statistics of large-scale motions in the considered confined flow system. While a limited number of large-scale invariant solutions of the filtered equations have been computed for confined Couette and channel flows, no exact invariant solutions representing the dynamics of LSMs in boundary layers are known.

Here, we construct relative periodic orbits and travelling wave solutions of filtered Navier-Stokes equations representing large-scale motions in developed turbulent ASBL at $Re_\tau = 1\,168$. The solutions satisfy precisely those model equations that have been shown to faithfully capture and isolate large-scale motions in the ASBL by Azimi *et al.* (2020). We present nine large-scale invariant solutions, including seven travelling waves and two relative periodic orbits. All invariant solutions contain large-scale streaks and quasi-streamwise vortices. The temporal interactions of streaks and vortices within these invariant solutions are reminiscent of several self-sustained processes underlying wall-bounded turbulence. Both relative periodic orbits capture characteristic features of the HKW cycle, including the periodic out-of-phase evolution of the streak and vortex amplitude. Three of the seven travelling wave solutions represent a large-scale hairpin-like vortex (Adrian, 2007). The remaining four travelling wave solutions are characterised by sinuously modulated streak-vortex structures. These travelling waves represent Waleffe's self-sustaining process, a process related to the HKW cycle, where the vortex lift-up and streak instability are in balance sustaining a steady structure (Waleffe, 1997). For a chaotic LSM trajectory the kinetic energies of streaks and vortices are positively correlated which captures the simultaneous energetic growth of both vortices and streaks during aperiodic bursting events. Three exact travelling wave solutions representing sinuously modulated streaks capture the same positive correlation, suggesting they are visited during different phases of the bursting process.

The structure of the chapter is as follows. In section 5.2, we introduce the flow system including its symmetry properties, specify the governing equations and discuss numerical methods for identifying invariant solutions. Section 5.3 describes all nine identified invariant solutions including two periodic orbits and seven travelling waves. Their relevance for the dynamics of large-scale motions in the asymptotic suction boundary layer flow is discussed. In section 5.4, we summarise results and provide suggestions for future research.

5.2 Methodology

5.2.1 Asymptotic suction boundary layer flow

We consider the flow of a uniform free stream of velocity U_∞ over a flat plate with uniform and constant wall-normal suction V_s. Far from the plate's leading edge, the growth of the boundary layer thickness is compensated by the wall suction and asymptotic suction boundary layer flow (ASBL) is reached (see figure 5.1). In ASBL the downstream momentum entering the boundary layer from the free stream exactly balances wall friction so that the boundary layer remains parallel. ASBL has a laminar solution of the form $\check{U}_l = U_\infty\left(1 - \exp\left(-\check{y}/\delta\right)\right)$, where $\check{U}_l$ is the (dimensional) streamwise velocity, $\check{y}$ the (dimensional) wall-normal coordinate and ν is the kinematic viscosity of the fluid. To non-dimensionalise the problem we choose the displacement thickness of the laminar solution $\delta^* = \nu/V_s$ as a length scale and measure velocity in units of the free-stream velocity U_∞. Time is measured in units of δ^*/U_∞. The flow has a single control parameter, namely the Reynolds number $Re = U_\infty(\nu/V_s)/\nu = U_\infty/V_s$

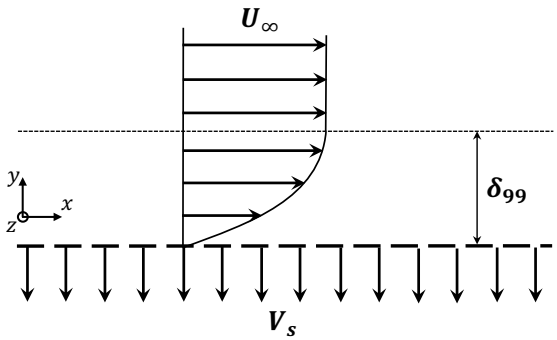

Figure 5.1 – Schematic of asymptotic suction boundary layer flow. The turbulent boundary layer thickness δ_{99} is the height where the mean streamwise velocity reaches 99% of the free stream velocity U_∞. The value of the Reynolds number $Re = U_\infty / V_s$, given by the ratio of the free steam velocity and the uniform suction velocity V_s, is fixed to $Re = 300$.

based on the free-stream velocity and the laminar displacement thickness.

At sufficiently high flow velocities, properties of wall-bounded turbulence become universal in the near-wall region when measured in wall units. In many flows wall or inner units need to be determined from experiments or simulations of turbulent flow. In ASBL, momentum balance allows us to express the inner velocity scale u_τ, and the inner length scale δ_τ relative to the outer units used for non-dimensionalisation in terms of the externally controlled Reynolds number, $u_\tau = U_\infty / \sqrt{Re}$ and $\delta_\tau = \delta^* / \sqrt{Re}$, respectively. Consequently, inner units are known a priori. The friction Reynolds number $Re_\tau = \delta_{99}/\delta_\tau = \delta_{99}\sqrt{Re}/\delta^*$ measures the scale separation between the characteristic length scale of the large-scale motions δ_{99} and the characteristic length scale of the near-wall small-scale structures δ_τ. Throughout this chapter, variables measured in inner units are denoted by a superscript plus sign.

We consider the flow at a fixed parameter value $Re = 300$, which corresponds to a friction Reynolds number $Re_\tau = 1168$. At this Reynolds number, the flow is fully developed and a large scale separation is observed Khapko *et al.* (2016).

5.2.2 LSM modelling method

For constructing invariant solutions underlying LSMs, we consider filtered Navier-Stokes equations (see e.g. Pope, 2000) that have been shown to faithfully capture and isolate LSMs at the chosen Reynolds number $Re = 300$ (Azimi *et al.*, 2020). The governing equations, numerical domain size, resolution and parameter values associated to the filter are identical to those in Azimi *et al.* (2020). The governing equations underlying LES describe the evolution of the filtered velocity, namely, the velocity contributions of spatial scales larger than a chosen filter width. The streamwise, wall-normal and spanwise coordinates are denoted by $\mathbf{x} = [x, y, z]$, respectively and the corresponding non-dimensional total velocity components are indicated

by $\mathbf{u} = [u, v, w]$. The governing equations for the filtered velocity are

$$\begin{aligned} &\frac{\partial \overline{u}_i}{\partial t} + \overline{u}_j \frac{\partial \overline{u}_i}{\partial x_j} = -\frac{\partial \overline{q}}{\partial x_i} + \nu \frac{\partial^2 \overline{u}_i}{\partial x_j^2} - \frac{\partial \overline{\tau}^r_{ij}}{\partial x_j} \\ &\frac{\partial \overline{u}_i}{\partial x_i} = 0. \end{aligned} \tag{5.1}$$

The action of the filter is denoted by an overbar. Zero pressure gradient is imposed in both streamwise and spanwise directions. The influence of the scales smaller than the filter width on the filtered velocity is captured by the residual stress tensor $\overline{\tau}^r = \overline{\tau}^R - tr(\overline{\tau}^R)\mathbf{I}/3$, with $\overline{\tau}^R = \overline{u_i u_j} - \overline{u_i}\,\overline{u_j}$ and $\overline{q} = \overline{p} + tr(\overline{\tau}^R)/3$. The residual stress depends on the total unfiltered velocity field and thus requires information on the unknown small scales. To close the equations, the residual stress tensor $\overline{\tau}^r$ thus needs to be modelled and expressed in terms of the filtered velocity. We choose the static Smagorinsky model (Smagorinsky, 1963) where the residual stress tensor is given by $\overline{\tau}^r_{ij} = -2\nu_t S_{ij}$ where S_{ij} is the rate of the strain tensor of the filtered velocity field and ν_t is the eddy viscosity. ν_t is given by

$$\nu_t = D(C_s\overline{\Delta})^2\overline{S},$$

with $\overline{S} = \sqrt{2\overline{S}_{ij}\overline{S}_{ij}}$ and $\overline{\Delta} = \sqrt[3]{\Delta x \Delta y \Delta z}$ given in terms of the grid spacing in all three directions. The wall damping function $D = 1 - \exp(-(y^+/A^+)^3)$ ensures the residual stress to be zero at the wall. Following Kim & Menon (1999) we choose $A^+ = 25$. The only parameter varied, is the Smagorinsky constant C_s which controls the filter width (Mason & Callen, 1986) and thereby the strength of the filtering. We use a numerical grid resolution fine enough to resolve small-scale structures, but by increasing C_s we explicitly filter out an increasingly large range of grid-resolved scales. For the considered flow, the value of the Smagorinsky constant $C_s = 0.3$ isolates large-scale motions and filters out smaller-scale structures (Azimi *et al.*, 2020). We furthermore impose the known and physically correct mean velocity profile in the overfiltered simulations. Technically, the mean profile is given by the (0,0) Fourier harmonic of the streamwise velocity. Imposing the known mean flow $U(y)$ via $\tilde{u}_{0,0}(y,t) \equiv U(y)$ ensures that isolated LSMs can extract their energy from the correct mean velocity profile. With the imposed mean flow and a parameter value of $C_s = 0.3$, the filtered Navier-Stokes equations faithfully describe the dynamics of isolated LSMs at $Re = 300$, as discussed in Azimi *et al.* (2020).

5.2.3 Numerical domain: large-scale minimal flow unit

We aim at studying the dynamics of a single LSM in isolation. To this end, a numerical domain accommodating a single large-scale motion is chosen. This numerical domain is a large-scale minimal flow unit (LSMFU) (Hwang & Cossu, 2010*c*; Rawat *et al.*, 2015), the large-scale equivalent of the minimal flow unit for near-wall turbulence (Jiménez & Moin, 1991). In the ASBL at the Reynolds number considered $Re = 300$, the numerical domain has

a length of $L_x = 2.85\delta_{99} = 192$ and width of $L_z = 1.25\delta_{99} = 84$ (Azimi *et al.*, 2020). In the wall-normal direction, an artificial top plate, sufficiently far from the wall, allows a finite box to approximate the semi-infinite space. A box height of $H = 100$ is found to be sufficiently large and allows flow structures to completely detach from the top plate. The domain is discretised with $N_x = 48,\ N_y = 61,\ N_z = 42$ collocation points in the streamwise, the wall-normal and the spanwise directions, respectively. Periodic boundary conditions are applied in the streamwise x and the spanwise z directions. Dirichlet boundary conditions are enforced on the wall $y = 0$ as well as on the top plane at $y = H$, $\overline{\mathbf{u}}(x,0,z) = [0,-1/Re,0]$; $\overline{\mathbf{u}}(x,H,z) = [1,-1/Re,0]$.

5.2.4 Symmetries

Asymptotic suction boundary layer flow is invariant under continuous translations in x and z directions as well as under the discrete reflection in z direction. Following the conventions of Gibson *et al.* (2008), symmetries of the governing equations and the boundary conditions of ASBL are expressed as

$$\sigma_z : [u,v,w](x,y,z) \to [u,v,-w](x,y,-z),$$
$$\tau : [u,v,w](x,y,z) \to [u,v,w](x+\delta x, y, z+\delta z),$$

where δx and δz are arbitrary displacements in the streamwise and spanwise directions, respectively. All products of σ_z and τ form the symmetry, or equivariance, group of ASBL. We specifically consider three particular symmetry operations contained within the equivariance group of ASBL, namely, the z-mirror symmetry σ_z, the shift-reflect symmetry $\tau_x\sigma_z$ and a conjugate to the z-mirror symmetry $\tau_z\sigma_z$:

$$\sigma_z : [u,v,w](x,y,z) \to [u,v,-w](x,y,-z),$$
$$\tau_x\sigma_z : [u,v,w](x,y,z) \to [u,v,-w](x+L_x/2, y, -z)$$
$$\tau_z\sigma_z : [u,v,w](x,y,z) \to [u,v,-w](x, y, -z+L_z/2).$$

The combination of a $z-$reflection about the origin and a half-box translation in the spanwise direction $\tau_z\sigma_z$ corresponds to a $z-$reflection about the quarter-box location $z = L_z/4$. This transformation should not be confused with the more commonly discussed shift-reflect symmetry $\tau_x\sigma_z$. The filtering and the Smagorinsky subgrid model are isotropic and do not break symmetries of the Navier-Stokes equations in ASBL geometry. Consequently, all symmetry considerations also apply to the filtered Navier-Stokes equations and the dynamics of LSMs under their governing evolution equations is symmetry preserving.

5.2.5 Numerical methods

The governing equations (5.1) are integrated in time using an extension of the code Channelflow 2.0 (channelflow.ch, Gibson *et al.* (2019)). Channelflow implements a pseudo-spectral method using a spectral Fourier-Chebychev-Fourier discretisation in the streamwise, the

wall-normal and the spanwise directions, respectively. A third-order accurate semi-implicit backward differentiation method is employed to advance the equations in time. The 2/3 dealiasing rule is applied in the streamwise and the spanwise directions.

Invariant solutions of the governing equations including travelling waves and periodic orbits are roots of

$$\sigma \mathbf{f}^T(\overline{\mathbf{u}}) - \overline{\mathbf{u}} = 0,$$

where σ is a shift operation and $\mathbf{f}^T$ describes the evolution of the state $\overline{\mathbf{u}}$ under the equations governing the dynamics of LSMs over a time period T. All invariant solutions presented in this study are identified numerically using the Newton-Krylov-Hookstep root-finding tools (Viswanath, 2007) contained in Channelflow 2.0.

5.3 Results and discussion

In this section we describe the identified invariant solutions of the filtered Navier-Stokes equations in the ASBL and discuss their dynamical relevance. First, we present two relative periodic orbits and discuss the evolution of the large-scale motion along these periodic orbits. Then, seven identified travelling wave solutions are described and the dynamics represented by these solutions is discussed. Finally, we investigate the dynamical relevance of the identified periodic orbits and travelling wave solutions for LSMs. All invariant solutions are presented for $Re = 300$ and the appropriate reference value of the Smagorinsky constant $C_s = 0.3$, for which the evolution equations faithfully describe the large-scale dynamics (Azimi *et al.*, 2020). Nevertheless, we allow the Smagorinsky constant to deviate from its reference value and consider C_s as a continuation parameter (Rawat *et al.*, 2015; Sasaki, Kawahara, Sekimoto & Jiménez, 2016). This allows us to investigate bifurcations connecting solution branches as well as the identification of additional solutions at the physically relevant reference value of $C_s = 0.3$.

5.3.1 Periodic orbits

We identified two relative periodic orbit solutions of the filtered Navier-Stokes equations in the ASBL. Both solutions are detected by the method of edge tracking (Skufca *et al.*, 2006; Schneider *et al.*, 2007). The first one, called $PO1$, is found within the shift-reflect symmetry subspace of fields invariant under $\tau_x\sigma_z$ at $C_s = 0.35$. $C_s = 0.35$ is slightly higher than the reference value required to isolate large-scale motions from the dynamics of smaller-scale structures $C_s = 0.3$. At $C_s = 0.35$, the filter width is larger than the value that preserves LSMs and filters out the smaller-scale structures, thus LSMs are artificially modified by the filter. We therefore continue $PO1$ to the reference value $C_s = 0.3$ by parametric continuation. Edge tracking does not allow us to identify $PO1$ directly at the reference value, because the periodic orbit has more than one unstable direction at $C_s = 0.3$ and only at the elevated value of $C_s = 0.35$ is it an edge state.

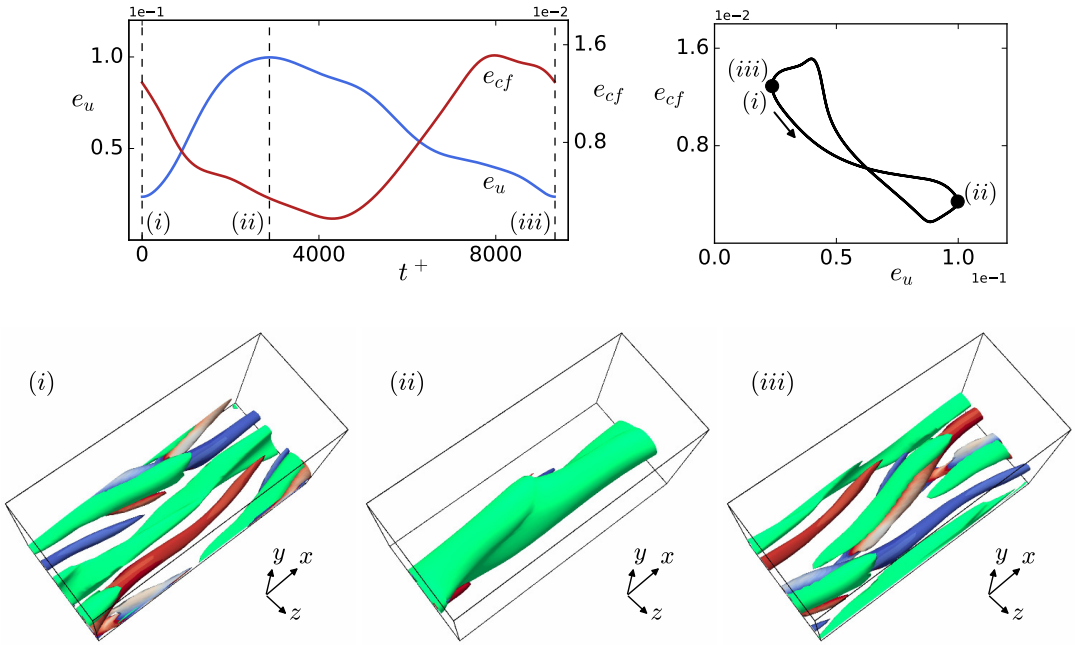

Figure 5.2 – Periodic orbit $PO1$. The temporal evolution of the streamwise kinetic energy e_u and the cross-flow energy e_{cf} is shown both as a time-series (top left panel) and phase portrait (top right panel). The periodic out-of-phase evolution of e_u, indicating the strength of streaks, and of e_{cf}, measuring the amplitude of vortices, is characteristic of the HKW cycle. Snapshots of the flow at selected times marked by dots in the phase portrait and vertical dashed lines in the time-series are shown in the bottom panels. Visualised are isosurfaces of streamwise deviations from the mean velocity with $u^+ = -0.52$ (green) and isosurfaces of the Q-criterion with $Q^+ = 10^{-5}$. Colours of the Q-isosurfaces indicate the streamwise vorticity ω_x with blue and red indicating the minimum and maximum value achieved over space and time. $PO1$ is a relative periodic orbit with the velocity field repeating up to a half-box shift in the spanwise direction and a shift in the streamwise direction (panel (iii) and (i)). The state evolves from (i) to (iii) in half the period, $T^+/2 = 9343.5$. $PO1$ has an average phase speed of $c_x = 0.892$.

At the reference value, edge tracking within the symmetry subspace of $PO1$ only approaches a chaotic attractor. However, edge tracking restricted to the z-mirror symmetric subspace of fields invariant under σ_z yields a second periodic orbit, named $PO2$. The orbit's accuracy is confirmed by converging Newton iterations.

In order to study the interaction and the temporal evolution of streaks and vortices along the identified periodic orbits, $PO1$ and $PO2$, we examine time series of the streamwise kinetic energy

$$e_u = 1/(L_x L_z) \int_{LSMFU} u^2 dxdydz,$$

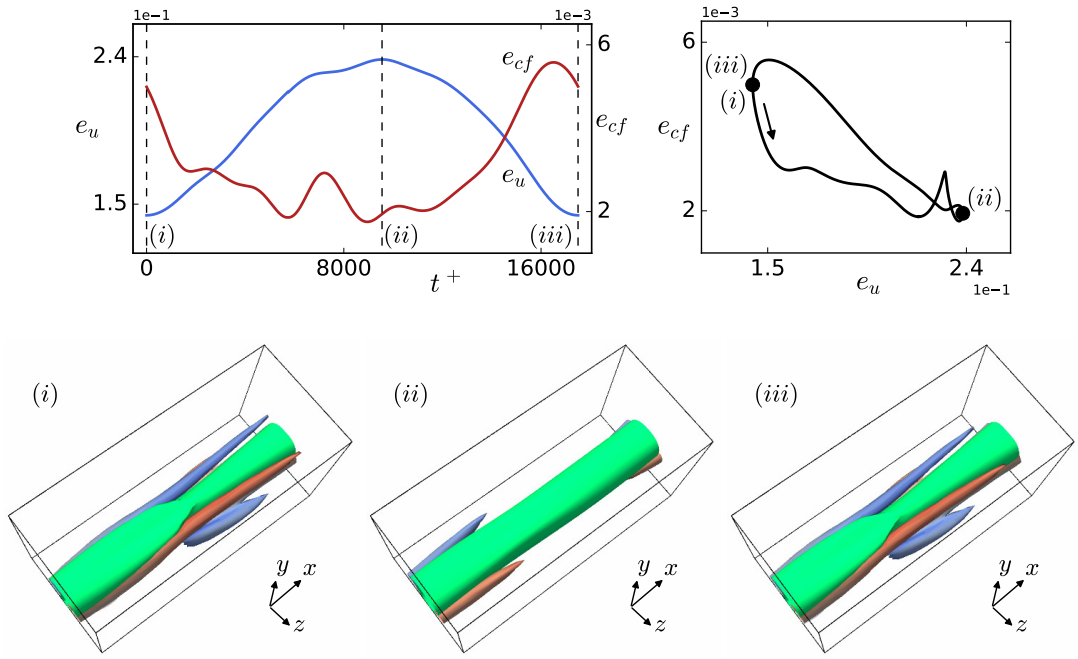

Figure 5.3 – Periodic orbit $PO2$ with temporal evolution and snapshots visualised as in figure 5.2. Like $PO1$, the opposing temporal phase relations between downstream streaks and vortices indicates the HKW cycle. Isosurfaces are shown for $u^+ = -0.78$ (green) and $Q^+ = 2 \cdot 10^{-6}$. $PO2$ is a relative periodic orbit with the velocity field repeating up to a shift in the streamwise direction only (panel (iii) and (i)). The state evolves from (i) to (iii) in the period, $T^+ = 17471.0$. $PO2$ has an average phase speed of $c_x = 0.900$.

which serves as a proxy for the intensity of streaks, and of the cross-flow kinetic energy

$$e_{cf} = 1/(L_x L_z) \int_{LSMFU} \left(v^2 + w^2\right) dxdydz,$$

measuring the strength of vortices. Along $PO1$ the periodic energy oscillations of streaks and vortices are in phase opposition. This is evidenced in figure 5.2, where the time series of e_u and e_{cf}, as well as their phase portrait is presented. The figure moreover shows snapshots of velocity fields along the cyclic dynamics. In the initial part of the orbit the energy of streaks e_u grows while the energy of the vortices e_{cf} decays (from i to ii); in the second part e_u decays while e_{cf} grows (from ii to iii). This alternating growth and decay of e_u and e_{cf} highlights two sequential parts of the cyclic dynamics and suggests that $PO1$ is following the HKW cycle: First, the streaks of the flow are amplified by the decaying vortices. Then, the vortices are regenerated while the streaks are breaking down. After half the period the velocity field along $PO1$ recovers its initial state up to a half-box shift in the spanwise direction and a shift in the streamwise direction. $PO1$ has a half-period of $T^+/2 = 9343.5$, and an average phase speed of $c_x = 0.892$.

Similar to $PO1$, $PO2$ exhibits temporal evolutions of the streamwise and cross-flow kinetic energies consistent with the HKW cycle. This is demonstrated in figure 5.3. Along $PO2$, the

Name	e_u	e_{cf}	c_x	symmetries
$TW1$	0.056	0.028	0.943	$\tau_x\sigma_z$
$TW2$	0.043	0.018	0.905	$\tau_x\sigma_z$
$TW3$	0.121	0.069	0.901	$\tau_x\sigma_z$
$TW4$	0.075	0.006	0.932	$\tau_x\sigma_z$
$TW5$	0.028	0.006	0.933	$\tau_x\sigma_z$ and $\tau_z\sigma_z$
$TW6$	0.013	0.004	0.957	$\tau_x\sigma_z$ and $\tau_z\sigma_z$
$TW7$	0.014	0.004	0.955	$\tau_x\sigma_z$

Table 5.1 – Properties of all seven identified travelling wave solutions. Given are the energy of streaks e_u, the energy of vortices e_{cf}, the phase speed c_x, and the symmetry of the specific solution.

streaks are first amplified by the decaying vortices ($i \rightarrow ii$). The amplified streaks then become unstable and start to decay ($ii \rightarrow iii$). Vortices are finally regenerated while the streaks decay. The time period of $PO2$ is $T^+ = 17471.0$. After the time period the flow recovers its initial structure up to a shift in the streamwise direction, and the entire process restarts. The average phase speed of $PO2$ is $c_x = 0.900$. Note that the very long periods measured in inner units demonstrates how slow the LSM evolution is compared to fast small-scale near-wall dynamics when the friction Reynolds number and thus the scale separation is large.

5.3.2 Travelling wave solutions

Seven travelling wave solutions of the overfiltered Navier-Stokes equations are identified in the large-scale minimal flow unit. These travelling wave solutions are converged by Newton iterations starting from initial guesses that are extracted from a typical trajectory of the flow restricted to the shift-reflect symmetry subspace. The idea is to identify slow evolution expected when the chaotic trajectory approaches a travelling wave. Instead of computing a differential state space velocity $||\partial_t \mathbf{u}||_2$, we measure the distance between two velocity fields separated by a fixed time $T = 20$ and factor out the continuous shift symmetry in the streamwise direction. Minima of $d(t) = \min_{\forall \delta x \in [0, L_x]} ||\overline{\mathbf{u}}(x+\delta x, y, z, t+T) - \overline{\mathbf{u}}(x, y, z, t)||_2$ with $||.||_2$ the conventional L2-norm suggest close visits to travelling wave solutions and yield initial guesses for the Newton search. In total, we extracted 78 different initial guesses. Among these, 19 searches converge to 6 different travelling wave solutions. These converged solutions are called $TW1$, $TW3$ to $TW7$. A seventh travelling wave solution, $TW2$, is obtained by continuing $TW1$ in C_s to its 'lower branch' (lower e_{cf}). The properties of the identified travelling wave solutions are summarised in table 5.1.

Having computed all travelling wave solutions at the physically relevant reference value of $C_s = 0.3$, we carry out parametric continuations, treating C_s as a parameter. The resulting bifurcation diagrams are shown in figure 5.4. Travelling waves $TW1$ and $TW2$ are connected under C_s-continuation and the branch appears in a saddle-node bifurcation at $C_s = 0.324$ (panel a). Likewise, $TW3$ and $TW4$ are located on a single branch emerging in a saddle-node

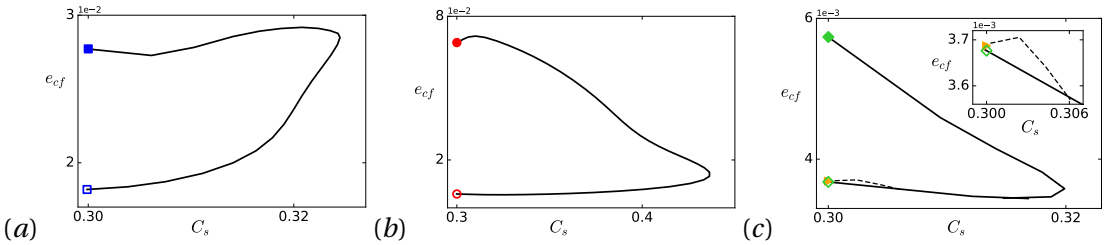

Figure 5.4 – Bifurcation diagrams of the identified travelling wave solutions. Parametric continuation in C_s for (*a*) $TW1$ (full blue square) and $TW2$ (empty blue square); (*b*) $TW3$ (full red circle) and $TW4$ (empty red circle); and (*c*) $TW5$ (full green diamond), $TW6$ (empty green diamond) and $TW7$ (full orange triangle). At the reference value of $C_s = 0.3$ the branches correspond to solutions relevant for the dynamics of LSMs. All solutions with the exception of $TW2$ are converged by Newton iterations from initial guesses extracted from a turbulent trajectory. $TW2$ is found by continuation of $TW1$ in C_s to its 'lower branch' (lower e_{cf}). The pair of $TW3$ and $TW4$, and also the pair of $TW5$ and $TW6$ emerge in saddle-node bifurcations. $TW7$ is created in a symmetry-breaking pitchfork bifurcation from the branch of $TW6$.

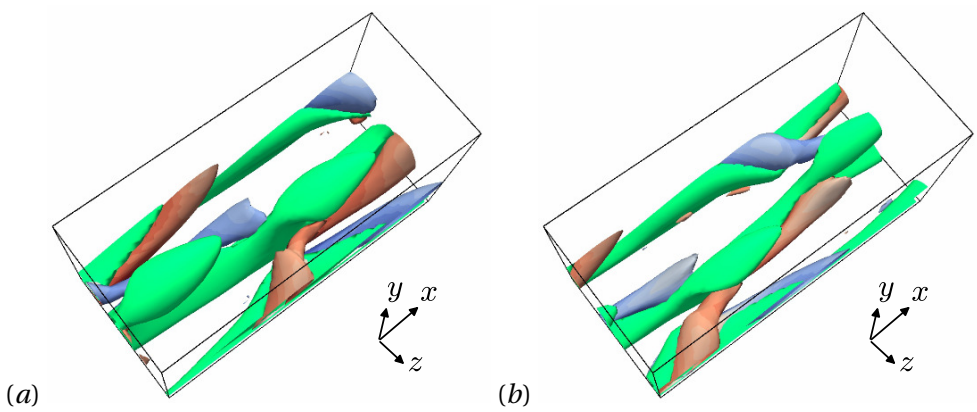

Figure 5.5 – Visualisation of $TW1$ (panel *a*) and $TW2$ (panel *b*) by the isosurface of streamwise deviation from the mean velocity with $u^+ = -0.52$ (green) and the isosurface of Q-criterion with $Q^+ = 1.2 \cdot 10^{-5}$. The isosurface of Q-criterion is coloured by contours of streamwise vorticity ω_x with blue to red indicating 20 levels between the minimum and the maximum. $TW1$ and $TW2$ consist of wavy streaks flanked by quasi-streamwise vortices.

bifurcation at $C_s = 0.436$ (panel *b*), and $TW5$ and $TW6$ emerge together at $C_s = 0.320$. A pitchfork bifurcation at $C_s = 0.306$ off $TW6$ creates the solution branch of $TW7$ (panel *c*). Although pairs of solutions are connected by saddle-nodes bifurcations we avoid a description in terms of upper and lower branch solutions because the bifurcation parameter is not the Reynolds number but a parameter of the subgrid model.

$TW1$ and $TW2$, visualised in figure 5.5, are invariant under the action of the shift-reflect symmetry $\tau_x \sigma_z$. The shift-reflect symmetry allows for a sinuously-modulated structure of the streaks. In the considered numerical domain, both $TW1$ and $TW2$ consist of two wavy low-speed streaks. The low-speed streaks are flanked by quasi-streamwise vortices. These

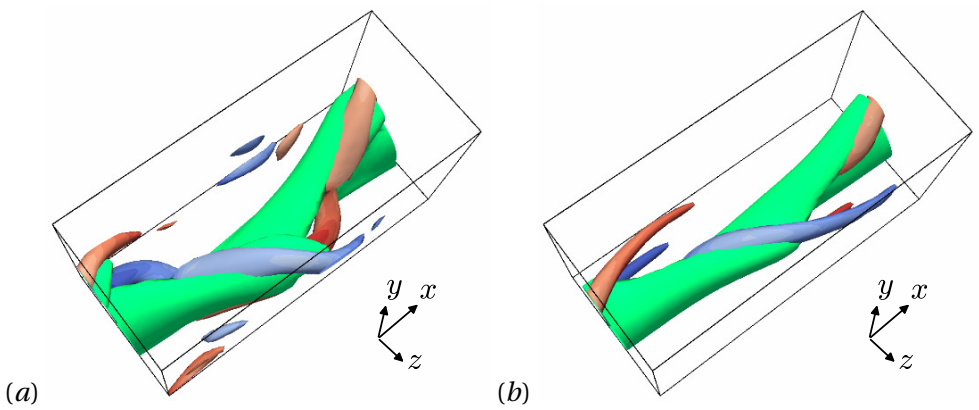

Figure 5.6 – Visualisation of $TW3$ (panel a) and $TW4$ (panel b) by the isosurface of streamwise deviation from the mean velocity with $u^+ = -0.52$ (green). The isosurface level of the Q-criterion is chosen as $Q^+ = 0.3\,Q^+_{max}$, 30% of the maximum value for each of the solutions. The isosurface of Q-criterion is coloured by the contours of streamwise vorticity ω_x with 20 levels between the minimum and the maximum shown by blue to red. $TW3$ and $TW4$ consist of sinuous streaks with quasi-streamwise vortices located on both sides of the streak.

vortices lift up the streaks whose sinuous modulation indicates an instability feeding back on the vortices. Both travelling waves $TW1$ and $TW2$ thus reflect the self-sustaining process by Waleffe (1997), where lift-up and streak breakdown are in equilibrium. The same geometry suggesting Waleffe's self-sustaining process is present in $TW3$ and $TW4$, visualised in figure 5.6. These solutions are invariant under the same symmetries as solutions $TW1/TW2$ but only contain a single low-speed streak within the LSMFU.

While travelling waves $TW1$ to $TW4$ are invariant under one discrete symmetry, $TW5$ and $TW6$ are invariant under both the shift reflect symmetry $\tau_x\sigma_z$ and $\tau_z\sigma_z$. A pitchfork bifurcation on the solution branch connecting $TW5$ and $TW6$ under Cs continuation creates a branch containing the final seventh travelling wave $TW7$. As the pitchfork bifurcation breaks the $\tau_z\sigma_z$ symmetry, $TW7$ is only invariant under the action of shift reflect symmetry $\tau_x\sigma_z$. Figure 5.7 visualises $TW5$, $TW6$ and $TW7$. The vortical structure of these solutions substantially differs from those observed in $TW1$ to $TW4$ and is reminiscent of hairpin vortices (Theodorsen, 1952; Adrian, 2007). Two quasi-streamwise counter-rotating vortices, inclined towards the bulk, form the 'legs' of the hairpin-like structure. Far from the wall and close to the edge of the boundary layer the legs join and form a spanwise-oriented vortex, called the 'head' of the hairpin-like structure. Below the head and between the legs, a low-speed region of the flow is formed. When periodically continued in the plane, the combination of the shift-reflect, $\tau_x\sigma_z$, and $\tau_z\sigma_z$ symmetries of $TW5$ and $TW6$, gives rise to a chequered pattern in which the hairpin-like vortical structures repeat. Further discussions on the hairpin-like structure of $TW5$, $TW6$ and $TW7$ are given in appendix 5.5.

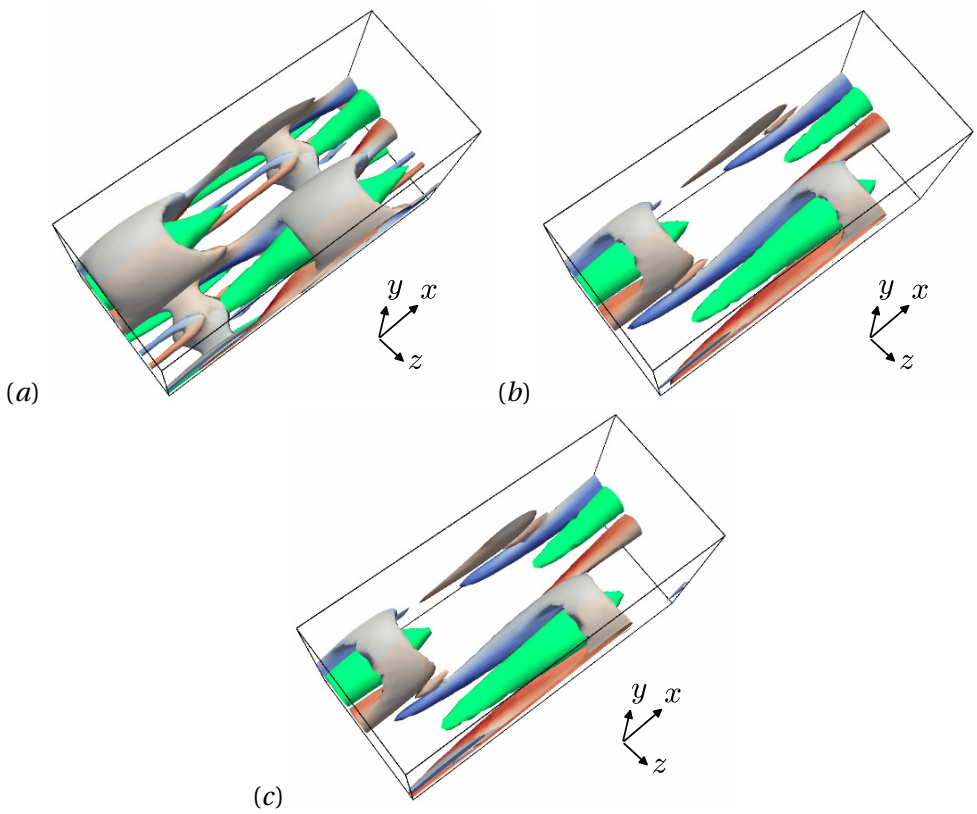

Figure 5.7 – Visualisation of $TW5$ (panel a), $TW6$ (panel b) and $TW7$ (panel c) by the isosurface of streamwise deviation from the mean velocity with $u^+ = -0.52$ (green) and isosurface of Q-criterion with $Q^+ = 1.5 \cdot 10^{-6}$. The isosurface of Q-criterion is coloured by contours of the streamwise vorticity ω_x with blue to red indicating 20 levels between the minimum and the maximum. $TW5$, $TW6$ and $TW7$ contain hairpin-like vortical structures with counter-rotating quasi-streamwise legs that are inclined from the wall and join close to the edge of the boundary layer to form the head. The low-speed large-scale streak is located below the head and between the legs.

5.3.3 Dynamical relevance of the solutions

In this section, we discuss the relevance of the computed invariant solutions for the dynamics of large-scale motions (LSMs). We compare the identified invariant solutions to a chaotic trajectory of the overfiltered large-eddy simulation (OLES) at the same reference $C_s = 0.3$ for which the dynamics of large-scale motions is captured and the invariant solutions have been identified. The simulation of large-scale motions by OLES is performed in the same large-scale minimal flow unit (LSMFU) where the invariant solutions are computed and no additional symmetries are enforced. Figure 5.8 shows the temporal evolution of the streamwise kinetic energy e_u and of the cross-flow kinetic energy e_{cf} for a simulated LSM. From this figure, it can be appreciated that during aperiodic bursting events the kinetic energy e_u associated with streaks varies mostly in phase with the kinetic energy e_{cf} associated with vortices.

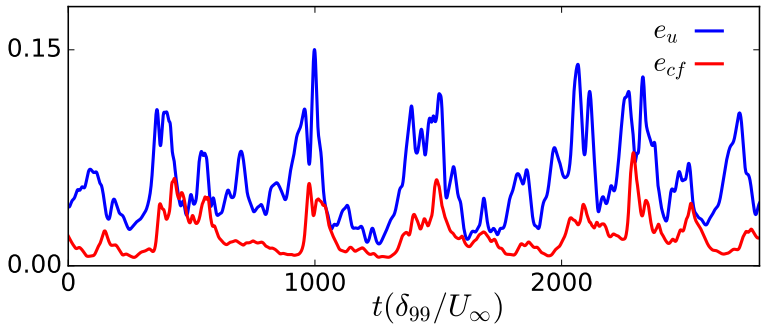

Figure 5.8 – Time-series of streamwise kinetic energy e_u and cross-flow kinetic energy e_{cf} for a simulation of an isolated LSM. The temporal evolution of both the streamwise kinetic energy and the cross-flow kinetic energy exhibit aperiodic bursting events. During the bursting events, both components of energy grow and decay in phase.

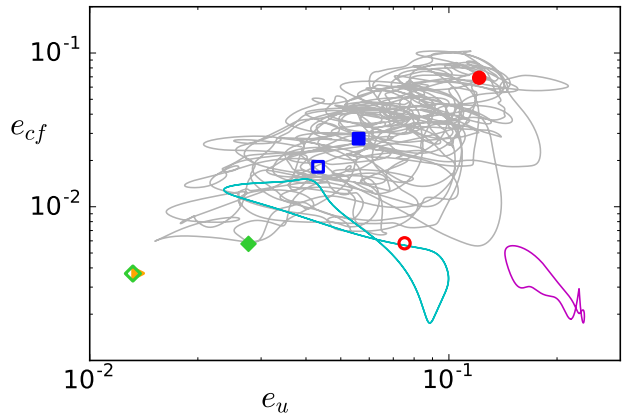

Figure 5.9 – State-space projection of the chaotic LSM trajectory together with all identified invariant solutions. The two-dimensional projection is defined by e_u and e_{cf} with the trajectory of a simulated large-scale motion indicated by a grey line. Invariant solutions are: $TW1$ (full blue square); $TW2$ (empty blue square); $TW3$ (full red circle); $TW4$ (empty red circle); $TW5$ (full green diamond); $TW6$ (empty green diamond); $TW7$ (full orange triangle); $PO1$ (cyan line); and $PO2$ (magenta line). Three travelling waves characterised by sinuous streak-vortex structures ($TW1$, $TW2$ and $TW3$) appear located within the attractor, the chaotic LSM trajectory evolves on, while both periodic orbits and the remaining travelling waves are apparently not visited with high frequency.

To compare the kinetic energy of streaks and vortices of the identified invariant solutions with those of the evolving large-scale motions, figure 5.9 shows the trajectory of a simulated large-scale motion together with the identified invariant solutions in the $e_u - e_{cf}$ plane. This plane defines a two-dimensional projection of the state space. The LSM trajectory in the $e_u - e_{cf}$ plane occupies a region associated with a positive inclination, consistent with the observation that e_u and e_{cf} are positively correlated and vary in phase. The LSM trajectory span a wide range in both e_u and e_{cf}. In the visualised two-dimensional projection of the state space in figure 5.9, the identified relative periodic orbits, $PO1$ and $PO2$, and hairpin-like

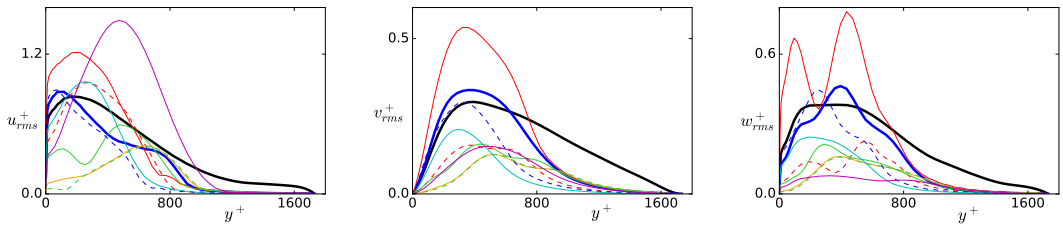

Figure 5.10 – Root mean squared (r.m.s.) velocity components $u^+_{i,rms}(y^+) = (1/(L^+_x L^+_z)\int_0^{L^+_x}\int_0^{L^+_z}(\overline{u_i}^+(x^+,y^+,z^+) - \overline{u_i}^+_{mean}(y^+))^2 dx^+ dz^+)^{1/2}$ of chaotic LSM trajectories and all identified invariant solutions. The r.m.s. profiles are reported for the streamwise velocity (left), the wall-normal velocity (middle) and the spanwise velocity (right) components as functions of the wall-normal coordinate. Statistical properties of LSMs (thick black lines) are compared to properties of $TW1$ (thick blue solid line); $TW2$ (blue dashed line); $TW3$ (red solid line); $TW4$ (red dashed line); $TW5$ (green solid line); $TW6$ (green dashed line); $TW7$ (orange solid line); $PO1$ (cyan solid line); and $PO2$ (magenta solid line). Especially, $TW1$ captures the statistics of LSM trajectories reasonably well.

travelling wave solutions $TW5$, $TW6$ and $TW7$ reside outside the region that is frequently visited by the LSM trajectory. Despite the existence of solutions capturing the HKW-type self-sustained processes and of solutions with hairpin-like topology, the sustained processes represented by both these solution types seem not very active in the ASBL. Unlike the rarely visited HKW and hairpin solutions, $TW1$, $TW2$ and $TW3$ lie in the region that is covered by the LSM trajectory. These travelling wave solutions consisting of sinuous streak-vortex structures have kinetic energies that are typical of different phases of the bursting events. $TW3$ lies in the region of the state space with large values of e_u and e_{cf} while $TW2$ is located in the low-energy part of the space. $TW1$ lies in the center of the region visited by the LSM trajectory.

The fact that a two-dimensional projection suggests three travelling waves and specifically $TW1$ to be located in the center of the chaotic attractor supporting the LSM dynamics suggests the travelling waves may capture statistical properties of the flow. In figure 5.10, the root mean squared (r.m.s.) velocity components of the chaotic solution are compared with those of the identified invariant solutions. The statistics of $TW1$ is particularly close to the statistics of the chaotic trajectory, supporting the idea that $TW1$ lies in the center of the chaotic attractor. Consequently, exact invariant solutions containing sinuous streak-vortex structures appear to be dynamically relevant for LSMs in ASBL, although details of their role in the bursting dynamics remain to be explored.

5.4 Summary and conclusion

Large-scale motions, LSMs, are important coherent structures dominating the energetics of boundary layer flow. They are shown to be self-sustained and to not require forcing by near-

wall structures (Hwang & Cossu, 2010*c*; Rawat *et al.*, 2015; Azimi *et al.*, 2020). Consequently, the question arises which physical processes sustain turbulent LSMs. While the interaction of large-scale streaks and vortices via lift-up effects is common to LSMs in all shear flows studied so far, differences between confined flows and open boundary layers have been reported. In confined flows, the amplitudes of quasi-streamwise streaks and associated quasi-streamwise vortices vary out of phase, suggesting a large-scale version of the HKW cycle (Hamilton *et al.*, 1995; Waleffe, 1995) sustains the flow. In a parallel boundary layer, namely ASBL, the characteristic phase delay between streaks and vortices is however not observed, but LSMs appear sustained by bursting events in which streaks and vortices grow and decay in phase. This suggests alternative self-sustaining processes are active in unconfined boundary layers.

Invariant solutions provide information on self-sustaining mechanisms. Travelling waves and periodic orbits are by definition self-sustained and thus reveal the self-sustaining mechanism supporting them. The dynamics of LSMs in ASBL is faithfully captured by filtered Navier-Stokes equations (Azimi *et al.*, 2020). Following Rawat *et al.* (2015, 2016) and Hwang *et al.* (2016), we therefore compute invariant solutions of these equations and describe self-sustaining mechanisms captured by invariant solutions underlying LSMs in ASBL.

We identified nine invariant solutions including two periodic orbits and seven travelling waves. These solutions capture multiple different self-sustaining mechanisms including the self-sustained HKW regeneration cycle, a hairpin-based self-sustained process, and the steady version of the HKW cycle, where vortex lift-up and streak breakdown are in exact balance. To investigate the importance of these different mechanisms, a chaotic LSM trajectory is analysed in a two-dimensional state-space projection. The frequency of visits to state-space regions occupied by the identified invariant solutions suggests which mechanisms, captured by the respective solutions, are dominating the dynamics and which are less active.

Of the nine identified invariant solutions, two are relative periodic orbits. These show characteristic out-of-phase modulations of streak and vortex amplitudes. The periodic orbits can thus be associated with the streak-vortex regeneration cycle of Hamilton *et al.* (1995) (HKW). The HKW cycle is identified as the main self-sustaining mechanism of LSMs in confined flows including plane channel and Couette flows (Hwang & Cossu, 2010*c*; Rawat *et al.*, 2015; Cossu & Hwang, 2017). As the identified periodic orbits demonstrate, the same self-sustaining mechanism also exists in ASBL. However, the periodic orbits capturing the HKW cycle are not visited by the LSM trajectory, suggesting the mechanism is not active in the parallel boundary layer.

Three of the seven travelling wave solutions represent hairpin-like vortical structures. These solutions document the existence of hairpin-based self-sustaining processes for LSMs in the ASBL. However, the hairpin travelling waves are not located within the state-space region covered by the turbulent LSM trajectory. Consequently, hairpin-based self-sustaining mechanisms do not appear to actively contribute to supporting the large-scale turbulent dynamics

in ASBL.

While neither periodic orbits capturing the quasi-periodic HKW cycle nor travelling waves representing hairpin vortices are frequently visited by the LSM dynamics, there are travelling wave solutions located within the state-space region covered by the LSM dynamics. These remaining travelling wave solutions contain sinuous streak-vortex structures with streak and vortex energies compatible with those observed in the LSM dynamics. Specifically, three travelling waves, $TW1$, $TW2$ and $TW3$ span a large range of kinetic energies with the kinetic energy of streaks remaining correlated with the kinetic energy of vortices. Consequently, those three travelling waves correspond to instantaneous states reached in different phases of the aperiodic correlated bursting of streaks and vortices. We thus hypothesise that bursting events, characterised by simultaneous in-phase growth and decay of streaks and vortices, are driven by dynamical connections between steady invariant solutions with large differences in the kinetic energy of both streaks and vortices. The explicit identification of heteroclinic connections remains challenging and requires the adaptation of suitable tools (Farano, Cherubini, Robinet, De Palma & Schneider, 2019) to filtered Navier-Stokes equations.

In summary, the analysis of exact invariant solutions capturing self-sustaining mechanisms of large-scale motions reveals that several mechanisms are present in ASBL. This includes the self-sustained HKW streak-vortex regeneration cycle that dominates LSMs in confined flows. However, in open ASBL flow the HKW cycle remains inactive and a different mechanism dominates. LSMs in the open boundary layer are mostly supported by self-sustained in-phase bursting events, reminiscent of the bursts sustaining buffer layer turbulence. Why LSMs in confined and in open flows appear sustained by different dominant mechanisms remains to be investigated. Similarities between bursting in boundary layer LSMs and buffer layer turbulence as well as similarities between the regeneration cycle of LSMs in confined flows and cycles in low Reynolds number transitional Couette and channel flows suggest, the number of dynamically relevant confining walls may select which self-sustaining mechanisms are active. Exploring detailed physical mechanisms driving large-scale coherent structures in fully developed turbulent boundary layers by applying dynamical systems methods to filtered Navier-Stokes equations underlying the LES simulation paradigm will hopefully lead to a deeper understanding of wall-bounded turbulence and open new avenues for turbulence control.

5.5 Appendix: Further visualisations of the hairpin-like travelling waves

$TW5$, $TW6$ and $TW7$ represent hairpin-like vortical large-scale structures. Here, we provide additional visualisations of $TW6$. Figure 5.11 shows cross-sections of the velocity field. The flow shows a large-scale vortex. Below its head, sandwiched between its legs, a low-speed streak is located. This streak is induced by lift-up effects of the counter-rotating legs in combination with the rotation of the vortex head. The rotation of the head induces a strong

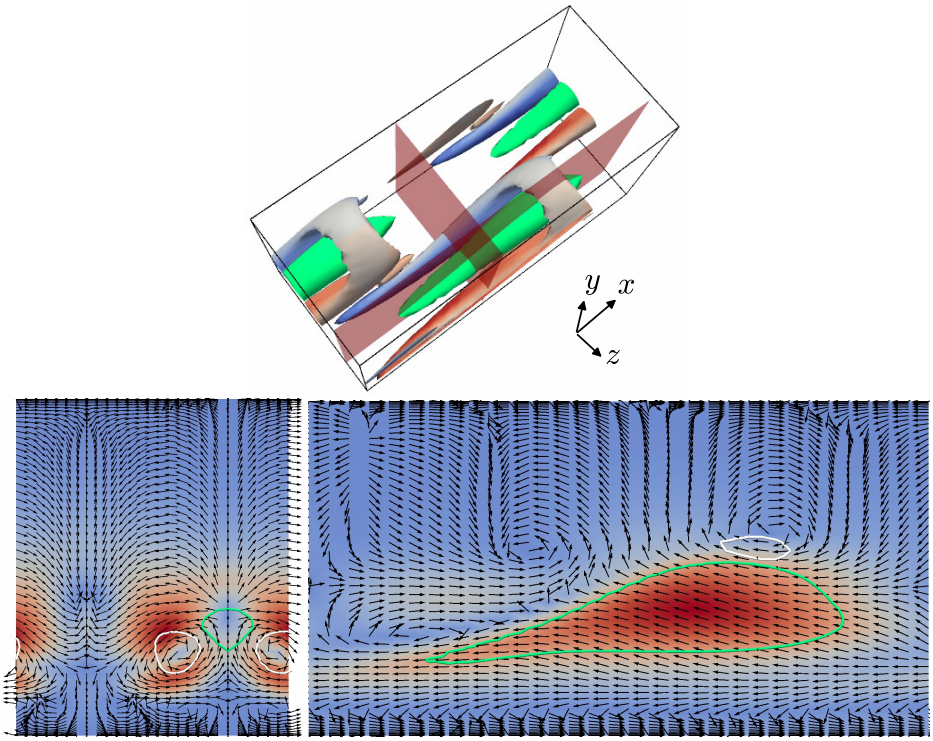

Figure 5.11 – Visualisations of the hairpin-like travelling wave $TW6$. Three-dimensional visualisation as in figure 5.7(b) with two-dimensional cross-sections indicated (top panel). Both the $y-z$ section (bottom left) and the $x-y$ section (bottom right) show in-plane velocity with the direction indicated by unit vectors and velocity magnitudes by colours, ranging from zero (blue) to the maximum (red). Contours of streamwise velocity fluctuations with $u^+ = -0.52$ (green lines) and contours of the Q-criterion with $Q^+ = 1.5 \cdot 10^{-6}$ (white lines) are overlaid in the bottom panels. These contour lines correspond to the intersections of the isosurfaces in the visualisation of the top panel with the indicated visualisation planes. Rotation of hairpin-like vortical structure (indicated by white contour lines) induces the low-speed large-scale streak (indicated by green contour lines).

ejection event ($u < 0$ and $v > 0$) below and behind the head. The lift-up effect of the legs and the ejection event are similarly observed in $TW5$ and $TW7$ (not shown). These observations provide further evidence that $TW5$, $TW6$ and $TW7$ represent hairpin-like vortices at large scale.

6 Modified snaking in plane Couette flow with wall-normal suction

Remark: This chapter is largely inspired by a pre-print titled "Modified snaking in plane Couette flow with wall-normal suction"

Sajjad Azimi[1] and Tobias M. Schneider[1]

[1]Emergent Complexity in Physical Systems Laboratory (ECPS),
École Polytechnique Fédérale de Lausanne, CH-1015 Lausanne, Switzerland

Submitted to *Journal of Fluid Mechanics*

Contents

In the previous chapters the dynamics of small- and large-scale structures in the ASBL are studied. The temporal evolution of large-scale streaks and vortices in the ASBL appears to differ from the temporal evolution in confined flows including plane Couette flow and channel flow. The difference of the ASBL with the confined flows is not only the dynamical relevance of one or two walls but also the symmetries of the two systems differ. To study the differing symmetries in ASBL and in confined flows, we consider the transformation of plane Couette flow under applying a non-vanishing suction. The non-vanishing suction breaks the up-down symmetry of plane Couette flow and yields a flow with equivariance group of the ASBL.

Chapter summary

A specific family of spanwise-localised invariant solutions of plane Couette flow exhibits homoclinic snaking, a process by which spatially localised invariant solutions of a nonlinear partial differential equation smoothly grow additional structure at their fronts while undergoing a sequence of saddle-node bifurcations. Homoclinic snaking is well understood in the context of simpler pattern forming systems such as the one-dimensional Swift-Hohenberg equation with cubic-quintic nonlinearity, whose solutions resemble the snaking solutions of plane Couette flow remarkably well. We study the structural stability of the characteristic snakes-and-ladders structure associated with homoclinic snaking for flow modifications that break symmetries of plane Couette flow. We demonstrate that wall-normal suction modifies the bifurcation structure of three-dimensional plane Couette solutions in the same way, a symmetry-breaking quadratic term modifies solutions of the one-dimensional Swift-Hohenberg equation. These modifications are related to the breaking of the discrete rotational symmetry. At large amplitudes of the symmetry-breaking wall-normal suction the connected snakes-and-ladders structure is destroyed. Previously unknown solution branches are created and can be parametrically continued to vanishing suction. This yields new localised solutions of plane Couette flow that exist in a wide range of Reynolds number.

6.1 Introduction

Invariant solutions of the Navier-Stokes equations play a key role for the dynamics of transitional shear flows (Kawahara *et al.*, 2012). These solutions, in the form of equilibria, travelling waves and periodic orbits, have been computed for many canonical shear flows including pipe flow (Faisst & Eckhardt, 2003), plane Couette flow (Gibson, Halcrow & Cvitanović, 2009), plane Poisuille flow (Waleffe, 2003), and asymptotic suction boundary layer flow (Kreilos *et al.*, 2013). Invariant solutions are mostly found in small periodic domains, or 'minimal flow units' (Jiménez & Moin, 1991). Later investigations have considered extended domains and identified localised invariant solutions that capture large scale flow patterns like turbulent spots, stripes and puffs (Avila *et al.*, 2013; Brand & Gibson, 2014; Reetz *et al.*, 2019; Reetz & Schneider, 2020*b*).

The first family of spatially localised invariant solutions in shear flows were calculated by Schneider, Marinc & Eckhardt (2010*b*) in plane Couette flow. This includes equilibria and travelling waves, which are equilibria in a frame of reference moving relative to the lab frame. These localised invariant solutions in plane Couette flow are specifically noteworthy because they exhibit the characteristic behaviour of homoclinic snaking (see review by Knobloch, 2015) under parametric continuation (Schneider *et al.*, 2010*a*). Homoclinic snaking is a phenomenon previously observed in many dissipative pattern-forming systems such as binary-fluid convection systems (Batiste, Knobloch, Alonso & Mercader, 2006) and optical systems (Firth, Columbo & Maggipinto, 2007), by which localised solutions grow in one direction while undergoing a sequence of successive saddle-node bifurcations (Woods & Champneys, 1999). Homoclinic snaking manifests itself by a characteristic snakes-and-ladders structure in the bifurcation diagram (Burke & Knobloch, 2007).

A well-studied one-dimensional model system which supports localized solutions that exhibit homoclinic snaking is the Swift-Hohenberg equation $\partial_t u = ru + (1+\partial_x^2)^2 u + \mathcal{N}(u)$, for a real-valued function $u(x)$ on the real axis with r the bifurcation parameter and a nonlinearity $\mathcal{N}(u)$ (Burke & Knobloch, 2006, 2007; Beck, Knobloch, Lloyd, Sandstede & Wagenknecht, 2009; Knobloch, Uecker & Wetzel, 2019). Several variants of the Swift-Hohenberg equation with differing forms of the nonlinear term have been considered. Most studied are both a quadratic-cubic $\mathcal{N} = b_2 u^2 - u^3$ and a cubic-quintic $\mathcal{N} = b_3 u^3 - u^5$ nonlinearity, where b_2 and b_3 are adjustable parameters. For both nonlinear terms, the Swift-Hohenberg equation supports localised solutions arranged in a snaking bifurcation structure. The localised invariant solutions of the Navier-Stokes equations in plane Couette geometry share remarkably similar properties with solutions of the Swift-Hohenberg equation with the cubic-quintic nonlinearity (Schneider *et al.*, 2010*a*):
(i) First, the bifurcation diagram with its characteristic snakes-and-ladders structure is almost indistinguishable from that of the Swift-Hohenberg equation.
(ii) Second, the three-dimensional snaking solutions of the Navier-Stokes equations very closely resemble one-dimensional snaking solutions of Swift-Hohenberg, when three-dimensional velocity fields are averaged in the streamwise direction and zero-sets of streamwise velocity are visualised as a function of the spanwise coordinate.
The almost perfect resemblance of three-dimensional Navier-Stokes and one-dimensional Swift-Hohenberg solutions is observed for the downstream wavelength of 4π studied in Schneider *et al.* (2010*a*). Subtle modifications related to internal deformations of the three-dimensional flow field appear when the downstream wavelength changes, but the characteristic snakes-and-ladders structure remains intact (Gibson & Schneider, 2016). Why localised solutions of the three-dimensional Navier-Stokes equations closely resemble solutions of the one-dimensional Swift-Hohenberg equation and are organized in a snakes-and-ladders bifurcation structure is not fully understood. The detailed analysis of model systems including Swift-Hohenberg using concepts such as spatial dynamics indicates the importance of discrete symmetries for an equation to support homoclinic snaking (Champneys, 1998; Burke, Houghton & Knobloch, 2009; Knobloch, 2015). In both the Navier-Stokes solutions

and in solutions of the Swift-Hohenberg equation with cubic-quintic nonlinearity, the snakes-and-ladders bifurcation structure is composed of two pairs of intertwined snaking branches along which the solutions are invariant under discrete symmetries that are part of the equivariance group of the respective system. The snaking branches of symmetric solutions are connected by so-called rungs which emerge in symmetry-breaking pitchfork bifurcations. The rungs do not possess discrete symmetries and together with the snaking branches form the snakes-and-ladders structure.

To investigate the importance of discrete symmetries for the snaking structure of the Swift-Hohenberg equation with cubic-quintic nonlinearity, Houghton & Knobloch (2011) introduced an additional quadratic term in the equation to break the odd symmetry of the system $R_2 : x \to -x,\ u \to -u$. When the amplitude ϵ of this symmetry-breaking term ϵu^2 is increased from zero, the bifurcation structure changes. One pair of snaking branches breaks into disconnected pieces while the other pair splits into two distinct curves in an amplitude versus r bifurcation diagram. Those curves are connected by z- and s-shaped non-symmetric solution branches that are composed of solutions that for $\epsilon = 0$ form rungs and the snaking branches that disappear when the symmetry is broken.

In the Swift-Hohenberg equation with cubic-quintic nonlinearity, breaking a specific discrete symmetry destroys the snakes-and-ladders bifurcation structure that solutions of Navier-Stokes in plane Couette geometry resemble remarkably well. To investigate the significance of discrete symmetries of the three-dimensional Navier-Stokes equations, we break a symmetry of plane Couette and study the structural stability of the snakes-and-ladders structure under controlled symmetry breaking. We specifically apply wall-normal suction at one wall (and wall-normal blowing with equal amplitude at the other wall) to break the rotational symmetry of plane Couette flow. At small amplitude, suction modifies the snakes-and-ladders structure of plane Couette flow in the same way as a quadratic term modifies the snakes-and-ladders structure of the Swift-Hohenberg equation with the cubic-quintic nonlinearity. At higher values of suction velocity, the snaking branches that remain intact at small suction velocity also break down. The solutions form separated branches which involve solutions that can be followed to zero suction velocity but are not part of the snakes-and-ladders structure of plane Couette flow without suction. We thereby identify previously unknown localised solutions of plane Couette flow that exist in a much wider range of Reynolds numbers than the snaking solutions studied previously. The structural modifications of the bifurcation structure at large amplitude of the symmetry breaking terms is not observed in the Swift-Hohenberg system where increasing the amplitude of the quadratic term transforms the snakes-and-ladders structure into a modified snakes-and-ladders structure similar to the bifurcation structure of the localised solutions of the Swift-Hohenberg equation with quadratic-cubic nonlinearity. Thus, at small suction amplitudes, suction has a similar effect as the symmetry-breaking term within the cubic-quintic Swift-Hohenberg case while at larger suction amplitudes, the bifurcation structure of 3D Navier-Stokes solutions significantly differs from that of the analogous Swift-Hohenberg problem. Both in the one-dimensional model system and in the full three-dimensional Navier-Stokes problem, the initial breakdown of the snakes-

and-ladders structure can be explained in terms of symmetry breaking.

This chapter is organised as follows: In section 6.2, we introduce the plane Couette system with wall-normal suction and discuss its symmetry properties. Section 6.3 reviews the snaking solutions and the snakes-and-ladders structure of plane Couette flow at zero suction. Section 6.4 presents the key observations on how wall-normal suction modifies the snaking structure. In section 6.5, features of the modified snaking structure are discussed and related to symmetry properties including symmetry subspaces of the flow. In the final section 6.6, results are summarised and an outlook for future work is provided.

6.2 System and methodology

Plane Couette flow (PCF) is the flow of a Newtonian fluid between two parallel plates at a distance of $2H$ which move in opposite directions with a constant relative velocity of $2U_w$. The laminar solution of the Navier-Stokes equations in plane Couette flow is a linear profile. We investigate the effect of wall-normal suction on the snaking solutions of plane Couette flow. The wall-normal suction modifies the laminar flow. After nondimensionalisation of the velocities with respect to half of the relative velocity of the plates, U_w, and the lengths with respect to half of the gap width between the plates, H, the laminar solution takes the form

$$\mathbf{U}(y) = U_x(y)\hat{e}_x - V_s\hat{e}_y,$$

where the coordinate system (x, y, z) is aligned with the streamwise $(\hat{e}_x)$, the wall-normal $(\hat{e}_y)$, and the spanwise directions $(\hat{e}_z)$; $\mathbf{U}(y)$ is the laminar solution; V_s is the nondimensionalised wall-normal suction velocity; and

$$U_x(y) = 1 - \frac{1}{\sinh(-ReV_s)}\left(\exp(-ReV_s) - \exp(-yReV_s)\right).$$

Decomposition of the total velocity into the laminar solution, $\mathbf{U}(y)$ as a base flow, and the deviation from the laminar solution, $\mathbf{u}(x, y, z, t)$, yields the Navier-Stokes equations in perturbative form

$$\frac{\partial \mathbf{u}}{\partial t} + U_x(y)\frac{\partial \mathbf{u}}{\partial x} - V_s\frac{\partial \mathbf{u}}{\partial y} + v\frac{dU_x(y)}{dy}\hat{e}_x + \mathbf{u}\cdot\nabla\mathbf{u} = -\nabla p + \frac{1}{Re}\nabla^2\mathbf{u}$$

where the Reynolds number is defined as $Re = UH/\nu$, with ν the kinematic viscosity of the fluid. The boundary conditions for $\mathbf{u}$ are periodic in the streamwise and the spanwise directions,

$$\mathbf{u}(-L_x/2, y, z, t) = \mathbf{u}(L_x/2, y, z, t),$$
$$\mathbf{u}(x, y, -L_z/2, t) = \mathbf{u}(x, y, L_z/2, t),$$

where L_x and L_z are the length and width of the computational domain in the streamwise and the spanwise directions, respectively. At the top and bottom plate Dirichlet conditions

$$\mathbf{u}(x,1,z,t) = (1,-V_s,0),$$
$$\mathbf{u}(x,-1,z,t) = (-1,-V_s,0)$$

are satisfied. Zero pressure gradient in both the streamwise and the spanwise directions is imposed.

Following Gibson & Schneider (2016), we present bifurcation diagrams in terms of energy dissipation of the deviation from the laminar solution, normalised by the length of the channel L_x. The considered solutions are localised and thus independent of the width L_z of the domain. Consequently, we do not normalise by the width L_z. The streamwise averaged energy dissipation for an equilibrium or travelling wave solution equals the energy input rate I and can be expressed as

$$D = I = \frac{1}{2L_x}\int_{-L_z/2}^{L_z/2}\int_{-L_x/2}^{L_x/2}\left(\frac{\partial \mathbf{u}}{\partial y}\bigg|_{y=-1} + \frac{\partial \mathbf{u}}{\partial y}\bigg|_{y=1}\right)dxdz$$

in units of U_w^2. D serves as a measure for the width of a localised solution that approaches laminar flow ($\mathbf{u} = 0$) and only generates nonzero dissipation in the non-laminar part of the solution.

Plane Couette flow ($V_s = 0$) is invariant under continuous translations in x and z directions, discrete reflection in z direction and a discrete rotation of 180° around the z axis. The rotation is equivalent to two successive discrete reflections in x and y directions. Following the conventions of Gibson *et al.* (2008), symmetries of the governing equations and the boundary conditions of PCF are expressed as

$$\sigma_z : [u,v,w](x,y,z) \to [u,v,-w](x,y,-z),$$
$$\sigma_{xy} : [u,v,w](x,y,z) \to [-u,-v,w](-x,-y,z),$$
$$\tau_{\delta x,\delta y} : [u,v,w](x,y,z) \to [u,v,w](x+\delta x, y, z+\delta z),$$

where δx and δz are arbitrary displacements in the streamwise and the spanwise directions, respectively. All products of σ_z, σ_{xy} and τ compose the symmetry, or equivariance, group of plane Couette flow ($V_s = 0$). The equivariance group contains the discrete symmetries under which the snaking solutions are invariant. These are the inversion symmetry σ_{xyz} and the shift-reflect symmetry $\tau_x\sigma_z$:

$$\sigma_{xyz} : [u,v,w](x,y,z) \to [-u,-v,-w](-x,-y,-z),$$
$$\tau_x\sigma_z : [u,v,w](x,y,z) \to [u,v,-w](x+L_x/2, y, -z).$$

A nonzero wall normal suction velocity breaks the rotational symmetry of the system, σ_{xy}. For plane Couette flow with a nonzero wall-normal suction, the equivariance group consists of

all products of the translational symmetry, $\tau_{\delta x,\delta y}$, and the reflection symmetry, σ_z. Thus, for nonzero wall-normal suction, the inversion symmetry σ_{xyz} of PCF is broken.

The significance of symmetries for the dynamics of the flow is twofold. First, all flow fields which are invariant under the action of a symmetry contained in the equivariance group form a symmetry subspace within the system's state space that the dynamics is invariant under. That means, if an initial condition **u** is located in a symmetry subspace, its evolution under the governing equations remains in the same symmetry subspace. Second, if an equilibrium or travelling wave solution is invariant under a symmetry and thus located in a symmetry subspace, parametric continuation will not change the symmetry of the solution; instead, the entire continuation branch remains in the same symmetry subspace. Symmetries can only change if the branch is created or terminates in a symmetry-breaking bifurcation such as a pitchfork bifurcation.

If an equilibrium or travelling wave solution is *not* invariant under a symmetry contained in the equivariance group of the system, then the action of that symmetry on the solution creates an additional solution. Two equilibria / travelling waves that are related by that symmetry have the same global integrated properties such as dissipation. Hence, symmetry-related invariant solution branches are represented by a single curve in bifurcation diagrams presenting a typical global integrated property as a function of a control parameter.

The invariant solutions presented in this study including equilibria and travelling waves are identified numerically using the Newton-Krylov-Hookstep root-finding tools contained in Channelflow 2.0 (www.channelflow.ch, Gibson *et al.* (2019)). To construct the required Krylov subspace, Channelflow employs successive time integrations of the Navier-Stokes equations to evaluate the action of the Jacobian by finite differencing. For integrating the Navier-Stokes equations in time, a third-order accurate semi-implicit backward differentiation scheme is used together with a pseudo-spectral Fourier-Chebychev-Fourier discretisation. In the homogeneous streamwise, and spanwise directions, we dealiase the nonlinear term according to the 2/3 rule. The computational domain has a length of $L_x = 4\pi$, a width of $L_z = 24\pi$, and a height of $2H = 2$ and is discretised by $N_x = 32$, $N_y = 35$, and $N_z = 432$ collocation points. All of the solutions are localised in the spanwise directions and thus independent of the width of the computational domain.

6.3 Symmetry properties of snaking solutions in plane Couette flow without suction

The snaking solutions found by Schneider *et al.* (2010*a*) in plane Couette flow are shown in figure 6.1 together with their bifurcation diagram. The solutions are computed for a periodic box with length $L_x = 4\pi$ and show the snakes-and-ladders structure characteristic of homoclinic snaking. Two snaking curves winding upward in dissipation while oscillating in Reynolds number represent equilibrium (EQ) and travelling wave (TW) solutions, respectively. Each of

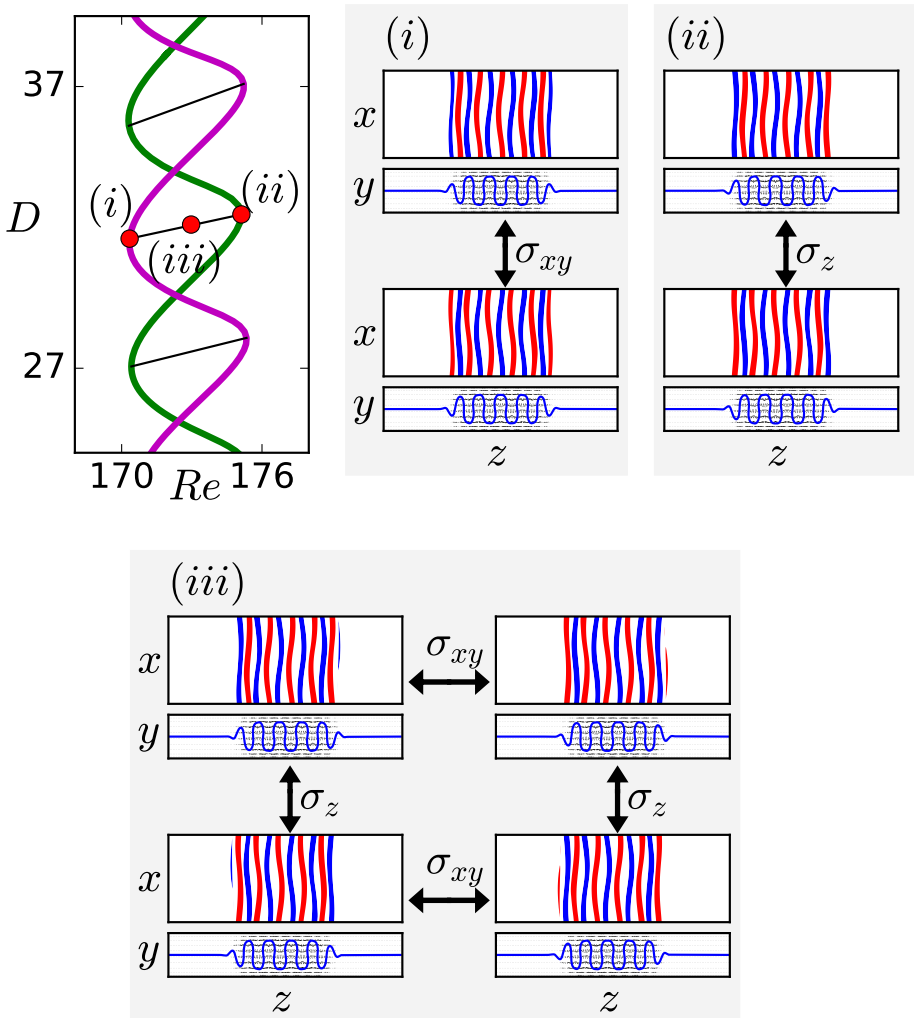

Figure 6.1 – (top left) A part of the snakes-and-ladders bifurcation structure of the localised invariant solutions in plane Couette flow in a box with a length of 4π and a width of 24π. The symmetry-related solutions are visualised at the points indicated on the bifurcation diagram: The flow fields at point (i) are two symmetry-related travelling waves; point (ii) corresponds to two symmetry-related equilibrium solutions; and point (iii) represents four symmetry-related rung states. All flow fields are visualised in terms of the midplane streamwise velocity (red/blue contours) and the streamwise averaged cross-flow velocity (vector plots). In addition, the contour line of zero average streamwise velocity is presented. The red/blue streaks indicate $\pm 0.2U_w$. The entire computational domain is shown. Note the localisation of all solutions in the spanwise direction.

the curves, both for EQs and TWs represents two symmetry-related solution branches. Pairs of equilibrium solutions and pairs of travelling waves are related by the rotational symmetry of

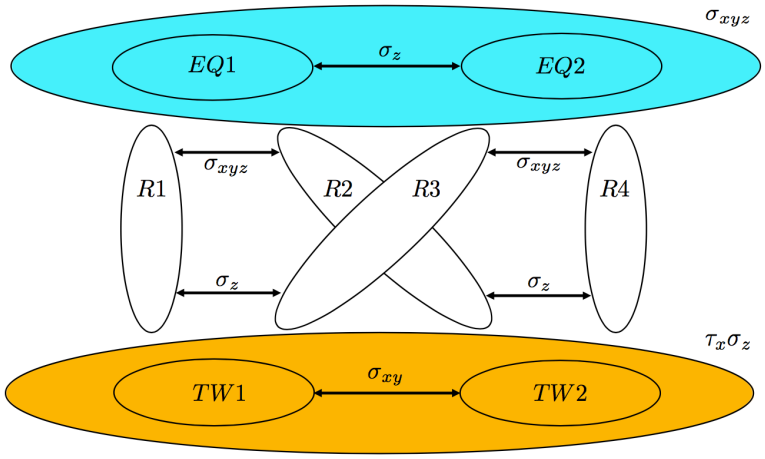

Figure 6.2 – Symmetry relations (arrows) between solution branches of plane Couette flow without suction. The pair of travelling waves $TW1/TW2$ is located within an invariant symmetry subspace (shaded orange ellipse). Likewise, the pair of equilibria $EQ1/EQ2$ shares a symmetry subspace (shaded cyan ellipse). All rungs $R1$, $R2$, $R3$ and $R4$ are non-symmetric.

PCF, $EQ1 = \sigma_{xy}EQ2$, and $TW1 = \sigma_{xy}TW2$. The operation of the discrete rotational symmetry leaves global solution measures such as the norm or the streamwise averaged energy dissipation unchanged. Consequently, both symmetry-related branches appear as a single curve in the dissipation D versus Re bifurcation diagram. In the snaking region between approximately $169 < Re < 177$ the dissipation of the snaking solutions increases. This is linked to the solution growing in the spanwise direction while undergoing sequences of saddle-node bifurcations that create additional streaks at the solution fronts. The internal structure of the solutions remains unchanged.

The equilibrium solutions are invariant under the inversion symmetry, σ_{xyz} which is the product of the rotational symmetry, σ_{xy}, and the reflection symmetry, σ_z. A non-trivial invariant solution which is invariant under inversion is phase locked and can neither travel in the streamwise nor the spanwise directions so that the solution is an equilibrium and not a travelling wave. In contrast, the travelling wave solutions are invariant under a different symmetry, the shift-reflect symmetry, $\tau_x\sigma_z$ which locks only the z phase of the solutions. As a result the travelling waves are free to travel in the streamwise direction. Since the equilibrium solutions are invariant under the inversion symmetry ($\mathbf{u} = \sigma_{xyz}\mathbf{u}$), the rotational symmetry relation between the two equilibria $EQ1 = \sigma_{xy}EQ2$ reduces to $EQ1 = \sigma_{xy}\sigma_{xyz}EQ2 = \sigma_z EQ2$. Consequently, the rotational symmetry relation between the equilibrium solutions is equivalent to a mirror z-reflection symmetry relation between them. The two symmetry-related equilibria are thus mirror images with respect to the spanwise direction. For the travelling waves, their rotational symmetry relation implies that $TW1$ and $TW2$ travel in opposite directions but at equal phase speed.

In addition to the snaking branches, there are non-symmetric localised solutions which form

rungs connecting the equilibrium branches to the travelling wave branches. Rungs are created in pitchfork bifurcations close to the saddle-node bifurcations along the snaking branches. There are four rung solution branches corresponding to each curve in the bifurcation diagram. They each connect one of the two equilibrium branches to one of the two travelling wave branches. Every pitchfork bifurcation on a specific equilibrium branch, creates two rung states which each connect this specific equilibrium branch to one of the two travelling waves. Since the rung states are non-symmetric invariant solutions which are created in symmetry-breaking pitchfork bifurcations off symmetric invariant solutions, the two simultaneously created rungs are related to each other by the symmetry of the symmetric solution branch which is broken. This is either the inversion symmetry of the equilibria $R1 = \sigma_{xyz}R2$ and $R3 = \sigma_{xyz}R4$ or the shift-reflect symmetry of the travelling waves. The shift-reflect symmetry relation between the two rung state solutions connecting to one travelling wave can be interpreted as only a z-reflection symmetry relation σ_z between the rungs $R1 = \sigma_z R3$ and $R2 = \sigma_z R4$, because the shift is absorbed in the continuous translation symmetry for a solution that is not phase locked but free to travel in the streamwise direction. Hence at any Reynolds number, the four rung state solutions have the same dissipation, and the four branches of the rung states in the bifurcation diagram are represented by a single curve. The symmetry relations between all branches of the snakes-and-ladders structure in PCF are schematically summarised in figure 6.2 together with all relevant invariant symmetry subspaces. The two equilibria are located in the inversion symmetry subspace and they are related to each other by a z-reflection symmetry. The two travelling waves are in the subspace of the shift-reflect symmetry, and are related by the rotational symmetry, σ_{xy}. The rung state solutions are non-symmetric and live outside these two symmetry subspaces.

6.4 Modified snakes-and-ladders bifurcation structure for non-vanishing suction

Wall-normal suction breaks the inversion symmetry of PCF and leads to modifications of all discussed solution branches. In the following we first discuss modifications of the bifurcation diagram due to suction. Then, we present how solutions along the solution branches are modified.

6.4.1 Effect of suction on the bifurcation diagram

Figure 6.3 shows how the snakes-and-ladders bifurcation structure is modified when wall-normal suction is applied. The two travelling wave branches undergoing snaking are symmetry-related at zero suction and thus appear as a single curve. For non-zero suction, the symmetry relating both branches is not contained in the equivariance group. Consequently, the symmetry relation vanishes and the two travelling wave branches split. The two travelling wave branches remain continuous and undergo snaking but the critical Re at which saddle-node bifurcations occur alternates. Following the terminology of Knobloch (2015), we refer to the

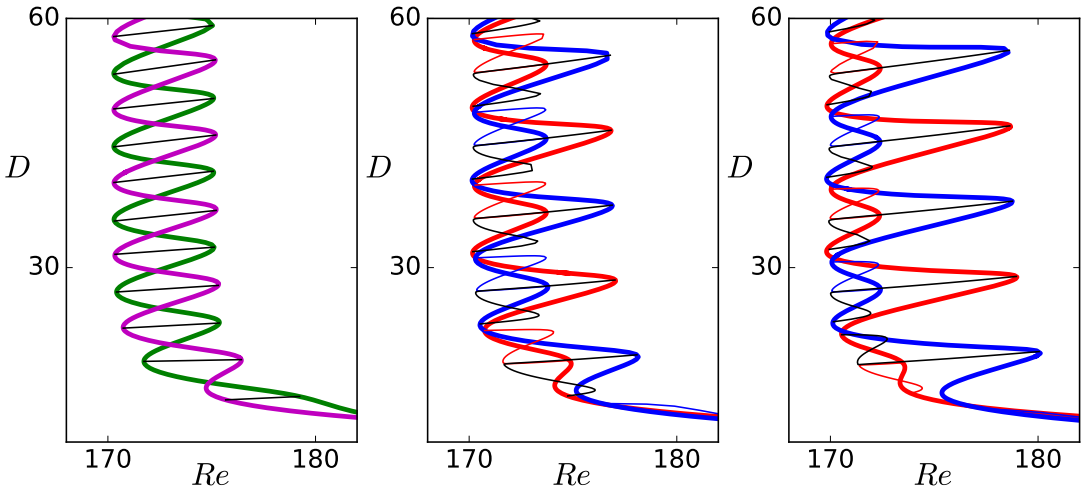

Figure 6.3 – Modification of the snaking diagram with increasing wall-normal suction. The suction velocity is increased from $V_s = 0$ (left) to $V_s = 10^{-4}$ (center) and $V_s = 2 \cdot 10^{-4}$ (right). Left panel: Travelling wave (magenta) and equilibrium (green) snaking branches are shown together with rungs (black). Centre and right panels: The travelling wave branch splits into $TW1$ (thick red) and $TW2$ (thick blue). The snaking equilibrium branch has broken into disconnected segments and together with remnants of rungs forms *returning states* RS and *connecting states* CS. Two types of RS (thin red / blue) connect to $TW1$ / $TW2$, respectively. The CS states (thin black) connect $TW1$ and $TW2$.

piece of a snaking curve between two forward saddle-node bifurcations including a backward saddle-node bifurcation as an *oscillation* in the snaking branch. In the snaking region, both travelling wave branches are composed of two alternating oscillations with different spans in Reynolds number, a narrow oscillation and a wide oscillation. Where travelling wave branch $TW1$ undergoes a narrow oscillation the other one $TW2$ undergoes a wide oscillation. For the next pair of oscillations the situation reverses with, $TW1$ undergoing a wide, and $TW2$ a narrow oscillation.

Equilibrium branches that undergo snaking in the zero-suction case are invariant under the inversion symmetry, which is broken by suction. As a result, for non-zero suction, the continuous equilibrium solution branches vanish. Instead the branch breaks into disconnected segments. The pitchfork bifurcations that – for the zero suction case – create rung states bifurcating from the equilibrium branches, are broken by the wall-normal suction. At non-zero suction the disconnected remnants of the equilibrium branches together with remnants of rung states form new branches that connect to travelling wave branches. These branches fall into two groups. Some branches emerge in a pitchfork bifurcation on one of the travelling wave branches and terminate on the same travelling wave branch in another pitchfork bifurcation. Hereafter, these branches are called *returning state, RS*. There are two RS branches which are related by a z-reflection symmetry, $RS1 = \sigma_z RS2$. All other non-symmetric branches connect $TW1$ to $TW2$. These branches are, hereafter, referred to as *connecting state, CS*. In the continuation

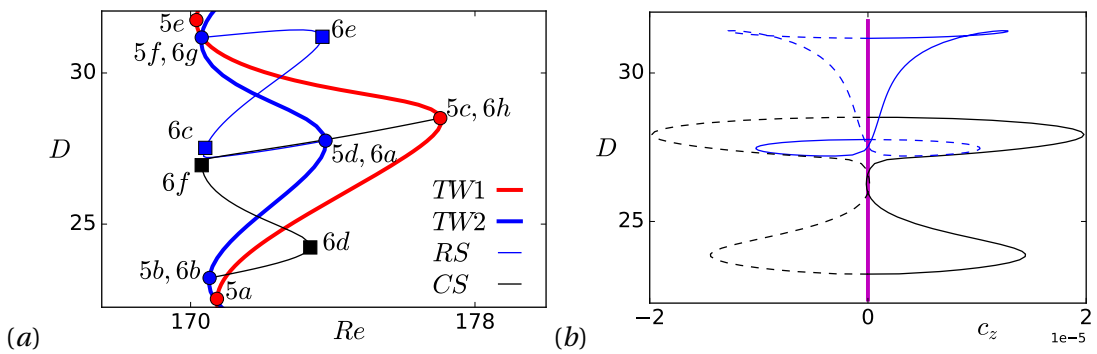

Figure 6.4 – (*a*) One oscillation of the two travelling waves. Flow fields at selected points on the travelling wave branches (indicated by circles) and on the connecting and returning state branches (indicated by squares) are visualised in figures 6.5 and 6.6. The colour coding is the same as in figure 6.3. (*b*) Variation of the spanwise wave speed illustrating the two symmetry-related *RS* (solid and dashed blue) and *CS* (solid and dashed black) branches.

diagram, each *CS* curve represents two symmetry-related branches, $CS1 = \sigma_z CS2$, which bifurcate from the travelling wave branches in pitchfork bifurcations.

The *RS* branches as well as the *CS* branches form closed bifurcation loops, as every branch has a symmetry-related counterpart starting and terminating in the same pitchfork bifurcation on *TW* branches. In figure 6.4(*a*) a part of the bifurcation diagram enlarging one oscillation of the travelling waves is shown. The loops can be directly observed in figure 6.4(*b*) where solutions are shown in terms of dissipation versus spanwise wave speed. The spanwise wave speed differentiates between both z-reflection symmetry-related branches. The spanwise wave speed of the two symmetry-related branches has the same magnitude but opposite sign. Due to their shift-reflect symmetry, the spanwise wave speed of the travelling wave branches is zero.

6.4.2 Evolution of the flow fields on the solution branches

Each saddle-node bifurcation along the snaking branches is associated with spanwise growth of the solution as evidenced by the increasing value of dissipation. The neutral eigenmode associated with each saddle-node is localised at the fronts of the localised solution where the spatially periodic internal pattern connects to unpatterned laminar flow (Schneider *et al.*, 2010*a*). When the snaking branch undergoes a saddle-node bifurcation, additional structures in form of downstream streaks together with associated pairs of counter-rotating downstream vortices is added to the solution. The solution thereby grows while its interior structure remains essentially unchanged.

Both travelling wave snaking branches *TW*1 and *TW*2 are invariant under shift-reflect symmetry. This symmetry is preserved and not broken by the saddle-node bifurcations along the branch. Consequently, the saddle-node bifurcations simultaneously add structures symmetri-

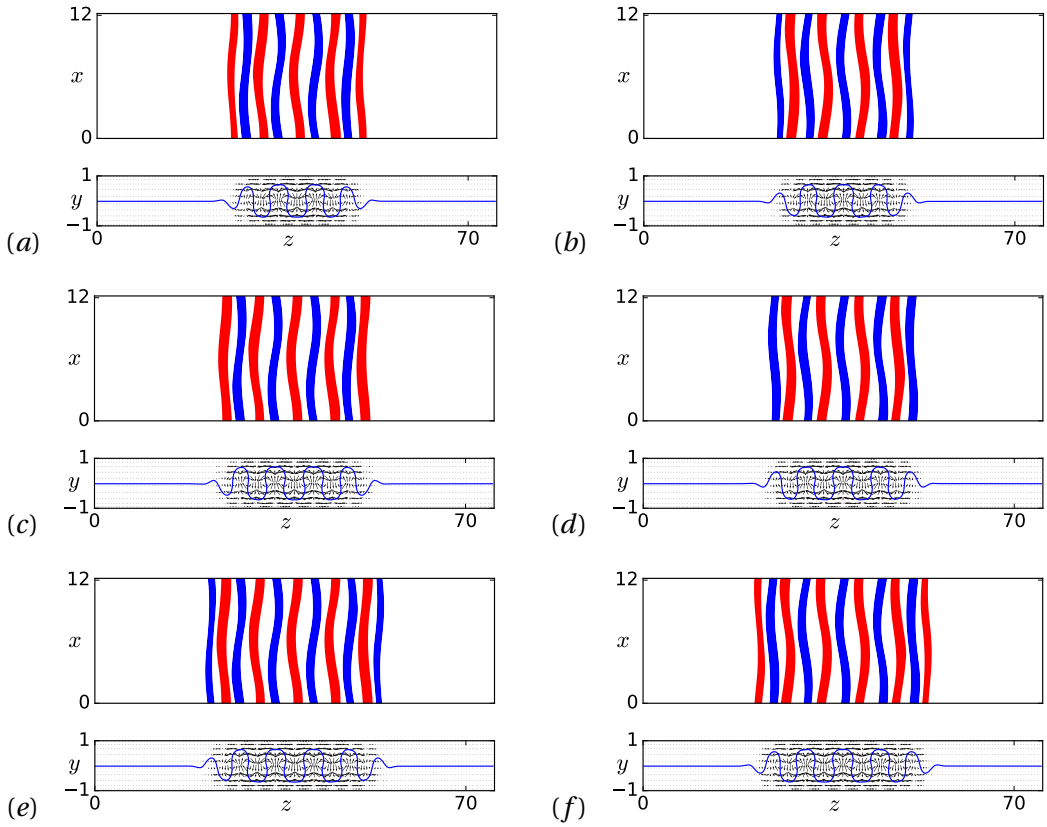

Figure 6.5 – Flow fields at points indicated in figure 6.4(a) on the travelling wave branches. In the left panels the flow fields of $TW1$, and in the right panels the flow fields of $TW2$ are shown. The visualisation of the flow fields are the same as the visualisations in figure 6.1.

cally at both fronts of the travelling wave. Figure 6.5 shows the evolution of the travelling waves in the snaking region for one oscillation. In this range, $TW1$ undergoes a wide oscillation and $TW2$ a narrow oscillation. Although the symmetry relation between $TW1$ and $TW2$ is broken for non-zero suction, for small values of the suction velocity the velocity fields visually still appear as if they were related by rotational symmetry.

Figure 6.6 visualises the flow fields of the returning state RS and the connecting state CS branches at the points indicated in figure 6.4(a). Each point along both branches corresponds to two velocity fields related by z-reflection symmetry σ_z. We only visualise one of the two symmetry-related velocity fields. Neither the RS nor the CS solutions are invariant under any discrete symmetry. Consequently, the growing and shrinking of the solution along the branch is not symmetric. To visualise changes in the velocity field along the branch, we overlay two successive solutions shown in figure 6.6. Figure 6.7 shows the zero contour line of the average streamwise velocity of two consecutive flow fields. The differences are small and located at the fronts. To further highlight the small differences and reveal growing and shrinking of the solution, contours of the amplitude difference of the average streamwise

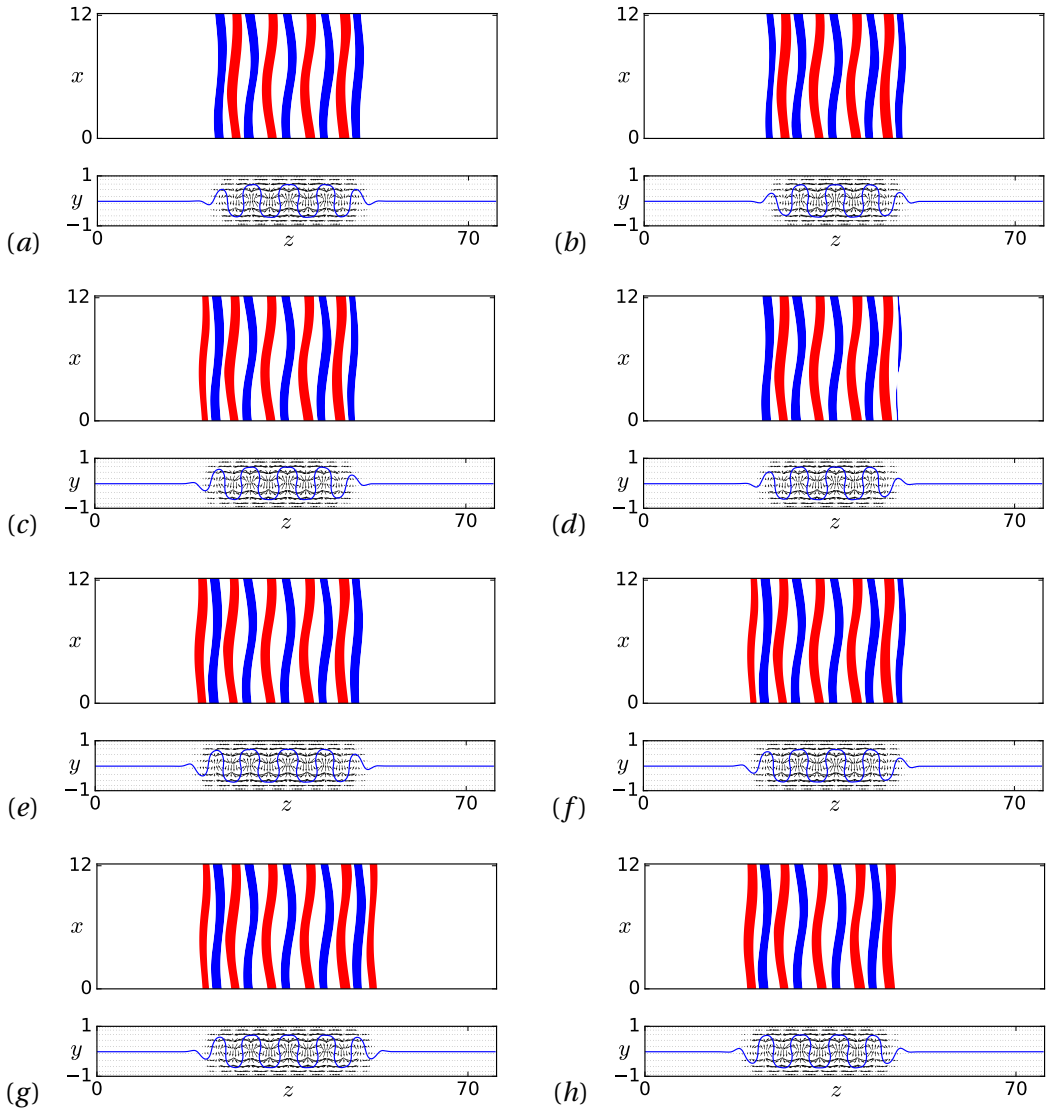

Figure 6.6 – Flow fields of the returning state branch RS (left) and the connecting state branch CS (right) at the points indicated in figure 6.4(a). The panel labels indicate the points in the continuation diagram in figure 6.4(a). The visualisation of the flow fields are the same as the visualisations in figure 6.1.

velocity $|\langle u_2\rangle_x| - |\langle u_1\rangle_x|$ are visualised.

The returning state branch RS (thin blue line in figure 6.4) bifurcates in a pitchfork bifurcation from $TW2$ at (6a). Towards (6c), while decreasing in Re, the solution increases in strength at its left front and weakens on its right. One may describe the localised solutions as a superposition of a periodic pattern with an envelope that supports the internal core structure and damps the exterior towards laminar flow. The change of the solution along (6a) → (6c) corresponds to a left-shift of the envelope (see figure 6.7 (top left panel)). From (6c) → (6e), close to the

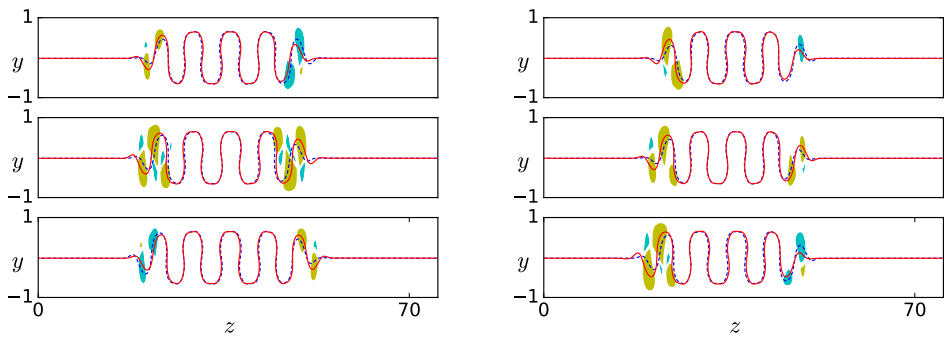

Figure 6.7 – The variations of flow field along the RS (left) and CS branch (right): Overlay of zero-contour lines of average streamwise velocity for pairs of flow fields shown in figure 6.6 as dashed blue / solid red line. (6a)/(6c) (top left), (6c)/(6e) (middle left), (6e)/(6g) (bottom left); (6b)/(6d) (top right), (6d)/(6f) (middle right), (6f)/(6h) (bottom right). Differences are visible close to the fronts. Colours indicate contours of the amplitude difference of the average streamwise velocity $|\langle u_2\rangle_x| - |\langle u_1\rangle_x|$ with yellow/cyan corresponding to $\pm 0.13 U_w$. Along the RS branch (left), the envelope of the localised solutions shifts to the left, grows symmetrically and shifts to the right. After the sequence, the contour line remains centered at a maximum. Along the CS branch the structure shifts left, grows symmetrically and shifts left again. As a result, the contour line in the center of the periodic pattern turns from a maximum into a minimum.

next saddle-node bifurcation, the flow field gets stronger at both sides (see figure 6.7 (middle left panel)). This segment of the RS branch is the remnant of an equilibrium branch at zero suction. The simultaneous and almost symmetric growth of the solution at both fronts along this segment resembles the growth of the equilibrium solution along the equilibrium branch at zero suction. Finally, from (6e) → (6g), close to the pitchfork bifurcation off $TW2$, the solution increases in strength on the right and weakens on the left front (figure 6.7 (bottom left panel)). The evolution along this part of the RS branch corresponds to a right-shift of the envelope. Along a full RS branch, the envelope of the localised solutions first shifts to the left, then grows symmetrically, and finally shifts to the right. After this sequence, both fronts have grown equally so that the RS branch acquires the symmetry of $TW2$ it bifurcated from. The symmetry related branch $RS' = \sigma_z RS$ bifurcates and reconnects to $TW2$ together with RS but the growth along the branch is inverted: A right-shift is followed by symmetric growth and a final left-shift.

The connecting state CS branch bifurcates from $TW2$ in a pitchfork bifurcation at point (6b). From (6b) → (6d) the flow fields on the CS branch strengthens on the left and weakens on the right front, which corresponds to a left-shift of the envelope (figure 6.7 (top right panel)). From (6d) → (6f) the flow fields grow almost symmetrically at both fronts (figure 6.7 (middle right panel)). This part of the CS branch is the remnant of an equilibrium branch at zero suction. Finally, from (6f) → (6h) the flow fields again strengthen on the left front and weaken at the right front, corresponding to a left-shift (figure 6.7 (bottom right panel)). At point (6h) the

CS branch connects to the $TW1$ branch in a pitchfork bifurcation. Along the CS branch the envelope first moves to the left, then grows symmetrically, and finally moves to the left again. As a result of this growth sequence involving a net shift to the left, the centrally located low speed streak (a blue streak in figure 6.6) is replaced by the neighbouring high speed streak at the left (a red streak in figure 6.6), which now sits at the center of the localised solution. A centrally located high speed streak is characteristic of $TW1$. Consequently, the CS branch starts on $TW2$ and terminates on $TW1$. The symmetry-related branch $CS' = \sigma_z CS$ bifurcates from $TW2$ and, as CS connects to $TW1$. However, along CS' the solution exhibits a net shift to the right until the solution is no longer centered at a low speed streak but on the next high-speed streak at the right. Since continuous shifts in the spanwise direction are part of the system's equivariance group, despite net shifts in opposite directions, both connecting state branches CS and CS' connect to the same $TW1$ branch.

6.5 Discussion

The presence of suction velocity V_s causes splitting of the $TW1$ and $TW2$ branches and creates new CS and RS branches from the remnants of EQ and rung branches. In this section we relate these modifications of the snakes-and-ladders bifurcation structure due to the suction to the breaking of symmetries of PCF with zero suction. Moreover, we discuss additional modifications of the bifurcation structure observed at large amplitudes of the suction velocity V_s.

6.5.1 Snaking solutions and symmetry subspaces in the presence of suction

Wall normal suction breaks the rotational symmetry of plane Couette flow. As a result, any symmetry subspace or symmetry relation originating from rotational symmetry is not present for non-zero suction velocity. Consequently, for non-zero suction, there is no inversion symmetry subspace, σ_{xyz} and states that are inversion-symmetric equilibria at zero suction travel in the streamwise and the spanwise directions. Moreover, the rotational symmetry relation between the two travelling wave branches and the inversion symmetry relation between rung states vanishes. Figure 6.8 schematically indicates the configuration of symmetry subspaces and symmetry relations of states in the presence of wall-normal suction. Since the symmetry relation between the two travelling wave branches is broken by the wall-normal suction, we expect a separation of the travelling wave branches $TW1$ and $TW2$ in the bifurcation diagram showing dissipation versus Reynolds number. Both solution branches that are equilibria at zero suction remain symmetry related, $EQ1 = \sigma_z EQ2$ which implies equal dissipation so that they remain represented by a single curve. At zero suction all four rung states are related by two different symmetry transformations. One of those two symmetries is broken by suction so that the four rungs split into two groups of two symmetry-related branches each, $R1 = \sigma_z R3$ and $R2 = \sigma_z R4$. Thus two separate curves in the bifurcation diagram represent two symmetry-related solution branches each. Rungs and equilibrium branches at zero suction transform

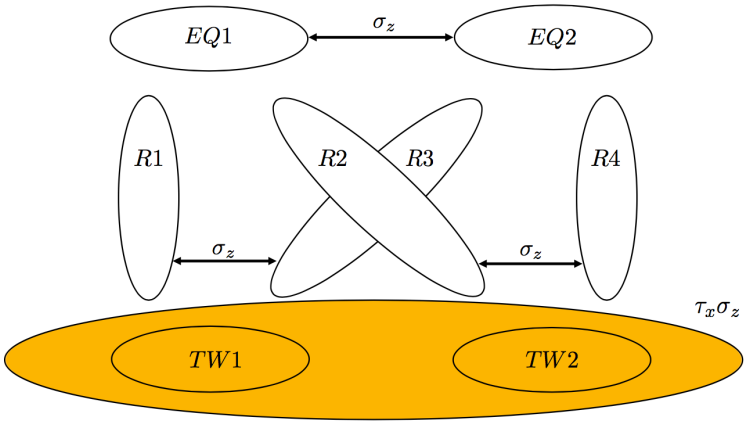

Figure 6.8 – Symmetry relations (arrows) between solution branches of plane Couette flow in the presence of non-vanishing wall-normal suction velocity. For $V_s \neq 0$, the inversion symmetry relation σ_{xyz} between $R1$ and $R2$ and between $R3$ and $R4$, the rotational symmetry relation σ_{xy} between $TW1$ and $TW2$ and the inversion symmetry subspace, all present for $V_s = 0$ (see figure 6.2) are broken.

into connecting states CS and returning states RS at non-zero suction.

6.5.2 Front growth controls bulk velocity and oscillation width

The mean pressure gradient in both spanwise and downstream direction is imposed to be zero and each solution selects its bulk velocity U_{bulk}, the $y-z$ averaged streamwise velocity. Figure 6.9 shows the variation of the bulk velocity of the snaking solutions both for PCF with zero suction and for a suction velocity of $V_s = 10^{-4}$. At zero suction, the EQ branch is invariant under σ_{xyz}, implying zero bulk velocity. The bulk velocity of the travelling wave solutions periodically varies around zero as the solution undergoes snaking. The magnitude of the U_{bulk} oscillations is independent of the spatial extent of the solution which suggests the non-zero bulk velocity is generated by the fronts, at which high- and low-speed streaks are growing symmetrically Gibson & Schneider (2016). While low-speed streaks are created, the bulk velocity becomes negative, and when high-speed streaks grow at the fronts the bulk velocity becomes positive. When suction is applied, the oscillations in bulk velocity are overlaid by an additional negative component that is linearly proportional in the dissipation. The linear dependence on dissipation and thereby size of the solution suggests that the linearly growing component of the bulk velocity is generated by an unchanging internal structure of the solution while the oscillations are due to growth at the fronts.

The front-mediated oscillations in bulk velocity relative to the linear trend are correlated with the width of snaking oscillations of the travelling wave branches. Excursions to higher bulk velocity are observed when the branch undergoes a wide oscillation, i.e. a wider range of Reynolds numbers (see figure 6.4). Likewise, narrow oscillations are observed when the

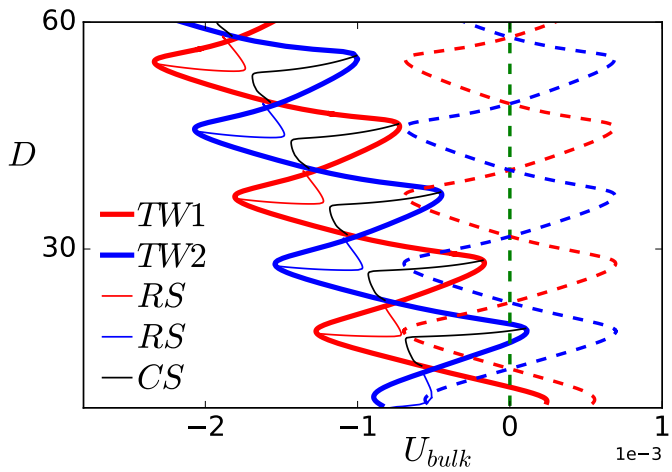

Figure 6.9 – Dissipation versus bulk velocity in snaking region of plane Couette flow at zero suction (dashed) and for suction velocity $V_s = 10^{-4}$. Solution branches are indicated in the legend. At zero suction the bulk velocity of both travelling wave branches oscillates around zero. With finite suction, an additional trend, linear in dissipation and thus size of the solution, is observed.

bulk velocity approaches local minima. Maxima of the bulk velocity are linked to high-speed streaks growing at the front while for minima in the bulk velocity, growing low-speed streaks are observed. Since $TW1$ remains related to $TW2$ by the approximate though broken rotational symmetry σ_{xy}, a growth of high-speed streaks along the $TW1$ branch implies the growth of low-speed streaks along $TW2$ and vice versa. The growth of high- and low-speed streaks of approximately symmetry-related travelling wave branches thus explains why wide and narrow oscillations of $TW1$ and $TW2$ both alternate and moreover occur such that a wide oscillation of $TW1$ coincides with a narrow one of $TW2$ and vice versa.

6.5.3 Splitting of the travelling waves

In PCF without suction, both travelling wave solution branches, $TW1$ and $TW2$, are represented by a single curve in the bifurcation diagram in terms of D versus Re. Wall-normal suction breaks the rotational symmetry of the system σ_{xy} and results in splitting of the travelling wave solution branches (see figure 6.3). A subset of the bifurcation diagram is enlarged in figure 6.10(a), where dissipation D as a function of Re is presented for $TW1$ and $TW2$. The branches are shown for three values of the wall-normal suction velocity, $V_s = 0$, $V_s = 10^{-4}$ and $V_s = 2 \cdot 10^{-4}$. For non-zero suction, branches split so that $TW1$ and $TW2$ curves are symmetrically located around the zero-suction curve, with equal distance but on opposing sides. The distance between both split curves grows linearly with the suction velocity. To rationalise this splitting behaviour we consider modifications of the solution of the governing equations at leading, namely linear, order in V_s. At zero wall-normal suction $V_s = 0$, the laminar flow solution is a linear profile $\mathbf{U}(y) = y\hat{e}_x$. Non-zero wall suction modifies the travelling wave solutions $TW1$ and $TW2$. When decomposing the velocity into a laminar flow and deviations,

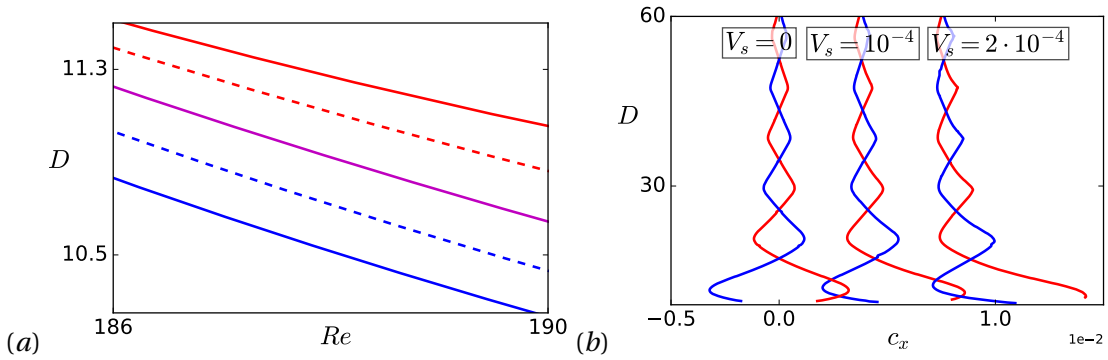

Figure 6.10 – (*a*) Bifurcation diagram of $TW1$ (red and magenta) and $TW2$ (blue and magenta) representing dissipation D as a function of Reynolds number Re for different values of the wall-normal suction velocity, $V_s = 0$ (magenta line), $V_s = 10^{-4}$ (dashed lines) and $V_s = 2 \cdot 10^{-4}$ (solid lines). For non-zero suction velocity, the branches of $TW1$ and $TW2$, which are represented by a single curve for $V_s = 0$ (magenta), split symmetrically. They are located at the same distance but on opposite sides of the curve with $V_s = 0$. (*b*) Dissipation D versus streamwise wave speed c_x of $TW1$ (red) and $TW2$ (blue) for the same values of the wall-normal suction velocity as in part (*a*). The values of the suction velocity are indicated on the curves in the figure. The wave speed of both $TW1$ and $TW2$ is shifted by equal amounts. The shift is proportional to the suction velocity V_s.

this modification affects both the laminar base flow **U** and the deviation from the modified laminar base flow **u**, as we will describe in this section.

Relation between travelling waves for inverted suction velocity

Solutions cannot only be followed from zero to positive suction velocity $V_s = +|V_s|$ but also to negative values $V_s = -|V_s|$. The latter physically implies blowing through the wall. Since the rotational symmetry σ_{xy}, relating $TW1$ to $TW2$ at $V_s = 0$ and broken by suction, transforms a flow with suction to a flow with equal amplitude blowing, the travelling wave branches for inverted suction velocity are related by

$$TW2|_{V_s} = \sigma_{xy}\, TW1|_{-V_s}\,. \tag{6.1}$$

The modification of the laminar solution

At linear order in V_s the laminar solution reads

$$\mathbf{U} = \left(y + \frac{ReV_s}{2}\left(1 - y^2\right)\right)\hat{e}_x - V_s\hat{e}_y.$$

Consequently, the modification of the laminar solution with respect to the laminar solution of PCF for zero suction velocity $\mathbf{U}' = \mathbf{U} - \mathbf{U}_{V_s=0}$ is

$$\mathbf{U}' = V_s \left[\frac{Re}{2} \left(1 - y^2\right) \hat{e}_x - \hat{e}_y \right] = V_s \bar{\mathbf{U}}(y, Re), \tag{6.2}$$

where $\bar{\mathbf{U}}$ is a function of Reynolds number and the wall-normal coordinate y only. $\bar{\mathbf{U}}$ is independent of the suction velocity so that the laminar flow modification $\mathbf{U}'$ is linearly proportional to the suction velocity V_s.

The modification of the deviation from the laminar solution

The travelling wave solutions $TW1$ and $TW2$ are equilibria in a moving frame of reference that translates at their specific wave speeds c_x in the $\hat{e}_x$ direction with respect to the lab frame. The travelling wave solutions thus satisfy the condition

$$(\mathbf{u}_t - c_x \hat{e}_x) \cdot \nabla \mathbf{u}_t = -\nabla p + \frac{1}{Re} \nabla^2 \mathbf{u}_t$$

where c_x is the wave speed associated with the total flow field $\mathbf{u}_t = \mathbf{U}(y) + \mathbf{u}(x, y, z)$. The solution of this equation $(\mathbf{u}_t, p, c_x)$ may be decomposed into three parts: the solution for zero suction, a modification of the laminar solution due to suction, and the modification of the deviation from the laminar solution:

$$\begin{cases} \mathbf{u}_t = \mathbf{u}_0 + \mathbf{U}' + \mathbf{u}' \\ p = p_0 + p' \\ c_x = c_{x0} + c_x', \end{cases} \tag{6.3}$$

where $(\mathbf{u}_0, p_0, c_{x0})$ denotes the total solution for zero suction, $\mathbf{U}'$ is the modification of the laminar solution, and $(\mathbf{u}', p', c_x')$ is the modification of the deviation from the laminar solution. For small suction velocity, quadratic interactions among $\mathbf{U}'$, $\mathbf{u}'$ and $c_x' \hat{e}_x$ resulting from the inertial term are neglected. At leading order, the condition for a travelling wave solution at small suction thus reads

$$\begin{aligned} &\mathbf{u}_0 \cdot \nabla \mathbf{U}' + \mathbf{u}_0 \cdot \nabla \mathbf{u}' + \mathbf{U}' \cdot \nabla \mathbf{u}_0 + \mathbf{u}' \cdot \nabla \mathbf{u}_0 - c_{x0} \cdot \nabla \mathbf{U}' - c_{x0} \cdot \nabla \mathbf{u}' - c_x' \cdot \nabla \mathbf{u}_0 \\ &\quad = -\nabla p' + \frac{1}{Re} \nabla^2 \mathbf{U}' + \frac{1}{Re} \nabla^2 \mathbf{u}'. \end{aligned}$$

Rearranging using the base flow modifications at linear order in V_s (equation 6.2), yields

$$\begin{aligned} &V_s \left[\mathbf{u}_0 \cdot \nabla \bar{\mathbf{U}} + \bar{\mathbf{U}} \cdot \nabla \mathbf{u}_0 - c_{x0} \cdot \nabla \bar{\mathbf{U}} - \frac{1}{Re} \nabla^2 \bar{\mathbf{U}} \right] \\ &\quad = -\nabla p' + \frac{1}{Re} \nabla^2 \mathbf{u}' - \mathbf{u}_0 \cdot \nabla \mathbf{u}' - \mathbf{u}' \cdot \nabla \mathbf{u}_0 + c_{x0} \cdot \nabla \mathbf{u}' + c_x' \cdot \nabla \mathbf{u}_0, \end{aligned} \tag{6.4}$$

where the suction velocity has been isolated. Only the primed variables depend on V_s so that the entire left-hand side is proportional to V_s. The equation determines $(\mathbf{u}', p', c_x')$ as a function of V_s. Since the operators acting on the primed variables are linear (right-hand side), the solution $(\mathbf{u}', p', c_x')$ is linearly proportional to the suction velocity V_s.

Dissipation of $TW1$ with wall-normal suction velocity V_s can be expressed as

$$D = D|_{V_s=0} + \frac{1}{2L_x}\int_{-L_z/2}^{L_z/2}\int_{-L_x/2}^{L_x/2}\left(\frac{\partial \mathbf{u}'}{\partial y}\Big|_{y=-1} + \frac{\partial \mathbf{u}'}{\partial y}\Big|_{y=1}\right) dxdz$$

where $D|_{V_s=0}$ is the dissipation of both $TW1$ and $TW2$ at zero suction velocity. According to relation (6.1), the dissipation of $TW2$ with suction velocity V_s is equal to the dissipation of $TW1$ for inverted suction velocity $(-V_s)$. As a result, the dissipation of $TW2$ follows from the same expression when the suction velocity in equation (6.4) is inverted $(V_s \to -V_s)$. Equation (6.4) implies $\mathbf{u}'(-V_s) = -\mathbf{u}'(V_s)$. Consequently, the dissipation of $TW2$ with wall-normal suction velocity V_s is given by

$$D = D|_{V_s=0} - \frac{1}{2L_x}\int_{-L_z/2}^{L_z/2}\int_{-L_x/2}^{L_x/2}\left(\frac{\partial \mathbf{u}'}{\partial y}\Big|_{y=-1} + \frac{\partial \mathbf{u}'}{\partial y}\Big|_{y=1}\right) dxdz\,.$$

Suction thus changes the dissipation of travelling wave solutions $TW1$ and $TW2$ relative to the zero suction case by amounts that are equal in magnitude but opposite in sign.

Equation (6.4) implies that the entire solution $(\mathbf{u}', p', c_x')$ is linear in V_s so that also modifications of the wave speed c_x' are proportional to the suction velocity. Equation (6.1) implies that the modification of the wave speed of $TW2$ with wall-normal suction velocity V_s is equal to *minus* the modification of the wave speed of $TW1$ for inverted suction velocity $(-V_s)$. Together with the linear dependence of wave speed modifications c_x' on V_s, this implies that the modifications of the wave speed are equal for both $TW1$ and $TW2$. Figure 6.10(b) presents the bifurcation diagram of $TW1$ and $TW2$, in terms of dissipation D versus wave speed c_x, for different values of the wall-normal suction velocity, $V_s = 0$, $V_s = 10^{-4}$ and $V_s = 2 \cdot 10^{-4}$. This data confirms that small values of the wall-normal suction velocity V_s change the wave speeds of both $TW1$ and $TW2$ by the same amount. The amount is linearly proportional to the suction velocity.

6.5.4 Alternating bifurcations of CS and RS off travelling wave branches

Both travelling wave branches, $TW1$ and $TW2$ undergo alternating wide and narrow oscillations in the dissipation versus Reynolds number bifurcation diagram. Along a wide oscillation a pair of high-speed streaks is added at the fronts of the solution, while along a narrow oscillation a pair of low speed streaks is added. After an entire period consisting of a successive wide and narrow oscillation, the fronts connecting the internal periodic pattern of the travelling waves to laminar flow recover their original structure and the solution has grown by two additional pairs of high- and low-speed streaks. The solution thus only grows at the fronts

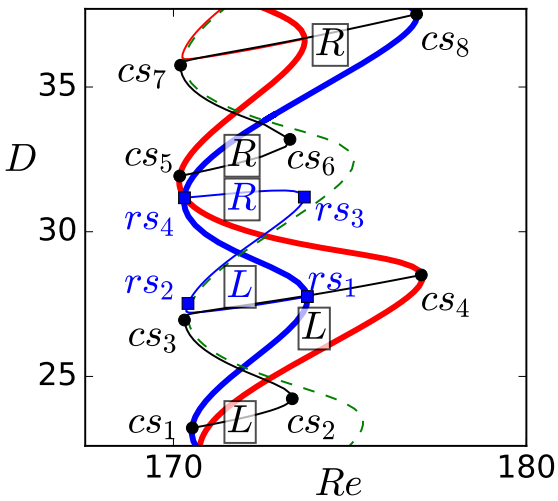

Figure 6.11 – Bifurcation diagram representing D versus Re showing both the $TW1$ (thick red) and $TW2$ (thick blue) branches, together with two successive CS branches (thin black) and an RS branch (thin blue) for $V_s = 10^{-4}$. For reference, also the curve representing $EQ1$ and $EQ2$ for $V_s = 0$ is shown (dashed green line). Along the CS and RS branches that inherit segments from $EQ1$ for $V_s = 0$, the direction of the shifts of the envelope of the localised solutions are indicated in the figure. The symmetry-related counterparts of these CS and RS solution branches, that contain remnants from $EQ2 = \sigma_z EQ1$ for $V_s = 0$, shift in opposite directions.

while its internal structure remains unchanged. As a result of this front-driven growth process, the critical Reynolds numbers of corresponding saddle-node bifurcations along successive wide or narrow oscillations line up. The spatial growth of the solution indicated by increasing values of dissipation D continues periodically.

The growth of the travelling wave branches is driven by saddle-node bifurcations with neutral modes that are localised at the solution fronts (Schneider *et al.*, 2010*a*). Likewise, the pitchfork bifurcations close to the saddle-nodes that create the RS and CS have neutral modes acting only at the fronts. As a result, the entire bifurcation structure, including the bifurcating RS and CS branches, repeats periodically after a pair of oscillations. Moreover, the front structure of $TW1$ reflects that of the $TW2$ branch shifted by half a period. Since all bifurcations are driven at the fronts, the equivalent front structure of both travelling wave branches implies that all branches bifurcating off $TW1$ have corresponding branches bifurcating off $TW2$. Consequently, the entire bifurcation structure of $TW1$ including bifurcations off the branch corresponds to that of the $TW2$ branch shifted by half a period.

As discussed in section 6.4.2, CS and RS branches are characterised by the sequence of directions in which the envelope of the localised solutions is shifted as one marches along the branch. Starting from the pitchfork bifurcations off a travelling wave at lower D where the branches emerge towards the pitchfork at higher D where the branches terminate on a travelling wave, both CS and RS encounter two envelope shifts. The connecting state CS

branch is characterised by two shifts to the same directions either to the right ($+\hat{e}_z$) or to the left ($-\hat{e}_z$). Two shifts in opposing directions (left after right or vice versa) characterise the returning state RS branch. Figure 6.11 enlarges a part of the bifurcation diagram showing both $TW1$ and $TW2$ branches, two successive CS branches and one RS branch connected to $TW2$. Note that each CS or RS curve in the bifurcation diagram represents a pair of z-reflection-related branches of CS or RS. In the figure, we indicate the shifts of the envelope for those CS and RS branches that inherit segments from $EQ1$ for $V_s = 0$ (from $cs_2 \rightarrow cs_3$, from $rs_2 \rightarrow rs_3$ and from $cs_6 \rightarrow cs_7$). The symmetry-related counterparts of these CS and RS branches contain remnants from $EQ2$. Due to the symmetry relation, any shift of the branch shown in the figure corresponds to a shift in the opposite direction for the (not shown) symmetry-related branch. If one CS branch twice shifts to the left (from $cs_1 \rightarrow cs_4$), the CS for the next higher dissipation (from $cs_5 \rightarrow cs_8$) twice shifts in the opposite, here right, direction.

For $V_s = 0$, the two rung state branches that bifurcate off an equilibrium branch in a pitchfork bifurcation are related by σ_{xyz}. For non-zero but small values of V_s, the remnants of these two rung state branches form segments of the CS and RS branches (in the figure, $cs_3 \rightarrow cs_4$ / $rs_1 \rightarrow rs_2$ and $rs_3 \rightarrow rs_4$ / $cs_5 \rightarrow cs_6$). The solutions on these remnants of the rung state branches remain visually almost symmetry-related at small V_s. As a result of the approximate inversion symmetry, along these two segments of the CS and RS branches, the directions of the shifts of the envelope has to be identical. Consequently, the shifts along segments of the RS branches are slaved to the shifts of the CS branches along the corresponding segments by the broken inversion symmetry relation of the rung states. The non-symmetric solution branch between two CS branches in the bifurcation diagram must thus be characterised by shifts in two opposing directions and is therefore an RS branch. Symmetry thus implies that CS and RS branches alternate in the bifurcation diagram.

6.5.5 Snaking breakdown

The effect of suction on plane Couette snaking solutions was studied for small suction velocities up to $V_s = 2 \cdot 10^{-4}$. At larger suction velocities, the bifurcation structure fundamentally changes. Figure 6.12(a) shows the bifurcation diagram of $TW1$, $TW2$, and CS branches for $V_s = 6 \cdot 10^{-4}$. The range in Re for which RS branches exist shrinks with increasing V_s (see figure 6.3) and at $V_s = 6 \cdot 10^{-4}$, RS branches are not computed. At $V_s = 6 \cdot 10^{-4}$, the snaking travelling wave solution branches, $TW1$ and $TW2$, have broken into multiple disconnected travelling wave branches that reach high Reynolds numbers far beyond the snaking range at $V_s = 0$. The two symmetry-related CS branches no longer connect $TW1$ and $TW2$. Instead each CS branch emerging in pitchfork bifurcations off each disconnected travelling wave branch now extends to high Reynolds numbers but no longer appears to terminate in a second pitchfork bifurcation.

Parametric continuation down in V_s starting from all branches identified at $V_s = 6 \cdot 10^{-4}$ including those reaching high Reynolds numbers yields previously unknown localised solution

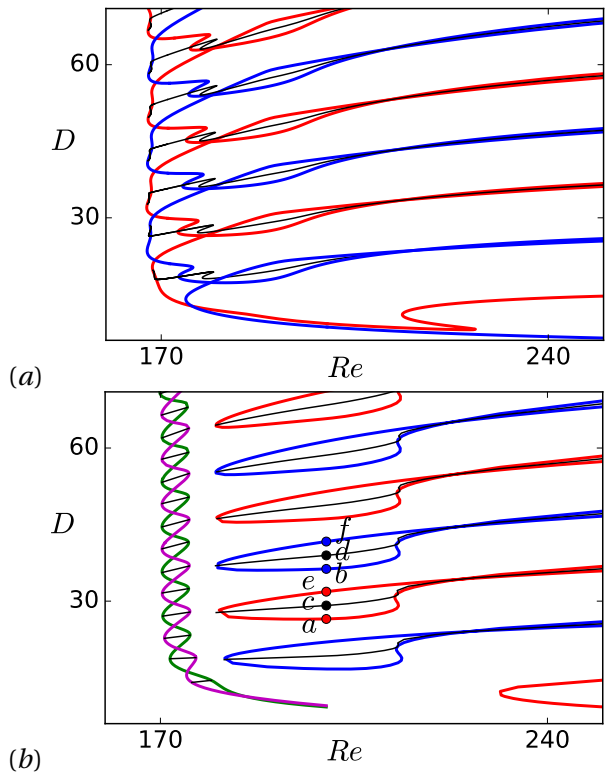

Figure 6.12 – Bifurcation diagram representing D versus Re for (a) $TW1$ (red), $TW2$ (blue) and CS (black) at $V_s = 6 \cdot 10^{-4}$; and (b) $TW1$- (red), $TW2$- (blue) and CS-connected (black) branches at $V_s = 0$. At $V_s = 0$, the bifurcation diagram of the snaking equilibrium branches (green), travelling waves (magenta) and rung states (black) are shown. The flow fields at the indicated points are visualised in figure 6.13. At $V_s = 6 \cdot 10^{-4}$, the snaking branches of $TW1$ and $TW2$ are broken, and $TW1$, $TW2$ and CS branches are merged with solution branches that for $V_s = 0$ are separated from the snakes-and-ladders bifurcation structure and extend to high Reynolds numbers.

branches of PCF without suction. Figure 6.12(b) shows the bifurcation diagram with the characteristic snakes-and-ladders structure together with these newly-found localised solution branches for $V_s = 0$. The non-snaking localised solutions include branches that for $V_s = 6 \cdot 10^{-4}$ are merged with the $TW1$ branch (hereafter referred to as $TW1$-connected), the $TW2$ branch (hereafter referred to as $TW2$-connected), and the CS branches (hereafter referred to as CS-connected). The solutions of $TW1$- and $TW2$-connected branches are invariant under the action of the shift-reflect symmetry, $\tau_x \sigma_z$. The solutions of the CS-connected branches are not invariant under any discrete symmetry of the system. Instead there are pairs of CS-connected solution branches related by σ_z. Each pair bifurcates from either a $TW1$- or $TW2$-connected branch in a pitchfork bifurcation. Snaking solutions in PCF at $V_s = 0$ only exist in a small Reynolds number range of approximately $169 < Re < 177$. The localised non-snaking solution branches, $TW1$-, $TW2$- and CS-connected, span a much wider range in Reynolds number (see figure 6.12(b)).

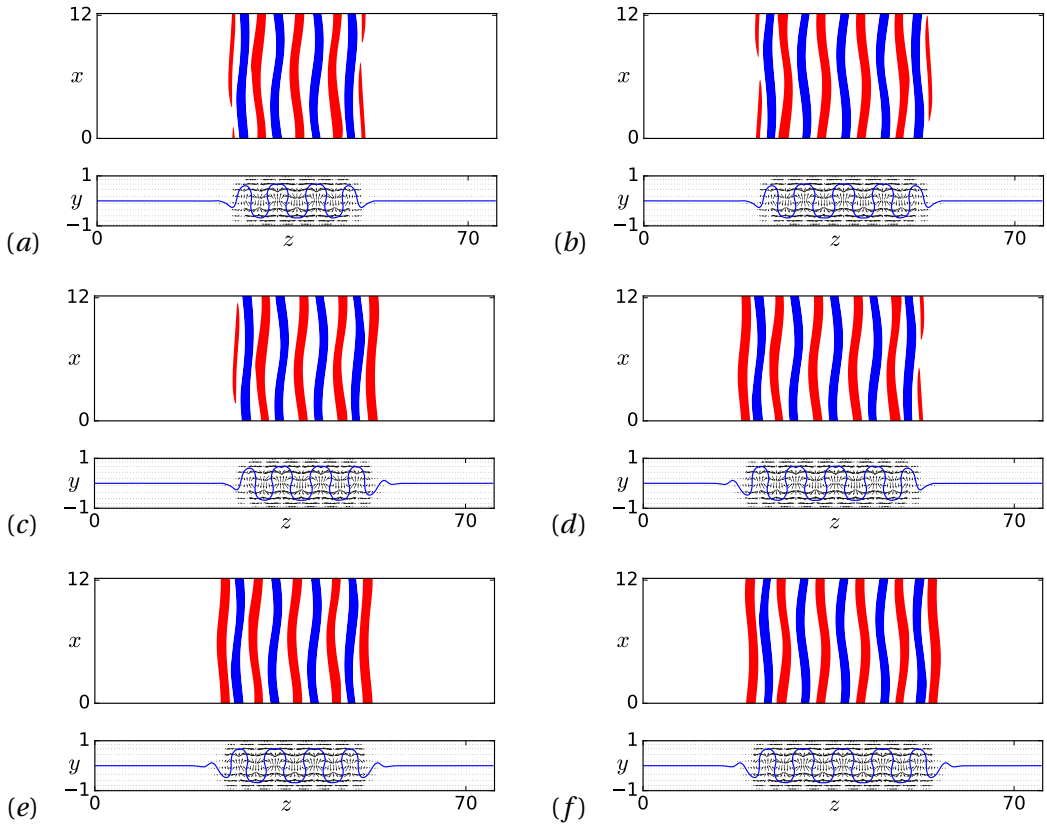

Figure 6.13 – Flow fields of plane Couette ($V_s = 0$) solutions at points indicated in figure 6.12(b). The flow fields in the left panels are located on the $TW1$-connected branch (panels a and e) and on the CS-connected branch that bifurcates from the $TW1$-connected branch (panel c). The right panels visualise the flow fields that are located on the $TW2$-connected branch (panels b and f) and on the CS-connected branch that bifurcates from the $TW2$-connected branch (panel d). The flow fields are visualised as in figure 6.1.

Figure 6.13 visualises the flow fields of $TW1$-, $TW2$- and two successive CS-connected branches at the points indicated in figure 6.12(b). The internal periodic part and the front structures of the lower branch $TW1$- and $TW2$-connected solutions (panels a and b); the upper branch $TW1$- and $TW2$-connected solutions (panels e and f); and the two successive CS-connected solutions (panels c and d, and their symmetry-related counterparts) appear identical. The solutions mainly differ in the number of high- and low-speed streaks. From lower to upper branches of both $TW1$- and $TW2$-connected two high-speed streaks grow at the solution fronts. The $TW1$-connected solution is centered at a high-speed streak while in the center of the $TW2$-connected solution a low-speed streak is located. Application of the rotational symmetry σ_{xy} to $TW1$-, $TW2$- and CS-connected solutions creates symmetry-related invariant solutions. However, the branches of these solutions do not merge with the snakes-and-ladders bifurcation structures in the presence of wall-normal suction.

6.6 Conclusion

We have investigated the structural stability of the snakes-and-ladders bifurcation structures of invariant solutions of the three-dimensional Navier-Stokes equations in plane Couette flow. Salewski, Gibson & Schneider (2019) show that adding a Coriolis force in PCF ($V_s = 0$) that maintains the equivariance group, preserves the snakes-and-ladders bifurcation structure. Here, we show that applying a non-vanishing suction velocity that breaks the rotational symmetry of PCF modifies the snakes-and-ladders bifurcation structure. For non-zero but small suction velocity, the curve representing the branches of both travelling waves $TW1$ and $TW2 = \sigma_{xy}TW1$ (at $V_s = 0$) in a bifurcation diagram showing dissipation D as a function of Re splits in two different snaking curves with alternating span of the oscillations in Reynolds number. The two equilibrium branches $EQ1$ and $EQ2 = \sigma_z EQ1$ (at $V_s = 0$) break up. The pitchfork bifurcations of the equilibrium branches that create rungs at $V_s = 0$ are broken. The results are new solution branches formed from remnants of both the broken equilibrium branches and the rungs. The returning state branches RS connect one of the travelling wave branches to itself while the connecting state branches CS connect $TW1$ and $TW2$. Specific features of the bifurcation diagram including the symmetric splitting of the $TW1$ and $TW2$ branches and the ordering of RS and CS follow from symmetry arguments.

At small but non-vanishing suction velocity, the modifications of the snakes-and-ladders bifurcation structure of three-dimensional solutions of Navier-Stokes equations in plane Couette flow are analogous to modifications of the snakes-and-ladders bifurcation structure observed within the one-dimensional Swift-Hohenberg equation with the cubic-quintic nonlinearity (SHE35), when a quadratic term is added. Introducing a quadratic term ϵu^2 with amplitude ϵ in the SHE35 breaks the odd symmetry of this system, $R_2 : x \to -x,\ u \to -u$ (Houghton & Knobloch, 2011). Breaking R_2 in the SHE35 modifies the snakes-and-ladders bifurcation structure in the following way. For non-vanishing ϵ both solution branches that are invariant under the action of the even symmetry, $R_1 : x \to -x,\ u \to u$ split into two distinct curves with alternating span of the oscillations in r in an amplitude versus control parameter r bifurcation diagram. This is analogous to the splitting of the $TW1$ and $TW2$ in the Navier-Stokes problem. As the EQ branches in Navier-Stokes, the continuous snaking branches of solutions that are invariant under R_2 at $\epsilon = 0$ break up into disconnected segments for non-zero ϵ. Together with remnants of rung states at $\epsilon = 0$ the remnants of these solutions form disconnected s- and z-shaped branches that connect to the split snaking solution branches that are invariant under R_1. The s- and the z-shaped solution branches in the modified snakes-and-ladders bifurcation structure of the one-dimensional SHE35 with the symmetry-breaking quadratic term thus behave analogously to the CS and RS solution branches in the modified snakes-and-ladders bifurcation structure of Navier-Stokes equations in PCF in the presence of non-vanishing but small wall-normal suction velocity. When the amplitude of the quadratic term ϵ is increased towards large values, the snakes-and-ladders bifurcation structure in the SHE35 eventually transforms into a modified bifurcation structure that resembles the snakes-and-ladders structure of the Swift-Hohenberg with the quadratic-cubic nonlinearity. This is not observed in the

Navier-Stokes problem, where large suction causes the modified snakes-and-ladders bifurcation structure to disintegrate into disconnected branches of localised solutions. In conclusion, at small amplitudes, wall-normal suction in plane Couette flow and the symmetry-breaking quadratic term in the SHE35 yield analogous effects on the snakes-and-ladders bifurcation structure. At larger amplitudes, however, the effect of wall-normal suction in plane Couette flow and the symmetry-breaking term in SHE35 affect the bifurcation structure in significantly different ways.

Following the solution branches generated by suction back to regular plane Couette flow with $V_s = 0$, additional disconnected branches of spatially localised invariant solutions of PCF are identified. Disconnected branches of solutions with varying width but matching front structure exists. The solutions thus share similarities with the snaking solutions but do not undergo homoclinic snaking themselves. While the snaking solutions only exist in a limited range of Reynolds number, the non-snaking solution branches span a much larger range of Reynolds numbers extending to those Reynolds numbers in which localised turbulent patterns are observed (Barkley & Tuckerman, 2005). Consequently, the non-snaking localised invariant solutions identified here might be more relevant for supporting localised transitional turbulence than the previously known snaking branches. The dynamical relevance of the non-snaking localised solutions should be investigated in the future.

7 Adjoint-based variational method for constructing periodic orbits

Remark: This chapter is largely inspired by a pre-print titled "Adjoint-based variational method for constructing periodic orbits of high-dimensional chaotic systems"

Sajjad Azimi[1], Omid Ashtari[1] and Tobias M. Schneider[1]

[1]Emergent Complexity in Physical Systems Laboratory (ECPS),
École Polytechnique Fédérale de Lausanne, CH-1015 Lausanne, Switzerland

Submitted to *SIAM Journal on Scientific Computing*

Contents

Chapter summary

Chaotic dynamics in systems ranging from low-dimensional nonlinear differential equations to high-dimensional spatio-temporal systems including fluid turbulence is supported by non-chaotic, exactly recurring time-periodic solutions of the governing equations. These unstable periodic orbits capture key features of the turbulent dynamics and sufficiently large sets of orbits promise a framework to predict the statistics of the chaotic flow. Computing periodic orbits for high-dimensional spatio-temporally chaotic systems remains challenging as known methods either show poor convergence properties because they are based on time-marching of a chaotic system causing exponential error amplification; or they require constructing Jacobian matrices which is prohibitively expensive. We propose a new matrix-free method that is unaffected by exponential error amplification, is globally convergent and can be applied to high-dimensional systems. The adjoint-based variational method constructs an initial value problem in the space of closed loops such that periodic orbits are attracting fixed points for the loop-dynamics. We introduce the method for general autonomous systems. An implementation for the one-dimensional Kuramoto-Sivashinsky equation demonstrates the robust convergence of periodic orbits underlying spatio-temporal chaos. Convergence does not require accurate initial guesses and is independent of the period of the orbit.

7.1 Introduction

Ideas from low-dimensional chaotic dynamical systems have recently led to new insights into high-dimensional spatio-temporally chaotic systems including fluid turbulence. The idea for a dynamical description of turbulence has a long history (Thomas, 1942; Lin, 1944; Hopf, 1948) and stems from the observation that turbulent flows often show recognisable transient coherent patterns that recur over time and space (Jiménez, 2018). Only in the last 15 years, however, has concrete progress allowed dynamical systems to be truly established as a new paradigm to study turbulence (Kerswell, 2005; Eckhardt *et al.*, 2007; Kawahara *et al.*, 2012). This progress is based on the discovery of unstable non-chaotic steady and time-periodic solutions of the fully nonlinear Navier-Stokes equations which leads to a description of turbulence as a walk through a connected forest of these dynamically connected invariant ('exact') solutions in the infinite-dimensional state space of the flow equations (Gibson *et al.*, 2008; Cvitanović & Gibson, 2010; Suri *et al.*, 2017; Reetz *et al.*, 2019).

Of special importance are time-periodic exactly recurring flows. These so-called unstable periodic orbits capture the evolving dynamics of the flow (Kawahara & Kida, 2001) and form the elementary building blocks of the chaotic dynamics. Periodic orbits have been recognised as being key for understanding chaos since the 1880s (Poincaré, 1892; Ruelle, 1978; Gutzwiller, 1990). Provided results from low-dimensional hyperbolic dissipative systems carry over to high-dimensional spatio-temporally chaotic systems, periodic orbits lie dense in the chaotic set supporting turbulence. The turbulent trajectory thus almost always shadows a periodic orbit. As a consequence, periodic orbit theory allows to express ergodic ensemble averages

of the turbulent flow as weighted sums over periodic orbits. In these 'cycle expansions', the statistical weight of an individual orbit is controlled by its stability features (Auerbach, Cvitanović, Eckmann, Gunaratne & Procaccia, 1987; Cvitanović, 1988; Artuso, Aurell & Cvitanović, 1990*a*,*b*; Lan, 2010; Cvitanović *et al.*, 2016). Sufficiently complete sets of periodic orbits for three-dimensional fluid flows may thus eventually allow to quantitatively describe statistical properties of turbulence in terms of exact invariant solutions of the underlying flow equations (Chandler & Kerswell, 2013). Even if a full description of turbulence in terms of periodic orbits remains beyond our reach, individual periodic orbits are of significant importance as they capture key physical processes underlying the turbulent dynamics and may inform control strategies (Lasagna, 2018). Consequently, robust tools for computing periodic orbits of high-dimensional spatio-temporally chaotic systems including three-dimensional fluid flows are needed.

High-dimensional spatio-temporal systems, including spectrally discretised three-dimensional fluid flow problems, are often characterised by more than $N = 10^6$ highly coupled degrees of freedom. Computing periodic orbits of such high-dimensional strongly coupled systems remains computationally challenging. The commonly used shooting method considers an initial value problem yielding trajectories satisfying the evolution equations and varies the initial condition until the solution closes on itself. To find the initial condition u_0 and the period T, the nonlinear equation $g(u_0, T) = f^T(u_0) - u_0 = 0$ is solved numerically. In this equation, f^T is the evolution of the state u_0 over time T. To solve this system of nonlinear coupled equations, Newton iteration can be used. A standard Newton method would require constructing the full Jacobian matrix with $\mathcal{O}(N^2)$ elements. This is practically impossible for high-dimensional strongly coupled systems with large N. Alternatively, the solution can be obtained by minimising $||g(u_0, T)||$ (Kazantsev, 1998). However, also this method requires constructing the full Jacobian matrix, and can only be applied to low-dimensional systems. Key for computing periodic orbits of high-dimensional systems are thus *matrix-free* Newton iteration methods that do not construct the Jacobian matrix but only require successive evaluations of the function g, implying time-stepping of the evolution equations. Commonly used algorithms are Krylov subspace methods (Kelley, 2003; Sanchez, Net, Garcıia-Archilla & Simo, 2004) including the Newton-GMRES-hook-step method by Viswanath (Viswanath, 2007, 2009; Cvitanović & Gibson, 2010) as well as slight variations with alternative trust-region optimisations (Dennis & Schnabel, 1996; Duguet, Pringle & Kerswell, 2008).

The matrix-free Newton approach is well suited for computing fixed points, where the 'period' T can be chosen arbitrarily, but the Newton approach poses fundamental challenges for periodic orbits. The defining property of a chaotic system is an exponential-in-time separation of trajectories which leads to a sensitive dependence on initial conditions. Very small changes in the initial condition u_0 are thus exponentially amplified by the required time-integration. Finding zeros of g thus becomes an ill-conditioned problem. Consequently, an extremely good initial guess is required for the Newton method to converge. Generating sufficiently accurate initial guesses is very challenging and often impossible. Owing to the finite numerical precision of double-precision arithmetic long and unstable orbits are even entirely

impossible to converge. Examples demonstrating the difficulty in finding periodic orbits of high-dimensional systems using shooting methods include the seminal work by Chandler and Kerswell (Chandler & Kerswell, 2013), who computed approximately 100 orbits for a two-dimensional model flow and describe the time-consuming and tedious manual work to find initial guesses and trying to converge them. Likewise van Veen et al. (van Veen, Vela-Martin & Kawahara, 2018) recently computed a single periodic orbit for box turbulence with only moderate resolution of 64^3 grid points. The authors reach a moderately small residual of $1.8 \cdot 10^{-4}$ and thus many orders of magnitude larger than machine precision only after "several months of computing on modern GPU cards, due to the poor conditioning of the linear problems associated with Newton's method". Consequently, more robust methods with larger radii of convergence than those of shooting methods are needed to compute periodic orbits of high-dimensional spatio-temporally chaotic systems.

For low-dimensional systems more robust methods for finding periodic orbits have been devised. Instead of starting from trajectories satisfying the evolution equations and varying the initial condition until the solution closes on itself, the variational approach suggested by Lan and Cvitanović (Lan & Cvitanović, 2004) reverses the approach: It starts from a closed loop in state space that does not satisfy the evolution equations and then adapts the loop until it solves the equations and a periodic orbit is found. To adapt the closed loop, the problem is recast as a minimization problem in the space of all closed loops. The loop is driven towards a periodic orbit by minimising a cost function that measures the deviation of the loop from an integral curve of the vector field induced by the governing equations. No time-marching along the orbit is required and the loop is adapted locally. Consequently, the variational method does not suffer from exponential error amplification and has a large radius of convergence. The robustness of the method has been demonstrated in the one-dimensional Kuramoto-Sivashinsky system (Lan & Cvitanović, 2008) for which Lasagna (Lasagna, 2018) recently found more than 20 000 periodic orbits using $N = 64$ Fourier modes to discretise the problem.

Unfortunately, the robust variational method of Lan and Cvitanović cannot be scaled to high-dimensional problems such as fluid turbulence. The method is not matrix-free but requires the explicit construction of Jacobian matrices and their inversion. Moreover, accurate computations of tangents to the loop by finite differences require the loop to be represented by a sufficiently large number of closely-spaced instantaneous fields. The size of the Jacobian matrix to be inverted scales with the number of instantaneous fields M and the spatial degrees of freedom N as $\mathcal{O}(M^2 N^2)$. This scaling reflects the prohibitively large memory requirements for high-dimensional systems. The only attempt to apply the method to a higher-dimensional system we are aware of is Fazendairo et al. (Fazendeiro, Boghosian, Coveney & Lätt, 2010; Boghosian, Brown, Lätt, Tang, Fazendeiro & Coveney, 2011) who study forced box-turbulence in a triple-periodic box using Lattice-Boltzmann computations. They provide evidence for the convergence of two periodic orbits but reaching a modestly small residual of $\mathcal{O}(10^{-5})$ on a relatively small 64^3 spatial lattice requires tens of thousands of CPU cores. As stated by Fazendeiro et. al., even finding the shortest orbits of 3D flows using the method by Lan and Cvitanović requires petascale computing resources. Despite its robustness, the variational

method by Lan and Cvitanović is thus too computationally expensive to be realistically used for high-dimensional spatio-temporally chaotic systems.

Here we propose a novel matrix-free method that provides the same favourable convergence properties of the variational method by Lan and Cvitanović (Lan & Cvitanović, 2004, 2008) but can be applied to high-dimensional systems. The method combines a variational approach similar to Lan and Cvitanović with an adjoint-based minimization technique inspired by recent work of Farazmand (Farazmand, 2016) on computing steady state solutions. Combining the variational approach with adjoints allows us to construct an initial value problem in the space of closed loops such that unstable periodic orbits become attracting fixed points of the dynamics in loop-space. Converging to a periodic orbit thus only requires evolving an initial guess under the dynamics in loop-space. We develop the matrix-free adjoint-based variational method for general autonomous dynamical systems. As a proof-of-concept, the introduced method is applied to the one-dimensional Kuramoto-Sivashinsky equation (KSE) (Kuramoto & Tsuzuki, 1976; Sivashinsky, 1977). The KSE is a model system showing spatio-temporal chaos that has commonly been used as a sandbox model to develop algorithms that are eventually applied to three-dimensional fluid flows. We demonstrate the robust convergence of multiple periodic orbits of varying complexity and periods. The implementation utilises a spectral Fourier discretization in the temporal direction to significantly reduce the prohibitively large memory requirements of the method by Lan and Cvitanović.

The structure of the chapter is as follows: First, the proposed method for computing periodic orbits is introduced for a general autonomous system. 7.2 describes the setup of the variational problem and 7.3 discusses the adjoint-based minimization technique. In 7.4, we apply the adjoint-based variational method to the KSE and demonstrate the convergence of periodic orbits in this spatio-temporally chaotic system. 7.5 summarises the chapter and discusses future applications to three-dimensional fluid turbulence.

7.2 Variational method for finding periodic orbits

We consider a general dynamical system for an n-dimensional real field $\vec{u}$ defined over a spatial domain $\Omega \subset \mathbb{R}^d$ and varying in time t,

$$\begin{aligned} &\vec{u} : \Omega \times \mathbb{R} \to \mathbb{R}^n, \\ &(\vec{x}, t) \mapsto \vec{u}(\vec{x}, t). \end{aligned}$$

The evolution of the field $\vec{u}$ is first-order in time and governed by an autonomous partial differential equation (PDE) of the form

$$\frac{\partial \vec{u}}{\partial t} = \mathcal{N}(\vec{u}). \tag{7.1}$$

The nonlinear differential operator $\mathcal{N}$ enforces boundary conditions at $\partial\Omega$, the boundaries of the spatial domain Ω. A periodic orbit is a temporally periodic solution of the governing equation,

$$f^T(\vec{u}) - \vec{u} = \vec{0}, \tag{7.2}$$

where $f^T = \int_t^{t+T} \mathcal{N}\, dt'$ indicates the nonlinear evolution over the period T.

The shooting method considers solutions of the initial value problem and varies the initial condition $\vec{u}_0(\vec{x})$ until the solution closes on itself and becomes periodic. (7.2) is thus treated as an algebraic equation for the initial condition and the period. An alternative approach is to consider already time-periodic fields and vary those until they satisfy the governing equations. Instead of identifying an initial condition as in a shooting method, we consider the entire orbit as a solution of a boundary value problem in the $(d+1)$-dimensional space-time domain. To ensure periodicity of the solution in time, the boundary conditions in space are augmented by periodic boundary conditions in time. The field $\vec{u}(\vec{x}, t)$ is thus defined on $\Omega \times [0, T)_{\text{periodic}}$.

The length of the domain in time T is unknown and needs to be determined as part of the solution. To convert the problem to a boundary value problem on a fixed domain, we rescale time $t \mapsto s := t/T$, where s denotes the normalised time coordinate. The rescaled field

$$\vec{\tilde{u}}(\vec{x}, s) := \vec{u}(\vec{x}, s \cdot T),$$

is defined on a fixed domain

$$\begin{aligned} &\vec{\tilde{u}} : \Omega \times [0, 1)_{\text{periodic}} \to \mathbb{R}^n, \\ &(\vec{x}, s) \mapsto \vec{\tilde{u}}(\vec{x}, s). \end{aligned}$$

A periodic orbit is characterised by the space-time field $\vec{\tilde{u}}(\vec{x}, s)$ and the period T satisfying

$$-\frac{1}{T}\frac{\partial \vec{\tilde{u}}}{\partial s} + \mathcal{N}(\vec{\tilde{u}}) = 0. \tag{7.3}$$

Boundary conditions in space remain unchanged with respect to the dynamical system (7.1) and are complemented by periodic boundary conditions in the temporal direction s. To simplify the notation, the overhead tilde is omitted in the remainder of the chapter.

A periodic orbit is defined by the combination of a field $\vec{u}(\vec{x}, s)$ and a period T that together satisfy the boundary value problem (7.3). Geometrically the periodic orbit is a closed trajectory in state space. To characterise general closed curves in state space, we define a *loop* $\mathbf{l}(\vec{x}, s)$ as a tuple of a field $\vec{u}(\vec{x}, s)$ and a period T. A loop does not necessarily satisfy the PDE of the boundary value problem (7.3) but shares all boundary conditions in space and time with

periodic orbits. We denote the space of all loops by

$$\mathscr{P} = \left\{ \mathbf{l}(\vec{x}, s) = \begin{bmatrix} \vec{u}(\vec{x}, s) \\ T \end{bmatrix} \middle| \begin{array}{c} \vec{u} : \Omega \times [0,1)_{\text{periodic}} \to \mathbb{R}^n,\ T \in \mathbb{R}^+ \\ \vec{u} \text{ satisfies BC at } \partial\Omega \text{ and is periodic in } s \end{array} \right\}. \tag{7.4}$$

Periodic orbits are specific elements of the loop-space $\mathscr{P}$ that satisfy the PDE (7.3). A general loop only satisfies the boundary conditions but not the PDE.

The idea of the variational method is to consider an initial loop $\mathbf{l}_0(\vec{x}, s) \in \mathscr{P}$ and to evolve the loop until it satisfies the boundary value problem (7.3). The loop thereby converges to a periodic orbit. To evolve a loop towards a periodic orbit we minimise the cost function J measuring the deviation of a loop from a solution of the boundary value problem,

$$\begin{aligned} &J : \mathscr{P} \to \mathbb{R}^+, \\ &\mathbf{l} \mapsto J(\mathbf{l}) := \int_0^1 \int_\Omega \vec{r} \cdot \vec{r}\, d\vec{x}\, ds. \end{aligned} \tag{7.5}$$

where $\vec{r}$ is the residual of (7.3):

$$\vec{r} = -\frac{1}{T}\frac{\partial \vec{u}}{\partial s} + \mathscr{N}(\vec{u}). \tag{7.6}$$

The cost function J penalises a nonzero residual $\vec{r}$. For a periodic orbit J is zero; otherwise it takes positive values. Thus, absolute minima of J correspond to periodic orbits. The problem of finding periodic orbits has thereby been converted into an optimization over loop-space $\mathscr{P}$.

Geometrically, minimising the cost function corresponds to deforming a closed curve, a loop, in the system's state space, the space spanned by all instantaneous fields $\vec{u}(\vec{x})$ satisfying the boundary conditions, until the loop becomes an integral curve of the vector field $\mathscr{N}(\vec{u})$ induced by the dynamical system. The loop thereby becomes a solution of the PDE and represents a periodic orbit. This is schematically shown in figure 7.1. At each point $\vec{u}$ along the loop, the vector field defines the flow direction $\mathscr{N}(\vec{u})$ while $\partial\vec{u}/\partial t = T^{-1}\partial\vec{u}/\partial s$ is the tangent vector along the loop (see panel *a*). The cost function J measures the misalignment between the vector field and the loop's tangent vectors integrated along the entire loop. Consequently, minimising J towards its absolute minimum $J = 0$ deforms the loop until the tangent vectors everywhere match the flow and the loop becomes an integral curve of the vector field, as exemplified in panel *b*. The loop is locally deformed to align with the vector field and no time-marching causing exponential instabilities is required.

7.3 Adjoint-based method for minimising the cost function J

We recast the problem of finding periodic orbits as a minimization problem in the space of all loops. Absolute minima of the cost function J with value $J = 0$ correspond to periodic orbits. To minimise J without constructing Jacobians we develop an adjoint-based approach inspired

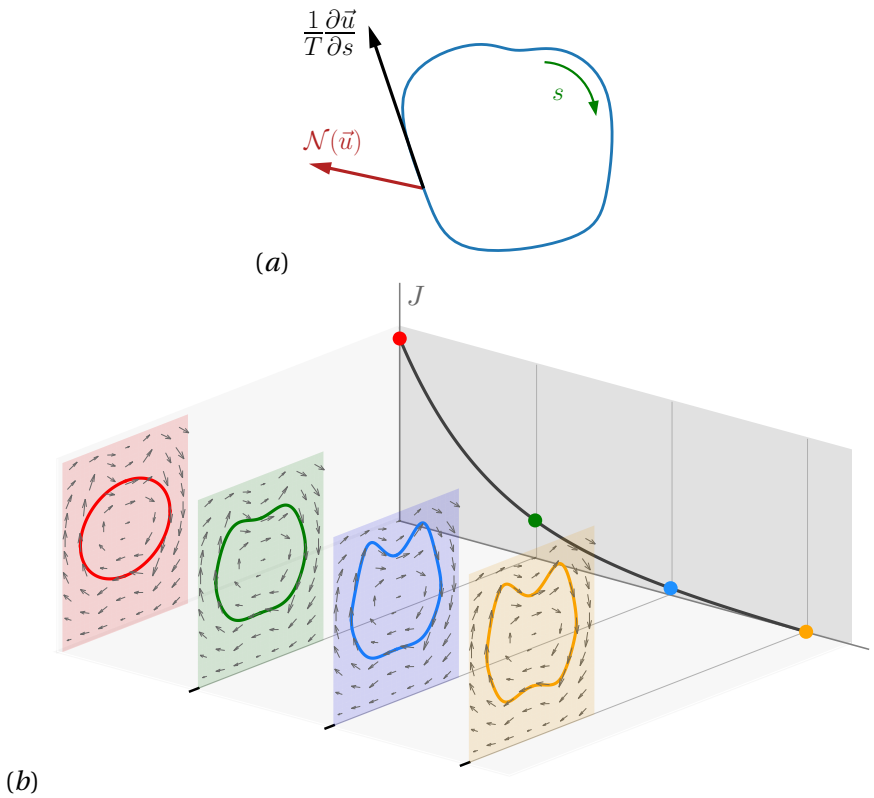

Figure 7.1 – Schematic of the variational method for finding periodic orbits. (a) An arbitrary closed loop (blue line) parametrised by $s \in [0,1)$ does not satisfy the governing equations as its loop tangent $\partial\vec{u}/\partial t = T^{-1}\partial\vec{u}/\partial s$ is misaligned relative to the vector field $\mathcal{N}(\vec{u})$ induced by the dynamical system. (b) Minimising a cost function J measuring the misalignment between the vector field and the loop tangent deforms the loop. When the global minimum of the cost function with $J = 0$ is reached the tangent vectors everywhere match the flow, $\partial\vec{u}/\partial t = \mathcal{N}(\vec{u})$. The loop becomes an integral curve of the vector field and a periodic orbit is identified.

by the recently introduced method by Farazmand (Farazmand, 2016) who computes equilibria of a two-dimensional flow. We construct an initial value problem in loop-space $\mathscr{P}$ whose dynamics monotonically decreases the cost function J until a minimum of J is reached.

To derive an appropriate variational dynamics in loop-space, we define the space of generalised loops:

$$\mathscr{P}_g = \left\{ \mathbf{q}(\vec{x}, s) = \begin{bmatrix} \vec{q}_1(\vec{x}, s) \\ q_2 \end{bmatrix} \middle| \begin{array}{c} \vec{q}_1 : \Omega \times [0,1)_{\text{periodic}} \to \mathbb{R}^n,\ q_2 \in \mathbb{R} \\ \vec{q}_1 \text{ is periodic in } s \end{array} \right\}. \tag{7.7}$$

Elements $\mathbf{q} \in \mathscr{P}_g$ do not necessarily satisfy the spatial boundary condition of periodic orbits at $\partial\Omega$ and are thus termed generalised loops. Obviously, the space of loops $\mathscr{P}$ is a subset of the space of generalised loops $\mathscr{P} \subset \mathscr{P}_g$. For a loop, the components of the generalised loop have specific meaning, $\vec{q}_1 = \vec{u}$ and $q_2 = T$. Throughout this chapter, generalised loops are denoted

by boldface letters. The space of generalised loops $\mathscr{P}_g$ carries a real-valued inner product

$$\begin{aligned} &\langle\, ,\, \rangle : \mathscr{P}_g \times \mathscr{P}_g \to \mathbb{R}, \\ &\langle \mathbf{q}, \mathbf{q}' \rangle = \langle \begin{bmatrix} \vec{q}_1 \\ q_2 \end{bmatrix}, \begin{bmatrix} \vec{q}_1' \\ q_2' \end{bmatrix} \rangle = \int_0^1 \int_\Omega \vec{q}_1 \cdot \vec{q}_1' \, d\vec{x} ds + q_2 q_2', \end{aligned} \tag{7.8}$$

and an L_2-norm

$$||\mathbf{q}|| = \sqrt{\langle \mathbf{q}, \mathbf{q} \rangle} = \sqrt{\int_0^1 \int_\Omega \vec{q}_1 \cdot \vec{q}_1 \, d\vec{x} ds + q_2^2}. \tag{7.9}$$

The objective is to construct a dynamical system in the space of loops $\mathscr{P}$ such that along its solutions the cost function J monotonically decreases and periodic orbits become attracting fixed points of the dynamical system. We parametrise the evolution of loops in $\mathscr{P}$ by a fictitious time τ: $\mathbf{l}(\tau) = [\vec{u}(\vec{x}, s; \tau); T(\tau)]$ and define an evolution equation,

$$\frac{\partial \mathbf{l}}{\partial \tau} = \mathbf{G}(\mathbf{l}) \tag{7.10}$$

with operator $\mathbf{G}$ chosen such that

$$\frac{\partial J}{\partial \tau} \leq 0 \quad \forall\, \tau. \tag{7.11}$$

The rate of change of J along solutions of (7.10) is (see 7.6.1 for details)

$$\frac{\partial J}{\partial \tau} = 2 \langle \mathscr{L}(\mathbf{l}; \mathbf{G}), \mathbf{R} \rangle . \tag{7.12}$$

where $\mathbf{R} \in \mathscr{P}_g$ is a generalised loop

$$\mathbf{R}(\mathbf{l}) = \begin{bmatrix} \vec{r} \\ 0 \end{bmatrix}, \tag{7.13}$$

with $\vec{r}(\mathbf{l})$ the residual field (7.6). $\mathscr{L}(\mathbf{l}; \mathbf{G})$ is the directional derivative of the residual $\mathbf{R}$ in the direction $\mathbf{G}$, evaluated for the current loop $\mathbf{l}$:

$$\mathscr{L}(\mathbf{l}; \mathbf{G}) = \lim_{\epsilon \to 0} \frac{\mathbf{R}(\mathbf{l} + \epsilon \mathbf{G}) - \mathbf{R}(\mathbf{l})}{\epsilon}. \tag{7.14}$$

Using the adjoint of the directional derivative, we express (7.12) as

$$\frac{\partial J}{\partial \tau} = 2 \langle \mathbf{G}, \mathscr{L}^\dagger(\mathbf{l}; \mathbf{R}) \rangle \tag{7.15}$$

where $\mathscr{L}^\dagger$ is the adjoint operator of $\mathscr{L}$ with

$$\langle \mathscr{L}(\mathbf{q};\mathbf{q}'),\mathbf{q}''\rangle = \langle \mathbf{q}',\mathscr{L}^\dagger(\mathbf{q};\mathbf{q}'')\rangle\,, \tag{7.16}$$

for all generalised loops $\mathbf{q}$, $\mathbf{q}'$ and $\mathbf{q}''$. This form allows us to enforce the monotonic decrease of the cost function J by explicitly choosing the operator $\mathbf{G}$:

$$\mathbf{G} = -\mathscr{L}^\dagger(\mathbf{l};\mathbf{R}). \tag{7.17}$$

With this choice for $\mathbf{G}$, the cost function evolves as

$$\frac{\partial J}{\partial \tau} = 2\,\langle -\mathscr{L}^\dagger(\mathbf{l};\mathbf{R}),\mathscr{L}^\dagger(\mathbf{l};\mathbf{R})\rangle = -2\left|\left|\mathscr{L}^\dagger(\mathbf{l};\mathbf{R})\right|\right|^2 \leq 0. \tag{7.18}$$

Thus, along solutions of $\partial\mathbf{l}/\partial\tau = \mathbf{G}(\mathbf{l}) = -\mathscr{L}^\dagger(\mathbf{l};\mathbf{R})$ the cost function J is guaranteed to monotonically decrease.

To find a periodic orbit using the adjoint approach, an initial loop is advanced under the dynamical system in loop-space, until a minimum of the cost function, corresponding to an attracting fixed point with $\partial_\tau\mathbf{l} = \mathbf{0}$, is reached. If an absolute minimum, $J = 0$, is reached, the loop satisfies the boundary value problem (7.3) and represents a periodic orbit. The cost function J is invariant under a reparametrisation $s \mapsto s' = (s+\sigma) \bmod 1$ corresponding to a phase shift by σ in the temporal periodic direction. Consequently, the phase of the minimising loop is not chosen by the adjoint-based variational method but depends on the initial condition.

7.4 Application to Kuramoto-Sivashinsky equation

We demonstrate the adjoint-based variational method for the one-dimensional Kuramoto-Sivashinsky equation (KSE) (Kuramoto & Tsuzuki, 1976; Sivashinsky, 1977). This nonlinear partial differential equation for a one-dimensional field $u(x,t)$ on a 1D periodic interval $x \in [0,L) = \Omega$ reads

$$\frac{\partial u}{\partial t} = -u\frac{\partial u}{\partial x} - \frac{\partial^2 u}{\partial x^2} - \nu\frac{\partial^4 u}{\partial x^4}\,; \qquad x \in [0,L)_{\text{periodic}},\ t \in \mathbb{R} \tag{7.19}$$

with a constant 'superviscosity' $\nu > 0$. The KSE has the general form of (7.1) with $n = d = 1$. We denote the scalar spatial coordinate by x. Rescaling the field u by the inverse of L indicates that the only control parameter is $\mathbb{L} = L/\sqrt{\nu}$ the ratio of the domain length and the square-root of the constant ν. Consequently, fixing the domain length L and varying ν is equivalent to fixing ν and treating L as a control parameter. Both scalings are used in literature. Here, we fix $\nu = 1$ and consider L as the control parameter. The equivariance group of the KSE contains continuous shifts in x and the discrete center symmetry,

$$x \to -x\,; \quad u \to -u. \tag{7.20}$$

We discuss periodic orbits both in the full unconstrained space and in the subspace of fields invariant under the discrete center symmetry.

The trivial solution of the KSE, $u = \text{const}$, is linearly unstable for $L/\sqrt{\nu} > 2\pi$ (Cvitanović, Davidchack & Siminos, 2010). A series of bifurcations leads to increasingly complex dynamics when L is increased. We consider the parameter value $L = 39$ where the KSE shows spatio-temporally chaotic dynamics reminiscent of turbulence (Smyrlis & Papageorgiou, 1996).

7.4.1 Formulation of the adjoint-based method for the KSE

For the 1D-KSE a loop consists of a one-dimensional field $u(x,s)$ defined over $[0,L) \times [0,1)$ and the period T. The residual of the boundary value problem for a periodic orbit (7.6), expressed as generalised loop $\mathbf{R}$ (see (7.13)), is

$$\mathbf{R}(\mathbf{l}) = \begin{bmatrix} r(\mathbf{l}) \\ 0 \end{bmatrix} = \begin{bmatrix} -\frac{1}{T}\frac{\partial u}{\partial s} - u\frac{\partial u}{\partial x} - \frac{\partial^2 u}{\partial x^2} - \frac{\partial^4 u}{\partial x^4} \\ 0 \end{bmatrix}, \tag{7.21}$$

where vector notation has been suppressed because the dimension of the field is $n = 1$.

The dynamical system in loop-space for which the cost function monotonically decreases and periodic orbits become attracting fixed points is based on the adjoint operator of the directional derivative of $\mathbf{R}$. Partial integration directly yields the adjoint operator for the KSE problem (see 7.6.2),

$$\mathscr{L}^{\dagger}(\mathbf{l};\mathbf{R}) = \begin{bmatrix} \frac{1}{T}\frac{\partial r}{\partial s} + u\frac{\partial r}{\partial x} - \frac{\partial^2 r}{\partial x^2} - \frac{\partial^4 r}{\partial x^4} \\ \int_0^1 \int_0^L \frac{1}{T^2}\frac{\partial u}{\partial s} r\,dx\,ds \end{bmatrix}. \tag{7.22}$$

Consequently, the dynamical system in loop-space $\partial\mathbf{l}/\partial\tau = -\mathscr{L}^{\dagger}(\mathbf{l};\mathbf{R})$ (see (7.17)) minimising the cost function J is

$$\frac{\partial \mathbf{l}}{\partial \tau} = \begin{bmatrix} \frac{\partial u}{\partial \tau} \\ \frac{\partial T}{\partial \tau} \end{bmatrix} = \begin{bmatrix} -\frac{1}{T}\frac{\partial r}{\partial s} - u\frac{\partial r}{\partial x} + \frac{\partial^2 r}{\partial x^2} + \frac{\partial^4 r}{\partial x^4} \\ -\int_0^1 \int_0^L \frac{1}{T^2}\frac{\partial u}{\partial s} r\,dx\,ds \end{bmatrix}. \tag{7.23}$$

The first component of (7.23) prescribes the deformation of the field $u(x,s)$, while the second component updates the period T.

The dynamical system in loop-space formulated for the KSE, (7.23), is equivariant with respect

to the discrete symmetry:

$$\Xi : (x, s) \to (-x, s) ; \quad \begin{bmatrix} u \\ T \end{bmatrix} \to \begin{bmatrix} -u \\ T \end{bmatrix}. \tag{7.24}$$

If an initial loop is invariant under the action of Ξ, the evolution in τ will preserve the symmetry. Since the transformation of the instantaneous field $x \to -x; u(\cdot, s) \to -u(\cdot, s)$ for all $s \in [0, 1)$ corresponds to the center-symmetry (7.20) of the KSE equation, the dynamical system in loop-space also preserves the center symmetry of the KSE. An initial loop with field component within the center-symmetric subspace of KSE is invariant under Ξ, which is preserved under τ-evolution. Consequently, the adjoint-based variational method preserves the discrete center-symmetry of the KSE.

7.4.2 Numerical implementation

Expressing the field component of the dynamical system (7.23) in terms of u using (7.21) yields,

$$\frac{\partial u}{\partial \tau} = G_{1,\mathrm{L}} + G_{1,\mathrm{NL}}, \tag{7.25}$$

where the linear and nonlinear terms have the form,

$$\begin{aligned} G_{1,\mathrm{L}} &= \frac{1}{T^2}\frac{\partial^2 u}{\partial s^2} - \frac{\partial^8 u}{\partial x^8} - 2\frac{\partial^6 u}{\partial x^6} - \frac{\partial^4 u}{\partial x^4} \\ G_{1,\mathrm{NL}} &= -5\frac{\partial^4 u}{\partial x^4}\frac{\partial u}{\partial x} - 10\frac{\partial^3 u}{\partial x^3}\frac{\partial^2 u}{\partial x^2} - 3\frac{\partial^2 u}{\partial x^2}\frac{\partial u}{\partial x} + u^2\frac{\partial^2 u}{\partial x^2} + u\left(\frac{\partial u}{\partial x}\right)^2 + \frac{2u}{T}\frac{\partial^2 u}{\partial x \partial s} + \frac{1}{T}\frac{\partial u}{\partial x}\frac{\partial u}{\partial s}. \end{aligned}$$

The field $u(x, s)$ is defined on a doubly-periodic space-time domain. We thus numerically solve the evolution equation with a pseudospectral method (Canuto, Hussaini, Quarteroni & Zang, 2006) using a Fourier discretization in both space and time. The spectral representation with M modes in space and N modes along the temporal direction is,

$$u(x_m, s_n) = \sum_{j=-\frac{M}{2}}^{\frac{M}{2}-1} \sum_{k=-\frac{N}{2}}^{\frac{N}{2}-1} \hat{u}_{j,k} \exp\left\{2\pi i \left(\frac{mj}{M} + \frac{nk}{N}\right)\right\}. \tag{7.26}$$

In physical space, the field is represented by grid values at the Gauss-Lobatto collocation points $\{u(x_m, s_n)\}$ with $(x_m, s_n) = (mL/M, n/N)$ and index ranges $0 \le m \le M-1$ and $0 \le n \le N-1$. In spectral space, the set of discrete Fourier coefficients $\{\hat{u}_{j,k}\}$ with $-M/2 \le j \le M/2-1$ and $-N/2 \le k \le N/2-1$ represents the field. In spectral space, the evolution equation (7.25) for each Fourier coefficient of the field takes the form

$$\frac{\partial \hat{u}_{j,k}}{\partial \tau} = \left[-\left(\frac{2\pi k}{T}\right)^2 - \left(\frac{2\pi j}{L}\right)^8 + 2\left(\frac{2\pi j}{L}\right)^6 - \left(\frac{2\pi j}{L}\right)^4\right] \hat{u}_{j,k} + (\hat{G}_{1,\mathrm{NL}})_{j,k}, \tag{7.27}$$

where the discrete Fourier transform is indicated by a hat. To evaluate the nonlinear term $\hat{G}_{1,\mathrm{NL}}$ derivatives are calculated in spectral space and transformed to physical space, where products are pointwise operations. Transforming the result back to spectral space yields the required terms. In both the spatial and temporal direction dealiasing following the 2/3 rule (Canuto *et al.*, 2006) is applied. To advance the evolution equation (7.25) in the fictitious time τ we implement a semi-implicit time-stepping method. An implicit-explicit Euler method treats the linear terms implicitly and the nonlinear terms $\hat{G}_{1,\mathrm{NL}}$ are discretised explicitly.

The second component of the evolution equation (7.23) evolves the period of the loop T. We use an explicit Euler method for time-stepping. The integral defining the right-hand-side is evaluated analogously to the pseudo-spectral treatment of the nonlinear terms in the evolution equation of the field. The integrand is evaluated in physical space followed by transformation to spectral space, where the integral is given by the $(0,0)$ Fourier mode multiplied by L.

Since the purpose of defining the initial value problem in loop-space is to identify attractors corresponding to solutions of the boundary value problem for periodic orbits, stability and simplicity of the implementation are more important than accuracy when choosing a time-stepping scheme. The simple Euler method is only first order accurate in τ but remains stable for the chosen fixed time step $\Delta\tau = 0.15$.

7.4.3 Initial guesses and convergence to periodic orbits

The adjoint-based variational method advances some initial loop under the dynamical system that minimises the cost function J. If a minimum with $J = 0$ is reached, the loop satisfies the boundary value problem for a periodic orbit. Initial guesses for the procedure are extracted from chaotic solutions of the KSE (7.19) $u(x,t)$. The common approach for generating guesses used in conjunction with Newton-GMRES-based shooting methods extracts close recurrences measured in terms of the L_2-distance from minima of the recurrence map $c(t,T) = ||u(\cdot, t+T) - u(\cdot,t)||$ (Auerbach *et al.*, 1987). Here, the L_2-norm is given by

$$||u||(t) = \sqrt{\int_0^L u(x,t)^2 dx}. \tag{7.28}$$

Exploiting the large radius of convergence of the variational method, we here choose a much simpler and computationally significantly cheaper method. Initial guesses are extracted from close recurrences in a one-dimensional projection of the solution. Specifically, we consider subsequent maxima in the time series of $||u||(t)$ where $||u||(t+T) \approx ||u||(t)$. The segment of the solution between those subsequent maxima yields the field component of the initial loop. To ensure a smooth closed loop with field component satisfying periodic boundary conditions in the temporal direction, the solution segment is Fourier-transformed in time and high-frequency components are filtered out (Lan & Cvitanović, 2004). The double-periodic field $u_0(x,s)$ complemented by the period defines an initial guess $\mathbf{l}_0 = [u_0(x,s); T]$.

The initial guess $\mathbf{l}_0$ is evolved under the dynamical system in loop-space (7.10). Along the evolution the cost function J is guaranteed to monotonically decrease and reach a minimum. Consequently, the adjoint-based variational method is globally convergent. However, it is not guaranteed that an absolute minimum with $J = 0$ is reached but the dynamics may asymptote towards a local minimum with $J > 0$. If a global minimum is reached, a periodic orbit satisfying the boundary value problem (7.3) has been found. We consider a periodic orbit converged when $\sqrt{J} < 10^{-12}$ is achieved. The periodic orbit corresponds to an attracting fixed point of the dynamical system in loop-space so that we expect exponential convergence at a rate controlled by the leading eigenvalue of the loop dynamics linearised around the attracting fixed point.

7.4.4 Results and discussion

We demonstrate the adjoint-based variational method to construct periodic orbits of the KSE for the parameter value $L = 39$. At this value, the dynamics is chaotic and a large number of unstable periodic orbits are known to exist (Lasagna, 2018). Periodic orbits of the KSE are found by evolving initial loops under the dynamical system in loop-space (7.23). The pseudo-spectral method uses 64×64 Fourier modes in spatial and temporal directions to discretise the field $u(x, s)$. A fixed time step of $\Delta\tau = 0.15$ leads to stable time-stepping.

Periodic orbits of the KSE are attracting solutions of an initial value problem in the space of loops $\mathscr{P}$ that monotonically decreases the cost function J, as shown in figure 7.2. In the top panel, the square root of the cost function, $\sqrt{J}$, as a function of the fictitious time τ is shown. After $\tau \approx 1.5 \cdot 10^6$ the convergence criterion $\sqrt{J} \leq 10^{-12}$ is reached. Since the cost function J is the average of $\int_\Omega r^2 dx$ over s, the square root of J scales with the L_2-norm (7.28) of the residual field r and should be used as the convergence criterion. Along the evolution of the loop with τ the cost function J monotonically decreases. After an initial fast decrease, $\sqrt{J}$ decays exponentially with τ. This suggests the convergence towards a periodic orbit along the leading eigendirection of the dynamical system in loop-space linearised about the attracting fixed point. Geometrically, the dynamical system in loop-space (7.23) continuously deforms the initial loop until the loop satisfies the KSE and thereby becomes a periodic orbit. The deformation is visualised in the bottom panel, where the evolution of the loop shown in a two dimensional projection of the state space. A very substantial deformation of the loop is associated with the fast decrease of J within the initial 10% of the integration time.

In addition to the two-dimensional field defined over the fixed space-time domain $[0, L) \times [0, 1)$, the corresponding period T is required to define a loop. Evolving a loop towards a periodic orbit implies finding the period T, which re-scales the temporal length of the space-time domain $s \to t = T \cdot s$ and thereby determines the length of extension of the domain in the direction of time t. Figure 7.3 shows the convergence of T to the period of the periodic orbit together with the space-time contours of the corresponding initial loop $u_0(x, t = T \cdot s)$ and the converged periodic orbit $u(x, t = T \cdot s)$. As for the geometry of the loop (figure 7.2) substantial

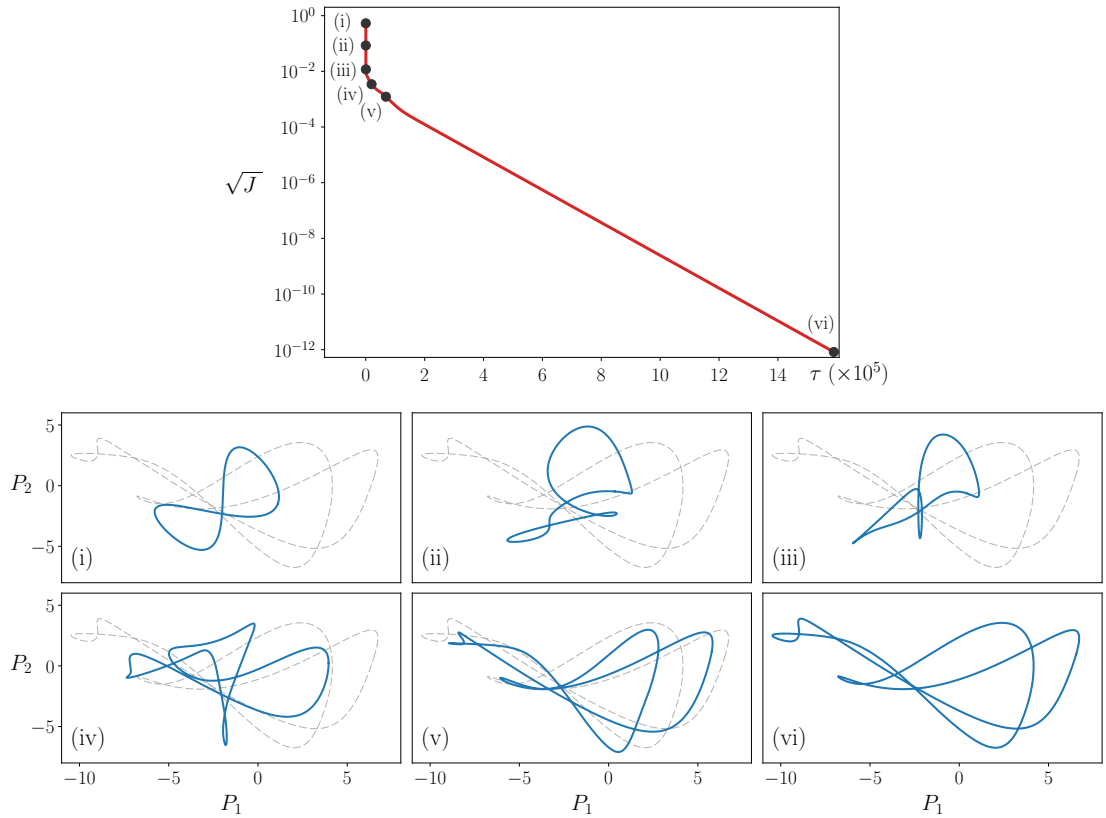

Figure 7.2 – Convergence of the adjoint-based variational method for finding periodic orbits of the KSE: The initial value problem in loop-space evolves loops such that the cost function J decreases monotonically along the fictitious time τ (top). The exponential decay of J towards zero indicates convergence towards a periodic orbit satisfying $J = 0$. Geometrically, the variational dynamics deforms a closed loop until it becomes an integral curve of the flow and thus a periodic orbit of the KSE. This is shown in the bottom panel, where the evolution of the loop is visualised in a two-dimensional projection of state space. Blue solid lines indicate the evolving loop at times indicated in the top panel. The dashed grey line is the converged periodic orbit. The state space projections $P_1(s)$ and $P_2(s)$ are defined by the imaginary parts of the first and second spatial Fourier coefficients of the field $u(x)$.

changes in the period T under the adjoint-based variational dynamics are mostly observed within the initial 10% of the integration of the dynamical system in loop-space (7.23). Already at $\tau = 2 \cdot 10^5$, T is very close to the period of the periodic orbit $T = 59.59$. We omit data beyond $\tau = 4 \cdot 10^5$ from figure 7.3 since changes would not be visible.

The fast initial decrease of the cost function J followed by a slow exponential decay towards zero suggests that the loop approaches the periodic orbit along the leading eigendirection of the loop dynamics linearised around the attracting fixed point. Most of the computational efforts are spent on following the exponential decay until the cost function has reached sufficiently low values, although this part of the dynamics is, at least approximately, linear.

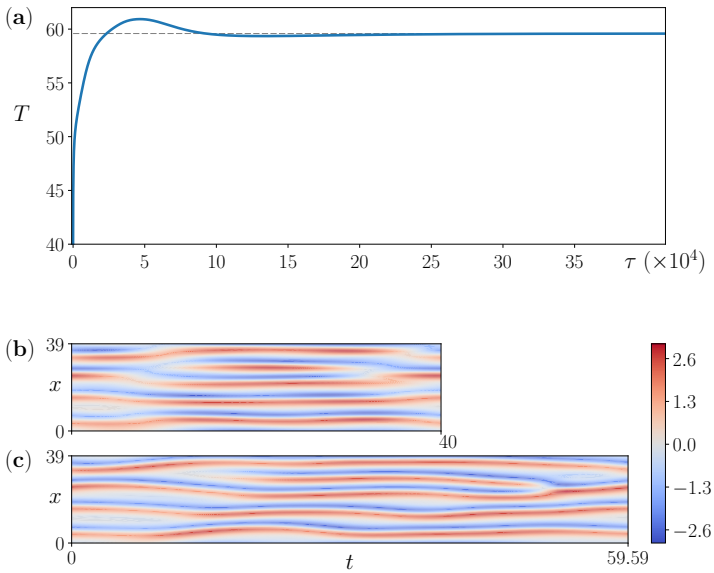

Figure 7.3 – A periodic orbit is characterised by the combination of the field $u(x,s)$ on a fixed double-periodic space-time domain and the time period T that rescales the temporal direction $s \to t = T \cdot s$. The variational dynamics adapts T until the period of the periodic orbit is determined (top). Finding the period T corresponds to determining the length of the domain in time t. This is evidenced by space-time contours of the solution $u(x, t = T \cdot s)$ for the initial condition (b) and the converged periodic orbit (c). The period of the initial loop and the periodic orbit are $T = 40$ and $T = 59.59$, respectively.

Consequently, the convergence of the method can be accelerated by explicitly exploiting the linearised dynamics in the vicinity of the attracting fixed point. A straightforward method reducing the computational costs by approximately 50% is discussed in 7.6.3. More sophisticated optimisations can be implemented and will be helpful when applying the adjoint-based variational method to three-dimensional fluid flows.

One major advantage of the adjoint-based variational method is that the successful convergence towards a periodic orbit is independent of the period of the orbit. This is in contrast to shooting methods, where the exponential amplification of errors during time-marching along the orbit can hinder computing long orbits. We demonstrate the convergence of orbits of increasing period and complexity in figure 7.4. Six converged periodic orbits with periods ranging from $T = 25.37$ to $T = 147.42$ are shown in terms of state-space projections, together with initial loops extracted from a chaotic time-series of the KSE. The apparent large difference between initial loop and converged orbit demonstrates that the adjoint-based variational method offers a very large radius of convergence and convergence therefore does not depend on an initial condition in the close vicinity of the converged orbit. The evolution of loops under the dynamical system in loop-space converges to minima of the cost function J for any initial condition. While globally convergent, the variational method is not guaranteed to converge to absolute minima of J with $J = 0$, corresponding to periodic orbits, but the dynamics

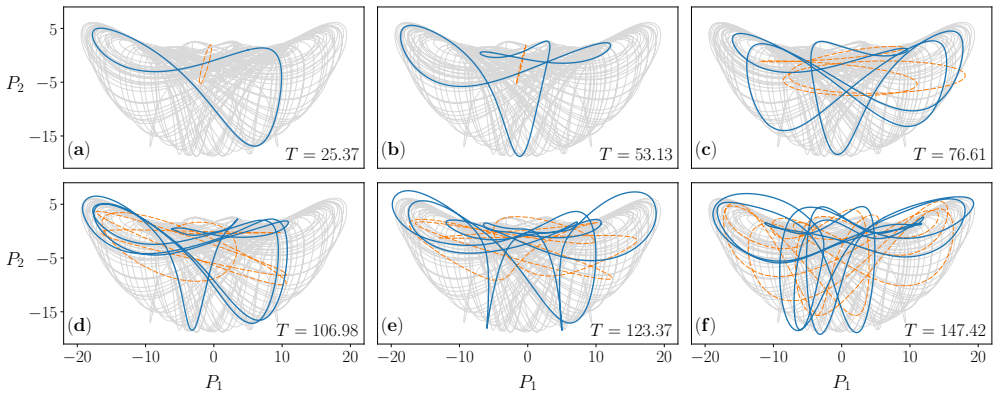

Figure 7.4 – Periodic orbits of increasing length and complexity converged by the adjoint-based variational method. The two-dimensional projection of state space as in figure 7.2 indicates, the initial loops (dashed orange lines) as well as the converged periodic orbits (solid blue lines). The period of the converged orbits are given in each panel. The grey line in the background of each panel is the trajectory of a long chaotic solution in the center symmetry subspace of the KSE (7.20). All initial loops are chosen from the center-symmetric subspace. The dynamical system in loop-space preserves the discrete symmetry of the initial loops Ξ so that all converged periodic orbits are also center-symmetric although the symmetry has not been imposed by the method. Note the large differences between initial loops and converged periodic orbits, highlighting the global convergence of the adjoint-based variational method.

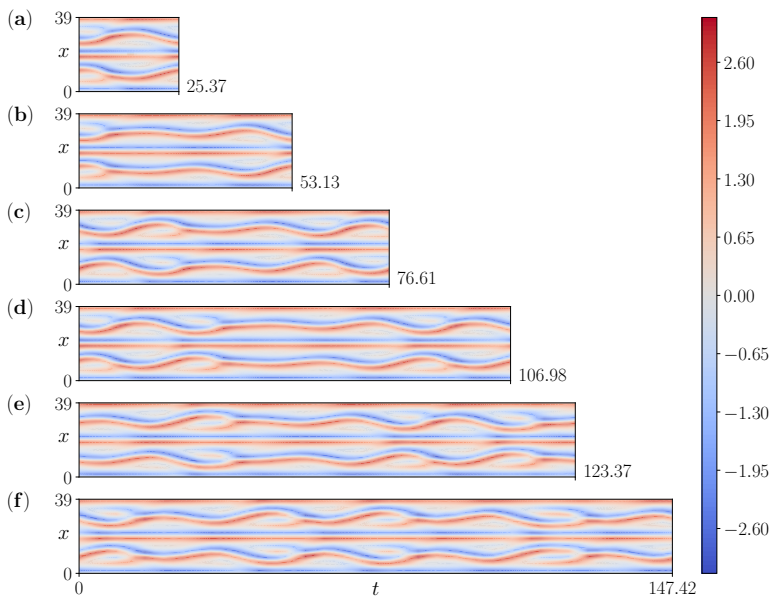

Figure 7.5 – Space-time contours of the converged periodic orbits from figure 7.4 with time periods of (a) $T = 25.37$, (b) $T = 53.13$, (c) $T = 76.61$, (d) $T = 106.98$, (e) $T = 123.37$, and (f) $T = 147.42$. Unlike shooting methods, where exponential error amplification during time-integration along the orbit renders long orbits inaccessible, the adjoint-based variational method deforms orbits locally and thus converges independent of the orbit period.

may approach a local minimum with $J > 0$. For initial loops extracted from recurrences in a one-dimensional projection of state space, as discussed in 7.4.3, we observe approximately 70% of all initial conditions to converge to periodic orbits with $J = 0$. An example of a loop approaching a local minimum of J is shown in 7.6.4.

Following Lasagna (Lasagna, 2018), initial loops for the six orbits discussed in figure 7.4 are extracted from a chaotic trajectory of the KSE in the subspace of center-symmetric fields. All initial conditions for the initial value problem in loop-space are therefore center symmetric. The dynamical system in loop-space (7.23) preserves the symmetry Ξ of loops (7.24) that corresponds to the center symmetry of instantaneous fields in the KSE system (7.20). Consequently, all converged periodic orbits also lie in the center symmetry subspace, as confirmed by figure 7.5, where space-time contours of the six periodic orbits are shown. Note that the method does not explicitly enforce the discrete symmetry but preserves the symmetry of the initial condition.

7.5 Summary and conclusion

Unstable periodic orbits have been recognised as building blocks of the dynamics in driven dissipative spatio-temporally chaotic systems including fluid turbulence. Periodic orbits capture key features of the dynamics and reveal physical processes sustaining the turbulent flow. Constructing a sufficiently large set of periodic orbits moreover carries the hope to eventually yield a predictive rational theory of turbulence, where 'properties of the turbulent flow can be mathematically deduced from the fundamental equations of hydrodynamics', as expressed by Hopf in 1948 (Hopf, 1948). Despite the importance of unstable periodic orbits, computing these exact solutions for high-dimensional spatio-temporally chaotic systems remains challenging. Known methods either show poor convergence properties because they are based on time-marching a chaotic system causing exponential error amplification; or they require constructing Jacobian matrices which is prohibitively expensive for high-dimensional problems. We therefore introduce a new matrix-free method for computing periodic orbits that is unaffected by exponential error amplification, shows robust convergence properties and can be applied to high-dimensional spatio-temporally chaotic systems. As a proof-of-concept we implement the method for the one-dimensional KSE and demonstrate the convergence of periodic orbits underlying spatio-temporal chaos.

The adjoint-based variational method constructs a dynamical system that evolves entire loops such that the value of a cost function measuring deviations of the loop from a solution of the governing equations monotonically decreases. Periodic orbits correspond to attracting fixed points of the variational dynamics. Due to the variational approach, the method provides a large radius of convergence so that periodic orbits can be found from inaccurate initial guesses. For the KSE we demonstrate the robust convergence properties by successfully computing periodic orbits from inaccurate initial guesses. These guesses are extracted from the projection of the free chaotic dynamics on a single scalar quantity, instead from close recurrences based

on the L_2-distance between spatial fields (Auerbach *et al.*, 1987). Reliable convergence to machine precision is observed independent of the period of the orbit.

The large convergence radius of the adjoint-based variational method relaxes accuracy requirements for initial guesses when those are extracted from the chaotic dynamics. Since initial guesses are characterised by an entire loop, one may use fast-to-compute models approximating the full dynamics to construct initial guesses for periodic orbits of the full dynamics. Such an approach would not be reasonable for classical shooting methods where initial guesses are characterised by an instantaneous initial condition and the difference between model and full dynamics would be amplified exponentially by the time-marching. Suitable models that may help provide initial guesses for constructing large sets of periodic orbits for a given chaotic system include under-resolved simulations, spatially filtered equations such as LES in fluids applications (Sagaut, 2006) and classical POD / DMD based models (McKeon, 2017). In addition, recent breakthroughs in machine learning create data-driven low-dimensional models of the chaotic dynamics that replicate spatio-temporal chaos in one- and two-dimensional systems with remarkable accuracy (Pathak, Hunt, Girvan, Lu & Ott, 2018; Zimmermann & Parlitz, 2018; Vlachas, Byeon, Wan, Sapsis & Koumoutsakos, 2018).

The feasibility of the proposed method has been demonstrated for a one-dimensional chaotic PDE but the method applies to general autonomous systems and we plan to implement it for the full three-dimensional Navier-Stokes equations. Specifically, we aim for an implementation within our own open-source software Channelflow (channelflow.ch) (Gibson *et al.*, 2019). In the context of this software not only the identification of periodic orbits but also their numerical continuation will benefit from the adjoint-based variational approach. When transferring the adjoint-based variational approach to three-dimensional fluid turbulence, we envision further optimisations of the method. First, we will exploit that during its approach to the attracting fixed point representing the periodic orbit, the evolution is well approximated by the linearization of the dynamics around the attracting fixed point. This accelerates the time-marching in loop-space and thereby the exponential convergence, as exemplified for the KSE. Second, one may complement the adjoint dynamics with Newton descent to identify the attracting fixed point in loop-space, following the analogous hybrid approach for identifying equilibrium solutions (Farazmand, 2016). Alternatively, we will combine the adjoint-based variational method with a Newton-GMRES-based shooting method. Such a hybrid method offers the large radius of convergence of the adjoint-based variational method in combination with the fast quadratic convergence of Newton's method. To converge long and unstable periodic orbits, a multi-shooting variant of the standard Newton-GMRES-hook-step method (Sánchez & Net, 2010) will be used.

7.6 Appendix

7.6.1 Rate of change of the cost function J

The rate of change of the cost function J with respect to the fictitious time τ is given in (7.12). Here we derive this expression including the specific form of $\mathbf{R}$. With the definition of the cost function J (7.5)

$$J(\mathbf{l}) = \int_0^1 \int_\Omega \vec{r}(\mathbf{l}).\vec{r}(\mathbf{l}) d\vec{x} ds,$$

the rate of change of J with respect to the fictitious time τ is

$$\frac{\partial J}{\partial \tau} = 2 \int_0^1 \int_\Omega (\nabla_{\mathbf{l}} \vec{r} \cdot \mathbf{G}) \cdot \vec{r} d\vec{x} ds.$$

where $\partial \mathbf{l}/\partial \tau = \mathbf{G}$ from definition (7.10) has been used. Using the definition of the inner product in the space of generalised loops (7.8), we can express the rate of change as

$$\frac{\partial J}{\partial \tau} = 2 \left\langle \begin{bmatrix} \nabla_{\mathbf{l}} \vec{r} \cdot \mathbf{G} \\ 0 \end{bmatrix}, \begin{bmatrix} \vec{r} \\ 0 \end{bmatrix} \right\rangle.$$

Here we choose the second component of both generalised loops to be zero. With this choice, the rate of change of J is given by

$$\frac{\partial J}{\partial \tau} = 2 \left\langle \mathscr{L}(\mathbf{l}; \mathbf{G}), \mathbf{R} \right\rangle,$$

where $\mathscr{L}(\mathbf{l}; \mathbf{G})$ indicates the directional derivative of $\mathbf{R} = [\vec{r}; 0]$ along $\mathbf{G}$, defined in (7.14).

7.6.2 Adjoint operator for KSE

We explicitly derive the form of the adjoint operator for the KSE problem given in (7.22). In this appendix, subscripts 1 and 2 denote the field component and the scalar component of generalised loops, respectively. The directional derivative of KSE along $\mathbf{G}$ is

$$\mathscr{L}(\mathbf{l}; \mathbf{G}) = \begin{bmatrix} \frac{G_2}{T^2} \frac{\partial u}{\partial s} - \frac{1}{T} \frac{\partial G_1}{\partial s} - \frac{\partial (u G_1)}{\partial x} - \frac{\partial^2 G_1}{\partial x^2} - \frac{\partial^4 G_1}{\partial x^4} \\ 0 \end{bmatrix}$$

To compute the adjoint operator, we expand the inner product of the directional derivative of the residual and the residual itself:

$$
\begin{aligned}
&\langle \mathscr{L}(\mathbf{l};\mathbf{G}),\mathbf{R}\rangle \\
&\quad= \int_0^1\int_0^L \mathscr{L}_1 R_1\,dx\,ds + \mathscr{L}_2 R_2 = \int_0^1\int_0^L \mathscr{L}_1 R_1\,dx\,ds + 0 \\
&\quad= \int_0^1\int_0^L \left(\frac{G_2}{T^2}\frac{\partial u}{\partial s} - \frac{1}{T}\frac{\partial G_1}{\partial s} - \frac{\partial (uG_1)}{\partial x} - \frac{\partial^2 G_1}{\partial x^2} - \frac{\partial^4 G_1}{\partial x^4}\right) R_1\,dx\,ds \\
&\quad= \int_0^1\int_0^L \frac{G_2}{T^2}\frac{\partial u}{\partial s} R_1\,dx\,ds \\
&\qquad+ \int_0^1\int_0^L \left(-\frac{1}{T}\frac{\partial G_1}{\partial s} - \frac{\partial (uG_1)}{\partial x} - \frac{\partial^2 G_1}{\partial x^2} - \frac{\partial^4 G_1}{\partial x^4}\right) R_1\,dx\,ds.
\end{aligned}
\tag{7.29}
$$

This inner product must be equal to

$$
\langle \mathbf{G},\mathscr{L}^\dagger(\mathbf{l};\mathbf{R})\rangle = \int_0^1\int_0^L \mathscr{L}_1^\dagger G_1\,dx\,ds + \mathscr{L}_2^\dagger G_2, \tag{7.30}
$$

where the adjoint operator is indicated by a dagger. Direct comparison of equations (7.29) and (7.30) results in

$$
\int_0^1\int_0^L \mathscr{L}_1^\dagger G_1\,dx\,ds = \int_0^1\int_0^L \left(-\frac{1}{T}\frac{\partial G_1}{\partial s} - \frac{\partial (uG_1)}{\partial x} - \frac{\partial^2 G_1}{\partial x^2} - \frac{\partial^4 G_1}{\partial x^4}\right) R_1\,dx\,ds \tag{7.31a}
$$

$$
\mathscr{L}_2^\dagger G_2 = \left(\int_0^1\int_0^L \frac{1}{T^2}\frac{\partial u}{\partial s} R_1\,dx\,ds\right) G_2. \tag{7.31b}
$$

The form of $\mathscr{L}_2^\dagger$ is directly given by (7.31b):

$$
\mathscr{L}_2^\dagger(\mathbf{q};\mathbf{R}) = \int_0^1\int_0^L \frac{1}{T^2}\frac{\partial u}{\partial s} R_1\,dx\,ds.
$$

Using integration by parts and the periodicity of the domain in space and time, (7.31a) becomes

$$
\int_0^1\int_0^L \mathscr{L}_1^\dagger G_1\,dx\,ds = \int_0^1\int_0^L \left(\frac{1}{T}\frac{\partial R_1}{\partial s} + u\frac{\partial R_1}{\partial x} - \frac{\partial^2 R_1}{\partial x^2} - \frac{\partial^4 R_1}{\partial x^4}\right) G_1\,dx\,ds.
$$

Consequently,

$$
\mathscr{L}_1^\dagger(\mathbf{l};\mathbf{R}) = \frac{1}{T}\frac{\partial R_1}{\partial s} + u\frac{\partial R_1}{\partial x} - \frac{\partial^2 R_1}{\partial x^2} - \frac{\partial^4 R_1}{\partial x^4}
$$

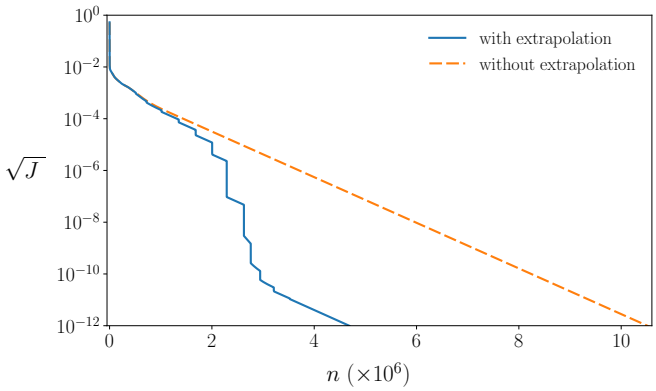

Figure 7.6 – Accelerated convergence of the adjoint-based variational method. Convergence history for the periodic orbit discussed in figures 7.2 and 7.3, for the standard method (orange dashed line) and the modified method involving linear extrapolations along the solution trajectory in the loop-space. The linear extrapolations are based on a linear approximation of the loop dynamics around the attracting fixed point in loop-space corresponding to the periodic orbit. The square root of the cost function is shown as a function of the number of fictitious time steps n. The first extrapolation is performed when $\sqrt{J} = 10^{-3}$. Between two consecutive extrapolations, the dynamical system in loop-space is integrated until the value $\sqrt{J}$ is halved. In this example case, extrapolations reduce the total number of fictitious time steps by more than 50%.

where $R_1 = r$. The adjoint operator acting on loops therefore has the form

$$\mathscr{L}^{\dagger}(\mathbf{l};\mathbf{R}) = \begin{bmatrix} \frac{1}{T}\frac{\partial r}{\partial s} + u\frac{\partial r}{\partial x} - \frac{\partial^2 r}{\partial x^2} - \frac{\partial^4 r}{\partial x^4} \\ \int_0^1 \int_0^L \frac{1}{T^2}\frac{\partial u}{\partial s} r\,dx\,ds \end{bmatrix}.$$

7.6.3 Acceleration of the convergence by linearised approximation

We demonstrate a straightforward method for accelerating the convergence of the adjoint-based variational method. We iterate between time-stepping of the dynamical system in loop-space (7.23) and a linear extrapolation along the evolution trajectory of the loops. This extrapolation is based on the assumption that the evolution follows the leading eigendirection of the linearization about the attracting loop. Extrapolations yield the initial conditions of the subsequent advancing of the loop in τ. This procedure is repeated until the periodic orbit is converged. Figure 7.6 compares the convergence of the periodic orbit shown in figures 7.2 and 7.3 by continuous integration of the dynamical system in loop-space (7.23) and the accelerated method iterating between time-stepping of the full dynamics and extrapolations, both from the same initial condition. Vertical drops of the cost function shown in the graph correspond to the extrapolations. In this example the accelerated method reduces the required

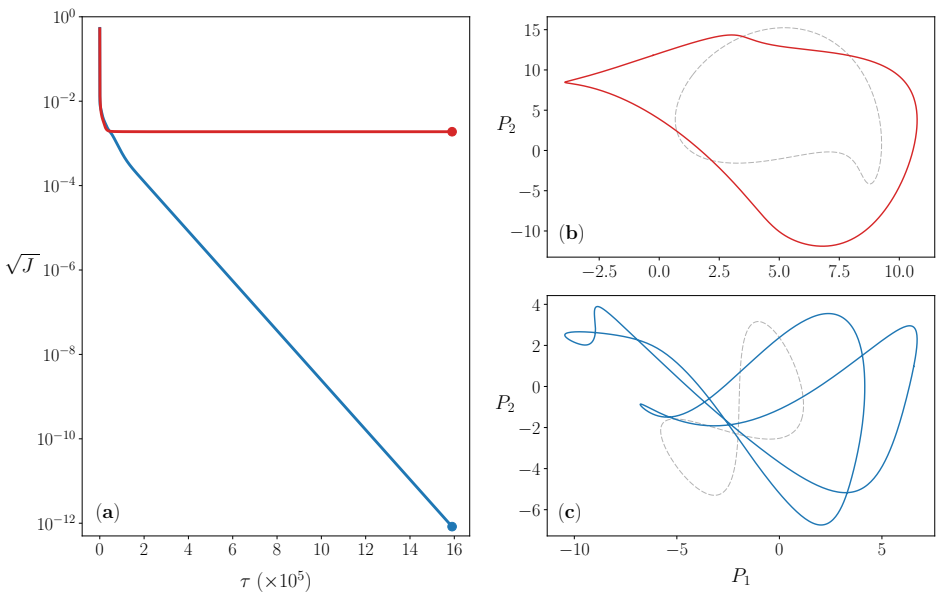

Figure 7.7 – Minimising J by the adjoint-based variational method. (a) Evolution of $\sqrt{J}$ with τ for two different initial loops. The blue line shows the convergence for the loop that approaches a periodic orbit with $J = 0$ while the red line shows the convergence for a loop that approaches a local minimum of J with a nonzero value $J > 0$. The corresponding initial (dashed lines) and converged loops (solid lines) in the two-dimensional projection of the state space as in figure 7.2 are visualised for the converged loop with $J > 0$ (panel b) and the periodic orbit with $J \to 0$ (panel c).

total number of numerical steps of integration by more than 50%.

7.6.4 Convergence to local and global minima of J

Here we show an example of time-stepping of the dynamical system in loop-space where the final loop corresponds to local minimum of J with a nonzero value. Consequently, no periodic orbit is found.

8 Conclusions and outlook

Contents

In this thesis, we have investigated coherent structures present in turbulent boundary layer flows. We study both small-scale structures in the near-wall region, and large-scale structures spanning the entire turbulent domain. Coherent structures at these two scales underlie recognisable peaks in power spectra of turbulent fluctuations. The studied coherent structures thus appear at the two most energetic scales of the flow. We follow a dynamical system approach to turbulence, and describe turbulence as a chaotic walk through a network of interconnected invariant solutions. Within this picture, coherent structures are observed in the flow when turbulent trajectories transiently visit invariant solutions. Invariant solutions thus act as building blocks of the dynamics and may capture characteristic features of the turbulent flow. The dynamical system approach to turbulence has been successful in describing properties of turbulent flows in the transitional regime. The objective of this research is to transfer dynamical systems concepts from the transitional regime to high-Reynolds-number boundary layer flows. We thereby aim for describing the dynamics of both small-scale structures in the near-wall region and of large-scale motions.

For the required numerical simulations we use the open-source software *channelflow 2.0*, that is developed within our group, ECPS, in collaboration with EPFL's SCITAS group and John Gibson of UNH. *channelflow 2.0* provides numerical tools to perform direct numerical simulations of turbulent flows, as well as linear algebra tools for dynamical system analysis. Selected numerical methods including a multishooting method to facilitate computations of long periodic orbits, the method of accumulating Krylov subspace to improve the convergence of Newton's method, and a modified arclength continuation method for following branches

of solutions are detailed in this thesis. Isolating large-scale motions requires solving the filtered equations embedded in large-eddy simulations. The code structure of *channelflow 2.0* allows for straightforward extensions and the inclusion of additional forcing terms in the Navier-Stokes equations. We have extended the code and implemented filtered Navier-Stokes equations so that large-eddy simulations can be performed and invariant solutions of the filtered equations can be computed.

8.1 Summary of the results

Universal near-wall dynamics: In the near-wall region, turbulence at sufficiently high Reynolds numbers becomes universal and independent of the specific flow system. A theoretical analysis of the Navier-Stokes equations expressed in inner units suggests that at high Reynolds numbers the near-wall flow becomes asymptotically independent of the Reynolds number. This implies that all state-space structures including invariant solutions but also their dynamical connections become asymptotically self-similar. Consequently any deterministic chaotic solutions of the governing equations will show the same self-similar behaviour. The self-similarity of state-space structures is evidenced by the identification of an invariant solution that captures the characteristic universal scaling of the near-wall region at high Reynolds numbers. Identifying all dynamically relevant state-space structures such as travelling waves, periodic orbits and their homoclinic connections may eventually allow for a full universal description of near-wall turbulence at arbitrarily high Reynolds numbers in terms of invariant solutions. Relevant solutions can either be directly computed at high Reynolds numbers or they can be found at transitional and moderate Reynolds numbers and continued to high Reynolds numbers. A full deterministic description of universal near-wall turbulence may be of practical importance and yield physically justified wall models for large-eddy simulations of turbulent flows at high Reynolds numbers.

Large-scale motions: We study large-scale motions, LSMS, in the asymptotic suction boundary layer, ASBL. LSMs in the ASBL can be isolated by filtering out smaller scale structures. The fact that large-scale motions survive in the absence of the smaller-scale structures implies that large-scale motions in the ASBL are self-sustained. In the ASBL, large-scale motions are weak when compared with large-scale motions in other shear flows. This is evidenced by a weak kinetic energy peak of LSMs in power spectra of turbulent fluctuations when compared with the peak of small-scale structures. The observation that large-scale motions are self-sustained even in the presence of especially strong small-scale structures suggest a generic and robust self-sustaining mechanism of large-scale motions in boundary layer flows. Despite being universally self-sustained, the typical temporal dynamics of large-scale motions in the ASBL appears to differ from the dynamics observed in the confined flows. In contrast to confined flows, in which the temporal evolution of the kinetic energy of the streaks and vortices are in phase opposition, in the boundary layer flow streaks and vortices evolve in phase during aperiodic bursting cycles.

The dynamics of large-scale motions are represented by the deterministic filtered Navier-Stokes equations. This suggests that the large-scale motions can be treated deterministically considering the filtered equations as the relevant dynamical system. LSMs can thus be described as chaotic trajectories supported by a network of invariant solutions of the filtered equations and their dynamical connections. We identify a number of invariant solutions of the filtered equations including travelling waves and periodic orbits representing the dynamics of LSMs. The identified solutions capture several coherent self-sustained processes of large-scale motions, including streak-vortex regeneration cycles and hairpin-like vortical structures. Our results suggest that the dynamics of large-scale motions at high scale separations can be described using the dynamical systems concepts transferred from transitional regime to high Reynolds numbers.

Symmetries of ASBL: Both invariant solutions underlying near-wall structures and invariant solutions capturing large-scale motions have been studied in the asymptotic suction boundary layer. ASBL differs from confined flow geometries including plane Couette and channel flow not only in that it is an unconfined flow but also in its symmetry properties. Specifically, ASBL does not have the up-down symmetries of plane Couette (PCF) and channel flow. To understand the effect of the different symmetries on invariant solutions and their bifurcation structure, we study the impact of symmetry breaking on snaking solutions in PCF. These solutions promise a fruitful avenue towards understanding symmetry properties because their bifurcation structure resembles solutions of one-dimensional Swift-Hohenberg equation (SHE) remarkably well. In the SHE, many features of the snakes-and-ladders bifurcation structure can be directly explained in terms of symmetries. We apply a non-vanishing wall-normal suction in the boundary conditions of PCF and study the response of localised homoclinic snaking solutions when suction is applied. The non-vanishing wall-normal suction breaks the up-down symmetry of PCF and results in a flow with equivariance group identical to the ASBL. We observe that the bifurcation structure of the homoclinic snaking solutions of PCF breaks down. The unmodified homoclinic snaking mechanism of PCF is thus not compatible with the symmetries of the ASBL. However, modifications of the bifurcation structures for PCF with non-vanishing suction are shown to be analogous to the modifications of the bifurcation structures of the SHE, if a symmetry-breaking term is added.

Variational method for finding periodic orbits: The identification of self-similar invariant solutions of the full Navier-Stokes equations expressed in inner units capturing universal flow properties of near-wall turbulence at high Reynolds numbers suggests that a deterministic description of near-wall turbulence in terms of invariant solutions may be possible. Likewise, first progress towards describing large-scale motions in terms of invariant solutions of appropriate model equations suggests the possibility of a deterministic description of large-scale coherent structures in terms of invariant solutions of filtered equations. While the individual invariant solutions presented here and elsewhere are suggestive and capture specific properties of the flow, a full quantitative and predictive description of any turbulent

flow in terms of invariant solutions requires sufficiently large sets of invariant solutions and in particular of periodic orbits. Currently, numerical tools for creating such libraries of periodic orbits are not available as the common shooting method lacks the necessary robustness. We therefore suggest a novel matrix-free variational method for constructing periodic orbits of a general dynamical system. The method is globally convergent. The feasibility of the method is tested for the Kuramoto-Sivashinsky system. Future research should extend the method to the dynamical systems of both the full Navier-Stokes equations for the near-wall turbulence and the filtered Navier-Stokes equations for large-scale motions. Implementing the method for the turbulent flows considered can lead to the computation of large sets of invariant solutions and may eventually provide the basis for a full deterministic description of chaotically evolving small- and large-scale coherent structures.

8.2 Outlook: From parallel to developing boundary layers

We have specifically studied coherent structures in the asymptotic suction boundary layer flow (ASBL). ASBL shares many properties with developing boundary layers but the presence of suction arrests the growth of the boundary layer thickness and thereby avoids complications due to non-parallel effects. Unlike in a developing boundary layer flow without wall-normal suction in which the statistics of the flow including the boundary layer thickness vary in the streamwise direction, ASBL flow is streamwise invariant. This continuous translational symmetry, which is broken in a developing boundary layer (DBL), allows for the existence of travelling wave solutions. Travelling waves cannot exist in the DBL so that periodic orbits are the simplest exact invariant solutions. While the dynamical systems description developed for the parallel ASBL can provide an approximate description of the DBL when non-parallel effects are negligible, fully transferring the approach to a non-parallel DBL requires taking the broken symmetry into account and constructing exact invariant solutions supported by the developing boundary layer flow. Consequently, robust numerical methods for finding periodic orbits such as the adjoint-based variational method introduced in this thesis are critical for dynamical systems studies of the DBL. We speculate that other invariant solutions corresponding to travelling waves within ASBL might exist in the form of similarity solutions. Employing similarity variables and rescaling spatial scales with the growing boundary layer thickness yields a rescaled system with streamwise translational symmetry that can support travelling waves. Travelling wave solutions of this rescaled system represent self-similar flow states up to rescaling spatial scales to account for the growth of the boundary layer. Technically, the travelling wave solutions identified in ASBL may be transferred to the rescaled DBL using homotopy approaches to explore the existence of self-similar invariant solutions of the DBL. Likewise, periodic orbits of the DBL may be identified starting from those found in ASBL.

8.3 Concluding remarks

The work described in this thesis is aimed at improving the understanding of boundary layer turbulence. Instead of describing turbulence as a stochastic process whose properties can be understood by means of statistical methods, we follow a deterministic approach aimed at describing the dynamics of recognisable coherent structures populating the flow (Jiménez, 2018). We specifically attempt to transfer the dynamical systems method from transitional flows to turbulent boundary layers by computing invariant solutions underlying both small- and large-scale coherent structures. For large-scale structures, we specifically propose to associate coherent structures which physically exist within a background of small-scale fluctuations, with exact solutions of model equations appropriate for describing the spatially filtered velocity field.

The treatment of coherent structures presented in this thesis has been simplified in two important aspects. First, by considering individual isolated structures in minimal flow units, spatial interactions between individual coherent structures in space have been removed. Second, coherent structures at large scales have been studied independently of coherent structures in the near-wall region; interactions across different scales are thus not fully considered. Isolating coherent structures in space and in scale allows to gain valuable insights into the dynamics of individual coherent structures. An accurate description of a fully turbulent flow, in which coherent structures coexist in space and interact over many spatial scales, however requires to take those interactions into account. A full description of turbulent boundary layer flows in terms of the dynamics of coherent structures thus requires considering not only the deterministic temporal dynamics of individual coherent structures but also their interactions. As turbulence is a true multi-scale phenomenon, studying interactions over varying scales will likely always be based on coarse-graining procedures in the spirit of spatially filtered evolution equations. Interactions in space can however be investigated by considering turbulent boundary layer flows in spatially extended numerical domains. In such domains, we expect spatially modulated or localized exact solutions to exist.

We have successfully captured small- and large-scale structures in a parallel boundary layer at high Reynolds numbers. This suggests that a dynamical systems description of boundary layer flows relevant for practical engineering applications might indeed be within reach. The presented work suggests specific future research and tool-developments needed to explore spatio-temporally localised exact invariant solutions in parallel boundary layers and to formally transfer the results to spatially developing flows. The envisioned research will bring us even closer to a predictive dynamical systems description of wall-bounded turbulence in practically relevant flow problems.

Bibliography

ADRIAN, R. J. 2007 Hairpin vortex organization in wall turbulence. *Physics of Fluids* **19** (4), 041301.

ALIZARD, F. 2015 Linear stability of optimal streaks in the log-layer of turbulent channel flows. *Physics of Fluids* **27** (10).

ANTOULAS, A. C. 2005 *Approximation of Large-Scale Dynamical Systems*. Society for Industrial and Applied Mathematics.

ARNOLDI, W. 1951 The principle of minimized iterations in the solution of matrix eigenvalue problem. *Quarterly of Applied Mathematics* **9** (1), 17–29.

ARTUSO, R., AURELL, E. & CVITANOVIĆ, P. 1990*a* Recycling of strange sets: I. Cycle expansions. *Nonlinearity* **3** (2), 325–359.

ARTUSO, R., AURELL, E. & CVITANOVIĆ, P. 1990*b* Recycling of strange sets: II. Applications. *Nonlinearity* **3** (2), 361–386.

AUERBACH, D., CVITANOVIĆ, P., ECKMANN, J.-P., GUNARATNE, G. & PROCACCIA, I. 1987 Exploring chaotic motion through periodic orbits. *Physical Review Letters* **58** (23), 2387–2389.

AVILA, M., MELLIBOVSKY, F., ROLAND, N. & HOF, B. 2013 Streamwise-Localized Solutions at the Onset of Turbulence in Pipe Flow. *Physical Review Letters* **110** (22), 224502.

AZIMI, S., COSSU, C. & SCHNEIDER, T. 2020 Self-sustained large-scale motions in the asymptotic suction boundary layer. *in preparation* .

AZIMI, S. & SCHNEIDER, T. M. 2020 Self-similar invariant solution in the near-wall region of a turbulent boundary layer at asymptotically high Reynolds numbers. *Journal of Fluid Mechanics* **888**, A15.

BARKLEY, D. & TUCKERMAN, L. S. 2005 Computational Study of Turbulent Laminar Patterns in Couette Flow. *Physical Review Letters* **94** (1), 014502, arXiv: 0403142v1.

BATISTE, O., KNOBLOCH, E., ALONSO, A. & MERCADER, I. 2006 Spatially localized binary-fluid convection. *Journal of Fluid Mechanics* **560**, 149.

BECK, M., KNOBLOCH, J., LLOYD, D. J. B., SANDSTEDE, B. & WAGENKNECHT, T. 2009 Snakes, Ladders, and Isolas of Localized Patterns. *SIAM Journal on Mathematical Analysis* **41** (3), 936–972.

BOBERG, L. & BROSA, U. 1988 Onset of Turbulence in Pipe. *Z. Für Naturforschung A* **43**, 697–726.

BOBKE, A., ÖRLÜ, R. & SCHLATTER, P. 2016 Simulations of turbulent asymptotic suction boundary layers. *Journal of Turbulence* **17** (2), 157–180.

BOGHOSIAN, B. M., BROWN, A., LÄTT, J., TANG, H., FAZENDEIRO, L. M. & COVENEY, P. V. 2011 Unstable periodic orbits in the Lorenz attractor. *Philosophical transactions. Series A, Mathematical, physical, and engineering sciences* **369**, 2345–53.

BRAND, E. & GIBSON, J. F. 2014 A doubly-localized equilibrium solution of plane Couette flow. *Journal of Fluid Mechanics* **750**, R3.

BRETHOUWER, G., DUGUET, Y. & SCHLATTER, P. 2012 Turbulent–laminar coexistence in wall flows with Coriolis, buoyancy or Lorentz forces. *Journal of Fluid Mechanics* **704**, 137–172.

BURKE, J., HOUGHTON, S. M. & KNOBLOCH, E. 2009 Swift-Hohenberg equation with broken reflection symmetry. *Physical Review E - Statistical, Nonlinear, and Soft Matter Physics* **80** (3), 3–7.

BURKE, J. & KNOBLOCH, E. 2006 Localized states in the generalized Swift-Hohenberg equation. *Physical Review E - Statistical, Nonlinear, and Soft Matter Physics* **73** (December 2005), 1–15.

BURKE, J. & KNOBLOCH, E. 2007 Homoclinic snaking: structure and stability. *Chaos* **17** (3), 15,37102.

CANUTO, C., HUSSAINI, M. Y., QUARTERONI, A. & ZANG, T. A. 2006 *Spectral Methods: Fundamentals in Single Domains*. Springer.

CHAMPNEYS, A. 1998 Homoclinic orbits in reversible systems and their applications in mechanics, fluids and optics. *Physica D: Nonlinear Phenomena* **112** (1-2), 158–186.

CHANDLER, G. J. & KERSWELL, R. R. 2013 Invariant recurrent solutions embedded in a turbulent two-dimensional Kolmogorov flow. *Journal of Fluid Mechanics* **722**, 554–595.

CLEVER, R. M. & BUSSE, F. H. 1992 Three-dimensional convection in a horizontal fluid layer subjected to a constant shear. *Journal of Fluid Mechanics* **234** (-1), 511–527.

COSSU, C. & HWANG, Y. 2017 Self-sustaining processes at all scales in wall-bounded turbulent shear flows. *Philosophical Transactions of the Royal Society A: Mathematical, Physical and Engineering Sciences* **375** (2089), 20160088.

CVITANOVIĆ, P. 1988 Invariant measurement of strange sets in terms of cycles. *Physical Review Letters* **61**, 2729–2732.

CVITANOVIĆ, P., ARTUSO, R., MAINIERI, G., TANNER, G. & VATTAY, G. 2016 *Chaos: Classical and quantum*. chaosbook.org, Niels Bohr Institute, Copenhagen.

CVITANOVIĆ, P., DAVIDCHACK, R. L. & SIMINOS, E. 2010 On the state space geometry of the Kuramoto-Sivashinsky flow in a periodic domain. *SIAM Journal on Applied Dynamical Systems* **9** (1), 1–33.

CVITANOVIĆ, P. & GIBSON, J. F. 2010 Geometry of the turbulence in wall-bounded shear flows: periodic orbits. *Physica Scripta* **T142**, 014007.

DEGUCHI, K. 2015 Self-sustained states at Kolmogorov microscale. *Journal of Fluid Mechanics* **781**, R6.

DEGUCHI, K. & HALL, P. 2014*a* Free-stream coherent structures in parallel boundary-layer flows. *Journal of Fluid Mechanics* **752**, 602–625.

DEGUCHI, K. & HALL, P. 2014*b* The high-Reynolds-number asymptotic development of nonlinear equilibrium states in plane Couette flow. *Journal of Fluid Mechanics* **750**, 99–112.

DENNIS, D. J. & NICKELS, T. B. 2011 Experimental measurement of large-scale three-dimensional structures in a turbulent boundary layer. Part 2. Long structures. *Journal of Fluid Mechanics* **673**, 218–244.

DENNIS, J. E. & SCHNABEL, R. B. 1996 *Numerical methods for unconstrained optimization and nonlinear equations*. SIAM.

DIJKSTRA, H. A., WUBS, F. W., CLIFFE, A. K., DOEDEL, E., HAZEL, A. L., LUCARINI, V., SALINGER, A. G., PHIPPS, E. T., SANCHEZ-UMBRIA, J., SCHUTTELAARS, H., TUCKERMAN, L. S. & THIELE, U. 2014 Numerical Bifurcation Methods and their Application to Fluid Dynamics: Analysis beyond Simulation. *Communications in Computational Physics* **15** (1), 1–45.

DUGUET, Y., PRINGLE, C. C. T. & KERSWELL, R. R. 2008 Relative periodic orbits in transitional pipe flow. *Physics of Fluids* **20** (11), 114102.

ECKHARDT, B., SCHNEIDER, T. M., HOF, B. & WESTERWEEL, J. 2007 Turbulence Transition in Pipe Flow. *Annual Review of Fluid Mechanics* **39** (1), 447–468.

ECKHARDT, B. & ZAMMERT, S. 2018 Small scale exact coherent structures at large Reynolds numbers in plane Couette flow. *Nonlinearity* **31** (2), R66–R77.

EDWARDS, W. S., TUCKERMAN, L. S., FRIESNER, R. A. & SORENSEN, D. C. 1994 Krylov Methods for the Incompressible Navier-Stokes Equations. *Journal of Computational Physics* **110** (1), 82–102.

FAISST, H. & ECKHARDT, B. 2003 Traveling waves in pipe flow. *Physical Review Letters* **91**, 224502.

FARANO, M., CHERUBINI, S., ROBINET, J.-C., DE PALMA, P. & SCHNEIDER, T. M. 2019 Computing heteroclinic orbits using adjoint-based methods. *Journal of Fluid Mechanics* **858**, R3.

FARAZMAND, M. 2016 An adjoint-based approach for finding invariant solutions of Navier-Stokes equations. *Journal of Fluid Mechanics* **795**, 278–312.

FAZENDEIRO, L. M., BOGHOSIAN, B. M., COVENEY, P. V. & LÄTT, J. 2010 Unstable periodic orbits in weak turbulence. *Journal of Computational Science* **1**, 13–23.

FELDMANN, D. & AVILA, M. 2018 Overdamped large-eddy simulations of turbulent pipe flow up to $\mathrm{Re}\tau = 1500$. *Journal of Physics: Conference Series* **1001** (1).

FIRTH, W. J., COLUMBO, L. & MAGGIPINTO, T. 2007 On homoclinic snaking in optical systems. *Chaos* **17**, 1–8.

FLORES, O. & JIMÉNEZ, J. 2006 Effect of wall-boundary disturbances on turbulent channel flows. *Journal of Fluid Mechanics* **566**, 357–376.

FLORES, O., JIMÉNEZ, J. & DEL ÁLAMO, J. C. 2007 Vorticity organization in the outer layer of turbulent channels with disturbed walls. *Journal of Fluid Mechanics* **591**, 145–154.

FRISCH, U. 1995 *Turbulence: The Legacy of A. N. Kolmogorov*. Cambridge university press.

GIBSON, J. F. 2011 Channelflow Website. www.channelflow.org.

GIBSON, J. F. 2012 Channelflow: A spectral Navier-Stokes simulator in C++. *Tech. Rep.*. U. New Hampshire.

GIBSON, J. F., HALCROW, J. & CVITANOVIĆ, P. 2008 Visualizing the geometry of state space in plane Couette flow. *Journal of Fluid Mechanics* **611**, 107–130.

GIBSON, J. F., HALCROW, J. & CVITANOVIĆ, P. 2009 Equilibrium and traveling-wave solutions of plane Couette flow. *Journal of Fluid Mechanics* **638**, 243–266.

GIBSON, J. F., REETZ, F., AZIMI, S., FERRARO, A., KREILOS, T., SCHROBSDORFF, H., FARANO, M., YESIL, A. F., SCHÜTZ, S. S., CULPO, M. & SCHNEIDER, T. M. 2019 Channelflow 2.0. *in preparation* .

GIBSON, J. F. & SCHNEIDER, T. M. 2016 Homoclinic snaking in plane Couette flow: bending, skewing and finite-size effects. *Journal of Fluid Mechanics* **794** (2013), 530–551.

GUALA, M., HOMMEMA, S. E. & ADRIAN, R. J. 2006 Large-scale and very-large-scale motions in turbulent pipe flow. *Journal of Fluid Mechanics* **554**, 521–542.

GUTZWILLER, M. C. 1990 Chaos in classical and quantum mechanics. *Journal of Physics A: Mathematical and Theoretical* **43**, 285302.

HAMILTON, J. M., KIM, J. & WALEFFE, F. 1995 Regeneration mechanisms of near-wall turbulence structures. *Journal of Fluid Mechanics* **287**, 317–348.

HÄRTEL, C. & KLEISER, L. 1998 Analysis and modelling of subgrid-scale motions in near-wall turbulence. *Journal of Fluid Mechanics* **356**, 327–352.

HOCKING, L. M. 1975 Non-linear instability of the asymptotic suction velocity profile. *The Quarterly Journal of Mechanics and Applied Mathematics* **28** (3), 341–353.

HOMMEMA, S. E. & ADRIAN, R. J. 2003 Packet structure of surface eddies in the atmospheric boundary layer. *Boundary-Layer Meteorology* **106**, 147–170.

HOPF, E. 1948 A mathematical example displaying features of turbulence. *Communications on Pure and Applied Mathematics* **1** (4), 303–322.

HOUGHTON, S. M. & KNOBLOCH, E. 2011 Swift-Hohenberg equation with broken cubic-quintic nonlinearity. *Physical Review E - Statistical, Nonlinear, and Soft Matter Physics* **84** (1), 1–10.

HUTCHINS, N. & MARUSIC, I. 2007 Large-scale influences in near-wall turbulence. *Philosophical Transactions of the Royal Society A: Mathematical, Physical and Engineering Sciences* **365** (1852), 647–664.

HWANG, Y. 2015 Statistical structure of self-sustaining attached eddies in turbulent channel flow. *Journal of Fluid Mechanics* **767**, 254–289.

HWANG, Y. & COSSU, C. 2010*a* Amplification of coherent streaks in the turbulent Couette flow: An inputoutput analysis at low Reynolds number. *Journal of Fluid Mechanics* **643**, 333–348.

HWANG, Y. & COSSU, C. 2010*b* Linear non-normal energy amplification of harmonic and stochastic forcing in the turbulent channel flow. *Journal of Fluid Mechanics* **664**, 51–73.

HWANG, Y. & COSSU, C. 2010*c* Self-Sustained Process at Large Scales in Turbulent Channel Flow. *Physical Review Letters* **105** (4), 044505.

HWANG, Y. & COSSU, C. 2011 Self-sustained processes in the logarithmic layer of turbulent channel flows. *Physics of Fluids* **23** (6).

HWANG, Y., WILLIS, A. P. & COSSU, C. 2016 Invariant solutions of minimal large-scale structures in turbulent channel flow for $\mathrm{Re}\tau$ up to 1000. *Journal of Fluid Mechanics* **802**, R1.

JEONG, J. & HUSSAIN, F. 1995 On the identification of a vortex. *Journal of Fluid Mechanics* **285**, 69–94.

JIMÉNEZ, J. 2018 Coherent structures in wall-bounded turbulence. *Journal of Fluid Mechanics* **842**, P1.

JIMÉNEZ, J. & MOIN, P. 1991 The minimal flow unit in near-wall turbulence. *Journal of Fluid Mechanics* **225**, 213–240.

JIMÉNEZ, J. & SIMENS, M. 2001 Low-dimensional dynamics of a turbulent wall flow. *Journal of Fluid Mechanics* **435**, 81–91.

KAWAHARA, G. & KIDA, S. 2001 Periodic motion embedded in plane Couette turbulence: regeneration cycle and burst. *Journal of Fluid Mechanics* **449**, 291–300.

KAWAHARA, G., UHLMANN, M. & VAN VEEN, L. 2012 The Significance of Simple Invariant Solutions in Turbulent Flows. *Annual Review of Fluid Mechanics* **44** (1), 203–225.

KAZANTSEV, E. 1998 Unstable periodic orbits and attractor of the barotropic ocean model. *Nonlinear Processes in Geophysics* **5** (4), 193–208.

KELLEY, C. T. 2003 *Solving Nonlinear Equations with Newton's Method*. Society for Industrial and Applied Mathematics.

KERSWELL, R. R. 2005 Recent progress in understanding the transition to turbulence in a pipe. *Nonlinearity* **18** (6), R17–R44.

KEVIN, K., MONTY, J. & HUTCHINS, N. 2019*a* The meandering behaviour of large-scale structures in turbulent boundary layers. *Journal of Fluid Mechanics* **865**, R1.

KEVIN, K., MONTY, J. & HUTCHINS, N. 2019*b* Turbulent structures in a statistically three-dimensional boundary layer. *Journal of Fluid Mechanics* **859**, 543–565.

KHAPKO, T., SCHLATTER, P., DUGUET, Y. & HENNINGSON, D. S. 2016 Turbulence collapse in a suction boundary layer. *J. Fluid Mech.* **795**, 356–379.

KIM, J., MOIN, P. & MOSER, R. 1987 Turbulence statistics in fully developed channel flow at low Reynolds number. *Journal of Fluid Mechanics* **177**, 133–166.

KIM, K. C. & ADRIAN, R. J. 1999 Very large-scale motion in the outer layer. *Physics of Fluids* **11** (2), 417–422.

KIM, W. W. & MENON, S. 1999 An unsteady incompressible Navier-Stokes solver for large eddy simulation of turbulent flows.

KLINE, S. J., REYNOLDS, W. C., SCHRAUB, F. A. & RUNSTADLER, P. W. 1967 The structure of turbulent boundary layers. *Journal of Fluid Mechanics* **30** (04), 741–773.

KNOBLOCH, E. 2015 Spatial Localization in Dissipative Systems. *Annual Review of Condensed Matter Physics* **6** (1), 325–359.

KNOBLOCH, E., UECKER, H. & WETZEL, D. 2019 Defectlike structures and localized patterns in the cubic-quintic-septic Swift-Hohenberg equation. *Physical Review E* **100** (1), 012204.

KOMMINAHO, J., LUNDBLADH, A. & JOHANSSON, A. V. 1996 Very large structures in plane turbulent Couette flow. *Journal of Fluid Mechanics* **320**, 259–285.

KOVASZNAY, L. S., KIBENS, V. & BLACKWELDER, R. F. 1970 Large-scale motion in the intermittent region of a turbulent boundary layer. *Journal of Fluid Mechanics* **41** (2), 283–325.

KREILOS, T., GIBSON, J. F. & SCHNEIDER, T. M. 2016 Localized travelling waves in the asymptotic suction boundary layer. *Journal of Fluid Mechanics* **795**, R3.

KREILOS, T., VEBLE, G., SCHNEIDER, T. M. & ECKHARDT, B. 2013 Edge states for the turbulence transition in the asymptotic suction boundary layer. *Journal of Fluid Mechanics* **726**, 100–122.

KURAMOTO, Y. & TSUZUKI, T. 1976 Persistent Propagation of Concentration Waves in Dissipative Media Far from Thermal Equilibrium. *Progress of Theoretical Physics* **55** (2), 356–369.

LAN, Y. 2010 Cycle expansions: From maps to turbulence. *Communications in Nonlinear Science and Numerical Simulation* **15** (3), 502–526.

LAN, Y. & CVITANOVIĆ, P. 2004 Variational method for finding periodic orbits in a general flow. *Physical Review E* **69** (1), 016217.

LAN, Y. & CVITANOVIĆ, P. 2008 Unstable recurrent patterns in Kuramoto-Sivashinsky dynamics. *Physical Review E* **78** (2), 026208.

LANDAU, L. D. & LIFSCHITZ, E. M. 1959 *Fluid mechanics*. Oxford: Pergamon.

LASAGNA, D. 2018 Sensitivity Analysis of Chaotic Systems Using Unstable Periodic Orbits. *SIAM Journal on Applied Dynamical Systems* **17** (1), 547–580.

LIAO, S. J. 1999 An explicit, totally analytic approximate solution for Blasius' viscous flow problems. *International Journal of Non-Linear Mechanics* **34** (4), 759–778.

LILLY, D. K. 1966 The representation of small-scale turbulence in numerical simulation experiments .

LIN, C. C. 1944 On the Stability of Two-Dimensional Parallel Flows. *Proceedings of the National Academy of Sciences* **30** (10), 316–324.

MARUSIC, I., MATHIS, R. & HUTCHINS, N. 2010 High Reynolds number effects in wall turbulence. *International Journal of Heat and Fluid Flow* **31** (3), 418–428.

MARUSIC, I. & MONTY, J. P. 2019 Attached Eddy Model of Wall Turbulence. *Annual Review of Fluid Mechanics* **51** (1), 49–74.

MASON, P. J. & CALLEN, N. S. 1986 On the magnitude of the subgrid-scale eddy coefficient in large-eddy simulations of turbulent channel flow. *Journal of Fluid Mechanics* **162**, 439–462.

MCKEON, B. J. 2017 The engine behind (wall) turbulence: perspectives on scale interactions. *Journal of Fluid Mechanics* **817**, P1.

VON MISES, R. & POLLACZEK-GEIRINGER, H. 1929 Praktische Verfahren der Gleichungsauflösung. *ZAMM - Zeitschrift für Angewandte Mathematik und Mechanik* **9** (2), 152–164.

NAGATA, M. 1990 Three-dimensional finite-amplitude solutions in plane Couette flow: bifurcation from infinity. *Journal of Fluid Mechanics* **217** (-1), 519–527.

NEELAVARA, S. A., DUGUET, Y. & LUSSEYRAN, F. 2017 State space analysis of minimal channel flow. *Fluid Dynamics Research* **49** (3), 035511.

PARK, J., HWANG, Y. & COSSU, C. 2011 On the stability of large-scale streaks in turbulent Couette and Poiseulle flows. *Comptes Rendus Mécanique* **339** (1), 1–5.

PARK, J. S. & GRAHAM, M. D. 2015 Exact coherent states and connections to turbulent dynamics in minimal channel flow. *Journal of Fluid Mechanics* **782**, 430–454.

PATHAK, J., HUNT, B., GIRVAN, M., LU, Z. & OTT, E. 2018 Model-Free Prediction of Large Spatiotemporally Chaotic Systems from Data: A Reservoir Computing Approach. *Physical Review Letters* **120** (2), 024102.

POINCARÉ, H. 1892 *Les méthodes nouvelles de la mécanique céleste*, , vol. 10. Paris: Gauthier-Villars.

POPE, S. B. 2000 *Turbulent flows*. Cambridge university press.

PUJALS, G., GARCÍA-VILLALBA, M., COSSU, C. & DEPARDON, S. 2009 A note on optimal transient growth in turbulent channel flows. *Physics of Fluids* **21** (1).

RAWAT, S., COSSU, C., HWANG, Y. & RINCON, F. 2015 On the self-sustained nature of large-scale motions in turbulent Couette flow. *Journal of Fluid Mechanics* **782**, 515–540.

RAWAT, S., COSSU, C. & RINCON, F. 2016 Travelling-wave solutions bifurcating from relative periodic orbits in plane Poiseuille flow. *Comptes Rendus - Mecanique* **344** (6), 448–455.

REETZ, F. 2019 Turbulent patterns in wall-bounded shear flows: invariant solutions and their bifurcations. PhD thesis, EPFL.

REETZ, F., KREILOS, T. & SCHNEIDER, T. M. 2019 Exact invariant solution reveals the origin of self-organized oblique turbulent-laminar stripes. *Nature Communications* **10** (1), 2277.

REETZ, F. & SCHNEIDER, T. M. 2020*a* Invariant states in inclined layer convection. Part 1. Temporal transitions along dynamical connections between invariant states. *under revision at JFM* pp. 1–30.

REETZ, F. & SCHNEIDER, T. M. 2020*b* Periodic orbits exhibit oblique stripe patterns in plane Couette flow. *under revision at PRF* .

REETZ, F., SUBRAMANIAN, P. & SCHNEIDER, T. M. 2020 Invariant states in inclined layer convection. Part 2. Bifurcations and connections between branches of invariant states. *under revision at JFM* pp. 1–36.

RUELLE, D. 1978 *Thermodynamic formalism: The mathematical structures of classical equilibrium statistical mechanics*, 1st edn. Addison-Wesley.

SAAD, Y. 2003 *Iterative Methods for Sparse Linear Systems*. Society for Industrial and Applied Mathematics.

SAAD, Y. & SCHULTZ, M. H. 1986 GMRES: A Generalized Minimal Residual Algorithm for Solving Nonsymmetric Linear Systems. *SIAM Journal on Scientific and Statistical Computing* **7** (3), 856–869.

SAGAUT, P. 2006 *Large eddy simulation for incompressible flows: an introduction*. Springer Science & Business Media.

SALEWSKI, M., GIBSON, J. F. & SCHNEIDER, T. M. 2019 Origin of localized snakes-and-ladders solutions of plane Couette flow. *Physical Review E* **100** (3), 031102.

SÁNCHEZ, J. & NET, M. 2010 On the Multiple Shooting Continuation of Periodic Orbits By Newton–Krylov Methods. *International Journal of Bifurcation and Chaos* **20** (01), 43–61.

SANCHEZ, J., NET, M., GARCIIA-ARCHILLA, B. & SIMO, C. 2004 Newton–Krylov continuation of periodic orbits for Navier–Stokes flows. *Journal of Computational Physics* **201** (1), 13–33.

SASAKI, E., KAWAHARA, G., SEKIMOTO, A. & JIMÉNEZ, J. 2016 Unstable periodic orbits in plane Couette flow with the Smagorinsky model. *Journal of Physics: Conference Series* **708**, 012003.

SCHLATTER, P., LI, Q., BRETHOUWER, G., JOHANSSON, A. V. & HENNINGSON, D. S. 2010 Simulations of spatially evolving turbulent boundary layers up to Reθ=4300. *International Journal of Heat and Fluid Flow* **31** (3), 251–261.

SCHLATTER, P. & ÖRLÜ, R. 2011 Turbulent asymptotic suction boundary layers studied by simulation. *Journal of Physics: Conference Series* **318** (2), 022020.

SCHLICHTING, H. 2004 *Boundary-layer theory*. Springer.

SCHNEIDER, T. M., ECKHARDT, B. & YORKE, J. A. 2007 Turbulence transition and the edge of chaos in pipe flow. *Physical Review Letters* **99**, 34502.

SCHNEIDER, T. M., GIBSON, J. F. & BURKE, J. 2010*a* Snakes and Ladders: Localized Solutions of Plane Couette Flow. *Physical Review Letters* **104** (10), 104501.

SCHNEIDER, T. M., MARINC, D. & ECKHARDT, B. 2010*b* Localized edge states nucleate turbulence in extended plane Couette cells. *Journal of Fluid Mechanics* **646**, 441.

SIVASHINSKY, G. I. 1977 Nonlinear analysis of hydrodynamic instability in laminar flames—I. Derivation of basic equations. *Acta Astronautica* **4** (11-12), 1177–1206.

SKUFCA, J. D., YORKE, J. A. & ECKHARDT, B. 2006 Edge of chaos in a parallel shear flow. *Physical Review Letters* **96**, 174101.

SMAGORINSKY, J. 1963 General Circulation experiments with the primitive equations. *MONTHLY WEATHER REVIEW* **91**, 99–164.

SMYRLIS, Y. S. & PAPAGEORGIOU, D. T. 1996 Computational study of chaotic and ordered solutions of the Kuramoto-Sivashinsky equation. *Tech. Rep.*. Institute for Computer Applications in Science and Engineering, NASA Langley Research Center.

SURI, B., TITHOF, J., GRIGORIEV, R. O. & SCHATZ, M. F. 2017 Forecasting Fluid Flows Using the Geometry of Turbulence. *Physical Review Letters* **118** (11), 114501.

THEODORSEN, T. 1952 Mechanism of turbulence. In *Proceedings of the Second Midwestern Conference on Fluid Mechanics*, pp. 1–18. Ohio State University.

THOMAS, T. Y. 1942 Qualitative Analysis of the Flow of Fluids in Pipes. *American Journal of Mathematics* **64** (1), 754–767.

TOMKINS, C. D. & ADRIAN, R. J. 2003 Spanwise structure and scale growth in turbulent boundary layers. *Journal of Fluid Mechanics* **490** (490), 37–74.

TOWNSEND, A. A. 1956 *The Structure of Turbulent Shear Flow*. Cambridge Univ Press.

TOWNSEND, A. A. 1976 *The structure of turbulent shear flow*, 2nd edn. Cambridge, UK: Cambridge U. Press.

VAN VEEN, L., VELA-MARTIN, A. & KAWAHARA, G. 2018 Time-periodic inertial range dynamics. *arXiv preprint* .

VISWANATH, D. 2007 Recurrent motions within plane Couette turbulence. *Journal of Fluid Mechanics* **580**, 339–358.

VISWANATH, D. 2009 The critical layer in pipe flow at high Reynolds number. *Philosophical Transactions of the Royal Society of London A: Mathematical, Physical and Engineering Sciences* **367** (1888), 561–576.

VLACHAS, P. R., BYEON, W., WAN, Z. Y., SAPSIS, T. P. & KOUMOUTSAKOS, P. 2018 Data-driven forecasting of high-dimensional chaotic systems with long short-term memory networks. *Proceedings of the Royal Society A: Mathematical, Physical and Engineering Science* **474** (2213), 20170844.

WALEFFE, F. 1995 Hydrodynamic stability and turbulence: beyond transients to a self-sustaining process. *Studies in applied mathematics* **95** (3), 319–343.

WALEFFE, F. 1997 On a self-sustaining process in shear flows. *Physics of Fluids* **9** (4), 883–900.

WALEFFE, F. 1998 Three-dimensional coherent states in plane shear flows. *Physical Review Letters* **81**, 4140–4143.

WALEFFE, F. 2001 Exact coherent structures in channel flow. *Journal of Fluid Mechanics* **435**, 93–102.

WALEFFE, F. 2003 Homotopy of exact coherent structures in plane shear flows. *Physics of Fluids* **15** (6), 1517–1534.

WANG, J., GIBSON, J. F. & WALEFFE, F. 2007 Lower Branch Coherent States in Shear Flows: Transition and Control. *Physical Review Letters* **98** (20), 204501.

WARK, C. E., NAGUIB, A. M. & NAGIB, H. M. 1989 Effect of flat-plate manipulation on the coherent structures in a turbulent boundary layer. *AIAA 2nd Shear Flow Conference, 1989* .

WILLIS, A. P., HWANG, Y. & COSSU, C. 2010 Optimally amplified large-scale streaks and drag reduction in turbulent pipe flow. *Physical Review E - Statistical, Nonlinear, and Soft Matter Physics* **82** (3), 1–11.

WOODS, P. D. & CHAMPNEYS, A. R. 1999 Heteroclinic tangles and homoclinic snaking in the unfolding of a degenerate reversible Hamiltonian-Hopf bifurcation. *Physica D: Nonlinear Phenomena* **129** (3-4), 147–170.

YANG, Q., WILLIS, A. P. & HWANG, Y. 2019 Exact coherent states of attached eddies in channel flow. *Journal of Fluid Mechanics* **862**, 1029–1059.

ZIMMERMANN, R. S. & PARLITZ, U. 2018 Observing spatio-temporal dynamics of excitable media using reservoir computing. *Chaos: An Interdisciplinary Journal of Nonlinear Science* **28** (4), 043118.

Sajjad Azimi

Curriculum Vitae

Date and Place of Birth: 15 January 1990, Iran
Current Address: Chemin des Bancels 6, 1004 Lausanne
Email: sajjad.azimi@epfl.ch or azimi576@gmail.com

Education

2015-2020 **PhD in mechanical engineering**, *EPFL*, Switzerland.
Thesis title: "Invariant solutions underlying small- and large-scale structures in turbulent boundary layers" under the supervision of Prof. Tobias M. Schneider

2012– 2015 **Master in mechanical engineering**, *Sharif University of Technology*, Iran, GPA 19.07/20.
Thesis title: "Simulation, optimization and design of Bosch process dry etching"

2008– 2012 **Bachelor in mechanical engineering**, *Sharif University of Technology*, Iran, GPA 18.75/20.
Thesis title: "Simulation, design and manufacturing of a device for surface cleaning"

Honours and Scholarships

2015-2018 **Swiss Government Excellence Scholarship** for foreign PhD students

2014 **Ranked** 1st among all the graduate students in mechanical engineering department, Sharif University of Technology

2013 **Best** BSc. thesis in mechanical engineering in the country from the Iranian Society of Mechanical Engineers (ISME)

2012 **Ranked** 1st among the undergraduate students in mechanical engineering department, Sharif University of Technology

Publications

S. Azimi, O. Ashtari, T.M. Schneider, "Adjoint-based variational method for constructing periodic orbits of high-dimensional chaotic systems", *submitted to SIAM Journal on Scientific Computing*

S. Azimi, C. Cossu, T.M. Schneider, "Invariant solutions representing large-scale motions of the turbulent asymptotic suction boundary layer", *in preparation*

S. Azimi, C. Cossu, T.M. Schneider, "Self-sustained large-scale motions in the asymptotic suction boundary layer", *submitted to Journal of Fluid Mechanics*

S. Azimi and T.M. Schneider, "Modified snaking in plane Couette flow with wall-normal suction", *submitted to Journal of Fluid Mechanics*

S. Azimi and T.M. Schneider (2020), "Self-similar invariant solution in the near-wall region of a turbulent boundary layer at asymptotically high Reynolds numbers", *Journal of Fluid Mechanics*, 888, A15

S. Azimi and M.S. Saidi (2018), "A new algorithm to solve sinusoidal steady-state Maxwell's equations on unstructured grids", *Scientia Iranica B*, 25(3), 1296-1302

A. Kiyoumarsioskouei, A. Shamloo, **S. Azimi**, M. Abeddoust, M.S. Saidi (2016), "A computational model for estimation of mechanical parameters in chemotactic endothelial cells", *Scientia Iranica B*, 23(1), 260-267

Conferences

2019 "Invariant solutions of the filtered Navier-Stokes equations representative of large-scale motions in the asymptotic suction boundary layer flow", ETC17, Torino, Italy

2018 "Exact invariant solutions in the near-wall region of boundary layer turbulence at high Reynolds numbers", EFMC12, Vienna, Austria

2017 "Modified snaking in plane Couette flow with wall-normal suction", Euromech Symp. 591: 3D instability mechanisms transitional and turbulent flows, Bari, Italy

Teaching Experiences

2016-2019 **Incompressible fluid mechanics** in EPFL by T.M. Schneider

Spring 2017 supervision of semester project **Chiral sinkers** in EPFL

Fall 2012 **Fluid mechanics** in Sharif University of Technology by A. Shamloo

Spring 2012 **Thermodynamics** in Sharif University of Technology by A. Moosavi

Spring 2012 **Fluid mechanics** in Sharif University of Technology by A. Shamloo

Fall 2011 **Fluid mechanics** Sharif University of Technology by A. Shamloo

Research Experiences

2013-2015 **Ehsan Tech Particle Engineering Co.**, *Part time*, Tehran, Iran.
Research, design and calibration of aerosols monitoring instruments

2012 **Micro and Nano Fluids Lab.**, *Internship*, Sharif University of Technology.
Numerical simulations of a viscous jet entering a bath of the same fluid

2011 **Biofluids Lab.**, *Internship*, Sharif University of Technology.
Numerical simulations of a micro bioreactor